High-valent dinuclear bis-μ-hydroxo complexes for PCET reactivity

A thesis submitted to the University of Dublin in fulfilment of the requirements for the degree of Doctor of Philosophy by

Giuseppe Spedalotto

Under the supervision of Dr A.R. McDonald

School of Chemistry
Trinity College Dublin
March 2021

I declare that this thesis has not been submitted as an exercise for a degree at this or any other university and is my own work. Parts of the work described herein are the product of collaboration and are acknowledged at the beginning of each chapter. I agree to deposit this thesis in the University's open access institutional repository or allow the library to so on my behalf, subject to Irish Copyright legislation and Trinity College Library conditions of use and acknowledgements.

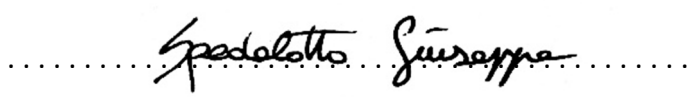

Giuseppe Spedalotto

Summary

High valent dinuclear bis-μ-hydroxo transition metals complexes are hypothesised to play a potentially crucial role in several enzymatic mechanisms involving their high-valent dinuclear bis-μ-oxo counterparts such as soluble Methane Monooxygenase and Tyrosinase. However, even though late transition metals such as Ni and Cu, are postulated to be extremely powerful oxidants, an overall dearth of high-valent late transition metals μ-hydroxo model systems is present in literature. The main topics reported in the present thesis are the preparation, characterisation and study of high-valent dinuclear bis-μ-hydroxo complexes based on Ni and Cu, supported by a novel tailored diamide ligand.

As the first step, in Chapter 2 we successfully identified the bidentate diamide $DMMA^{Me_2}$ ligand as a suitable platform for the synthesis of the desired complexes. The ligand was designed to be oxidatively robust and bear anionic nitrogen donor functionalities in order to stabilise high valent oxidants. In chapter 3, starting from the synthesised diamide ligand, the dinuclear $[\mathbf{L}Ni^{II}(\mu\text{-}OH)]_2$ species ($\mathbf{L}$ = $DMMA^{Me_2}$) was successfully synthesised and characterised by a series of techniques, such as XRD, FT-IR, NMR, cyclic voltammetry, mass spectrometry and electronic absorption spectroscopy. Notably, $[\mathbf{L}Ni^{II}(\mu\text{-}OH)]_2$ exhibited a diamond core structure with two hydroxide ligands bridging the Ni^{II} ions, which lie in a distorted square planar environment.

Cyclic voltammetry experiment showed the presence of two accessible higher oxidation states that were thoroughly explored by chemical oxidation. The low valent complex $[\mathbf{L}Ni^{II}(\mu\text{-}OH)]_2$ was reacted with a one electron oxidant (*i.e.* CAN) at low temperature (-45 °C), leading to the formation of the metastable mixed valent $Ni^{II}Ni^{III}$ and high valent Ni^{III}_2 species upon addiction of 1 equiv. and 3.4 equiv. of oxidant respectively. X-band EPR monitored titration of CAN with $[\mathbf{L}Ni^{II}(\mu\text{-}OH)]_2$ showed the clear conversion of the $S = 0$ low valent Ni^{II}_2 precursor into the $S = 1/2$ mixed valent species $Ni^{II}Ni^{III}$.

Further addition of oxidant led to the high valent Ni^{III}_2, which exhibited a silent spectrum in perpendicular mode EPR, due to antiferromagnetic ($S = 0$) or ferromagnetic coupling ($S = 1$) between the unpaired electrons on the Ni^{III} centres. The possibility of such coupling was confirmed by DFT calculations, which found that both configurations are possible under the experimental conditions, with negligible differences in energy. X-ray absorption spectroscopy and DFT calculations were consistent with the assigned oxidations

states and confirmed that the bridging hydroxide ligands were maintained in the mixed and high valent species despite the increase in oxidation state, making $\mathbf{L}_2Ni^{II}Ni^{III}(\mu\text{-}OH)_2$ and $[\mathbf{L}Ni^{III}(\mu\text{-}OH)]_2$ the first examples of high-valent bis-μ-hydroxo-Ni_2 reported to date.

In Chapter 4, $\mathbf{L}_2Ni^{II}Ni^{III}(\mu\text{-}OH)_2$ and $[\mathbf{L}Ni^{III}(\mu\text{-}OH)]_2$ were demonstrated to be competent in the oxidation of phenolic O−H bonds using a series of *para*-X-2,6-di-*tert*-butylphenols (X = $-OCH_3$, $-CH_3CH_2$, $-CH_3$, $-C(CH_3)_3$, −H, −Br, −CN, $-NO_2$). Analysis of the kinetic data showed that both species were capable of performing O−H bond oxidation through a hydrogen atom transfer mechanism. Notably, upon reaction with the substrates, the $[\mathbf{L}Ni^{III}(\mu\text{-}OH)]_2$ complex decayed in a biphasic fashion, leading in the first step to the formation of the proposed reactive intermediate species $\mathbf{L}_2Ni^{II}Ni^{III}(\mu\text{-}OH\text{-}\mu\text{-}OH_2)$. ESI mass spectrometry and ^{1}H-NMR experiments of the post reaction mixtures of $\mathbf{L}_2Ni^{II}Ni^{III}(\mu\text{-}OH)_2$ and $[\mathbf{L}Ni^{III}(\mu\text{-}OH)]_2$ displayed the presence of the free pristine ligand, suggesting the formation of an intermediate unstable $[\mathbf{L}Ni^{II}(\mu\text{-}OH_2)]_2$ species as end reaction product and allowing for the determination of an overall reaction mechanism.

The formation of the proposed $[\mathbf{L}Ni^{II}(\mu\text{-}OH_2)]_2$ species was corroborated by the reaction of $[\mathbf{L}Ni^{II}(\mu\text{-}OH)]_2$ with 2,6-dimethylbenzoic acid, which led to the formation of a double protonated species with p*K*a values of 9.7 and 10 in DMF. In addition, the high valent species $[\mathbf{L}Ni^{III}(\mu\text{-}OH)]_2$ was also able to oxidise 9,10- dihydroanthracene ($BDE_{C–H}$ = 78 kcal/mol) to yield anthracene in ≈ 80% yield (GC-FID), albeit a proper kinetic study was not possible as this reaction occurred at comparable rates with the self-decay of the complex.

Finally, in Chapter 5, we extended our study to Cu, applying the acquired knowledge on the $DMMA^{Me2}$ based complexes to successfully synthesise complex $[\mathbf{L}Cu^{II}(\mu\text{-}OH)]_2$. The complex was characterised by FT-IR, ESI mass spectrometry and X-ray diffraction, identifying $[\mathbf{L}Cu^{II}(\mu\text{-}OH)]_2$ as characterized by a diamond core structure almost identical to what was observed in $[\mathbf{L}Ni^{III}(\mu\text{-}OH)]_2$. Cyclic voltammetry experiment detected the presence of only one accessible higher oxidation state, which was probed reacting the low valent Cu^{II} precursor with CAN (1.5 equiv.) at low temperature (-45 °C) in DMF leading to the formation of a new species, tentatively identified as the $\mathbf{L}_2Cu^{II}Cu^{III}(\mu\text{-}OH)_2$, in parallel to what has been observed for the Ni complex. Both EPR and Cu K-edge absorption spectroscopy experiments were consistent with the proposed structure of the mixed valent species, although none of them confirmed it unequivocally. Nevertheless,

reactivity of $\mathbf{L}_2Cu^{II}Cu^{III}(\mu\text{-}OH)_2$ towards phenolic O−H bonds was analysed by reaction with a series of *para*-X-2,6-di-*tert*-butylphenols (X = $-OCH_3$, $-CH_2CH_3$, $-CH_3$, $-C(CH_3)_3$, −H, $-NO_2$), showing its capability of performing the oxidation of phenolic O−H bonds through a hydrogen atom transfer mechanism.

Acknowledgements

I would like to express my gratitude to all the people who have given encouragement, assistance and support during this PhD adventure. If I am at this stage, at the end of the line, it is also thanks to you. First of all, I want to thank my advisor, Dr Aidan McDonald, for his guidance and teachings, and for motivating me throughout my PhD. I'll be forever grateful for all the opportunities he has offered me in these four years, allowing my growth as a scientist and man.

I would like to thank all the collaborators and technical staff in the School of Chemistry that contributed and helped me in this project. My first thanks are for Dr Eric R. Farquhar (Brookhaven National Laboratory) for his teachings about X-Ray absorption spectroscopy and the valuable time spent together at the SSRL. I would also like to thank Prof Robert Barkley (School of Physics, TCD) for providing access to the EPR spectrometer and Dr Brendan Twamley for X-ray diffraction data collection, solution and refinement of the crystal structures reported in this thesis. I thank Dr Martin Feeney and Dr Gary Hessman for the measurement of mass spectra, and Dr John O'Brien and Dr Manuel Ruether for their help with NMR spectroscopic measurements.

I would like to thank all the present and past members of the McDonald group: Andy, Xin, Adriana, Ciara, Paolo, Marta, Jackie, Bertrand, Ankita, Prasenjit, Philipp, Daniel, Lorna, Robert, Chaka, Duenpen and Alex. It's been a pleasure to work with you guys! Anyway, a special thank goes to some people in particular. In the first place to Robert, for all the hard work on DFT calculations, for helping me reading over part of this thesis and for all the precious conversations had during these years. Another special thanks goes to Marta, not only for performing all EPR experiments and simulation reported in this thesis but for being such a valid friend and colleague, sharing with me questionable musical tastes and helping me to keep the lab alive. All my gratitude to Ciara, for your incredible help revising the language of the whole thesis, and for being such a nerd as I am! Last, but not least, thank you, Paolo. You were the first person I met once arrived in the group and probably the one that I annoyed more (and I keep doing it) over these years. I'll be forever grateful for your patience.

I also want to thank all my friends in the department and the Italian group for all the fun and support, helping me feel less far from home during these years.

A huge thanks to my family back home, for everything they have done for me and for the support they have always shown to me. Finally, a special thanks to Martina. Thank you for believing in me, supporting me and suffering with me every day. I wouldn't be here without you.

Abbreviations

ATR-FTIR	attenuated total reflection Fourier transform infrared spectroscopy
BDE	bond dissociation energy
BDFE	bond dissociation free energy
bispicen	*N*, *N'*-bis(2-pyridylmethyl)ethane-l,2-diamine
bispicMe_2en	*N*, *i*-bis(2-pyridylmethyl)-*N*, *N*'-dimethylethane-1,2-diamine
bitripy	1,2-bis[2-(bis(6-methyl-2-pyridyl)methyl)6-pyridyl]ethane
BMM	bacterial multicomponent monooxygenases
Bn_2en	*N*,*N'*-dibenzylethylenediamine
BnBQA	*N*-benzyl-*N*,*N*-di(quinolin-2-ylmethyl)amine
Bnen	*N*-benzyl-ethylenediamine
6-Me_2bpg	*N*,*N*-bis(6-methyl-2-pyridylmethyl)glycinate
BPQA	bis(2-quinolylmethyl)-(2-pyridylmethyl)amine
Bpy	bipyridine
Bz_3-tacn	1,4,7-tribenzyl-1,4,7-triazacyclononane
BzPY1	*N*,*N*-bis[2-(2-pyridyl)-ethyl]benzylamine
CPET	concerted proton electron transfer
DFT	density functional theory
DHA	9,10-dihydroanthracene
DMEGdmae	N^1-(1,3-dimethylimidazolidin-2-yliden)-N^2,N^2-dimethylethan-1,2-diamine
DMF	*N*,*N'*-dimethylformamide
$DMMA^{R2}$	N^1,N^3-bis(2,6-di-R-phenyl)-2,2-dimethylmalonamide
dpema	*N*,*N*-(di-[2-pyridine-2-yl]ethyl)methylamine
6-Me-DPEN	*N*,*N*-Bis(6-methyl-2-pyridilmethyl)ethane-1,2- diamine
DPMN	2,7-bis(dipyridyl)methyl)-1-8-naphthyridine
DPX	xanthene-bridged cofacial bis-porphyrin
2,4-DTBP	2,4-di-*tert*-butyl phenol
2,6-DTBP	2,4-di-*tert*-butyl phenol

EPR	electron paramagnetic resonance
ESI-MS	electronspray ionisation mass spectrometry
ET	electron transfer
EXAFS	extended X-ray absorption fine structure
FAD	flavin adenine dinucleotide
FMN	flavin mononucleotide
FTF 4-2,1-NH	face-to-face porphyrin dimer
GC-FID	gas chromatography - flame ionisation detector
^{H,tBu}ed	N^1,N^2-di-tert-butylethane-1,2-diamine
HAA	hydrogen atom transfer
HAT	hydrogen Atom transfer
HBPMP	2,6-bis{[(bis(2-pyridylmethyl)amino]methyl}-4-methylphenol
HERFD-XAS	high energy resolution fluorescence detection X-ray absorption spectroscopy
H-L	N^1,N^1,N^3-tris((6-methylpyridin-2-yl)methyl)-N^3-(pyridin-2-ylmethyl)benzene-1,3-diamine
6-HPA	1,2-bis{2-[bis(2-pyridylmethyl)aminomethyl]pyridin-6-yl}ethane
H-PYA*N*	*N*-[2-(pyridin-2-yl)-ethyl]-*N*,*N*′,*N*′-trimethyl-propane-1,3-diamine
iPr$_2$H-tacn	1,7-bisisopropyl-1,4,7-triazacyclononane
iPr$_3$-tacn	1,4,7-triisopropyl-1,4,7-triazacyclononane
L_1^H	*N*,*N*-bis[2-(2-pyridyl)ethyl]-2-phenylethylamine
L5	*N*,*N*'-(1,3-phenylenebis(methylene))bis(2-(pyridin-2-yl)-*N*-(2-(pyridin-2-yl)ethyl)ethan-1-amine)
L-DOPA	3,4-dihydroxy-L-phenylalanine
L-DOPA-quinone	4-(2-carboxy-2-aminoethyl)-1,2-benzoquinone
L_H	*N*-ethyl-*N*-phenethyl-2-(pyridin-2-yl)ethan-1-amine
L_{nBuBIM}	bis(1-butyl-1*H*-imidazol-2-yl)methane
L_{Py1Bz}	*N*-ethyl-*N*-(phenylmethyl-d_2)-2-(pyridin-2-yl)ethan-1-amine
L^{Py2}	*N*-(phenylmethyl-d_2)-2-(pyridin-2-yl)-*N*-(2-(pyridin-2-yl)ethyl)ethan-1-amine
L^{PzTACN}	3,5-bis((4,7-diisopropyl-1,4,7-triazonan-1-yl)methyl)-4*H*-pyrazole
Me$_2$-imdz	1,2-dimethyl-1*H*-imidazole

Me_2TPA	1-(6-methylpyridin-2-yl)-*N*-((6-methylpyridin-2-yl)methyl)-*N*-(pyridin-2-ylmethyl)methanamine
Me_3NTB	tris((1-methyl-1*H*-benzo[d]imidazol-2-yl)methyl)amine
Me_3-tacn	1,4,7-trimethyl-1,4,7-triazacyclononane
Me_4dtne	1,2-bis(4,7dimethyl-1,4,7-triazacyclonon-1-yl)ethane
MMOB	sMMO regulatory protein
MMOH	sMMO hydroxylase
$MMOH_{ox}$	MMOH with a diiron(III) site
$MMOH_{red}$	MMOH with a diiron(II) site
MMOR	sMMO reductase
MO	monooxygenase
N3	(-$(CH_2)_3$-linked bis[2-(2-pyridyl)ethyl]amine)
N4py	(1,1-di(pyridin-2-yl)-*N*,*N*-bis(pyridin-2-ylmethyl)methanamine
NAD(H)	nicotinamide adenine dinucleotide
NADP	nicotinamide adenine dinucleotide phosphate
N-Et-HPTB	*N*,*N*,*N*',*N*'-tetrakis(2-(1-ethylbenzimidazolyl))-2-hydroxy-1,3-diaminopropane
NMR	nuclear Magnetic resonance
OAT	oxygen atom transfer
OEC	oxygen evolution complex
^{O}L	*N*-(5-(tert-butyl)-2-methoxybenzyl)-1-(pyridin-2-yl)-*N*-(pyridin-2-ylmethyl)methanamine
PCET	proton coupled electron transfer
PDB	protein Data Bank
$PhTt^{tBu}$	phenyl-tris((*tert*-butylthio)methyl)borate
pMMO	particulate methane monooxygenase
PN2	4,4-di-*tert*-butyl-2,2,6,6-tetramethyl-3λ^2,5λ^2-diaza-4λ^4-phospha-2,6-disilaheptane
PSII	photosystems II
PT	proton transfer
$(py{N_2}^{Bz})_2$	1,4,10,13-tetraaza-cyclo-2,3,11,12-dibenzo-6,8,15,17-dipyridyl-octadecan-5,9,14,18-tetraone
QM/MM	quantum mechanics/molecular mechanics

R*N*R	ribonucleotide reductase
(2-OH)salpn	2-hydroxyl-[*N*,*N*′-bis(salicylidene)-1,2-propanediamine]
(2-OH)-5-*N*O_2salpn	2-hydroxyl-5-nitro-[*N*,*N*′-bis(salicylidene)-1,2-propanediamine]
SMA	small molecule activation
sMMO	soluble methane monooxygenase
SSRL	Stanford Synchrotron Radiation Lightsource
tacn	1,4,7-trimethyl-1,4,7-triazacycIononane
TAML	tetra-amido macrocyclic ligand
^{tBu}DPA	bis(2-pyridylmethyl)*tert*-butylamine
terpy	terpyridine
THF	tetrahydrofuran
tmc	1,4,8,11-tetramethyl-1,4,8,11-tetraazacyclotetradecane
TMEDA	tetramethyl ethylenediamine
TPA	*N,N,N*-tri(2-pyridylmethyl)amine)
TPA*	tris(3,5-dimethyl-4-methoxypyridyl-2-methyl)amine)
5-Et3-TPA	tris(5-ethyl-2-pyridylmethyl)amine
5-Me3-TPA	tris(5-methyl-2-pyridylmethyl)amine
6-Me3-TPA	tris(6-methyl-2-pyridylmethyl)amine
Tp^{iPr2}	hydrotris(3,5-diisopropyl-1-pyrazolyl)borate
Tp^{iPrMe}	hydrotris(3-isopropyl-5-methylpyrazolyl)borate)
Tp^{Me3}	hydrotris(3,4,5-trimethyl-1-pyrazolyl)borate
XANES	X-ray absorption near edge spectroscopy

Contents

Chapter 1

Introduction

1.1. Small molecule activation

Small molecule activation (SMA) is a large class of chemical transformations that are considered the pillars on which of the modern chemical industry has been built on in the last century. The Haber-Bosch process, namely the main industrial procedure for the synthesis of NH_3,[1] and the steam methane reforming process,[2] responsible of the 95% of H_2 world production starting from natural gas,[3] are both wonderful examples of small molecule activation reactions and also two of the more important and impacting reactions performed worldwide in terms of amount of products and costs.[1, 4] Both of these processes requires harsh conditions (extremely high pressure and temperature) due to the inertness towards functionalisation of their substrates, making them not sustainable in the long term from an economical and environmental point of view. Therefore, research into more cost effective and greener processes, such nitrogen fixation,[5] oxidative methane coupling (namely the catalytic conversion of methane to ethylene),[6, 7] or mild oxidation of methane ($BDE_{C–H}$ = 105 kcal/mol)[8] to methanol became one of the main aims of the chemistry community.

In particular, the catalytic oxidation of the C–H bonds present in saturated hydrocarbons is one of the most important modern challenges. Hydrocarbons constitute the most abundant and utilised feedstock for organic-based chemical industry; however, as mentioned above, this class of compound exhibits an overall inertness to functionalisation due to the strength of their C–H bonds (BDE = 75–105 kcal/mol). Such inertness represents a crucial problem, since the conversion of hydrocarbons to more valuable and reactive refined products, such as the corresponding oxygenated derivatives, is indispensable for their use in the productive cycles.[9] Moreover, for gaseous hydrocarbon feedstocks such as methane or propane, their conversion to the corresponding liquid oxygenated products is sometimes necessary for mere logistic and transportation issues. Conversion of hydrocarbons to functionalised products occurs nowadays only under harsh-conditions (elevated temperature and high pressure), in unsustainable processes such cracking, dehydrogenation or reforming, which are pillars of the modern petroleum-derived industry. Moreover, the low selectivity of such processes leads to the formation of enormous amounts of unwanted, often toxic, by-products, increasing the costs for their disposal and worsening the environment pollution. Consequently, the development of

more sustainable catalytic routes for the replacement of these methods with exothermic, green, highly-selective single-step oxidation processes is indispensable.[4]
Metalloenzymes, and oxygenases, could appear to be a solution, since they are able to activate atmospheric dioxygen and oxidise strong C–H bonds such as methane (BDE_{C-H} = 104kcal/mol) at physiological conditions. However, they are not suitable for large scale processes. In the light of such consideration, the development of biomimetic catalysts, synthetically accessible but capable of performing similar processes to their enzymatic counterparts is the most promising path to pursue. This greener and more sustainable approach is inspired by nature, understanding that enzymes are capable of activating such challenging substrates and trying to synthetically replicate their functions, obtaining metal complexes able to perform such difficult reactions in a sustainable way.[10]

1.2. SMA in biology: Dioxygen activation

As anticipated above, among all the enzymatic systems performing small molecule activation, those capable of oxidising strong O/C−H bonds through activation of atmospheric O_2 are definitely the more intriguing and relevant from both a chemical and industrial point of view.[4, 10] The enzymes capable of such reactivity are iron and copper based systems defined as *oxygenases*,[11] and can be divided in *dioxygenases*, which catalyse the incorporation of a molecule of O_2 in the substrate (Scheme 1.1), and *monooxygenases*, which transfer one oxygen atom to the substrate and reduce the second one to H_2O (Scheme 1.1).[12]

In spite of the different mechanisms and active sites proposed for the oxygenase enzymes, it is possible to identify common features regarding how the O_2 molecule is activated in the presence of metal cofactors (Scheme 1.1).[10, 13] In the first step, a dioxygen molecule binds to the metal centre and, simultaneously, is converted to the superoxide ligand (O_2^-) through a one-electron reduction. The O_2 moiety is then further reduced, leading to the formation of a hydroperoxide/peroxide ligand for mononuclear metal centres; in the case of di-nuclear metal centres, the superoxide ligand evolves into a μ-peroxide unit (Scheme 1.1). The increase of the electron population of the antibonding orbitals upon reduction

of the O_2 molecule leads to the scission of the O–O bond, forming the actual oxidant responsible for the substrate oxidation, albeit superoxide, peroxide and hydroperoxide intermediates have been demonstrated to react directly with the substrates in particular cases.[13] The species obtained upon O–O bond scission are high-valent mononuclear metal oxygen adducts bearing terminal oxo or oxyl ligands (*e.g.* $(L^{\bullet+})Fe^{IV}=O\leftrightarrow(L)Fe^{V}=O$, $Fe^{IV}=O$, $Fe^{V}(OH)=O$, $Cu^{III}=O\leftrightarrow Cu^{II}-O^{\bullet}$)[10, 13, 14] or dinuclear μ-oxo bridging species (e.g. $Fe^{IV}(\mu\text{-}O)_2$, $Cu^{III}_2(\mu\text{-}O)_2$). Although no direct evidence has been found to date, these oxo and μ-oxo species could be in partial equilibrium with their hydroxo/μ-hydroxo counterparts, according to the local pH of the enzymatic pocket in which the active sites reside. The necessary reducing equivalents are generally provided by a plethora of different electron transfer proteins and co-factors, such as NAD(P)H, flavin, ascorbate and α-ketoacids,[12] even if in some enzymes no external reductant is required.[15]

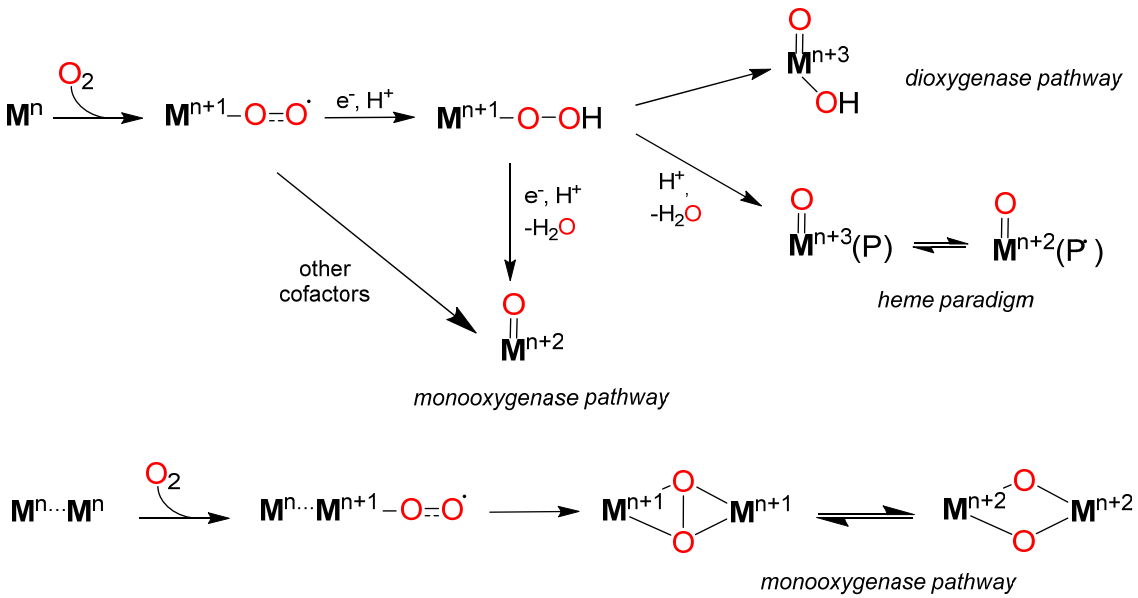

Scheme 1.1 – Dioxygen activation pathways for oxygenases enzymes containing mononuclear or dinuclear metal active sites.

1.2.1. Dioxygenases

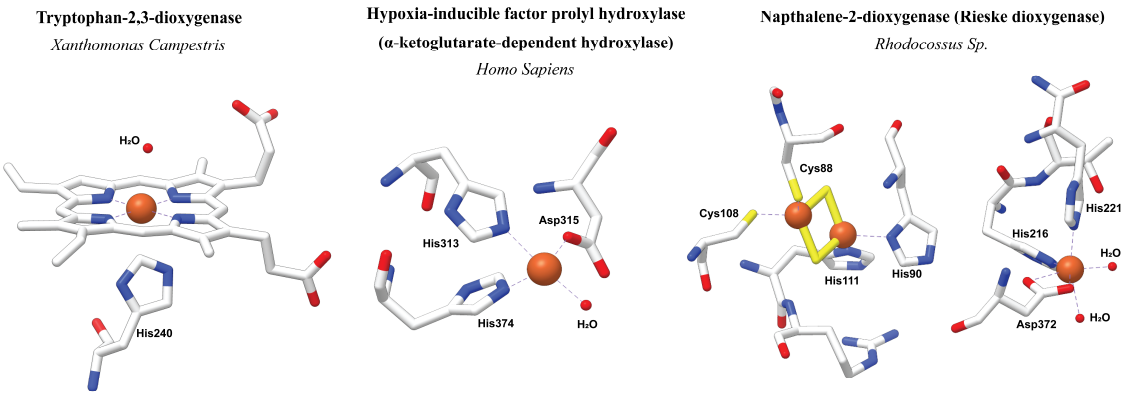

Figure 1.1 – Active sites of the tryptophan-2,3-dioxygenase (PDB: 3E08), hypoxia-inducible factor prolyl hydroxylase (α-ketoglutarate-dependent hydroxylase, centre, 2G19) and the naphthalene-1,2-dioxygenase (Rieske dioxygenase, right, 2B1X). Iron atoms displayed as orange-red spheres.

The majority of the dioxygenase enzymes contain iron in the active site and, based on their coordination site and nuclearity, can be classified into heme-containing, mononuclear non-heme iron dependent and the Rieske dioxygenases. Dioxygenases with heme-containing active sites are not particularly widespread and mainly related to the tryptophan metabolism, such as the tryptophan-2,3-dioxygenase[16, 17] (Figure 1.1) or the indoleamine-pyrrole-2,3-dioxygenase.[18] Quite the opposite, the majority of the dioxygenases enzymes present a mononuclear non-heme iron centre. One of the most widely studied examples are the α-ketoacid dependent hydroxylase enzymes, which require an α-ketoacid (usually α-ketoglutarate, Figure 1.1) as a co-factor.[19-21] Such classes of enzymes, which share a N,N,O "facial triad" coordination motif (2-His-1-Glu/Asp)[22] of the Fe^{II} site, are involved in the biosynthesis of several biological molecules, being capable of catalysing a wide range of oxygenation reactions (e.g. hydroxylation, demethylation, ring formation, desaturation).[23] However, it is noteworthy to clarify that the dioxygenase activity is exhibited only for hydroxylase reactions, in which one atom of the activated dioxygen is incorporated in the substrate, while the other ends up in the carboxylate derived from the α-ketoacid (*i.e.* succinate in the case of α-ketoglutarate).[19, 21] In the case of reaction pathways other than hydroxylation, the enzyme exhibits a monooxygenase behaviour where one oxygen atom is incorporated into the succinate by-

product while the other is reduced to H_2O.[19, 21] Other examples of mononuclear non-heme iron dioxygenases are catechol dioxygenases, responsible for the oxidative degradation of catechols through the scission of aromatic C–C bonds,[24] and lipoxygenases, which convert unsaturated fatty acids containing *cis,cis*-1,4 pentadiene moiety into the corresponding 1-hydroperoxy-trans,cis-2,4-diene.[24] The Rieske dioxygenases are the main class of multinuclear dioxygenases and are characterised by a reductase unit (containing flavin and a ferredoxin [2Fe-2S] unit), alongside with a terminal oxygenase unit composed by a Rieske [2Fe-2S] cluster and a non-heme iron active site (Figure 1.1).[19] Such class of dioxygenases catalyse the aromatic hydrocarbon degradation in soil bacteria.[25]

1.2.2. Monooxygenases

Monooxygenases are the second class of oxygenases and are quite widespread both in bacteria and eukaryotes. Contrary to dioxygenases, monooxygenases catalyse the insertion of only one oxygen atom into the substrate (reducing the second one to H_2O) and are capable of oxidising also very recalcitrant substrates such as methane (*e.g.* methane monooxygenases).[26] Monooxygenases can be classified into several different groups according to their active site and cofactors: heme-dependent, copper dependent, non-heme iron dependent, pterin dependent, flavin dependent and cofactor independent monooxygenases.[12]

Heme-dependent monooxygenases, also called cytochrome P450 monooxygenases (Figure 1.2),[12] constitute one of the most known and studied families of monooxygenases. Quite abundant in eukaryotes, they display a b-type heme cofactor at the active site (Figure 1.2). They are extremely versatile systems, and catalyse a plethora of oxidations, such as epoxidations, hydroxylations, heteroatom-oxidations and oxidative de-aminations, but also dehalogenations and dehydrogenations.[18] The chemistry of the catalytic cycle of cytochrome P450 has been extensively studied, and displays, in the first part, the dioxygen activation by the reduced enzyme (Fe^{II}) to form a $Fe^{III}–OO^{\bullet-}$ superoxide adduct, which is then reduced to its peroxide counterpart. The electrons required for the

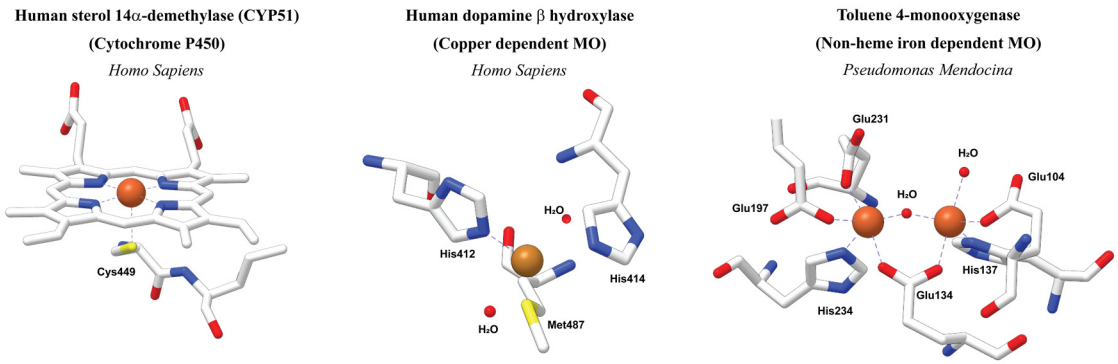

Figure 1.2 - Active sites of the human sterol 14α-demethylase (left, cytochrome P450, PDB: 6Q2T), human dopamine β-hydroxylase (centre, copper-dependent MO, 4ZEL) and toluene 4-monooxygenase (right, non-heme iron dependent MO, right, 3Q14). Iron atoms displayed as orange spheres. Copper atoms displayed as copper coloured spheres.

O_2 activation are provided by NAD(P)H coenzymes. Upon O–O cleavage, the Fe^{III}–OO^{-} is converted to the ferryl $(P^{\bullet+})Fe^{IV}$=O↔Fe^{V}=O intermediate (i.e. Compound I),[27] which performs the two-electrons oxidation of the substrate leading to a Fe^{III}–OH_2 species. However, upon comparison with the structurally analogous heme peroxidases,[28] a further reactive species, called compound II, has been postulated. Compound II has been identified as the formal one-electron reduction product of compound I, namely Fe^{IV}=O. However, some studies suggested that, under acidic conditions or as product of an hydrogen atom transfer reaction, compound II could also be in a protonated form, *i.e.* Fe^{IV}–OH.[29, 30] Theoretical calculations demonstrated that such unprecedented species is in principle capable of activating moderately strong C–H bond in an equal manner compared to its deprotonated counterpart,[31] suggesting that high valent hydroxide species can be powerful oxidant as well as their oxo analogues.

Other classes of iron-based monooxygenases are the non-heme iron dependent and the pterin-dependent monooxygenase. The distinctive feature of the non-heme iron dependent monooxygenases, also referred to as bacterial multicomponent monooxygenases (BMM), is the presence of a diiron active site, by which they catalyse mainly hydroxylation and epoxidation reactions. The best-known example of this class is soluble methane monooxygenase, capable of oxidising methane to methanol in some methanotrophic bacteria (see chapter 1.2.1) through a high valent diiron-oxygen intermediate, whose structure is still under debate (see section 1.3.1).

Other examples are alkene monooxygenase[32] as well as phenol hydroxylases.[33] Pterin-dependent monooxygenases are iron-based systems that require the presence of tetrahydrobiopterin as coenzymes to perform hydroxylation of phenylalanine, tyrosine and tryptophan. The best studied example of this sub-class of enzymes is phenylalanine 4-monooxygenase.[12]

Copper-dependent monooxygenases are a relatively small sub-class of monooxygenase that require copper ions in their catalytic active sites. Well studied examples of enzymes belonging to this class are the dopamine β-monooxygenase (Figure 1.2), which hydroxylates the β-carbon of dopamine[34] and particulate methane monooxygenase (pMMO, see chapter 1.2.2), which is capable, on par with sMMO, of oxidising methane to methanol under physiological conditions.[35, 36] Another important example of copper-dependent monooxygenase is tyrosinase (see chapter 1.2.3), which catalyses the oxidations of phenols, such as in tyrosine and dopamine, and catechols. Tyrosinase's active site contains a dicopper centre that is proposed to form a (μ-η^2:η^2-peroxo) dicopper(II) species as reactive intermediate, with the oxygen molecule bound to both metal ions.[37]

Alongside the previously reported metal-based systems, there are other classes of monooxygenases that do not require metal ions in their active site, such as the flavin-dependent and the cofactor independent monooxygenase. Flavin-dependent systems utilise FMN (flavin mononucleotide) and FAD (flavin adenine dinucleotide) flavin cofactors to catalyse several reactions, including epoxidations, halogenation and Baeyer-Villiger oxidations. The active intermediate is generated by covalent bonding of the O_2 to the C4a of the flavin.[38] Luciferase and styrene monooxygenase belong to this sub-class. Cofactor-independent monooxygenase is a class of monooxygenases that have been found not dependent by either organic or metal cofactors, relying on the substrate as reducing agent. Examples of this sub-class, such as tetracenomycin F1 monooxygenase, are mainly found in streptomycetes, and appear to be correlated with the biosynthesis of polyketide antibiotics.[12]

1.3. Relevant dinuclear oxygen activating enzymes

Oxygenase enzymes and in particular monooxygenases, have been proven to catalyse challenging oxidation reactions in bacteria and eukaryotic organisms such as O/C−H activation. Except for the presence of some metal independent systems (see chapter 1.2), the majority of them display mono and di-nuclear metal based active sites, containing mainly iron or copper. Mononuclear systems, such as the aforementioned heme-dependent Cytochrome P450 and α-ketoglutarate-dependent dioxygenases (see chapter 1.2), have been extensively studied and characterised, giving rise to a plethora of possible biomimetic complexes.[39-41]

In the present chapter, attention will be focused on the di-nuclear monooxygenases enzymes involved in the oxidation of challenging substrates, such as methane or phenols. Understanding how these systems work in nature is mandatory to design biomimetic systems capable of reproducing a similar reactivity.[10] In particular we will analyse in detail two of the most relevant examples of di-nuclear monooxygenases, the iron-based soluble methane monooxygenase (sMMO), capable of oxidising methane to methanol, and the copper-based tyrosinase, involved in the hydroxylation and oxidation of phenols and catechols, such as for L-tyrosine and L-DOPA.

1.3.1. sMMO

Methanotrophic bacteria are a family of microorganism that play a crucial role in nature, using the methane anaerobically produced in sediment as the sole source of energy. The metabolism of methanotrophic bacteria involves, as the first step, one of the most challenging reactions performed in nature, namely the biological oxidation of methane to methanol (Scheme 1.2). This reaction, which is incredibly relevant from an industrial point of view (see chapter 1.1), is biologically performed by a class of enzymes known as *methane monooxygenases* (MMO). Two genetically unrelated enzymes belong to this class: soluble methane monooxygenase (sMMO) and the particulate methane monooxygenase (pMMO).

$$CH_4 + NADH + H^+ + O_2 \longrightarrow CH_3OH + NAD^+ + H_2O$$

Scheme 1.2 – Biological oxidation of methane catalysed by methane monooxygenase enzymes in methanotrophic bacteria

In spite of the shared capability of oxidising the C–H bond of methane (BDE_{C-H} = 105 kcal/mol),[8] sMMO and pMMO display quite different active sites: sMMO has been widely studied and crystallographically demonstrated to bear a diiron active site,[42, 43] while the nature of the pMMO active site is still a matter of debate. Crystallographic studies confirmed the active site to be copper based, whereas the nuclearity of the site, namely its mononuclear or di-nuclear nature, remained unclear.[35, 36] Only recently, studies performed by Rosenzweig and co-workers, added support for the mononuclear nature of the copper site of pMMO in *Methylococcus capsulatus (Bath)*, although the debate is still ongoing.[44, 45]

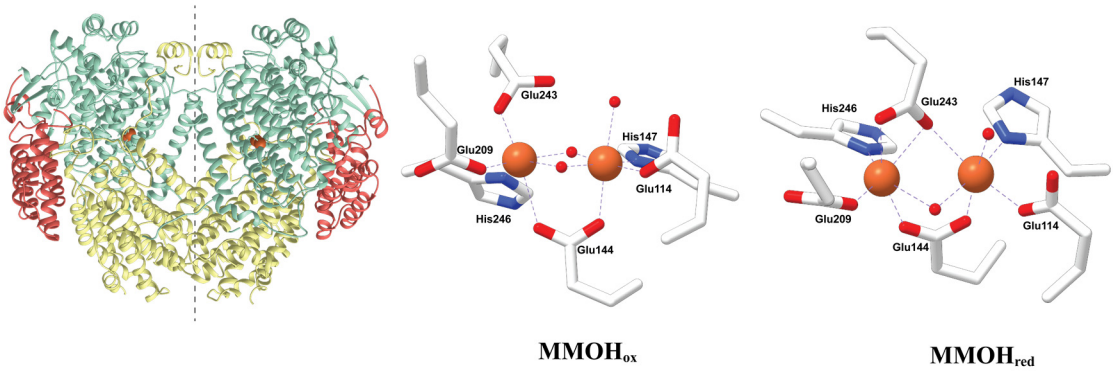

Figure 1.3 – *Left:* Crystallographic structure of sMMO from *M. capsulatus* (Bath) (PDB: 1MTY) showing the α subunits in green, the β subunits in yellow and the γ subunits in red. *Centre:* Active site of MMOH in the oxidised state (1MTY). Right: Active site of MMOH in the reduced state (1FYZ). Iron ions depicted as orange-brown spheres.

Soluble methane monooxygenase is a non-heme iron dependent monooxygenase (see chapter 1.2.2) belonging to the family referred to as bacterial multicomponent monooxygenases (BMM). The enzyme is composed of a hydroxylase component (MMOH) containing the metal active site, a reductase protein (MMOR) and a regulatory

protein (MMOB). MMOR (~40 kDa) reductase protein is composed of three domains (i.e. NADH-binding, FAD-binding and [2Fe-2S] ferredoxin domain) and is responsible for supplying the required reducing equivalents from NADH to the di-iron centre.[46] The MMOB regulatory protein (~16 kDa) binds to the MMOH, affecting the structure and the diiron centre redox potential, increasing dramatically the rate of dioxygen activation.[47]

The hydroxylase protein MMOH is a 251 kDa three-subunit homodimer ($\alpha_2\beta_2\gamma_2$, Figure 1.3), composed mostly of α helices. The diiron active site is the sole metal centre present in the enzymes and is located in the α subunit of each homodimer (Figure 1.3).[36] The resting state of the active site corresponds to the oxidised form $MMOH_{ox}$ (Figure 1.3), and is composed of two Fe^{III} ions. Each metal centre is coordinated by H_2O, Glu and His residues (Glu209, Glu243 and His246 for Fe1, Glu114, His147 and H_2O for Fe2,) in a pseudo-octahedral fashion. The two iron centres are bridged by two molecules of solvent and the Glu144 residue, lying at 3.1Å apart. The two-electron reduced state of $MMOH_{ox}$, namely $MMOH_{red}$, has been crystallographically characterised (Figure 1.3), displaying an increase of the distance between the two iron centres (both reduced to Fe^{II}) from 3.1 to 3.3Å. Moreover, a solvent molecule is displaced by Glu243, in a rearrangement known as carboxylate shift.[42]

The catalytic cycle of sMMO and the intermediates involved in the O_2 activation have been extensively studied and characterised. In the first step of the catalytic cycle (Scheme 1.3), the antiferromagnetically coupled, high spin Fe^{III}_2 site $MMOH_{ox}$[35, 43] undergoes a two-electron reduction to the high spin, weakly ferromagnetically coupled Fe^{II}_2 site $MMOH_{red}$.[48] The electrons involved in such reductions are provided by the NADH cofactor through the MMOR protein.[46] The aforementioned carboxylate shift observed in $MMOH_{red}$ is related to the change in magnetic coupling between the iron centres and provides an open coordination sites for the O_2 binding.[42] In the next step, O_2 interacts with $MMOH_{red}$ generating intermediate O, which is proposed to be a complex of $MMOH_{red}$ with O_2 in which the diiron active site is not directly involved.[35, 47] Intermediate O is then converted to the diferrous Fe^{II}_2–O_2 intermediate P*,[49-51] which, upon proton transfer, is subsequently re-arranged as the μ-1,2 peroxo bridged Fe^{III}_2 intermediate P (Scheme 1.3).[51, 52] Species P is demonstrated to be generated also by the reaction of $MMOH_{ox}$ with an excess of hydrogen peroxide, through a mechanism known as peroxide shunt.[53]

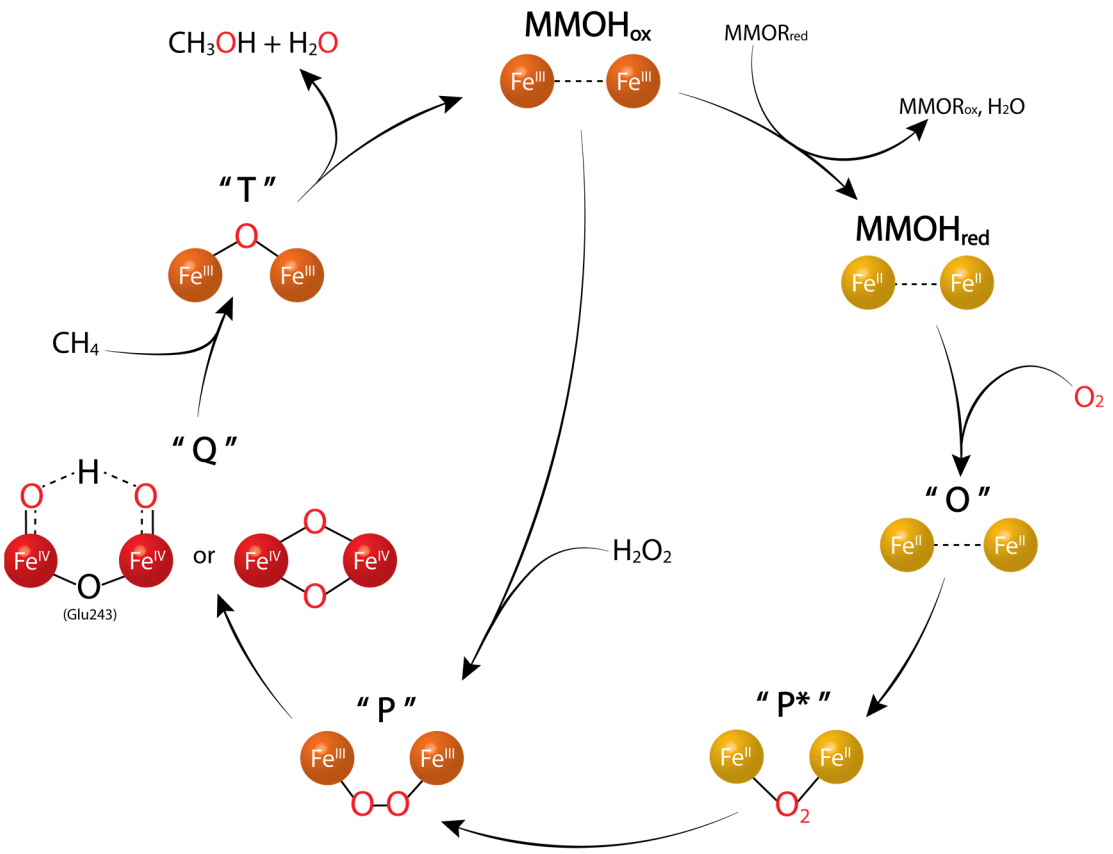

Scheme 1.3 – Proposed catalytic cycle for sMMO. Iron ions are shown as spheres. Colours reflect the corresponding oxidation state, which is also described in each sphere: Fe^{II} in yellow, Fe^{III} in orange, Fe^{IV} in red. Oxygen atoms deriving from O_2 are labelled in red. Depiction of intermediate P* is not indicative of its structure, since the binding mode of this species is unknown. Two possible structures are reported for intermediate Q, reflecting the controversial nature of its structure.

The μ-1,2 peroxo bridged intermediate P undergoes proton transfer and homolytic cleavage of the O–O bond, generating intermediate Q.[35, 54] The structure of Q, which is the putative methane-oxidising species, is still controversial. Intermediate Q was initially characterised by extended x-ray absorption fine structure (EXAFS) spectroscopy, obtaining a dramatically short Fe···Fe distance (i.e. 2.46 Å) for the diiron site, suggesting a "diamond" like closed core bis-μ-oxo-Fe^{IV}_2 structure,[55] which was further proved by time resolved Raman.[56] However, neither computational[57] nor synthetic[10, 58] evidence was found supporting a structure with similar short Fe···Fe distance. Recent studies by De Beer and co-workers re-analysed intermediate Q by Fe K-edge *high-energy resolution*

fluorescence detected X-ray absorption spectroscopy (HERFD-XAS/EXAFS) observing a longer higher Fe···Fe distance (3.4 Å), which suggests a di-nuclear open core structure.[59, 60]

Nevertheless, several possible structures, which try to take into account the results provided by both Raman and Mössbauer experiments, were proposed (Scheme 1.4). A simple open-core structure, in which one of the two Fe^{IV} bear a terminal oxo, (Scheme 1.4, left) is not compliant with the equivalent nature of the two sites suggested by Mössbauer;[56] therefore, an open core structure in which both the Fe^{IV} have an oxygen ligand bound to them was proposed (Scheme 1.4, centre).[59] Such a structure, which could be formed from either cleavage of the peroxide moieties in intermediate P, or opening of the aforementioned diamond core closed structure, finds partial experimental and computational support, relying on the presence of a strong hydrogen bond network to justify the similar electronic environments spectroscopically observed for the oxo/hydroxo ligands. Moreover, albeit this potential model considers the incorporation of both oxygen atoms from O_2, it requires a further bridging or terminal oxygen atom of unknown origin. In order to support such thesis, a model

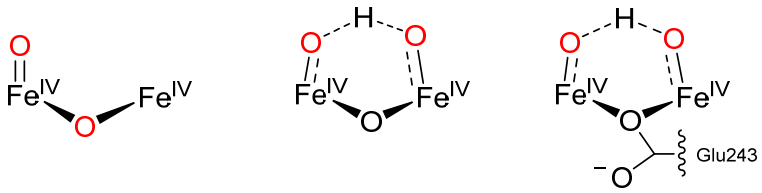

Scheme 1.4 – Proposed open-core structure for the intermediate Q.[59] Oxygen atoms deriving from O_2 are labelled in red.

in which the carboxylate moiety from Glu243 observed for $MMOH_{red}$ is retained has been proposed (Scheme 1.4, right). However, such a model would imply a shift from terminal to bridging oxo upon reaction with the substrate, as found in the well characterised subsequent intermediate T.[56] Quite recently Que and co-workers reported the first example of Sc^{3+} assisted conversion of a (μ-1,2 peroxo)Fe^{III}_2 complex to a diamond core bis-μ-oxo-Fe^{IV}_2, mimicking the proposed conversion of species P to Q.[61] However, the refined Fe···Fe distance for the high-valent diiron oxo core was of ~2.7 Å, a value similar to the previously reported synthetic diamond core bis-μ-oxo-Fe^{IV}_2 complexes,[58] but quite different from the experimentally found values for Q,[59] suggesting once more the open-

core structure hypothesis. No definitive conclusions can be drawn regarding the controversial structure of intermediate Q and only advanced modelling tools, such as advanced QM/MM (quantum mechanics/molecular mechanics) approach, could provide clear insight.

Independently from its structure, the mechanism through which intermediate Q reacts with methane was widely computationally and experimentally studied.[57] Concerted reaction mechanisms, as well as radical and cationic mechanisms were proposed.[62] The widely accepted mechanism suggested an initial hydrogen abstraction by intermediate Q, leading to the formation of a "bound-radical" intermediate in which the methyl radical rotation in constrained by interaction with the diiron centre. The model also includes a second nonsynchronous concerted pathway.[63, 64] Radical clock probe experiments were consistent with this proposal,[62] although the mechanism of C–H activation could be dependent on the nature of the probe substrates,[65] as MMOH is capable of oxidising the C–H bond of several different carbon compounds which may react following different pathways.[66, 67] After reaction with methane, intermediate Q evolves into T, which has been identified as a mono-μ-oxo bridged Fe^{III}_2 site (Scheme 1.3).[56] Methanol and water are then released and the $MMOH_{ox}$ resting state is regenerated (Scheme 1.3), concluding the catalytic cycle.

In conclusion, although most of the mechanisms and structures of sMMO intermediates are widely understood and accepted, some key pieces of the puzzle are still missing. The debate regarding the identity of the intermediate Q is still ongoing and the recent hypotheses formulated by Que and et al.[59] raised new questions about the real structure of this intermediate. The involvement of a dinuclear high valent terminal hydroxo μ-oxo iron species is a feasible option, especially considering the aqueous environment and the strong H-bonds network provided by the nearby aminoacidic residues. Di-nuclear open core complexes with both terminal oxo and hydroxo ligands, such as the $(HO)Fe^{III}(\mu\text{-}O)Fe^{IV}(O)$ complex,[68, 69] have been demonstrated to be exceptional oxidants, suggesting that dinuclear high valent terminal/bridging hydroxo complexes could play a more important role than previously believed.

1.3.2. Tyrosinase

Alongside iron, copper is the second most abundant metal cofactor present in di-nuclear monooxygenases enzymes (see chapter 1.2.2). In spite of the large number of multicopper enzymes present in nature,[41] tyrosinase is by far the most well-studied. Tyrosinase, which contains a di-nuclear coupled copper active site, is a versatile enzyme exhibiting both a monophenolase and a diphenolase activity (Scheme 1.5).

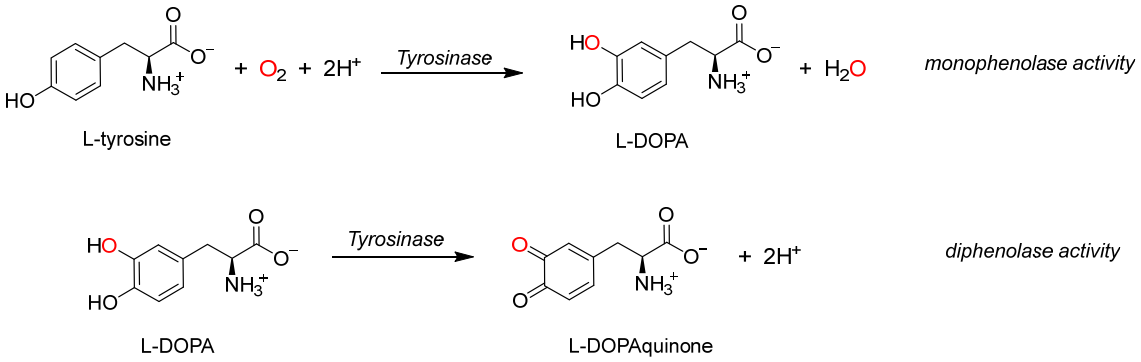

Scheme 1.5 – Schematic tyrosinase activity showing the conversion of L-tyrosine to L-DOPA (monophenolase activity) and conversion of L-DOPA to L-DOPA quinone (diphenolase activity).

Monophenolase activity, also referred to as cresolase activity, consists of the ortho-hydroxylation of monophenol to ortho-diphenol (Scheme 1.5), which is then converted to the corresponding ortho-quinone through a two-electron oxidation, exhibiting its diphenolase activity (Scheme 1.5). Biologically, tyrosinase catalyses the conversion of the amino acid L-tyrosine to L-DOPA (3,4-dihydroxy-L-phenylalanine), and its subsequent conversion to L-DOPA quinone (4-(2-carboxy-2-aminoethyl)-1,2-benzoquinone), a precursor of the pigment melanin,[41] incorporating in the final product an oxygen atom that originates from the activated molecular O_2.[70] Notably, tyrosinase can be classified as an internal monooxygenase, since the required electrons for the reduction of the second oxygen atom to H_2O are provided by the substrate itself.

In spite of its wide distribution in nature, tyrosinases from different species can exhibit completely different structures. High-resolution crystallographic studies showed stark evolutionary and structural similarities between bacterial (*S. castaneoglobisporus*)[71] and fungal (*Ag. Bisporus*)[72] tyrosinases and mollusc hemocyanin, which share highly

conserved aminoacidic sequences coordinating Cu_A (i.e. His-X(*n*)-His-X(8)-His) and Cu_B (i.e. His-X(3)-His-X(*n*)-His). Insect tyrosinase (*M. sexta*)[73] are instead closer to arthropod hemocyanin,[41, 74] having the same His-X(3)-His-X(*n*)-His motif coordinating both Cu centre.

However, all the structures contain a common central globular domain, composed by four α-helix bundles (Figure 1.4). In addition, in insect tyrosinase, the presence of three domains and a heterodimers interface has been observed (Figure 1.4).[73]

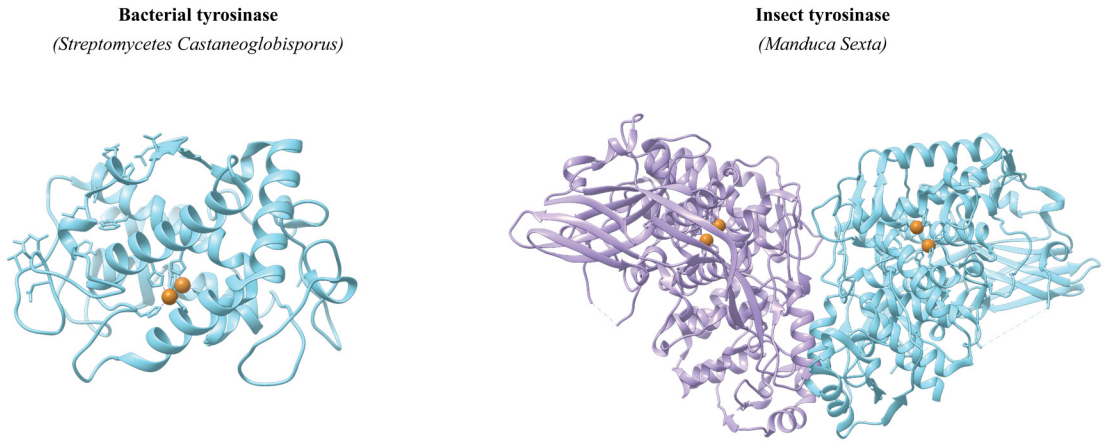

Figure 1.4 – Structures of bacterial tyrosinase (from *S. Castaneoglobisporus*, PDB: 2ZMZ) and insect tyrosinase (from *M. sexta*, PDB:3HHS).

In spite of the different structure, all tyrosinases are type 3 copper protein enzymes and contain the same di-nuclear copper active site, in which each copper ion is coordinated by three histidine ligands. By use of caddie proteins, the copper active site of tyrosine from *Streptomyces castasneoglobisporus*[71] has been for the first time crystallographically proven to exists in three different redox forms, corresponding to different steps of dioxygen activation: *deoxy*, *oxy and met* forms (Figure 1.5).[71] The resting state configuration, corresponding to the *deoxy* form, is characterised by the two copper ions, called Cu_A and Cu_B, in Cu(I) oxidation state, each ion exhibiting a mostly planar distorted tetrahedron coordination environment with a $Cu_A \cdots Cu_B$ distance greater than 4.0 Å.[71] The four coordination sites are provided by three histidine residues, with a labile bridging solvent molecule as a fourth ligand (Figure 1.5).

The *oxy* form of tyrosinase active site, generated upon binding of O_2 to the *deoxy* form, is composed by a side-on μ-η^2:η^2-peroxo Cu^{II}_2 core (Figure 1.5). Each Cu^{2+} ion lies in a staggered trigonal coordination environment with respect to the histidine residue. The peroxide bridging moiety causes a stark decrease of the $Cu_A \cdots Cu_B$ distance (3.4 Å for the analysed *S. castasneoglobisporus*),[71] although the extent of such a decrease might be affected by interaction of the peroxo-core with the caddie protein used for crystallization.[41]

The *met* form is the third state in which the tyrosinase active site has been observed during its catalytic cycle (Scheme 1.6). Several crystal structures of tyrosinase *met* form are reported (Figure 1.5),[71] exhibiting different numbers of bridging solvent-derived ligands (from zero to two) between the two Cu^{2+} ions, with an extremely flexible $Cu_A \cdots Cu_B$ distance (2.9 – 4.9 Å), which assists the oxygen binding.[41] However, due to the steric repulsion between the bridging atoms, only systems with a $Cu_A \cdots Cu_B$ distance below 3.1 Å can accommodate two solvent derived ligands. In the presence of $Cu_A \cdots Cu_B$ distances up to 4.0 Å, only one bridging molecule will be present.[75]

All three forms are EPR silent, suggesting a strong antiferromagnetic coupling between the Cu^{2+} ions in the *oxy* and *met* forms. Such evidence supports the presence of a bridging hydroxide anion and not a bridging water molecule in the met forms, since μ-hydroxo bridge would be a far more efficient superexchange pathway than water.[41, 76] The presence of a bridging hydroxide anion is also strongly supported by EXAFS experiments.[77]

Several spectroscopic experiments have been carried out to understand in which fashion the substrate interacts with the active site. Studies on the synthetic EPR active (S = 1/2) Cu(I)Cu(II) mixed valent *half-met* derivative demonstrated that the substrate binds directly to Cu_A. Recent studies by Itoh et al.[78] demonstrated that the initial binding of the substrate (*e.g.* L-tyrosine) into the binding pocket of the enzymes triggers a conformational change in the dicopper core, reducing the distance between Cu_A and the phenolic group of the substrate from 3.8 Å to 3.3 Å. The migration of the Cu_A towards the substrate causes the detachment of one of the coordinated histidines, which can act as base to form the phenolate, allowing the coordination of the substrate to Cu_A. The geometric change also causes rotation of the Cu_2O_2 plane, favouring the interaction with the aromatic ring of the substrate.

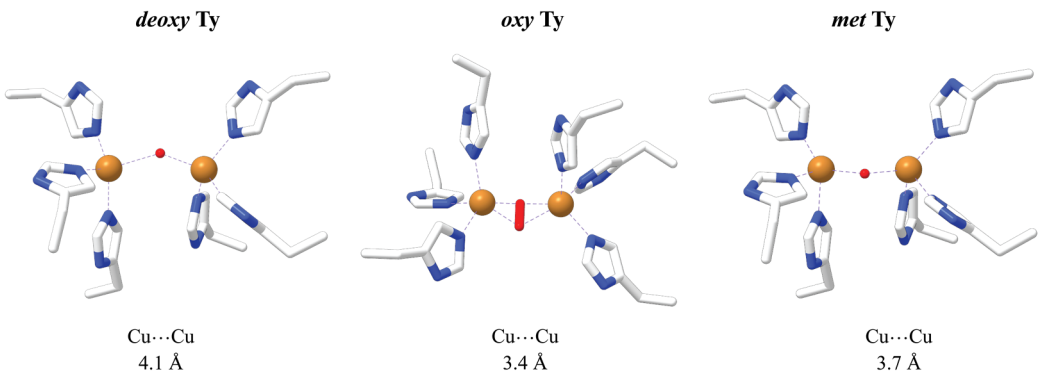

Figure 1.5 – Structure of the *deoxy* (PDB: 2ZMZ), *oxy* (1WX2) and *met* tyrosinase (2ZMX) forms from S. *Castaneoglobisporus* with relative Cu···Cu distances. Copper ions depicted as copper-brown spheres.

As previously mentioned, Tyrosinase displays a dual activity, catalysing both the ortho-hydroxylation of monophenol (monophenolase activity, Scheme 1.5) and the oxidation of the ortho-diphenols to ortho-quinone (diphenolase activity, Scheme 1.5). The two catalytic cycles (i.e. monophenolase and diphenolase cycle) have been extensively studied and are known to be strictly connected each other, sharing several intermediates (Scheme 1.6);[41, 79] however, in the interest of clarity, they will be analysed separately.

The monophenolase catalytic cycle (Scheme 1.6, inner cycle) begins with the binding of O_2 by the *deoxy* form of the active site to generate the μ-η^2:η^2-peroxo Cu^{II}_2 *oxy* state. Subsequently, the *oxy* state interacts with the substrate, forming the postulated key intermediate oxy-T (Scheme 1.6, inner cycle). Although it has never been observed, the oxy-T intermediate is supposed to be an enzyme-oxygen-phenol ternary complex, in which the phenol is directly coordinated to one of the Cu ions (generally Cu_A) before undergoing electrophilic aromatic substitution. However, it has been demonstrated in model complexes that the monooxygenation can occur even in absence of a direct coordination to the copper centre.[80] Another hypothesis suggest that a bis-μ-oxo-Cu^{III}_2 species could be generated upon interaction of the oxy state with the substrate. Such a hypothesis arose from the discovery by Tolman and co-workers of an equilibrium between the two isomers μ-η^2:η^2-peroxo Cu^{II}_2 bis-μ-oxo-Cu^{III}_2 in model complexes.[81, 82] Despite experimental studies by Stack[83] and Karlin[80] that showed both isomers are competent in the monooxygenation reaction, DFT studies considered the bis-μ-oxo-Cu^{III}_2 isomers to be prohibitively higher in energy compared to μ-η^2:η^2-peroxo Cu^{II}_2 and, therefore, an unlikely intermediate.[84]

After coordination of the phenol and formation of the *oxy*-T state (Scheme 1.6, inner cycle), the phenol ring rotates towards the core-oxygen, orienting itself to allow electrophilic attack on the *ortho*-carbon. C−O bond is formed upon electron transfer to dioxygen, whereas subsequent rearrangement of the proton to the distal oxygen atom brings to the *met*-D state, in which the ortho-diphenolate bridges the Cu ions (Scheme 1.6, inner cycle). Finally, in the last step, upon protonation μ-OH ligand of *met*-D, H_2O is released; the concomitant reduction of the Cu ions (from Cu^{2+} to Cu^{+}) leads to the release of the quinone and reformation of the *deoxy* state (Scheme 1.6, inner cycle). In summary, each catalytic turnover requires one equivalent of phenol substrate and dioxygen molecules to generate one equivalent of quinone product and water.[41]

The diphenolase catalytic cycle (Scheme 1.6, outer cycle) requires two equivalents of substrate and one equivalent of dioxygen in each turnover to perform a formally four electron reduction of O_2 to H_2O in two discrete two-electron steps, with the required electrons provided by the catechol substrates.[41] The diphenolase cycle can be divided in an *oxidative* (red, Scheme 1.6) and *reductive* (green, Scheme 1.6) phase. The first step of the oxidative phase is analogous to the one observed for the monophenolase activity and consists of the conversion of the *deoxy* to the *oxy* state through binding of O_2 (Scheme 1.6, outer cycle). Subsequently, the *oxy* state interacts with the 1,2 catechol to generate the oxy-D state, which rapidly evolves in the *met* state with concomitant release of a molecule of quinone and H_2O (Scheme 1.6, outer, cycle). The *oxy*-D intermediate is generally postulated to display a catechol molecule bridging both the Cu ions, albeit, due to the strong antiferromagnetic coupling between the metal centres, the two-electron oxidation of catechol could occur even in presence of a single copper coordination.[41]

Once the *met* intermediate is formed, which determines the beginning of the reductive phase of the cycle, it reacts with another molecule of 1,2-catechol (Scheme 1.6, outer cycle) generating the *met*-D intermediate (see above). In the last step, analogous to the monophenolase cycle, the catechol substrate reduces the copper ions, regenerating the *deoxy* state, a molecule of quinone and one of H_2O.[41]

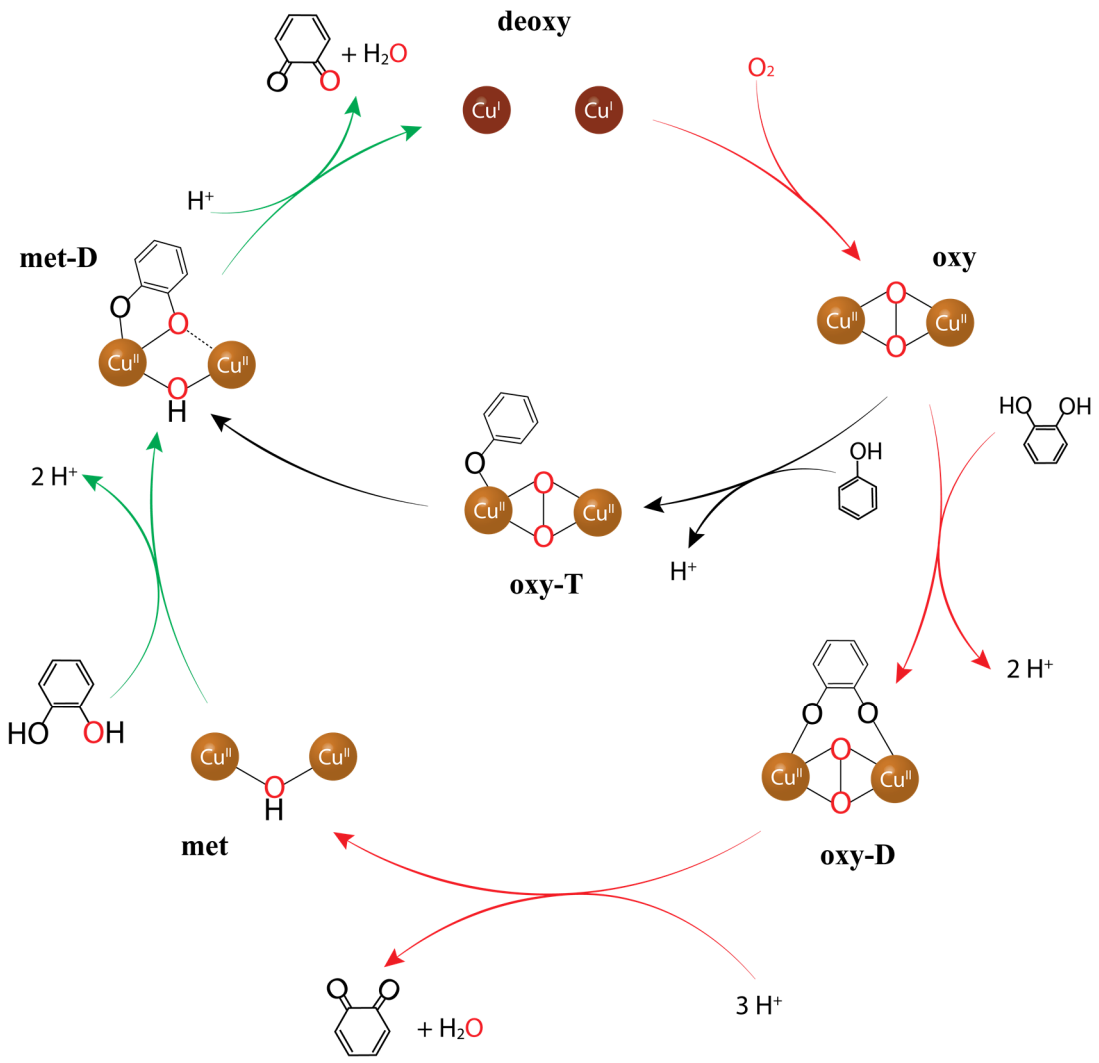

Scheme 1.6 – Catalytic cycle of tyrosinase showing the monophenolase catalytic cycle (inner cycle) and the diphenolase cycle (outer cycle). The red and green arrows indicate respectively the oxidative and reductive phase of diphenolase cycle. Copper ions depicted as mahogany brown spheres (Cu^{+}) and copper-brown spheres (Cu^{2+}).

Contrary to sMMO, in which catalytic intermediates are still partially debated (see 1.3.1), the wide diffusion of the tyrosinase enzymes and the vast amount of studies on the topic allowed us to have direct proof of the structure of almost every intermediate involved. Such a plethora of information highlights the critical role of the dinuclear metal-oxygen adducts in this monooxygenase system. Moreover, although the relevance of the side-on peroxo adducts $Cu^{II}_2(\mu\text{-}\eta^2\text{:}\eta^2\text{-}O_2)$ present in the *oxy* intermediate is undeniable and widely discussed, from our point of view the *met* intermediate constitutes an equally interesting system, being an uncommon example of μ-hydroxo adducts capable of performing oxidative reactivity. The critical role of *met* intermediate in the tyrosinase catalytic cycle

proves once more the importance of μ-hydroxo adducts in enzymatic system, encouraging us to explore the properties of these complexes from a synthetic point of view.

1.4. Reactivity mechanisms

1.4.1. PCET

As mentioned in the previous chapter, dinuclear monooxygenase enzymes and their biomimetic and bioinspired complexes have been demonstrated to perform a plethora of biological and synthetic oxidation reactions via a wide range of different mechanisms. In order to better understand the reactivity of such systems and of the topic debated in the next chapters, a brief introduction to the reactivity mechanisms involved will be discussed here. More accurate analyses will be provided where necessary in the relevant chapters.

The main critical step involved in the O/C–H activation and in the subsequent oxidation reactions (i.e. aliphatic hydroxylation, N/O-dealkylation, oxidative dehydrogenation, etc) is the hydrogen atom abstraction (HAA). Hydrogen atom abstraction mechanism is common to different fields (e.g. atmospheric chemistry), resulting in a variety of definitions and nomenclature. In the interest of the clarity and coherence, for the work herein reported we will refer to the nomenclature scheme proposed for transition metal complexes by Mayer and co-workers.[85]

In particular, we will consider as HAA the general class of reaction in which a proton and an electron (formally an H atom) are transferred from a donor to an acceptor. Concerning the reaction of metal complexes, such reactions have been defined as *proton-coupled electron transfers* (PCET).[86-90] Mayer and co-workers defined three possible limiting mechanisms (Scheme 1.7) through which such transfer can occur. In the case in which H^+ and the e^- are transferred stepwise, we can observe a *proton transfer* (PT), followed by an *electron transfer* (ET), or inversely an ET, followed by a PT according to which transfer event is the rate determining step. If the H^+ and e^- are transferred with a concerted mechanism in a single kinetic step, we observe a *concerted proton electron transfer* or CPET reaction.[91, 92]

Hydrogen atom transfer (i.e. HAT) reactions are formally considered as a subclass of CPET reactions in which the H^+/e^- couple comes from the same donor and is transferred to the same acceptor synchronously. However, some theoretical studies dictated that only adiabatic reaction could be considered HAT,[93] making a distinction between HAT and CPET subtle and often misleading, clearly almost impossible to be drawn from only experimental results.[91-93] Therefore, in the interest of clarity, as recently suggested by Mayer,[90] any mechanism in which the H^+ and e^- are transferred in a concerted mechanism, form the same donor to the same acceptor in a single kinetic step will be addressed as HAT.

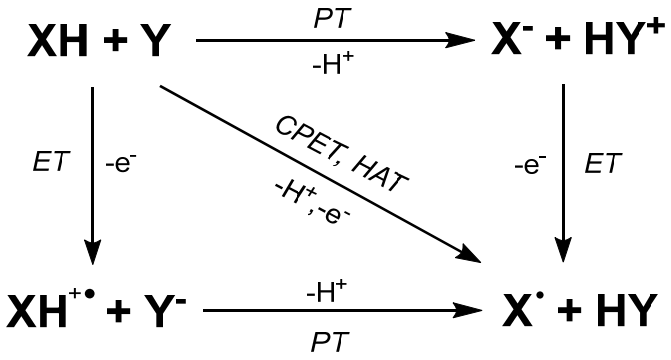

Scheme 1.7 - Thermodynamic square scheme for proton coupled electron transfer reaction

1.4.2. Other mechanisms

In addition to the HAT/CPET mechanism, several other mechanisms can be involved in the oxidations of organic substrates. An example is the oxidation of aromatic C–H bonds, whose activation via a HAT process is thermodynamically unfavourable due to the large homolytic bond dissociation energies (*e.g.* benzene has $BDE_{C–H}$= 120 kcal/mol).[8] In such cases, a hydroxylation reaction by terminal or bridging oxo complexes has been demonstrated to occur via a more favourable electrophilic aromatic substitution mechanism.[94]

Aside to the HAT reaction, there is a different class of oxidation reactions in which a net transfer of an oxygen atom occurs. This class of reactions include alkene epoxidation and

the oxidation of heteroatoms such as P (*e.g.* phosphine to phosphine oxide), S (*e.g.* sulphide to sulfoxide and sulfone) and N (*e.g.* amine to N-oxide). Analogously to HAT, the transfer of the oxygen atom can happen in a single, concerted step; such process is defined oxygen atom transfer or OAT. However, the transfer can be initiated through formation of a radical cation which then reacts further to give the oxygenated product. These reaction pathways are generally favoured for oxidants with a large reduction potential.

1.5. Biomimetic dinuclear metal–oxygen adducts

In the previous chapters, we analysed the crucial role of the di-nuclear metal-oxygen adducts in enzymatic small molecule activation, focusing on the O/C−H bond oxidation performed by monooxygenases enzymes. Soluble methane monooxygenase and tyrosinase are examples of di-nuclear monooxygenase enzymes, although this structural motif is also present in other enzymatic class such as the Mn-based ribonucleotide reductase.[95]

The importance of these enzymes and the necessity of understanding how they perform such challenging reactions led to the development of a plethora of biomimetic di-nuclear complexes.[58] Although di-nuclear oxygen adducts of all the first row transition metals are present in the literature, the systems containing oxygen adducts with elements from the first half of the row, such as Ti,[96] V,[97] Cr[98] and Mn,[99] are weakly reactive towards O/C−H activation. However, di-nuclear manganese-oxygen adducts are relevant from a biomimetic point of view since they are important mimicking systems of fundamental Mn-based enzymes such as the oxygen evolving complex (OEC) of the photosystem II[100] and the class Ib ribonucleotide reductase.[95] Biomimetic di-nuclear metal oxygen adducts containing Fe, Co, Ni and Cu are more reactive toward O/C−H,[101] and are ideal model complexes for systems such as sMMO and tyrosinase. However, their great reactivity results in a significant instability, particularly in presence of high oxidation states, making them extremely challenging from a synthetic point of view.

In this chapter we analyse and compare the most relevant biomimetic di-nuclear metal oxygen adducts containing Fe, Co, Ni and Cu present in literature. Mn containing di-nuclear complexes will be treated as well, albeit separately, due to their poor O/C–H bond activation reactivity.

Table 1.1 – Most relevant examples of di-manganese oxygen adducts reported in literature

#	Core	Ligand	M…M	Ref.
	Manganese			
1	$Mn^{II}(\mu\text{-}OH)_2Mn^{II}$	Tp^{iPr2}	3.31	[102]
2	$Mn^{III}(\mu\text{-}O)_2Mn^{III}$	Tp^{iPr2}	2.70	[102]
3	$Mn^{IV}(\mu\text{-}O)_2(\mu\text{-}\eta^1\text{:}\eta^1\text{-}O_2)Mn^{IV}$	tacn	2.53	[103]
4	$Mn^{III}(\mu\text{-}O)(\mu\text{-}OAc)Mn^{III}$	bispicen	3.28	[104]
5		$bispicMe_2en$	3.29	[104]
6	$Mn^{III}(\mu\text{-}O)_2Mn^{IV}$	(H_2O)(terpy)	2.72	[105-107]
7		$(bpy)_2$	2.70	[108-110]
8		N4py	2.65	[111]
9	$Mn^{IV}(\mu\text{-}O)_2Mn^{IV}$	(2-OH)salpn	2.73	[112-115]
10	$Mn^{IV}(\mu\text{-}OH)_2Mn^{IV}$	(2-OH)salpn	3.01	[114, 115]
11	$Mn^{IV}(\mu\text{-}O)(\mu\text{-}OH)Mn^{IV}$	(2-OH)salpn	2.84	[114, 115]
12	$Mn^{II}(\mu\text{-}\eta^1\text{:}\eta^1\text{-}O_2)Mn^{III}$	N-Et-HPTB		[116]
13		BPMP		[117]
14	$Mn^{III}(\mu\text{-}\eta^1\text{:}\eta^1\text{-}O_2)Mn^{III}$	$S^{Me2}N_4$(6-Me-DPEN)	4.11	[118]
15	$Mn^{III}(\mu\text{-}O)Mn^{III}$	$S^{Me2}N_4$(6-Me-DPEN)	3.52	[118]
16	$Mn^{III}(\mu\text{-}OH)_2Mn^{III}$	(2-OH)5-NO_2-salpn	3.23	[115, 119]
17		(2-OH)salpn		[120]
18	$Mn^{III}(\mu\text{-}O)_2(\mu\text{-}OAc)Mn^{IV}$	tacn	2.59	[121]
19		Me_4dtne	2.57	[122]
20	$Mn^{IV}(\mu\text{-}O)_2(\mu\text{-}OAc)Mn^{IV}$	Me_4dtne	2.60	[122]
	Iron			
21	$Fe^{II}_2(\mu\text{-}OH)_2$	Me_3NTB		[61]
22		6-Me_3TPA	3.19	[123]
23		BnBQA	3.14	[123]
24	$Fe^{III}(\mu\text{-}O)_2Fe^{IV}$	5-Et_3tpa	2.68	[124]
25		5-Me3tpa	2.89	[125]
26		TPA*		[126]
28	$Fe^{III}_2(\mu\text{-}O)(\mu\text{-}OH)$	6-Me_2bpg	1.90	[127]

#	Core	Ligand	M…M	Ref.
29	$Fe^{III}_2(\mu\text{-}OH)_2$	$ArCO_2^-$, Bn_2en/Bnen	2.98	[128]
30		O^{Me2}-N_4(6-Me-DPEN)	3.17	[129]
31	$Fe^{III}_2(\mu\text{-}O)(\mu\text{-}O_2)$	Me_3NTB	3.07	[61]
32		BnBQA	3.16	[130]
33		6-Me_3tpa	3.14	[131, 132]
34		6-HPA		[133]
35	$Fe^{III}_2(\mu\text{-}OH)(\mu\text{-}O_2)$	Me_3NTB	3.09	[61]
36		BnBQA	3.46	[130]
37	$Fe^{IV}_2(\mu\text{-}O)_2$	Me_3NTB	2.70	[61]
38		TPA*	2.73	[126]
39	$Fe^{IV}_2(\mu\text{-}O)$	TAML	3.35	[134]
40	$(H_2O)Fe^{III}(\mu\text{-}O)Fe^{IV}(O)$	6-Me_3tpa		[135]
41	$(HO)Fe^{III}(\mu\text{-}O)Fe^{IV}(O)$	TPA*		[68, 69]
42	$(HO)Fe^{IV}(\mu\text{-}O)Fe^{IV}(O)$	TPA*		[136]
43	$(O)Fe^{IV}(\mu\text{-}O)Fe^{IV}(O)$	6-HPA		[133]
	Cobalt			
44	$Co_2^{II}(\mu\text{-}OH)_2$	Tp^{iPr2}		[137]
45		Tp^{Me3}	3.14	[138]
46	$Co_2^{II}(\mu\text{-}\eta^2\text{:}\eta^2\text{-}O_2)$	Tp^{iPr2}		[137]
47	$Co_2^{III}(\mu\text{-}\eta^1\text{:}\eta^1\text{-}O_2)$	FTF 4-2,1-NH		[139]
48		DPX	4.58	[140, 141]
49	$Co_2^{III}(\mu\text{-}O)_2$	Tp^{Me3}	2.73	[138, 142]
50	$Co_2^{II}(\mu\text{-}O_2)_2$	Tp^{iPrMe}	3.50	[143]
	Nickel			
51	$Ni^{II}_2(\mu\text{-}OH)_2$	L_1^H	3.11	[144]
52		Tp^{Me3}		[138]
53		L5		[145]
54		dpema		[146]
55		6-Me_3TPA	3.09	[147]
56		Tp^{iPr2}	3.20	[148]
57		TPA		[149]
58		tBuDPA	3.10	[150]
59	$Ni^{II}_2(\mu\text{-}O_2)_2$	6-Me_3TPA	3.92	[147]
60	$Ni^{II}_2(\mu\text{-}\eta^1\text{:}\eta^1\text{-}O_2)$	tmc		[151]
61	$Ni^{III}_2(\mu\text{-}O)_2$	L_1^H		[144]
62		Tp^{Me3}	2.88	[138]
63		L5		[145]

#	Core	Ligand	M…M	Ref.
64		dpema	2.86	[146]
65		6-Me_3TPA	2.92	[147]
66		$PhTt^{tBu}$	2.83	[152, 153]
67	$Ni^{IV}(\mu\text{-}O)_3$	Me_3-tacn		[154]
	Copper			
68	$Cu^{II}_2(\mu\text{-}OH)_2$	Bz_3-tacn	2.98	[82]
69		*i*Pr_2H-tacn	3.01	[82]
70		Tp^{iPr2}	2.94	[155, 156]
71		^{O}L	2.89	[157]
72		DMEGdmae	2.86	[158]
73		TMEDA		[159]
74	$Cu^{II}Cu^{III}(\mu\text{-}OH)_2$	DPMN		[160, 161]
75	$Cu^{II}_2(\mu\text{-}OH)$	$(pyN_2^{Bz})_2$	2.66	[162]
76	$Cu^{II}Cu^{III}(\mu\text{-}OH)$	$(pyN_2^{Bz})_2$		[162]
77	$Cu^{III}_2(\mu\text{-}OH)$	$(pyN_{2Bz})_2$		[162]
78	$Cu^{II}_2(\mu\text{-}\eta^1\text{:}\eta^1\text{-}O_2)$	TPA	4.36	[163, 164]
79		L^{PzTACN}	3.80	[165]
80		^{O}L		[157]
81		BPQA		[166]
82	$Cu^{II}_2(\mu\text{-}\eta^2\text{:}\eta^2\text{-}O_2)$	Tp^{iPr2}	3.56	[155, 156]
83		bitripy	3.48	[167]
84		*i*Pr_3-tacn		[168]
85		^{H,tBu}ed	3.45	[169]
86		H-PYAN		[170]
87		H-L		[171]
88		L^{Py2}		[172]
89		Me_2-imdz		[173]
90		N3		[174]
91	$Cu^{III}_2(\mu\text{-}O)_2$	Bz_3-tacn	2.97	[82]
92		PN2	2.90	[175]
93		*i*Pr_3-tacn		[82]
94		Me_2TPA	2.76	[176]
95		L^{H}		[177]
96		L^{Py1Bz}		[172, 178]
97		L_{nBuBIM}	2.78	[179]
98		BzPY1		[174]

1.5.1. Manganese

Di-nuclear manganese-oxygen complexes $Mn^{n}(\mu\text{-}OX)Mn^{n}$ (n = II, III, IV) have been extensively studied in the literature, as they are perfect model complexes for many important Mn dependent enzymes.[180] As a matter of fact, several important enzymes have their active site composed by one or more $Mn^{n}(\mu\text{-}OX)Mn^{n}$ units. One of the most important is the oxygen evolving complex (OEC) of the photosystem II (PSII, Figure 1.6), the main enzyme responsible for the biological water oxidation (and therefore dioxygen release) in photosynthetic processes.[100, 181, 182] The high resolution (1.95 Å) crystal structure of the active site has been resolved only relatively recently,[183] showing a complex multinuclear Mn_4O_5Ca cluster (Figure 1.6), that evolved from five possible intermediate states S_n (n = 0–4),[184] passing stepwise from a $Mn^{III}_3Mn^{IV}$ to a Mn^{IV}_4 system before to release O_2.[185] Despite its nature as a tetramer, several di-nuclear manganese-oxygen adducts were proposed as successful model complexes. A plethora of $Mn^{III}(\mu\text{-}O)_2Mn^{IV}$ and $Mn^{IV}(\mu\text{-}O)_2Mn^{IV}$ systems with different ligand systems (terpy, bpy, salpn, Table 1.6, compounds **6**–**9**),[105-110, 112-115] alongside with the first examples of $Mn^{III}(\mu\text{-}O)_2Mn^{III}$ and $Mn^{IV}(\mu\text{-}O)_2(\mu\text{-}O_2)Mn^{IV}$ (**2**–**3**)[102, 103] have been synthesised, showing a very good correlation of the Mn···Mn distance (2.53-2.75 Å) with the value obtained by EXAFS analysis of the enzyme (~2.7 Å).[186, 187] Moreover, Pecoraro and co-workers demonstrated the possibility of protonating $Mn^{IV}(\mu\text{-}O)_2Mn^{IV}$ complexes achieving $Mn^{IV}(\mu\text{-}O)(\mu\text{-}OH)Mn^{IV}$ and $Mn^{IV}(\mu\text{-}OH)_2Mn^{IV}$ systems (**9**–**11**).[114, 115] Such complexes showed a strong correlation of the Mn···Mn distance and magnetic coupling from the protonation state, helping understanding the changes in the OEC in the different S-states.

Another important class of $Mn^{n}(\mu\text{-}OX)Mn^{n}$ (n = II, III) are the model complexes for class Ib ribonuclease reductase (RNR, Figure 1.6), an enzyme responsible for reduction of nucleotides to deoxynucleotides and therefore involved in DNA synthesis and repair in bacteria.[188] Stubbe and co-workers proposed the reaction of the Mn^{II}_2 core with superoxide anion yielding to a $Mn^{II}Mn^{III}$-peroxide entity that, by subsequent O–O cleavage, generates a $Mn^{III}(\mu\text{-}O)(\mu\text{-}OH)Mn^{IV}$ species.[95, 189] Stubbe's observations raised the interest of the community about class Ib RNR, leading to the report of the first examples of $Mn^{II}(\mu\text{-}O_2)Mn^{III}$ (**12**–**13**) and $Mn^{III}(\mu\text{-}O_2)Mn^{III}$ (**14**) by the McDonald and Kovacs groups, respectively.[116-118]

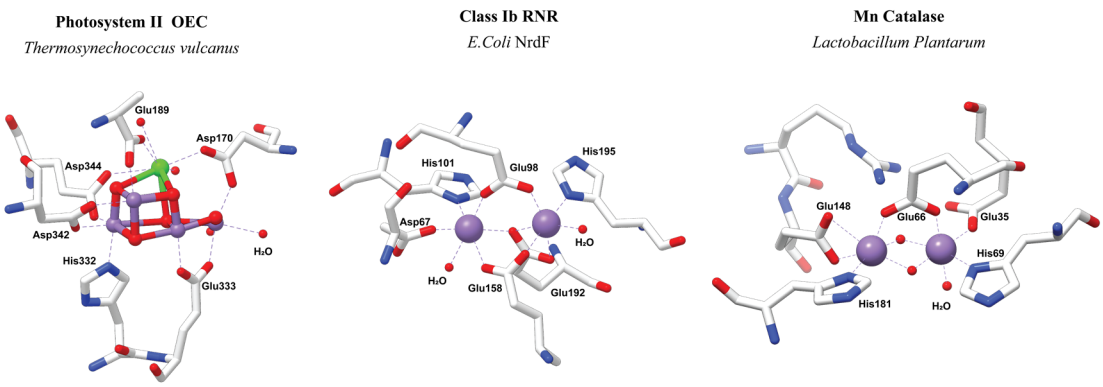

Figure 1.6 – Crystallographic structure of the subunits of PS II OEC (PDB: 4UB6), Class Ib RNR (3N37) and Manganese catalase (1JKU), alongside with the respective active sites. Mn ions are depicted as purple spheres, calcium ion is depicted as a green sphere.

Several of the $Mn^{n}(\mu\text{-}OX)Mn^{n}$ model complexes reported for PSII OEC (see above) have also been postulated to be mimicking systems for Mn catalase (Figure 1.6), a relevant dimanganese enzyme capable of dismutating hydrogen peroxide.[190, 191] The structure of its active site is known and is composed of a $Mn^{n}(\mu\text{-}O)_2Mn^{n}$ (n = III, IV) unit, with the two manganese ions further connected by the carboxylate of a glutamic acid residue (Figure 1.6). Examples of $Mn^{n}(\mu\text{-}O)_2(\mu\text{-}OAc)Mn^{IV}$ (n = III, IV) systems have been reported (**18**–**20**),[121, 122] attempting to mimic the structure of the catalase active site. Moreover, Pecoraro and co-workers reported one of the first efficient functional models for Mn catalase, namely a $Mn^{III}(\mu\text{-}OH)Mn^{III}$ complex (**17**) capable of reacting with H_2O_2 with a turnover number > 1000.[120]

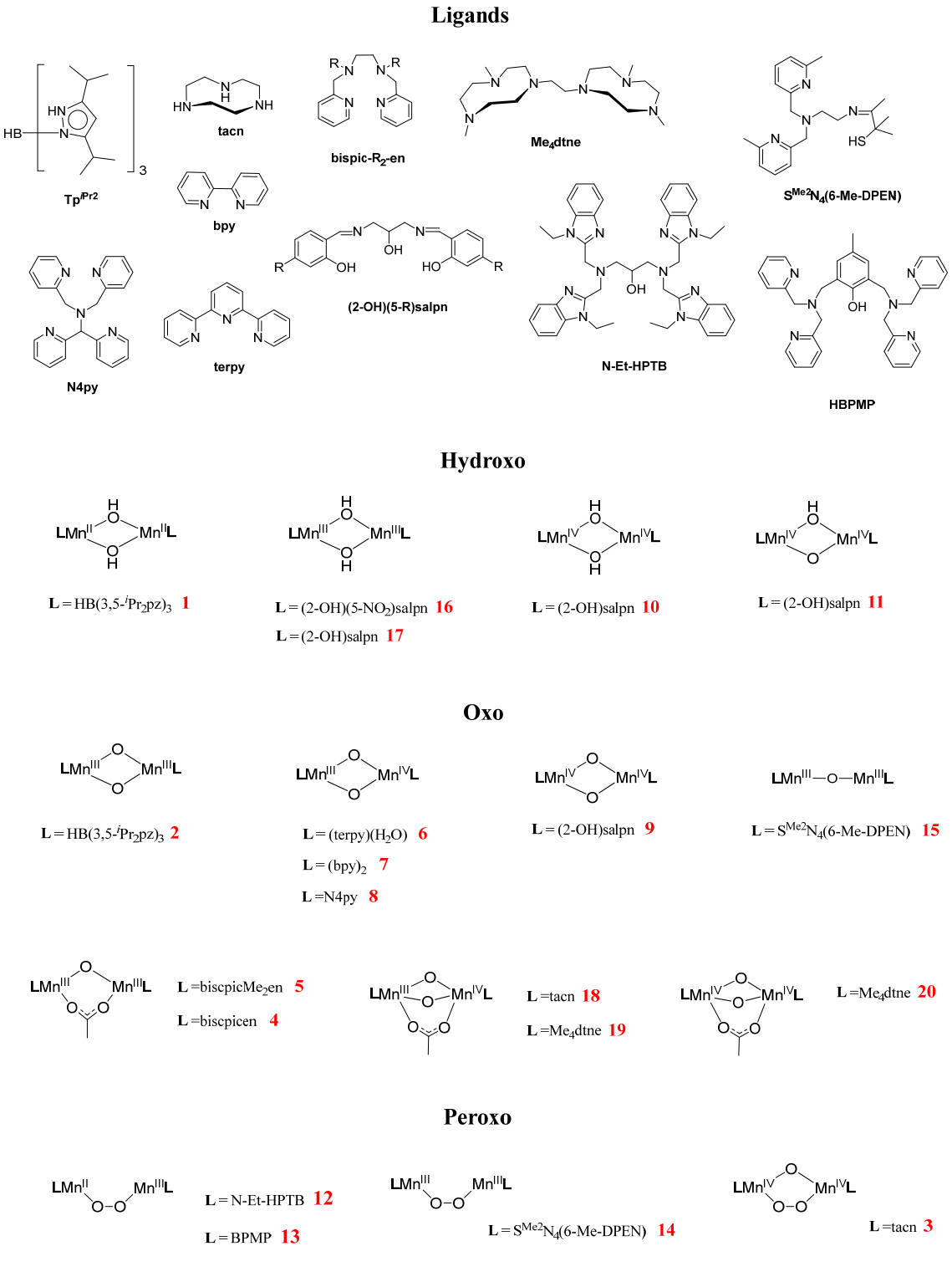

Figure 1.7 – Structures of the ligand and complexes present in Table 1.1

1.5.2. Iron

As mentioned before, the di-nuclear motif is quite common for the manganese-based enzyme and, therefore, for their corresponding biomimetic complexes. The situation is different for iron systems, in which the di-nuclear compound are outnumbered compared to the mononuclear counterpart.[39] Almost the totality of the synthesised biomimetic di-nuclear iron oxygen adducts are related to two specific enzymatic systems, the soluble methane monooxygenase (sMMO, see chapter 1.3.1) and the R2 subunit of class Ia ribonucleotide reductase (RNR R2). In particular, the majority of the reported diiron systems aim to shed light on the structure and reactivity of two elusive species: the intermediate Q from sMMO, postulated to be an open core Fe^{IV}_2 oxo system,[35, 59] and the intermediate X from RNR R2, postulated to be closed core $Fe^{III}Fe^{IV}$ oxo species.[192, 193]

All the species reported can be considered as interconnected with each other (Scheme 1.8) and have been achieved by different pathways in the presence of different ligand systems. A huge role in the field of biomimetic high valent diiron complexes has been performed by Que and co-workers, which reported and characterised the first examples of diamond core $Fe^{III}_2(\mu\text{-}O)_2$ (**27**),[194, 195] $Fe^{III}Fe^{IV}(\mu\text{-}O)_2$ (**24**)[124, 125] as well as $Fe^{IV}_2(\mu\text{-}O)_2$ (**38**).[126] Moreover, they synthetized also $Fe^{II}(\mu\text{-}OH)_2$ systems (L = Me_3NTB **21**,[61] 6-Me_3TPA **22**,[123] BnBQA **23**[123]) capable of fixing dioxygen, achieving the formation of a $Fe^{III}(\mu\text{-}O)(\mu\text{-}O_2)$ (**31**,[61] **32**,[130] **33**[131, 132]) that mimics intermediate P of sMMO (see chapter 1.3.1). Notably, in the case of L = Me_3NTB (**31**), they demonstrated that a Lewis acid such as Sc^{3+} promotes the cleavage of the peroxo O–O bond, achieving the $Fe^{IV}_2(\mu\text{-}O)_2$ species (**37**) in a single step[61] (Scheme 1.8), without formation of any intermediate $Fe^{III}Fe^{IV}(\mu\text{-}O)_2$, such as for L= TPA* (**26**).[126]

Alongside such interesting closed core high valent diiron oxo species, several open core examples were also synthesised. Que and co-workers reported the formation of an open core $(HO)Fe^{III}(\mu\text{-}O)Fe^{IV}(O)$ (L = TPA* **41**),[68, 69] notably one of the stronger high valent diiron oxidants reported so far. This species demonstrated the ability to oxidise the C–H bond of 9,10 dihydroanthracene (k_2 = 28 $M^{-1}s^{-1}$ at -80\degree C; $BDE_{C–H}$ = 78 kcal/mol)[8] seven and six orders of magnitude faster compared to the isoleptic closed cores $Fe^{III}Fe^{IV}(\mu\text{-}O)_2$ (**26**) and $Fe^{IV}_2(\mu\text{-}O)_2$ (**38**) complexes respectively,[126] and four orders of magnitude faster than the analogous open core $(HO)Fe^{IV}(\mu\text{-}O)Fe^{IV}(O)$ species (**42**).[136] Moreover, although the high valent diiron complexes are generally less reactive than

equivalent mononuclear species, complex **41** has been demonstrated to react 1000-fold faster than the corresponding $Fe^{IV}(O)$. The game-changing reactivity of **41** compared to the previously reported diiron system is also related to its high spin configuration ($S = 2$), which is analogous to the one observed for sMMO intermediate Q.

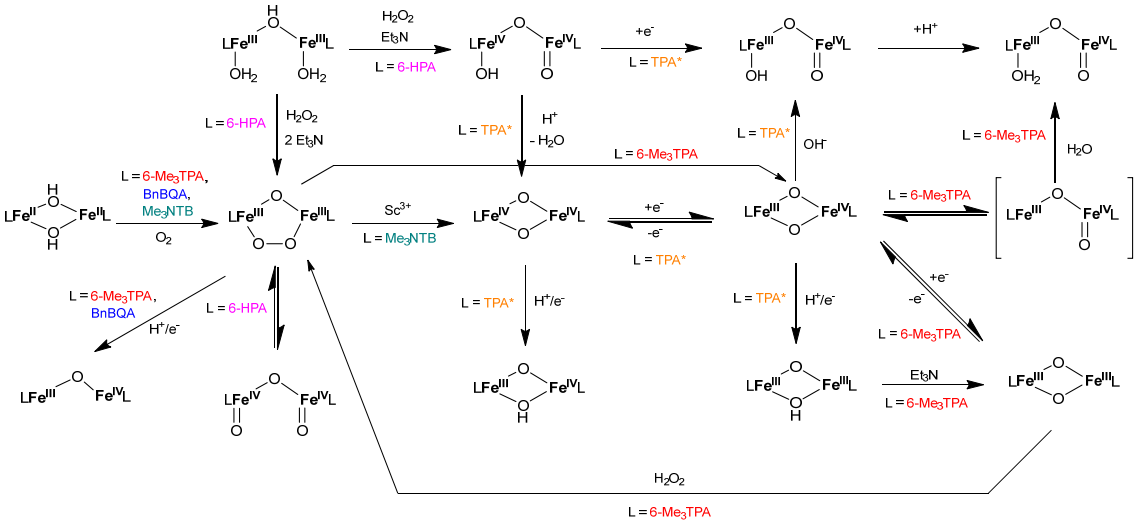

Scheme 1.8 – Relevant diiron oxygen adducts and their interconnected synthetic pathways.

In parallel to Que's discoveries, Kodera and co-workers reported the first example of the open core $(O)Fe^{IV}(\mu\text{-}O)Fe^{IV}(O)$ (L = 6-HPA **43**),[133] in which both Fe^{IV} atoms bear a terminal oxo ligand. Notably, this species is the first example of $S = 2$ oxo diiron (IV) complexes reported to date and therefore one of the best candidates to provide more insight into the sMMO intermediate Q. Moreover, species **43** was in equilibrium with its corresponding $Fe^{III}(\mu\text{-}O)(\mu\text{-}O_2)$ (**36**),[133] suggesting an alternative pathway for the conversion of intermediate P to Q.

Other examples of high valent diiron oxygen adducts mimicking the catalytic intermediate of both sMMO and RNR R2 are $Fe^{III}_2(\mu\text{-}OH)_2$ (**29**, **30**[128, 129, 196] and $Fe^{III}_2(\mu\text{-}O)(\mu\text{-}OH)$ complexes (**28**).[127] In particular compound **29** reported by Lippard[128] is one of the few diiron O_2 activating complexes bearing carboxylate ligands, therefore useful to understand the role of the carboxylate residue (mainly glutamate) present in the RNR R2 and sMMO active sites. Another relevant example of diiron oxygen complex is the catalytically active TAML supported $Fe^{IV}_2(\mu\text{-}O)$ (**39**).[134] This compound, reported by Collins and co-workers, is one of the few examples of mono μ-oxo Fe^{IV} complex, and the

first example of Fe^{III} centre able to perform direct dioxygen activation. Notably, the stability of the high valent Fe^{IV} centres in this configuration is provided by the strong electron-donating contributions of the four amidato nitrogens present in the TAML ligand, which has been reported to stabilise the first example of non-heme Fe^{V}=O complex.[197]

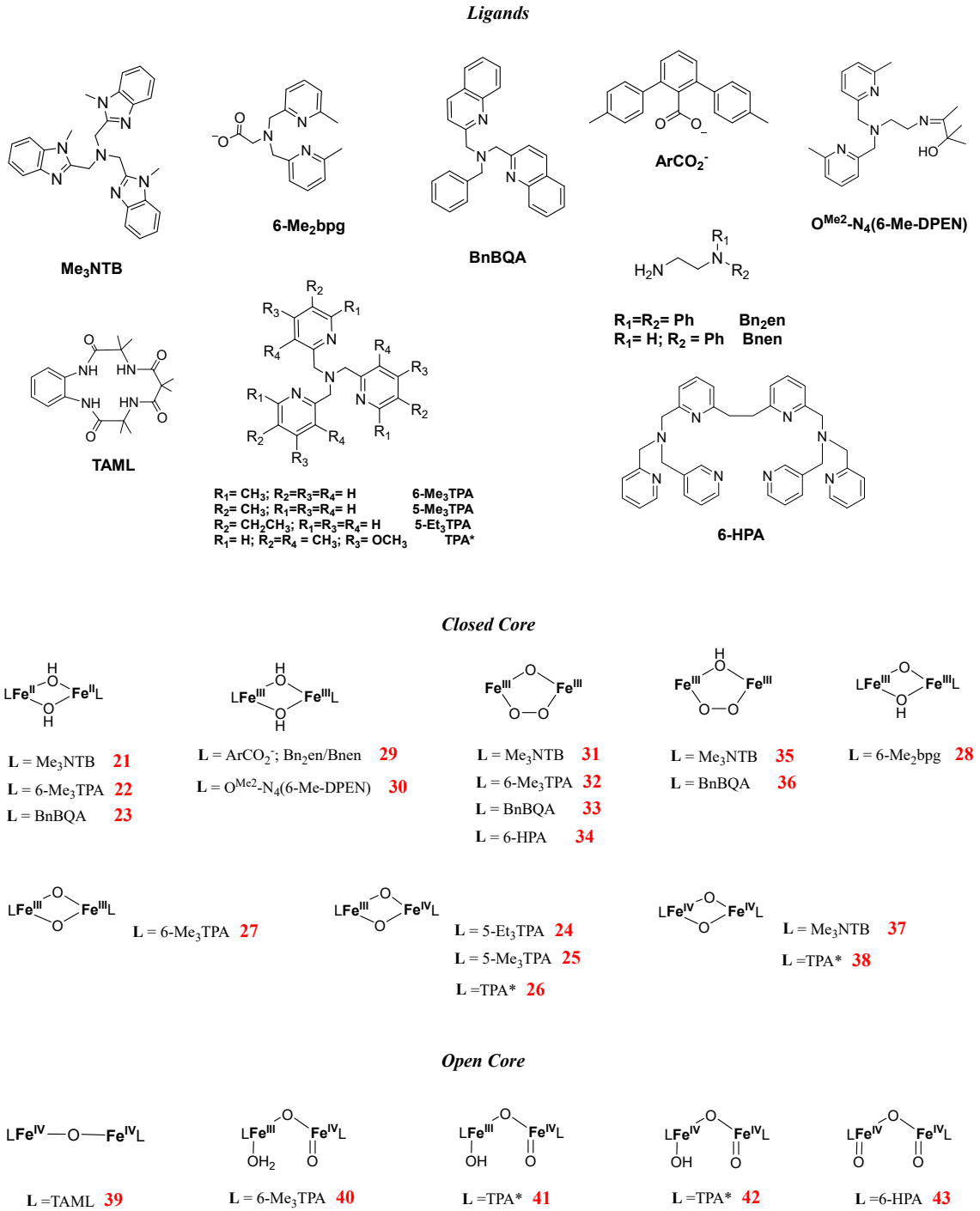

Figure 1.8 – Structures of the diiron complexes and ligands reported in Table 1.1.

1.5.3. Cobalt

In spite of the absence of corresponding enzymes bearing a dicobalt active site, some examples of di-nuclear cobalt-oxygen adducts are however present in the literature (Table 1.1), although restricted to biomimetic analogues of non-cobalt based systems.

The first relevant example of dicobalt oxygen adducts is the $Co_2^{II}(\mu\text{-}OH)_2$, supported by Tp^{iPr2} ligand (**44**), reported by Hikichi and co-worker.[137] Interestingly, in the presence of H_2O_2, compound **44** acts as precursor for the thermally unstable side-on peroxo species **46**, which is the first examples of $Co_2^{II}(\mu\text{-}\eta^2\text{:}\eta^2\text{-}O_2)$ reported.[137] Moreover, species **46** has been demonstrated to be competent in C–H activation, performing intramolecular hydrogen atom abstraction via thermal decomposition, leading to the corresponding μ-alkoxo−μ-hydroxo dicobalt adduct.[137]

Another relevant dicobalt oxygen system is compound **49**, the first structurally characterised diamond core $Co_2^{III}(\mu\text{-}O_2)$ complex, obtained from the corresponding Tp^{Me3} based $Co_2^{II}(\mu\text{-}OH)_2$ (**45**) upon addition of hydrogen peroxide.[138] Interestingly, in the presence of the same oxidant, the structurally analogous species **44** and **45** result in a different outcome according to the nature of the substituent on the ligand, although a transient peroxo species could be common to both. In the presence of Tp^{iPr2} ligand, the isopropyl C–H bonds are weak enough to be intramolecularly oxidised, leading to the quick decay of compound **46** into the μ-alkoxo−μ-hydroxo species. For Tp^{Me3} instead, the oxidation of the methyl C–H bond is not achievable at the experimental conditions used (-50 ˚C) and, therefore, compound **45** evolves into the relatively stable species **49** (Scheme 1.9).

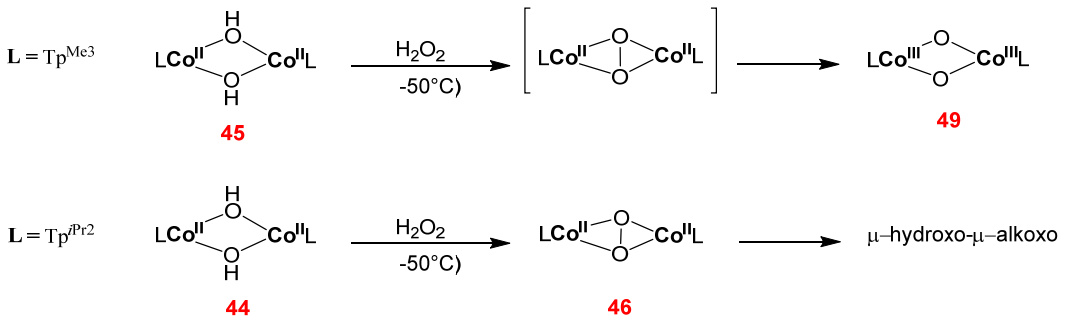

Scheme 1.9 – Influence of the nature of the ligand on the chemistry of $Co^{II}_2(\mu\text{-}OH)_2$

Alongside the more common closed-core μ-hydroxo, μ-peroxo and μ-hydroxo systems mentioned above, Theopold and co-workers reported and characterised also the first example of $Co^{II}_2(\mu\text{-}O_2)_2$ complex (**50**), in which the two cobalt atoms are linked by two bridging superoxide ligands, forming a six member ring.[143]

Although structurally quite different from all the aforementioned examples, cobalt-porphyrin systems have also been demonstrated to form di-nuclear oxygen adducts. In particular, both Collman[139] and Fukuzumi[140, 141], have observed the formation of $Co_2^{III}(\mu\text{-}\eta^1\text{:}\eta^1\text{-}O_2)$ complexes (**47**-**48**) as key intermediates in the four-electrons reduction of dioxygen to water performed by face-to-face cobalt porphyrins.[141]

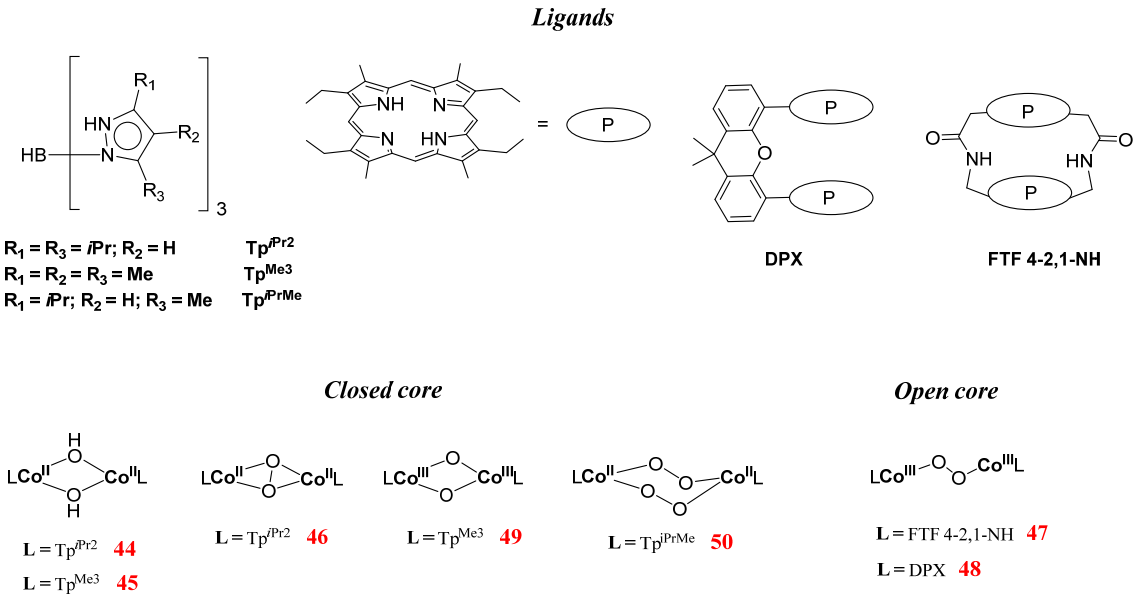

Figure 1.9 – Structures of the di-cobalt complexes and ligands reported in Table 1.1.

1.5.4. Nickel

Although dinickel oxygen adducts are rare in enzymatic systems (*e.g. urease*),[198] a plethora of dinickel-oxygen model complexes mimicking O_2 activation by Cu and Fe-based monooxygenases are reported in the literature (Table 1.1). The main aim of these studies is to have a better understanding of how such enzymes activate strong C–H bonds, comparing the reactivity of the different dinuclear adducts in the presence of different metals and ligands. Moreover, theoretical studies suggested that high valent late transition metals could be significantly stronger oxidants, albeit such high reactivity would result in increasing instability, making these species often quite elusive.[101, 199]

Several examples of dinuclear $Ni^{II}_2(\mu\text{-}OH)_2$ are present in the literature (**51**-**58**), albeit the role of the majority of them is to act as a precursor for their high valent counterparts, in which no cases reported to date preserve the (μ-hydroxo) ligands. However, some of them have been reported to be capable of performing nucleophilic attack on atmospheric CO_2 (**56**,[148] **57**[149] and **58**[150]), with formation of the analogous μ-carbonate complexes (i.e. CO_2 fixation). Such systems have raised attention for their ability to mimic CO_2 fixation enzymes and particularly the Zn-based carbonic anhydrase, although the enzyme displays a monomeric and not dimeric metal-hydroxo unit.[200]

The first examples of high valent dinuclear $Ni^{III}_2(\mu\text{-}O)$ complex were almost simultaneously reported by Fukuzumi (**61**)[144] and Hikichi (**62**)[138], both by conversion of the related $Ni^{II}_2(\mu\text{-}OH)_2$ upon addition of H_2O_2. Complexes **61** and **62**, as well as species **63**[145] (see Table 1.1), display a similar closed core structure and are competent of both intramolecular[138, 144] and intermolecular[145] hydrogen atom abstraction. Analogously to what was observed by Tolman for $Cu^{III}_2(\mu\text{-}O)$[81] (see below), the presence of a $\mu\text{-}\eta^2\text{:}\eta^2$-peroxo intermediate has been invoked (Scheme 1.10) for the formation of $Ni^{III}_2(\mu\text{-}O)$, although no direct experimental evidence has been reported to date. Such an observation suggests that, contrary to Cu, the Ni ion strongly promotes the homolysis of the O–O bond in the peroxo intermediate to immediately form a more stable $Ni^{III}_2(\mu\text{-}O)$ species, highlighting, opposite to Cu,[201] a stark difference in energies between the peroxo and oxo species. In spite of such considerations, Brunold and co-workers reported the observation of the first example of μ-1,2-peroxo $Ni^{II}_2(\mu\text{-}O_2)$ species (**60**),[151] supported by bulky tetradentate macrocyclic ligand. Another relevant example of $Ni^{III}_2(\mu\text{-}O)$ is species **64**,

reported by Itoh and co-workers, which is the first and only example of $Ni^{III}_2(\mu\text{-}O)$ exhibiting a triplet ground state.[146] It is also worth mentioning compound **66**,[152]

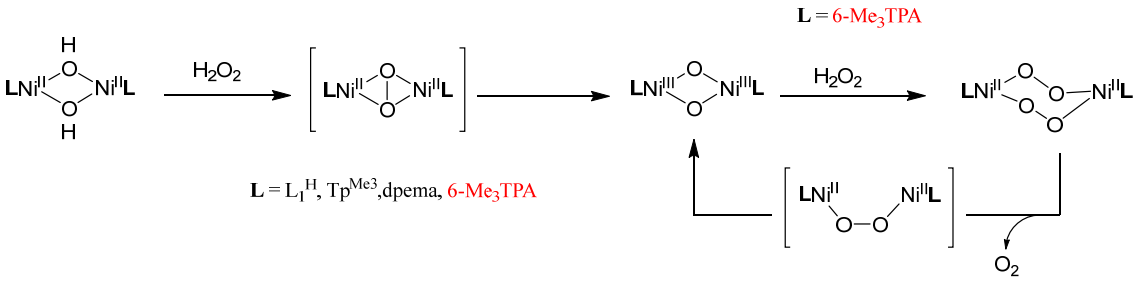

Scheme 1.10 – Conversion of $Ni^{II}_2(\mu\text{-}OH)_2$ to $Ni^{III}_2(\mu\text{-}O)$ (for L = $L_1{}^H$, Tp^{Me3}, dpema, 6-Me_3TPA) and further conversion of $Ni^{III}_2(\mu\text{-}O)$ to $Ni^{II}_2(\mu\text{-}O_2)_2$ (for L = 6-Me_3TPA).

which is the first example of $Ni^{III}_2(\mu\text{-}O)$ species generated through direct dioxygen fixation by the monomeric thioether ligand supported Ni^I precursor. In this particular case, the role of the ligand is crucial, since the borato ligands containing thioether sulphur donors (PhTt$^{t\text{Bu}}$, see Figure 1.10) stabilise the lower Ni(I) oxidation state, making accessible the Ni(I)/Ni(III) couple necessary for $Ni^{III}_2(\mu\text{-}O)$ formation from O_2. Notably, similar two-electron Ni(I)/Ni(III) processes are not accessible in complexes stabilised with nitrogen donor ligands.[152]

Analogous to what was reported by Theopold for Co[143] (see chapter 1.5.3), Suzuki and co-workers reported the first example of a $Ni^{II}_2(\mu\text{-}O_2)_2$ complex (**59**).[147] The bridging superoxo dinickel species is achieved upon reaction of the $Ni^{III}_2(\mu\text{-}O)$ with an excess of H_2O_2. The system seems to perform hydrogen atom abstraction both intra and intermolecularly, however,a deeper analysis demonstrated that the $Ni^{II}_2(\mu\text{-}O_2)_2$ species is not capable of such reactivity and, therefore $Ni^{III}_2(\mu\text{-}O)$ is proposed as reactive species. Dioxygen evolution upon thermal decomposition of $Ni^{II}_2(\mu\text{-}O_2)_2$ suggested a possible disproportionation of the two coordinated superoxide ligands to O_2 and a postulated μ-1,2-peroxo $Ni^{II}_2(\mu\text{-}O_2)$ species, which is then converted to the reactive $Ni^{III}_2(\mu\text{-}O)$ through homolytic scission of the peroxo O–O bond (Scheme 1.11).[147] Finally, it is noteworthy mention compound **67**, which is a unique example of a transient $Ni^{IV}_2(\mu\text{-}O)_3$ complex.[154] The highly reactive Ni(IV) oxidation state, which is achieved by reaction of the $Ni^{II}_2(\mu\text{-}Cl)_3$ precursor with NaOCl, is stabilised by the formation of a tris-μ-oxo-bridging structure.

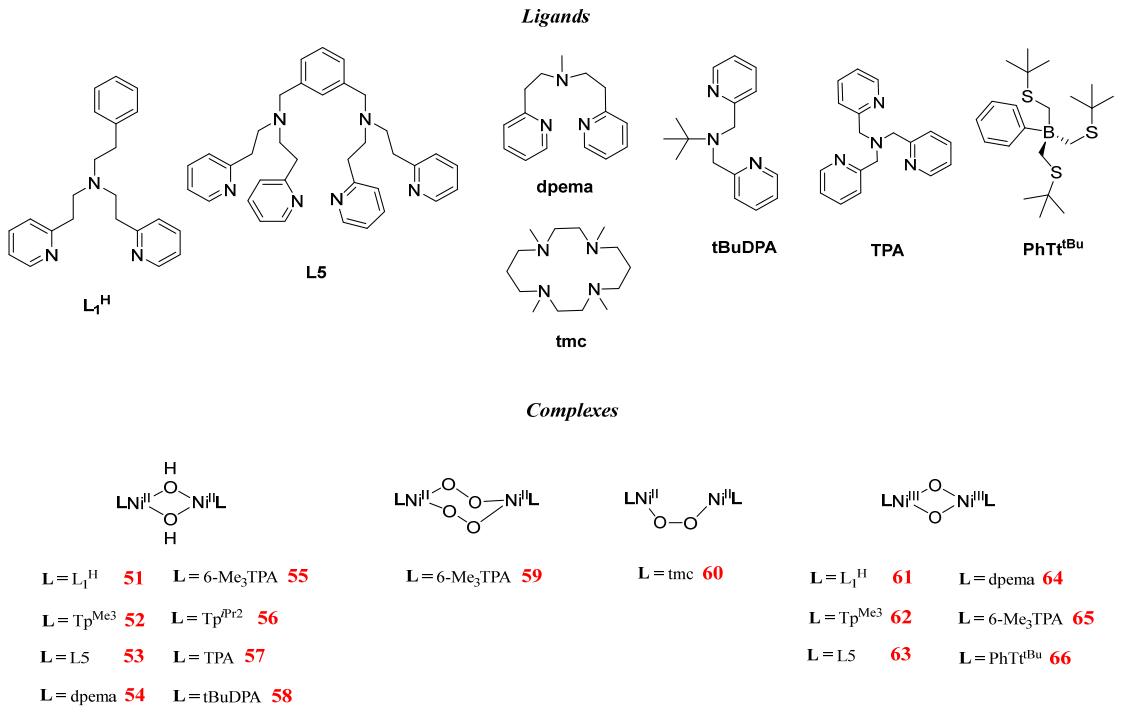

Figure 1.10 - Structures of the dinickel complexes and ligands reported in Table 1.1. For ligand 6-Me$_3$TPA, see Figure 1.8. For ligands Tp^{iPr2} and Tp^{Me3}, see Figure 1.9.

1.5.5. Copper

Copper plays a central role in enzymatic dioxygen activation and has been widely proven to be able to ligate O_2 forming diverse types of dinuclear copper oxygen adducts such as in hemocyanin[202] and tyrosinase (see chapter 1.3.2). The outstanding capability of copper (particularly Cu^I) to interact with dioxygen led to a myriad of different biomimetic dicopper oxygen species with different structures and binding modes. The dinuclear oxygen adduct motif is far more common for copper than for the rest of the first-row transition metals, and hundreds of complexes have been reported.[203] Therefore, in the interest of comprehension and legibility, only the systems that from our point of view represented a breakthrough in this field will be considered in this review.

For the dinickel oxygen adducts analysed in chapter 1.5.4. we observed that the $Ni^{II}_2(\mu\text{-}OH)_2$ is the precursor of choice for almost all of the high valent dinuclear complexes. In

the case of the copper we have a completely different situation. The precursor for almost the totality of the dicopper oxygen adducts are the Cu^{I} mononuclear counterparts, which directly react with O_2 leading to the corresponding high valent species, mimicking the dioxygen activation in enzymes such as tyrosinase. Several $Cu^{II}_2(\mu\text{-}OH)_2$ are reported in the literature, even if in many cases they constitute the preferred decay product of the corresponding μ-oxo/μ-peroxo species, such as for **68**-**71**. However, in the presence of excellent electron donor ligands such as guanidine-based systems, $Cu^{II}_2(\mu\text{-}OH)_2$ complexes have been reported to be obtained by the reaction of dioxygen with the corresponding Cu^{I} precursors (**72**).[158] Moreover, although generally stable and unreactive, $Cu^{II}_2(\mu\text{-}OH)_2$ systems have been reported to catalyse the aerobic oxidation of catechol if supported by peralkylated ethylenediamines such as TMEDA (**73**).[159] Only a few examples of mixed valent $Cu^{II}Cu^{III}_2(\mu\text{-}OH)_2$ (**74**)[160, 161] are known, mainly formed in the presence of binucleating ligands, whereas no high valent $Cu^{III}_2(\mu\text{-}OH)_2$ complexes are reported to date. Alongside the $Cu^{II}_2(\mu\text{-}OH)_2$, few examples of dinuclear copper systems with only one bridging hydroxide unit are reported. In particular, Tolman *et al.*[162] reported the synthesis of a $Cu^{II}_2(\mu\text{-}OH)$ system (**75**) supported by a dipyridindicarboxamide macrocyclic ligand (i.e. $(pyN_2^{Bz})_2$, Scheme 1.16), which was able to act as precursor for the corresponding $Cu^{II}Cu^{III}(\mu\text{-}OH)$ (**76**) and $Cu^{III}_2(\mu\text{-}OH)$ (**77**). Critically, **77** constitutes one of the first examples of dinuclear copper complex which maintains its μ-OH ligand despite both the metal centres being oxidised to Cu^{III}_2.

Apart from the example **72**, O_2 interacts with Cu^{I} leading to three possible isomeric dinuclear high valent systems, characterised by a diverse binding fashion and in which geometry and denticity of the ligand play a huge role:[203] the $Cu^{II}_2(\mu\text{-}\eta^1\text{:}\eta^1\text{-}O_2)$ (trans: ^{T}**P**; cis: ^{C}**P**), the $Cu^{II}_2(\mu\text{-}\eta^2\text{:}\eta^2\text{-}O_2)$ (^{S}**P**) and the $Cu^{III}_2(\mu\text{-}O)_2$ (**O**) (Scheme 1.14). The $Cu^{II}_2(\mu\text{-}\eta^1\text{:}\eta^1\text{-}O_2)$ complexes are very sensitive to ligand denticity and have been reported only in the presence of tetradentate ligands providing an average Cu···Cu of ~4.4 Å for ^{T}**P** and ~3.8 Å for ^{C}**P**.[204] The first example of structurally characterised ^{T}**P** (**78**) was reported by Karlin et al.[163, 164] whereas compound **79** constitutes the first cis-$\mu\text{-}\eta^1\text{:}\eta^1\text{-}O_2$ ^{C}**P** (**79**) complex, reported Meyer and co-workers.[165] $Cu^{II}_2(\mu\text{-}\eta^1\text{:}\eta^1\text{-}O_2)$ complex are generally not entropically favourite, although the energy cost can be reduced by tethering the two mononuclear complexes together or using binucleating ligands.[203, 205] Contrary to its $Cu^{II}_2(\mu\text{-}\eta^2\text{:}\eta^2\text{-}O_2)$ counterpart, ^{T}**P** acts as a nucleophilic oxidant,[206] albeit reactivity towards strong C–H bond activation (toluene, $BDE_{C\text{-}H}$ = 89.6 kcal/mol)[8] has been

observed in **80**.[157] $Cu^{II}_2(\mu\text{-}\eta^2\text{:}\eta^2\text{-}O_2)$ or $Cu^{III}_2(\mu\text{-}O)_2$ species were invoked as active oxidants, although no evidence was presented. This hypothesis was corroborated only later, when Karlin et al. successfully demonstrated the presence of an equilibrium between ^{T}**P** and **O** (**81**, Scheme 1.11).[166]

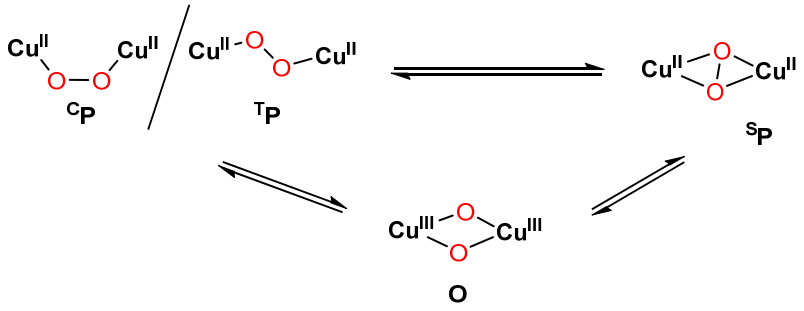

Scheme 1.11 – Structure of the three possible isomeric high valent species ^{C}**P**/^{T}**P**, ^{S}**P** and **O** and the interconnection between them.

The ^{S}**P** complexes are probably the most relevant from a biomimetic point of view, since they share the same unique $Cu^{II}_2(\mu\text{-}\eta^2\text{:}\eta^2\text{-}O_2)$ core with the oxy-Ty (see chapter 1.3.2) and oxyHemocyanin.[207] Such a binding mode for dicopper-peroxide adducts was reported for the first time by Kitajima and co-workers, who isolated and structurally characterised compound **82**, while recently Stack and co-worker reported the first example of ^{S}**P** complex supported uniquely by imidazole ligands (**89**), which is considered the more accurate biomimetic complex of the oxy-Ty active site.[173] The ^{S}**P** species is favoured in the presence of the tridentate ligand (average Cu···Cu ~3.5 Å), even if cases of bidentate ligand leading exclusively to this species are reported (**85**).[169] Similarly to what was observed for ^{T}**P**, binucleating ligands (**83**) are often employed to stabilise the bridging peroxo moiety, reducing the entropic cost.[167] ^{S}**P** complexes exhibit an electrophilic reactivity: species **87** was the first example of ^{S}**P** species to perform intramolecular and intermolecular hydroxylation, as well as epoxidation of styrenes;[171] complex **88** is instead the first $Cu^{II}_2(\mu\text{-}\eta^2\text{:}\eta^2\text{-}O_2)$ species reported to react with phenols.[172] In addition, a study reported by Fukuzumi et al. reported that species **90** is capable of catalysing the four-electron reduction of water by ferrocene.[174]

Although no evidence of its participation in biological processes are present, the high valent $Cu^{III}_2(\mu\text{-}O)_2$ bridging oxo (**O**) is, by far, the most reactive and deeply studied.[204] Such a species was first characterised by Tolman and co-workers (**91**).[82] **O** complexes

are generally stabilised by bidentate ligands, following the preference of Cu^{III} for square planar geometry (average Cu···Cu ~2.8 Å). Systems with tri- and tetradentate ligands are common as well.[203] Due to its strong reactivity, **O** is generally stable at low temperature (-80 ˚C) for limited periods of time, albeit examples of complexes indefinitely stable at -80 °C have been reported (**92**).[175] **O** generally undergoes thermal decay leading to the corresponding $Cu^{II}_2(\mu\text{-}OH)_2$ species, although the release of dioxygen (therefore a reversible dioxygen binding system) has been reported (**94**).[176] Similarly to compound **89**, also for **O**, a complex with only imidazole ligands (**97**) has been reported by Stack and co-workers.[179]

Analogously to ^{S}**P, O** complexes display electrophilic reactivity. Their capability of performing intramolecular C−H activation was initially observed by Tolman (**91**),[82] although the first proper study was conducted by Fukuzumi *et al.* [177] on compound **95**. Compound **96** was the first reported **O** complex capable of the oxidation of external substrates containing C−H bonds, as well as phenols.[172] Finally, in the same way as and ^{S}**P** (see above), **O** has been observed catalysing the reduction of H_2O by ferrocene (**98**).[174]

Although ^{S}**P** and **O** are structurally and electronically different isomers, in specific conditions they can interconvert with each other. This involves the formation and cleavage of the O−O and concurrent oxidation/reduction of the Cu^{III}/Cu^{II} couple. Tolman and co-workers were the first group to report this equilibrium (^{S}**P 84**; **O 93**)[168, 208] in which the two isomers were both present in optically measurable amounts (^{S}**P** λ_{max} = 340 nm, 380 nm; **O** λ_{max} = 300 nm, 400 nm) as a result of the oxygenation reaction. Although computational studies revealed that the two species are almost isoenergetic, with a negligible energetic interconversion barrier,[201] several studies were performed to understand the parameters that influence such equilibria. **O** species is enthalpically favoured and therefore preferentially formed at lower temperatures, while ^{S}**P** is entropically favoured, and is lower in energy in the presence of bulkier ligands.[208, 209] Karlin *et al.*, analysed the electronic effects of ligand substituents on the ^{S}**P**/**O** equilibrium (**86**),[170] showing that ^{S}**P** is more stabilised in presence of electron withdrawing groups, while electron donating groups favour the **O** isomer. Solvent also plays a major role in the ^{S}**P**/**O** equilibrium, with the **O** isomer favoured in the presence of coordinating solvents.[208] However, axial coordination of a bridging ligand or the presence of a more coordinating ion could trigger the isomerisation of **O** to ^{S}**P**, as demonstrated with bidentate ligands by Stack et al.[210]

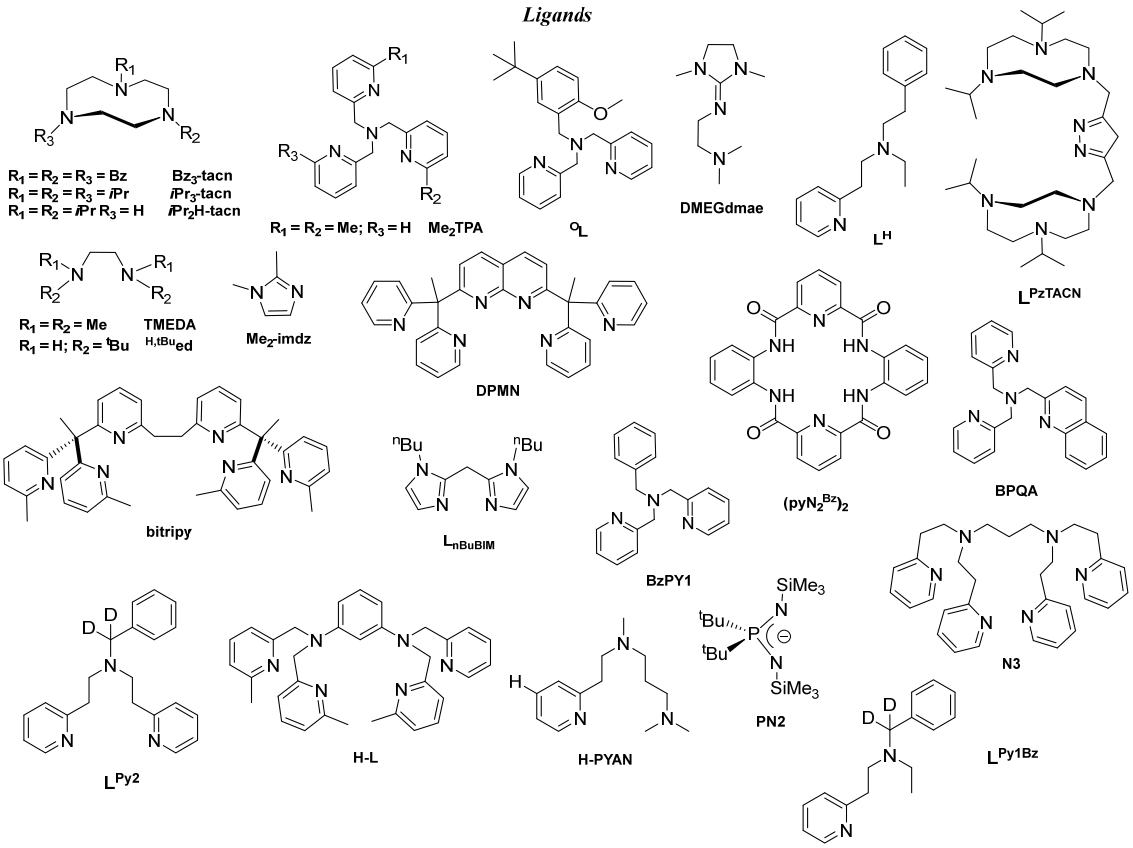

Hydroxo

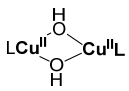

L = Bz_3-tacn **68** L = iPr_2H-tacn **69**

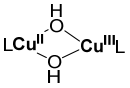

L = DPMN **74**

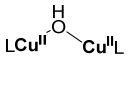

L = $(pyN_2^{Bz})_2$ **75**

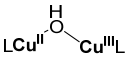

L = $(pyN_2^{Bz})_2$ **76**

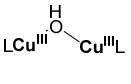

L = $(pyN_2^{Bz})_2$ **77**

L = Tp^{iPr2} **70** L = ^{O}L **71**

L = DMEGdmae **72** L = TMEDA **73**

Peroxo

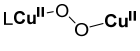

L = TPA **78**
L = ^{O}L **80**
L = BPQA **81**

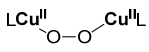

L = L^{PzTACN} **79**

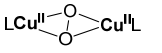

L = Tp^{iPr2} **82**
L = bitripy **83**
L = iPr_3-tacn **84**
L = ^{H,tBu}ed **85**
L = H-PYAN **86**
L = H-L **87**
L = L^{Py2} **88**
L = Me_2-imdz **89**
L = N3 **90**

Oxo

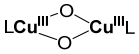

L = Bz_3-tacn **91**
L = PN2 **92**
L = iPr_3-tacn **93**
L = Me_2-TPA **94**
L = L^{H} **95**
L = L^{Py1Bz} **96**
L = L_{nbuBIM} **97**
L = BzPY1 **98**

Figure 1.11 - Structures of the dicopper complexes and ligands reported in Table 1.1. For ligand TPA, see Figure 1.10. For ligand Tp^{iPr2} see Figure 1.9.

1.5.6. Comparisons and final considerations

As anticipated above, the dinuclear-oxygen structural motif is quite common for elements belonging to the centre of the first row transition metals such manganese, which exhibited the widest speciation of all the series herein reported, reflecting the important biological role that dimanganese oxygen complexes and Mn-clusters in general (see chapter 1.5.1) play. Moreover, due to the low *d-count*, high oxidation states such as Mn^{IV} (d^3) are not uncommon, even if not exceptionally reactive, a behaviour that mirrors the biological functions of Mn clusters. In a similar way to Mn, Fe also shows a high speciation and high valent oxidation state. However, in this case, the high valent species Fe^{IV} (d^4) is extremely reactive and capable of performing strong C−H bond activation. Its noteworthy that Fe is unique among the others herein reported as it displays high valent open core structures, quite relevant for the understanding of enzymatic intermediate such as sMMO's intermediate Q (see chapter 1.3.1).

Contrary to what was observed for Mn and Fe, late transition metals display diminished speciation, particularly for Co and Ni. Cu exhibits a huge number of dinuclear oxygen complexes, demonstrating the important role that dicopper adducts play in enzymatic systems such as tyrosinase (see chapter 1.3.2) and the O_2-carrier hemocyanin.[202] However, the structures of the reported examples are mainly limited to the four isomers ^{C}**P**, ^{T}**P**, ^{S}**P**, **O** and the corresponding low valent μ-hydroxo complexes. Due to the increase in the *d*-electron count, the observable higher oxidation state is generally M^{III} (M = Co, Ni, Cu). The highly unstable M^{IV} has been often postulated as a transient species and has been observed only in rare cases.[154]

Table 1.2 – Average M···M distance (Å) for the $M^{II}_2(\mu\text{-OH})_2$ and $M^{III}_2(\mu\text{-O})_2$ reported in Table 1.1

M =	**$M^{II}_2(\mu\text{-OH})_2$**	**$M^{III}_2(\mu\text{-O})_2$**
Mn	3.31 Å	2.70 Å
Fe	3.17(4) Å	2.72 Å
Co	3.14 Å	2.73 Å
Ni	3.13(5) Å	2.87(4) Å
Cu	2.94(6) Å	2.85(10)

As mentioned, the speciation widely differs among the element considered; however, its noteworthy that two adducts are common to all of them, μ-hydroxo and μ-oxo, therefore allowing us a comparison across the transition metals first row. Considering the average M···M distance for the μ-hydroxo adducts in the common M^{II} oxidation state (M^{II}_2(μ-OH)$_2$ M = Mn, Fe, Co, Ni, Cu), we can observe a progressive contraction of the dinuclear core going from Mn to Cu, with Mn > Fe ~ Co ~ Ni > Cu (Table 1.2).

An analogous consideration can be made considering the average M···M distances for the M^{III}_2(μ-oxo) adducts (Table 1.3), with Ni ~ Cu > Mn ~ Fe ~ Co. Its noteworthy to observe that, although Co belongs to the late transition metals, its structural characteristics are more similar to Fe than Ni. However, such considerations are not representative of all the complexes reported in the literature and, above all, the M···M distance is strictly related to the steric hindrance and geometry imposed by the ligand system, which is widely different for each complex reported. Therefore, although the considerations done before suggested a trend, they are restricted to the examples herein reported and can be considered valid only in the context of the present review.

All the transition metals herein reported, with the exception of Ni, exhibited one or more μ-peroxo species. However, it is interesting to underline that the side-on μ-η^2:η^2-O_2 binding mode was observed exclusively for Cu, while for Mn, Fe and Co only the cis/trans end-on μ-η^1:η^1-O_2 binding modes have been observed. Although, the formation of a side-on μ-η^2:η^2-O_2 species has been invoked as a transient species in the formation of Ni^{III}(μ-O)$_2$,[144] no experimental evidence has been found, reflecting a more accentuated tendency of Ni to promote O–O cleavage, with respect to Cu. Moreover, Cu is the only metal in which the peroxo-oxo isomerism has been observed, and no other first row transition metals display a similar reversible formation/cleavage of the O–O bond.

In the end it is noteworthy that, although quite uncommon, Co and Ni are the unique elements to exhibit a (μ-O_2)$_2$ structure,[143, 147] in which two O_2^- units are bound to both metal centres forming a six-member ring. Such unusual systems are quite interesting from a synthetic point of view, since they are overoxidation products of the corresponding μ-oxo complexes. Moreover, they are reported to easily undergo thermal decomposition releasing dioxygen and reforming the starting μ-oxo complex.

1.5.7. Dearth of bis(μ-hydroxo) high valent metal-oxygen adduct

In this section we want to focus in particular on the high valent μ-hydroxo adducts. As mentioned in chapter 1.3, the dinuclear μ-hydroxo complexes may in fact play a more important role rather than act exclusively as precursor. Indeed, it is not difficult to believe that, in an aqueous environment such as the physiological one in which the enzymes operate, the main high valent species generally identified as μ-oxo or μ-peroxo could exist, even if transiently, as protonated species, taking part in some form of equilibrium dependent on local pH. Moreover, these species might be the actual species involved in the oxidation reactions or even possible intermediates formed upon an initial HAA event. Therefore, the analysis of the role of such systems will be fundamental to have a complete picture of the mechanism involved at biological level. The new discoveries about the real structures of sMMO's intermediate Q and the studies on the role of *met*-Ty form in tyrosinase corroborate such hypotheses.[59, 71]

However, analysing the complexes reported in Tables 1.1 we can observe that high valent dinuclear hydroxo complexes are reported only for Mn and Fe. Manganese exhibits closed core $Mn^{IV}_2(\mu\text{-}OH)_2$ (**10**),[114, 115] whereas for Fe only open core structure with terminal hydroxo ligands such as $(HO)Fe^{III}(\mu\text{-}O)Fe^{IV}(O)$ (**41**)[68, 69] and $(HO)Fe^{IV}(\mu\text{-}O)Fe^{IV}(O)$ (**42**)[136] are reported. Critically species **41** is also one of the most reactive diiron complexes towards C–H activation. Notably, although the M^{III} is considered an highly reactive oxidation state for late transition metal and in particular Ni (d^7) and Cu (d^8), thisoxidation state is quite stable for Mn (d^4) and Fe (d^5) and therefore the $M^{III}(\mu\text{-}OH)_2$ species reported for both Mn (**16**-**17**) and Fe (**29**) have not been considered as relevant.

Almost no examples of dinuclear high valent hydroxide species are reported for late transition metals, with the only exception being the mono bridged $Cu^{III}_2(\mu\text{-}OH)$ reported by Tolman and co-workers.[162] Such observations, alongside the few relevant examples reported for Fe, lead us to claim that, in spite of their potential biological relevance, there is a dearth of dinuclear high valent μ-hydroxo complexes.

1.6. Aims and methods

The primary aim of our research is the preparation and characterization of high valent bis(μ-hydroxo) complexes of late transition metals, particularly Ni and Cu, and the study of their reactivity towards O/C−H activation. As mentioned in the previous chapters, despite their potential crucial role in several enzymatic mechanism involving their high-valent μ-oxo counterparts, an overall dearth of high-valent late transition metals μ-hydroxo systems is present in the literature. Moreover, late transition metals such as Ni and Cu are postulated to be extremely powerful oxidants.[101] Therefore, preparation and studying of such metastable species would allow us to partially shed light on the involvement and role of the high-valent late transition metals μ-hydroxo systems in catalytic processes.

In order to stabilise the high valent μ-hydroxo species, it will be mandatory to employ a ligand system structurally and electronically capable of stabilising high oxidation state species, avoiding at the same time the conversion of the μ-hydroxo ligands to the corresponding μ-oxo and the intramolecular chemical oxidation. Our choice fell on the dianionic malonamidate bidentate ligand DMMA (*N,N'*-bis(2,6-R-phenyl)-2,2-dimethylmalonamide) reported in Figure 1.11. The two anionic amidate donors are ideal choices for stabilising high valent species due to their exceptional σ-donating abilities and their resistance to oxidative and hydrolytic degradation.[211] Moreover, the bidentate nature of the malonamidate, will facilitate the formation of dinuclear adducts with a square planar geometry, which will help to stabilise the π-donating O ligands.

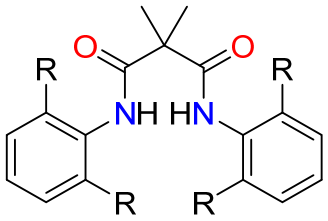

Figure 1.11 – Proposed malonamidate ligand $DMMA^{R_2}$ (R = –H, CH_3, $–CH(CH_3)_2$)

In the first step, the synthesis of the malonamidate ligand will be carried out, followed by a thorough characterization of this new ligand system through several spectroscopic techniques such as ^{1}H and ^{13}C NMR and FT-IR. Subsequently, our efforts will be focused on the synthesis and characterisation of the low valent $M^{II}_2(\mu\text{-}OH)_2$ precursors (M = Ni, Cu), which have been never reported to date for the chosen ligand system. Characterisation will be performed using a set of different techniques, including ^{1}H-NMR, UV-Vis, FT-IR, X-ray diffraction, mass spectrometry and cyclic voltammetry, in order to have clear picture of the structural, spectroscopic and electrochemical properties of these complexes.

The low valent $M^{II}_2(\mu\text{-}OH)_2$ precursor will be then converted into the corresponding high valent species by chemical oxidation, notably using only one-electron oxidants, attempting to achieve stepwise single electron oxidations. The use of two electron oxidants (often peroxide based systems) will be avoided in this phase, as they lead more easily to undesired μ-oxo complexes. The metastable species ideally formed, $M^{II}M^{III}(\mu\text{-}OH)_2$ and $M^{III}_2(\mu\text{-}OH)_2$, will be trapped through the use of low temperature techniques. Spectroscopic and structural characterisation of these species will be provided through the employment of EPR, UV-Vis, X-ray absorption near the edge structure (*i.e.* XANES) and, critically, extended X-ray absorption fine structure (*i.e.* EXAFS). The X-ray absorption spectroscopy experiments will be performed in collaboration with Dr. Erik R. Farquhar at SSRL Synchrotron facility in Stanford, USA. The obtained results will be supported and validated by DFT computational calculation were necessary. Further evidence will be provided indirectly by analysis of reaction kinetics and products.

An important part of this study will be focused on the reactivity properties of these metastable species, and their capability of performing O/C−H activation. Reactivity with model substrates and kinetic analyses, including kinetic isotopic effect studies, will be thoroughly performed, allowing us to have an insight into the mechanism involved.

The crucial point of our study is to probe whether the high valent dinuclear μ-hydroxo species are as potent as oxidants as the widely analysed μ-oxo, and whether, therefore, they are feasibly involved in catalytic cycles. A further point will be to assess the role of the *d*-electron count on the stability and reactivity of such species, analysing the properties and reactivity changes across the late transition metals, and in particular from Ni to Cu. In a later stage moreover, a comparison of the obtained complexes with their

mononuclear isoleptic analogues, as well as with the corresponding μ-oxo counterparts, will be performed in order to have a complete picture of the role of both ancillary ligands (oxide/hydroxide) and nuclearity on the properties of these systems. We believe that the result achieved in the present work could be beneficial for the bioinorganic chemistry community, helping to shed light on the role of the high valent late transition metal μ-hydroxo.

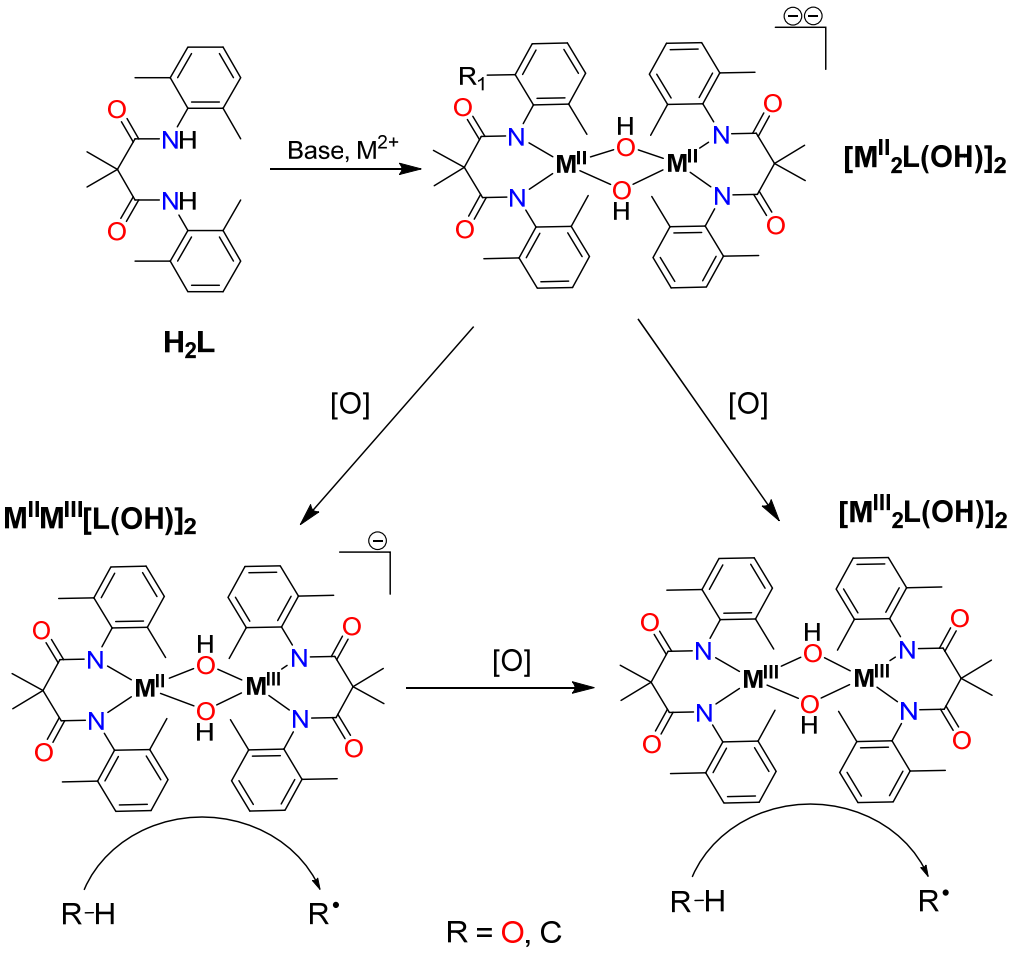

Schemes 1.13 – Summary scheme of the proposed aims for L = $DMMA^{Me2}$.

1.7. References

(1) J. W. Erisman, M. A. Sutton, J. Galloway, Z. Klimont and W. Winiwarter, *Nat. Geosci*, 2008, **1**, 636-639.
(2) M. C. J. Bradford and M. A. Vannice, *Catal. Rev.*, 1999, **41**, 1-42.
(3) J. M. Ogden, *Annu. Rev. Energy Env.*, 1999, **24**, 227-279.
(4) H. Arakawa, M. Aresta, J. N. Armor, M. A. Barteau, E. J. Beckman, A. T. Bell, J. E. Bercaw, C. Creutz, E. Dinjus, D. A. Dixon, K. Domen, D. L. DuBois, J. Eckert, E. Fujita, D. H. Gibson, W. A. Goddard, D. W. Goodman, J. Keller, G. J. Kubas, H. H. Kung, J. E. Lyons, L. E. Manzer, T. J. Marks, K. Morokuma, K. M. Nicholas, R. Periana, L. Que, J. Rostrup-Nielson, W. M. H. Sachtler, L. D. Schmidt, A. Sen, G. A. Somorjai, P. C. Stair, B. R. Stults and W. Tumas, *Chem. Rev.*, 2001, **101**, 953-996.
(5) B. M. Hoffman, D. Lukoyanov, Z. Y. Yang, D. R. Dean and L. C. Seefeldt, *Chem. Rev.*, 2014, **114**, 4041-4062.
(6) E. V. Kondratenko, T. Peppel, D. Seeburg, V. A. Kondratenko, N. Kalevaru, A. Martin and S. Wohlrab, *Catal. Sci. Technol.*, 2017, **7**, 366-381.
(7) J. H. Lunsford, *Angew. Chem. Int. Ed. Engl.*, 1995, **34**, 970-980.
(8) Y.-R. Luo, *Handbook of bond dissociation energies in organic compounds*, CRC press, 2002.
(9) R. H. Crabtree, *Chem. Rev.*, 2010, **110**, 575-575.
(10) L. Que, Jr. and W. B. Tolman, *Nature*, 2008, **455**, 333-340.
(11) O. Hayaishi, *Biochem. Biophys. Res. Commun.*, 2005, **338**, 2-6.
(12) D. E. Torres Pazmino, M. Winkler, A. Glieder and M. W. Fraaije, *J. Biotechnol.*, 2010, **146**, 9-24.
(13) K. Ray, F. F. Pfaff, B. Wang and W. Nam, *J Am Chem Soc*, 2014, **136**, 13942-13958.
(14) S. M. Huber, M. Z. Ertem, F. Aquilante, L. Gagliardi, W. B. Tolman and C. J. Cramer, *Chem. Eur. J.*, 2009, **15**, 4886-4895.
(15) S. Fetzner, *Appl. Microbiol. Biotechnol.*, 2002, **60**, 243-257.
(16) S. J. Thackray, C. G. Mowat and S. K. Chapman, *Biochem. Soc. Trans.*, 2008, **36**, 1120-1123.
(17) F. Forouhar, J. L. R. Anderson, C. G. Mowat, S. M. Vorobiev, A. Hussain, M. Abashidze, C. Bruckmann, S. J. Thackray, J. Seetharaman, T. Tucker, R. Xiao, L.-C. Ma, L. Zhao, T. B. Acton, G. T. Montelione, S. K. Chapman and L. Tong, *Proc. Natl. Acad. Sci. USA*, 2007, **104**, 473-478.
(18) M. Sono, M. P. Roach, E. D. Coulter and J. H. Dawson, *Chem. Rev.*, 1996, **96**, 2841-2888.
(19) E. I. Solomon, T. C. Brunold, M. I. Davis, J. N. Kemsley, S.-K. Lee, N. Lehnert, F. Neese, A. J. Skulan, Y.-S. Yang and J. Zhou, *Chem. Rev.*, 2000, **100**, 235-350.
(20) B. J. Wallar and J. D. Lipscomb, *Chem. Rev.*, 1996, **96**, 2625-2658.
(21) M. Costas, M. P. Mehn, M. P. Jensen and L. Que, *Chem. Rev.*, 2004, **104**, 939-986.
(22) K. D. Koehntop, J. P. Emerson and L. Que, Jr., *J. Biol. Inorg. Chem.*, 2005, **10**, 87-93.
(23) S. Martinez and R. P. Hausinger, *J. Biol. Chem.*, 2015, **290**, 20702-20711.
(24) L. Que and R. Y. N. Ho, *Chem. Rev.*, 1996, **96**, 2607-2624.
(25) M. M. Abu-Omar, A. Loaiza and N. Hontzeas, *Chem. Rev.*, 2005, **105**, 2227-2252.

(26) V. C. Wang, S. Maji, P. P. Chen, H. K. Lee, S. S. Yu and S. I. Chan, *Chem. Rev.*, 2017, **117**, 8574-8621.
(27) I. G. Denisov, T. M. Makris, S. G. Sligar and I. Schlichting, *Chem. Rev.*, 2005, **105**, 2253-2278.
(28) M. Zederbauer, P. G. Furtmüller, S. Brogioni, C. Jakopitsch, G. Smulevich and C. Obinger, *Nat. Prod. Rep.*, 2007, **24**, 571-584.
(29) A. Gumiero, C. L. Metcalfe, A. R. Pearson, E. L. Raven and P. C. Moody, *J. Biol. Chem.*, 2011, **286**, 1260-1268.
(30) H. P. Hersleth, T. Uchida, A. K. Rohr, T. Teschner, V. Schunemann, T. Kitagawa, A. X. Trautwein, C. H. Gorbitz and K. K. Andersson, *J. Biol. Chem.*, 2007, **282**, 23372-23386.
(31) X. X. Li, V. Postils, W. Sun, A. S. Faponle, M. Sola, Y. Wang, W. Nam and S. P. de Visser, *Chemistry*, 2017, **23**, 6406-6418.
(32) S. C. Gallagher, R. Cammack and H. Dalton, *Eur. J. Biochem.*, 1997, **247**, 635-641.
(33) G. M. Whited and D. T. Gibson, *J. Bacteriol.*, 1991, **173**, 3010-3016.
(34) E. Y. Levin, B. Levenberg and S. Kaufman, *J. Biol. Chem.*, 1960, **235**, 2080-2086.
(35) M. O. Ross and A. C. Rosenzweig, *J. Biol. Inorg. Chem.*, 2017, **22**, 307-319.
(36) S. Sirajuddin and A. C. Rosenzweig, *Biochemistry*, 2015, **54**, 2283-2294.
(37) S. Itoh and S. Fukuzumi, *Acc. Chem. Res.*, 2007, **40**, 592-600.
(38) S. GHISLA and V. MASSEY, *Eur. J. Biochem.*, 1989, **181**, 1-17.
(39) A. R. McDonald and L. Que, *Coord. Chem. Rev.*, 2013, **257**, 414-428.
(40) J. E. M. N. Klein and L. Que, in *Encyclopedia of Inorganic and Bioinorganic Chemistry*, 2016, pp. 1-22.
(41) E. I. Solomon, D. E. Heppner, E. M. Johnston, J. W. Ginsbach, J. Cirera, M. Qayyum, M. T. Kieber-Emmons, C. H. Kjaergaard, R. G. Hadt and L. Tian, *Chem. Rev.*, 2014, **114**, 3659-3853.
(42) A. C. Rosenzweig, P. Nordlund, P. M. Takahara, C. A. Frederick and S. J. Lippard, *Chem. Biol.*, 1995, **2**, 409-418.
(43) A. C. Rosenzweig, C. A. Frederick, S. J. Lippard, P. Nordlund and auml, *Nature*, 1993, **366**, 537-543.
(44) M. O. Ross, F. MacMillan, J. Wang, A. Nisthal, T. J. Lawton, B. D. Olafson, S. L. Mayo, A. C. Rosenzweig and B. M. Hoffman, *Science*, 2019, **364**, 566-570.
(45) L. Cao, O. Caldararu, A. C. Rosenzweig and U. Ryde, *Angew. Chem. Int. Ed.*, 2018, **57**, 162-166.
(46) J. Lund, M. P. Woodland and H. Dalton, *Eur. J. Biochem.*, 1985, **147**, 297-305.
(47) Y. Liu, J. C. Nesheim, S.-K. Lee and J. D. Lipscomb, *J. Biol. Chem.*, 1995, **270**, 24662-24665.
(48) M. P. Hendrich, E. Munck, B. G. Fox and J. D. Lipscomb, *J. Am. Chem. Soc.*, 1990, **112**, 5861-5865.
(49) R. Banerjee, K. K. Meier, E. Munck and J. D. Lipscomb, *Biochemistry*, 2013, **52**, 4331-4342.
(50) C. E. Tinberg and S. J. Lippard, *Biochemistry*, 2009, **48**, 12145-12158.
(51) S.-K. Lee and J. D. Lipscomb, *Biochemistry*, 1999, **38**, 4423-4432.
(52) C. E. Tinberg and S. J. Lippard, *Acc. Chem. Res.*, 2011, **44**, 280-288.
(53) Y. Jiang, P. C. Wilkins and H. Dalton, *Biochim. Biophys. Acta, Protein Struct. Mol. Enzymol.*, 1993, **1163**, 105-112.
(54) S.-K. Lee, J. C. Nesheim and J. D. Lipscomb, *J. Biol. Chem.*, 1993, **268**, 21569-21577.

(55) L. Shu, J. C. Nesheim, K. Kauffmann, E. Münck, J. D. Lipscomb and L. Que, *Science*, 1997, **275**, 515-518.
(56) R. Banerjee, Y. Proshlyakov, J. D. Lipscomb and D. A. Proshlyakov, *Nature*, 2015, **518**, 431-434.
(57) S. P. Huang, Y. Shiota and K. Yoshizawa, *Dalton Trans.*, 2013, **42**, 1011-1023.
(58) L. Que Jr and W. B. Tolman, *Angew. Chem. Int. Ed.*, 2002, **41**, 1114-1137.
(59) G. E. Cutsail, 3rd, R. Banerjee, A. Zhou, L. Que, Jr., J. D. Lipscomb and S. DeBeer, *J. Am. Chem. Soc.*, 2018, **140**, 16807-16820.
(60) R. G. Castillo, R. Banerjee, C. J. Allpress, G. T. Rohde, E. Bill, L. Que, J. D. Lipscomb and S. DeBeer, *J. Am. Chem. Soc.*, 2017, **139**, 18024-18033.
(61) S. Banerjee, A. Draksharapu, P. M. Crossland, R. Fan, Y. Guo, M. Swart and L. Que, Jr., *J. Am. Chem. Soc.*, 2020, **142**, 4285-4297.
(62) M.-H. Baik, M. Newcomb, R. A. Friesner and S. J. Lippard, *Chem. Rev.*, 2003, **103**, 2385-2420.
(63) V. Guallar, B. F. Gherman, W. H. Miller, S. J. Lippard and R. A. Friesner, *J. Am. Chem. Soc.*, 2002, **124**, 3377-3384.
(64) B. F. Gherman, B. D. Dunietz, D. A. Whittington, S. J. Lippard and R. A. Friesner, *J. Am. Chem. Soc.*, 2001, **123**, 3836-3837.
(65) D. A. Kopp and S. J. Lippard, *Curr. Opin. Chem. Biol.*, 2002, **6**, 568-576.
(66) J. Green and H. Dalton, *J. Biol. Chem.*, 1989, **264**, 17698-17703.
(67) K. J. Burrows, A. Cornish, D. Scott and I. J. Higgins, *Microbiology*, 1984, **130**, 3327-3333.
(68) G. Xue, R. De Hont, E. Munck and L. Que, Jr., *Nat. Chem.*, 2010, **2**, 400-405.
(69) R. F. De Hont, G. Xue, M. P. Hendrich, L. Que, Jr., E. L. Bominaar and E. Munck, *Inorg. Chem.*, 2010, **49**, 8310-8322.
(70) H. Mason, W. Fowlks and E. Peterson, *J. Am. Chem. Soc.*, 1955, **77**, 2914-2915.
(71) Y. Matoba, T. Kumagai, A. Yamamoto, H. Yoshitsu and M. Sugiyama, *J. Biol. Chem.*, 2006, **281**, 8981-8990.
(72) W. T. Ismaya, H. J. Rozeboom, A. Weijn, J. J. Mes, F. Fusetti, H. J. Wichers and B. W. Dijkstra, *Biochemistry*, 2011, **50**, 5477-5486.
(73) Y. Li, Y. Wang, H. Jiang and J. Deng, *Proc. Natl. Acad. Sci.*, 2009, **106**, 17002-17006.
(74) R. Morrison, K. Mason and S. Frost-Mason, *Pigment Cell Res.*, 1994, **7**, 388-393.
(75) K. D. Karlin, J. C. Hayes, Y. Gultneh, R. W. Cruse, J. W. McKown, J. P. Hutchinson and J. Zubieta, *J. Am. Chem. Soc.*, 1984, **106**, 2121-2128.
(76) P. W. Anderson, *Phys. Rev.*, 1950, **79**, 350-356.
(77) C. Eicken, F. Zippel, K. Büldt-Karentzopoulos and B. Krebs, *FEBS Lett.*, 1998, **436**, 293-299.
(78) N. Fujieda, K. Umakoshi, Y. Ochi, Y. Nishikawa, S. Yanagisawa, M. Kubo, G. Kurisu and S. Itoh, *Angew. Chem. Int. Ed.*, 2020.
(79) D. A. Quist, D. E. Diaz, J. J. Liu and K. D. Karlin, *J. Biol. Inorg. Chem.*, 2017, **22**, 253-288.
(80) K. D. Karlin, M. S. Nasir, B. I. Cohen, R. W. Cruse, S. Kaderli and A. D. Zuberbuehler, *J. Am. Chem. Soc.*, 1994, **116**, 1324-1336.
(81) J. A. Halfen, S. Mahapatra, E. C. Wilkinson, S. Kaderli, V. G. Young, L. Que, A. D. Zuberbuhler and W. B. Tolman, *Science*, 1996, **271**, 1397-1400.
(82) S. Mahapatra, J. A. Halfen, E. C. Wilkinson, G. Pan, X. Wang, V. G. Young, C. J. Cramer, L. Que and W. B. Tolman, *J. Am. Chem. Soc.*, 1996, **118**, 11555-11574.
(83) L. M. Mirica, M. Vance, D. J. Rudd, B. Hedman, K. O. Hodgson, E. I. Solomon and T. D. P. Stack, *Science*, 2005, **308**, 1890-1892.

(84) C. J. Cramer, M. Włoch, P. Piecuch, C. Puzzarini and L. Gagliardi, *J. Phys. Chem. A*, 2006, **110**, 1991-2004.
(85) J. J. Warren, T. A. Tronic and J. M. Mayer, *Chem. Rev.*, 2010, **110**, 6961-7001.
(86) J. M. Mayer, *Acc. Chem. Res.*, 1998, **31**, 441-450.
(87) J. P. Roth, J. C. Yoder, T.-J. Won and J. M. Mayer, *Science*, 2001, **294**, 2524-2526.
(88) J. M. Mayer, *Acc. Chem. Res.*, 2011, **44**, 36-46.
(89) J. M. Mayer, *J. Phys. Chem. Lett*, 2011, **2**, 1481-1489.
(90) J. W. Darcy, B. Koronkiewicz, G. A. Parada and J. M. Mayer, *Acc. Chem. Res.*, 2018, **51**, 2391-2399.
(91) J. J. Warren and J. M. Mayer, *Biochemistry*, 2015, **54**, 1863-1878.
(92) D. R. Weinberg, C. J. Gagliardi, J. F. Hull, C. F. Murphy, C. A. Kent, B. C. Westlake, A. Paul, D. H. Ess, D. G. McCafferty and T. J. Meyer, *Chem. Rev.*, 2012, **112**, 4016-4093.
(93) A. Sirjoosingh and S. Hammes-Schiffer, *J. Phys. Chem. A*, 2011, **115**, 2367-2377.
(94) S. P. de Visser and S. Shaik, *J. Am. Chem. Soc.*, 2003, **125**, 7413-7424.
(95) A. K. Boal, J. A. Cotruvo, J. Stubbe and A. C. Rosenzweig, *Science*, 2010, **329**, 1526-1530.
(96) Y. N. Belokon', S. Caveda-Cepas, B. Green, N. S. Ikonnikov, V. N. Khrustalev, V. S. Larichev, M. A. Moscalenko, M. North, C. Orizu and V. I. Tararov, *J. Am. Chem. Soc.*, 1999, **121**, 3968-3973.
(97) Z. Duan, M. Schmidt, V. G. Young Jr, X. Xie, R. E. McCarley and J. G. Verkade, *J. Am. Chem. Soc.*, 1996, **118**, 5302-5303.
(98) H. Nishino and J. Kochi, *Inorg. Chim. Acta*, 1990, **174**, 93-102.
(99) R. Manchanda, G. W. Brudvig and R. H. Crabtree, *Coord. Chem. Rev.*, 1995, **144**, 1-38.
(100) J. P. McEvoy and G. W. Brudvig, *Chem. Rev.*, 2006, **106**, 4455-4483.
(101) A. W. Pierpont and T. R. Cundari, *Inorg. Chem.*, 2010, **49**, 2038-2046.
(102) N. Kitajima, U. P. Singh, H. Amagai, M. Osawa and Y. Morooka, *J. Am. Chem. Soc.*, 1991, **113**, 7757-7758.
(103) U. Bossek, T. Weyhermueller, K. Wieghardt, B. Nuber and J. Weiss, *J. Am. Chem. Soc.*, 1990, **112**, 6387-6388.
(104) N. Arulsamy, J. Glerup, A. Hazell, D. J. Hodgson, C. J. McKenzie and H. Toftlund, *Inorg. Chem.*, 1994, **33**, 3023-3025.
(105) J. Limburg, J. S. Vrettos, L. M. Liable-Sands, A. L. Rheingold, R. H. Crabtree and G. W. Brudvig, *Science*, 1999, **283**, 1524-1527.
(106) C. W. Cady, K. E. Shinopoulos, R. H. Crabtree and G. W. Brudvig, *Dalton Trans.*, 2010, **39**, 3985-3989.
(107) H. Yamazaki, S. Igarashi, T. Nagata and M. Yagi, *Inorg. Chem.*, 2012, **51**, 1530-1539.
(108) H. H. Thorp, J. E. Sarneski, G. W. Brudvig and R. H. Crabtree, *J. Am. Chem. Soc.*, 1989, **111**, 9249-9250.
(109) A. F. Jensen, Z. Su, N. K. Hansen and F. K. Larsen, *Inorg. Chem.*, 1995, **34**, 4244-4252.
(110) C. Baffert, S. Dumas, J. Chauvin, J.-C. Leprêtre, M.-N. Collomb and A. Deronzier, *Phys. Chem. Chem. Phys.*, 2005, **7**, 202-210.
(111) D. F. Leto, S. Chattopadhyay, V. W. Day and T. A. Jackson, *Dalton Trans.*, 2013, **42**, 13014-13025.
(112) E. J. Larson and V. L. Pecoraro, *J. Am. Chem. Soc.*, 1991, **113**, 3810-3818.
(113) J. W. Gohdes and W. H. Armstrong, *Inorg. Chem.*, 1992, **31**, 368-373.

(114) V. Krewald, B. Lassalle-Kaiser, T. T. Boron, 3rd, C. J. Pollock, J. Kern, M. A. Beckwith, V. K. Yachandra, V. L. Pecoraro, J. Yano, F. Neese and S. DeBeer, *Inorg. Chem.*, 2013, **52**, 12904-12914.
(115) M. J. Baldwin, T. L. Stemmler, P. J. Riggs-Gelasco, M. L. Kirk, J. E. Penner-Hahn and V. L. Pecoraro, *J. Am. Chem. Soc.*, 1994, **116**, 11349-11356.
(116) A. M. Magherusan, A. Zhou, E. R. Farquhar, M. García-Melchor, B. Twamley, L. Que Jr. and A. R. McDonald, *Angew. Chem. Int. Ed.*, 2018, **57**, 918-922.
(117) A. M. Magherusan, S. Kal, D. N. Nelis, L. M. Doyle, E. R. Farquhar, L. Que Jr. and A. R. McDonald, *Angew. Chem. Int. Ed.*, 2019, **58**, 5718-5722.
(118) M. K. Coggins, X. Sun, Y. Kwak, E. I. Solomon, E. Rybak-Akimova and J. A. Kovacs, *J. Am. Chem. Soc.*, 2013, **135**, 5631-5640.
(119) A. Gelasco, M. L. Kirk, J. W. Kampf and V. L. Pecoraro, *Inorg. Chem.*, 1997, **36**, 1829-1837.
(120) A. Gelasco and V. L. Pecoraro, *J. Am. Chem. Soc.*, 1993, **115**, 7928-7929.
(121) K. Wieghardt, U. Bossek, L. Zsolnai, G. Huttner, G. Blondin, J.-J. Girerd and F. Babonneau, *J. Chem. Soc., Chem. Commun.*, 1987, 651-653.
(122) K.-O. Schäfer, R. Bittl, W. Zweygart, F. Lendzian, G. Haselhorst, T. Weyhermüller, K. Wieghardt and W. Lubitz, *J. Am. Chem. Soc.*, 1998, **120**, 13104-13120.
(123) S. V. Kryatov, S. Taktak, I. V. Korendovych, E. V. Rybak-Akimova, J. Kaizer, S. Torelli, X. Shan, S. Mandal, V. L. MacMurdo, A. Mairata i Payeras and L. Que, *Inorg. Chem.*, 2005, **44**, 85-99.
(124) H.-F. Hsu, Y. Dong, L. Shu, V. G. Young and L. Que, *J. Am. Chem. Soc.*, 1999, **121**, 5230-5237.
(125) Y. Dong, H. Fujii, M. P. Hendrich, R. A. Leising, G. Pan, C. R. Randall, E. C. Wilkinson, Y. Zang and L. Que, *J. Am. Chem. Soc.*, 1995, **117**, 2778-2792.
(126) G. Xue, D. Wang, R. De Hont, A. T. Fiedler, X. Shan, E. Münck and L. Que, *Proc. Natl. Acad. Sci.*, 2007, **104**, 20713-20718.
(127) H. Furutachi, Y. Ohyama, Y. Tsuchiya, K. Hashimoto, S. Fujinami, A. Uehara, M. Suzuki and Y. Maeda, *Chem. Lett.*, 2000, **29**, 1132-1133.
(128) D. Lee and S. J. Lippard, *J. Am. Chem. Soc.*, 2001, **123**, 4611-4612.
(129) M. K. Coggins, S. Toledo and J. A. Kovacs, *Inorg. Chem.*, 2013, **52**, 13325-13331.
(130) M. A. Cranswick, K. K. Meier, X. Shan, A. Stubna, J. Kaizer, M. P. Mehn, E. Munck and L. Que, Jr., *Inorg. Chem.*, 2012, **51**, 10417-10426.
(131) A. T. Fiedler, X. Shan, M. P. Mehn, J. Kaizer, S. Torelli, J. R. Frisch, M. Kodera and J. L. Que, *J. Phys. Chem. A*, 2008, **112**, 13037-13044.
(132) Y. Dong, Y. Zang, L. Shu, E. C. Wilkinson, L. Que, K. Kauffmann and E. Münck, *J. Am. Chem. Soc.*, 1997, **119**, 12683-12684.
(133) M. Kodera, Y. Kawahara, Y. Hitomi, T. Nomura, T. Ogura and Y. Kobayashi, *J. Am. Chem. Soc.*, 2012, **134**, 13236-13239.
(134) A. Ghosh, F. Tiago de Oliveira, T. Yano, T. Nishioka, E. S. Beach, I. Kinoshita, E. Münck, A. D. Ryabov, C. P. Horwitz and T. J. Collins, *J. Am. Chem. Soc.*, 2005, **127**, 2505-2513.
(135) H. Zheng, S. J. Yoo, E. Münck and L. Que, *J. Am. Chem. Soc.*, 2000, **122**, 3789-3790.
(136) G. Xue, A. T. Fiedler, M. Martinho, E. Münck and L. Que, *Proc. Natl. Acad. Sci.*, 2008, **105**, 20615-20620.
(137) S. Hikichi, H. Komatsuzaki, N. Kitajima, M. Akita, M. Mukai, T. Kitagawa and Y. Moro-oka, *Inorg. Chem.*, 1997, **36**, 266-267.

(138) S. Hikichi, M. Yoshizawa, Y. Sasakura, M. Akita and Y. Moro-oka, *J. Am. Chem. Soc.*, 1998, **120**, 10567-10568.
(139) J. P. Collman, P. Denisevich, Y. Konai, M. Marrocco, C. Koval and F. C. Anson, *J. Am. Chem. Soc.*, 1980, **102**, 6027-6036.
(140) S. Fukuzumi, K. Okamoto, C. P. Gros and R. Guilard, *J. Am. Chem. Soc.*, 2004, **126**, 10441-10449.
(141) S. Fukuzumi, *Bull. Chem. Soc. Jpn.*, 2006, **79**, 177-195.
(142) S. Hikichi, M. Yoshizawa, Y. Sasakura, H. Komatsuzaki, Y. Moro-oka and M. Akita, *Chem. Eur. J.*, 2001, **7**, 5011-5028.
(143) O. M. Reinaud, G. P. A. Yap, A. L. Rheingold and K. H. Theopold, *Angew. Chem. Int. Ed. Engl.*, 1995, **34**, 2051-2052.
(144) S. Itoh, H. Bandoh, S. Nagatomo, T. Kitagawa and S. Fukuzumi, *J. Am. Chem. Soc.*, 1999, **121**, 8945-8946.
(145) S. Itoh, H. Bandoh, M. Nakagawa, S. Nagatomo, T. Kitagawa, K. D. Karlin and S. Fukuzumi, *J. Am. Chem. Soc.*, 2001, **123**, 11168-11178.
(146) Y. Morimoto, Y. Takagi, T. Saito, T. Ohta, T. Ogura, N. Tohnai, M. Nakano and S. Itoh, *Angew. Chem. Int. Ed.*, 2018, **57**, 7640-7643.
(147) K. Shiren, S. Ogo, S. Fujinami, H. Hayashi, M. Suzuki, A. Uehara, Y. Watanabe and Y. Moro-oka, *J. Am. Chem. Soc.*, 2000, **122**, 254-262.
(148) N. Kitajima, S. Hikichi, M. Tanaka and Y. Morooka, *J. Am. Chem. Soc.*, 1993, **115**, 5496-5508.
(149) M. Ito and Y.-s. Takita, *Chem. Lett.*, 1996, **25**, 929-930.
(150) J. P. Wikstrom, A. S. Filatov, E. A. Mikhalyova, M. Shatruk, B. M. Foxman and E. V. Rybak-Akimova, *Dalton Trans.*, 2010, **39**, 2504-2514.
(151) R. Schenker, M. T. Kieber-Emmons, C. G. Riordan and T. C. Brunold, *Inorg. Chem.*, 2005, **44**, 1752-1762.
(152) B. S. Mandimutsira, J. L. Yamarik, T. C. Brunold, W. Gu, S. P. Cramer and C. G. Riordan, *J. Am. Chem. Soc.*, 2001, **123**, 9194-9195.
(153) R. Schenker, B. S. Mandimutsira, C. G. Riordan and T. C. Brunold, *J. Am. Chem. Soc.*, 2002, **124**, 13842-13855.
(154) S. K. Padamati, D. Angelone, A. Draksharapu, G. Primi, D. J. Martin, M. Tromp, M. Swart and W. R. Browne, *J. Am. Chem. Soc.*, 2017, **139**, 8718-8724.
(155) N. Kitajima, K. Fujisawa, C. Fujimoto, Y. Morooka, S. Hashimoto, T. Kitagawa, K. Toriumi, K. Tatsumi and A. Nakamura, *J. Am. Chem. Soc.*, 1992, **114**, 1277-1291.
(156) N. Kitajima, K. Fujisawa, Y. Morooka and K. Toriumi, *J. Am. Chem. Soc.*, 1989, **111**, 8975-8976.
(157) H. R. Lucas, L. Li, A. A. N. Sarjeant, M. A. Vance, E. I. Solomon and K. D. Karlin, *J. Am. Chem. Soc.*, 2009, **131**, 3230-3245.
(158) R. Haase, T. Beschnitt, U. Flörke and S. Herres-Pawlis, *Inorg. Chim. Acta*, 2011, **374**, 546-557.
(159) M. Kodera, T. Kawata, K. Kano, Y. Tachi, S. Itoh and S. Kojo, *Bull. Chem. Soc. Jpn.*, 2003, **76**, 1957-1964.
(160) J. A. Isaac, F. Gennarini, I. Lopez, A. Thibon-Pourret, R. David, G. Gellon, B. Gennaro, C. Philouze, F. Meyer, S. Demeshko, Y. Le Mest, M. Reglier, H. Jamet, N. Le Poul and C. Belle, *Inorg. Chem.*, 2016, **55**, 8263-8266.
(161) J. A. Isaac, A. Thibon-Pourret, A. Durand, C. Philouze, N. Le Poul and C. Belle, *Chem. Commun.*, 2019, **55**, 12711-12714.

(162) M. R. Halvagar, P. V. Solntsev, H. Lim, B. Hedman, K. O. Hodgson, E. I. Solomon, C. J. Cramer and W. B. Tolman, *J. Am. Chem. Soc.*, 2014, **136**, 7269-7272.
(163) R. R. Jacobson, Z. Tyeklar, A. Farooq, K. D. Karlin, S. Liu and J. Zubieta, *J. Am. Chem. Soc.*, 1988, **110**, 3690-3692.
(164) Z. Tyeklar, R. R. Jacobson, N. Wei, N. N. Murthy, J. Zubieta and K. D. Karlin, *J. Am. Chem. Soc.*, 1993, **115**, 2677-2689.
(165) K. E. Dalle, T. Gruene, S. Dechert, S. Demeshko and F. Meyer, *J. Am. Chem. Soc.*, 2014, **136**, 7428-7434.
(166) M. T. Kieber-Emmons, J. W. Ginsbach, P. K. Wick, H. R. Lucas, M. E. Helton, B. Lucchese, M. Suzuki, A. D. Zuberbuhler, K. D. Karlin and E. I. Solomon, *Angew. Chem. Int. Ed.*, 2014, **53**, 4935-4939.
(167) M. Kodera, K. Katayama, Y. Tachi, K. Kano, S. Hirota, S. Fujinami and M. Suzuki, *J. Am. Chem. Soc.*, 1999, **121**, 11006-11007.
(168) J. A. Halfen, S. Mahapatra, E. C. Wilkinson, S. Kaderli, V. G. Young Jr, L. Que Jr, A. D. Zuberbühler and W. B. Tolman, *Science*, 1996, 1397-1400.
(169) L. M. Mirica, M. Vance, D. J. Rudd, B. Hedman, K. O. Hodgson, E. I. Solomon and T. D. P. Stack, *J. Am. Chem. Soc.*, 2002, **124**, 9332-9333.
(170) L. Q. Hatcher, M. A. Vance, A. A. Narducci Sarjeant, E. I. Solomon and K. D. Karlin, *Inorg. Chem.*, 2006, **45**, 3004-3013.
(171) T. Matsumoto, H. Furutachi, M. Kobino, M. Tomii, S. Nagatomo, T. Tosha, T. Osako, S. Fujinami, S. Itoh, T. Kitagawa and M. Suzuki, *J. Am. Chem. Soc.*, 2006, **128**, 3874-3875.
(172) T. Osako, K. Ohkubo, M. Taki, Y. Tachi, S. Fukuzumi and S. Itoh, *J. Am. Chem. Soc.*, 2003, **125**, 11027-11033.
(173) C. Citek, C. T. Lyons, E. C. Wasinger and T. D. Stack, *Nat. Chem.*, 2012, **4**, 317-322.
(174) L. Tahsini, H. Kotani, Y. M. Lee, J. Cho, W. Nam, K. D. Karlin and S. Fukuzumi, *Chem. Eur. J.*, 2012, **18**, 1084-1093.
(175) B. F. Straub, F. Rominger and P. Hofmann, *Chem. Commun.*, 2000, 1611-1612.
(176) H. Hayashi, S. Fujinami, S. Nagatomo, S. Ogo, M. Suzuki, A. Uehara, Y. Watanabe and T. Kitagawa, *J. Am. Chem. Soc.*, 2000, **122**, 2124-2125.
(177) S. Itoh, M. Taki, H. Nakao, P. L. Holland, W. B. Tolman, J. Que, Lawrence and S. Fukuzumi, *Angew. Chem. Int. Ed.*, 2000, **39**, 398-400.
(178) M. Taki, S. Itoh and S. Fukuzumi, *J. Am. Chem. Soc.*, 2001, **123**, 6203-6204.
(179) W. Keown, T. A. G. Large, L. Chiang, E. C. Wasinger and T. D. P. Stack, *Chem. Commun.*, 2019, **55**, 7390-7393.
(180) G. C. Dismukes, *Chem. Rev.*, 1996, **96**, 2909-2926.
(181) M. M. Najafpour, I. Zaharieva, Z. Zand, S. Maedeh Hosseini, M. Kouzmanova, M. Hołyńska, I. Tranca, A. W. Larkum, J.-R. Shen and S. I. Allakhverdiev, *Coord. Chem. Rev.*, 2020, **409**.
(182) J. R. Shen, *Annu. Rev. Plant Biol.*, 2015, **66**, 23-48.
(183) M. Suga, F. Akita, K. Hirata, G. Ueno, H. Murakami, Y. Nakajima, T. Shimizu, K. Yamashita, M. Yamamoto, H. Ago and J.-R. Shen, *Nature*, 2015, **517**, 99-103.
(184) B. Kok, B. Forbush and M. McGloin, *Photochem. Photobiol.*, 1970, **11**, 457-475.
(185) N. Cox, M. Retegan, F. Neese, D. A. Pantazis, A. Boussac and W. Lubitz, *Science*, 2014, **345**, 804-808.
(186) J. E. Penner-Hahn, R. M. Fronko, V. L. Pecoraro, C. F. Yocum, S. D. Betts and N. R. Bowlby, *J. Am. Chem. Soc.*, 1990, **112**, 2549-2557.

(187) A. E. McDermott, V. K. Yachandra, R. D. Guiles, J. L. Cole, S. L. Dexheimer, R. D. Britt, K. Sauer and M. P. Klein, *Biochemistry*, 1988, **27**, 4021-4031.
(188) A. Willing, H. Follmann and G. Auling, *Eur. J. Biochem.*, 1988, **175**, 167-173.
(189) J. A. Cotruvo and J. Stubbe, *Annu. Rev. Biochem*, 2011, **80**, 733-767.
(190) P. J. Pessiki and G. C. Dismukes, *J. Am. Chem. Soc.*, 1994, **116**, 898-903.
(191) P. Pessiki, S. Khangulov, D. Ho and G. Dismukes, *J. Am. Chem. Soc.*, 1994, **116**, 891-897.
(192) P. J. Riggs-Gelasco, L. Shu, S. Chen, D. Burdi, B. H. Huynh, L. Que and J. Stubbe, *J. Am. Chem. Soc.*, 1998, **120**, 849-860.
(193) B. E. Sturgeon, D. Burdi, S. Chen, B.-H. Huynh, D. E. Edmondson, J. Stubbe and B. M. Hoffman, *J. Am. Chem. Soc.*, 1996, **118**, 7551-7557.
(194) H. Zheng, Y. Zang, Y. Dong, V. G. Young and L. Que, *J. Am. Chem. Soc.*, 1999, **121**, 2226-2235.
(195) Y. Zang, Y. Dong, L. Que, K. Kauffmann and E. Muenck, *J. Am. Chem. Soc.*, 1995, **117**, 1169-1170.
(196) C.-C. Ou, R. A. Lalancette, J. A. Potenza and H. J. Schugar, *J. Am. Chem. Soc.*, 1978, **100**, 2053-2057.
(197) F. T. de Oliveira, A. Chanda, D. Banerjee, X. Shan, S. Mondal, L. Que, E. L. Bominaar, E. Münck and T. J. Collins, *Science*, 2007, **315**, 835-838.
(198) C. Follmer, *Phytochemistry*, 2008, **69**, 18-28.
(199) J. R. Winkler and H. B. Gray, *Struct. Bond.*, 2011, **142**, 17-28.
(200) S. Lindskog, *Pharmacol. Therapeut.*, 1997, **74**, 1-20.
(201) C. J. Cramer, B. A. Smith and W. B. Tolman, *J. Am. Chem. Soc.*, 1996, **118**, 11283-11287.
(202) K. A. Magnus, H. Ton-That and J. E. Carpenter, *Chem. Rev.*, 1994, **94**, 727-735.
(203) L. M. Mirica, X. Ottenwaelder and T. D. P. Stack, *Chem. Rev.*, 2004, **104**, 1013-1046.
(204) W. Keown, J. B. Gary and T. D. Stack, *J. Biol. Inorg. Chem.*, 2017, **22**, 289-305.
(205) D.-H. Lee, N. Wei, N. N. Murthy, Z. Tyeklar, K. D. Karlin, S. Kaderli, B. Jung and A. D. Zuberbuehler, *J. Am. Chem. Soc.*, 1995, **117**, 12498-12513.
(206) P. P. Paul, Z. Tyeklar, R. R. Jacobson and K. D. Karlin, *J. Am. Chem. Soc.*, 1991, **113**, 5322-5332.
(207) M. E. Cuff, K. I. Miller, K. E. van Holde and W. A. Hendrickson, *J. Mol. Biol.*, 1998, **278**, 855-870.
(208) J. Cahoy, P. L. Holland and W. B. Tolman, *Inorg. Chem.*, 1999, **38**, 2161-2168.
(209) V. Mahadevan, M. J. Henson, E. I. Solomon and T. D. P. Stack, *J. Am. Chem. Soc.*, 2000, **122**, 10249-10250.
(210) X. Ottenwaelder, D. J. Rudd, M. C. Corbett, K. O. Hodgson, B. Hedman and T. D. P. Stack, *J. Am. Chem. Soc.*, 2006, **128**, 9268-9269.
(211) T. J. Collins, *Acc. Chem. Res.*, 2002, **35**, 782-790.

Chapter 2

Synthesis and characterisation of dimethyl malonamidate ligands ($DMMA^{R2}$)

The XRD data collection and structure solutions and refinements were done by Dr Brendan Twamley (Trinity College Dublin).

2.1 Introduction

As mentioned in section 1.6, in order to stabilise high valent μ-hydroxo species it will be necessary to develop a suitable ligand system with specific characteristics to stabilise high valent species. Therefore, the rational design and synthesis of the ligand has been a crucial part of the present study. The main required features for the desired system are the presence of functional groups capable of structurally and electronically stabilising the high valent oxidation states and an overall oxidative robustness, to guarantee the redox innocence of the ligand and avoid any intramolecular oxidation pathways. Ease of synthesis in bulk constitutes an additional desired feature, albeit not fundamental.

Carboxamides have been extensively studied and their capability to support metals in high oxidation states is widely documented.[1] Indeed, their ability to act as σ and/or π-electron donor alongside their resistance to oxidation and hydrolytic stability, makes them ligand systems of choice for coordinating metals in many biomimetic complexes. Inspired by the widely studied biuret[1] and pyridindicarboxamide[2-4] ligand systems, which have been proven to form high valent metal complexes with first-row transition metals, we designed a new bidentate malonamidate ligand DMMA^{R2} (Figure 2.1).

The proposed DMMA^{R2} exhibits C_{2v} symmetry (Figure 2.1) with tuneable steric hindrance (*i.e.* –R groups on the aromatic rings), designed to coordinate to an unsaturated metal ion in a 1:1 ratio through a bidentate ligand field, ideally forcing low coordination number geometries, such as trigonal planar (i.e. 3-coordinated) and square planar (i.e. 4-coordinated).

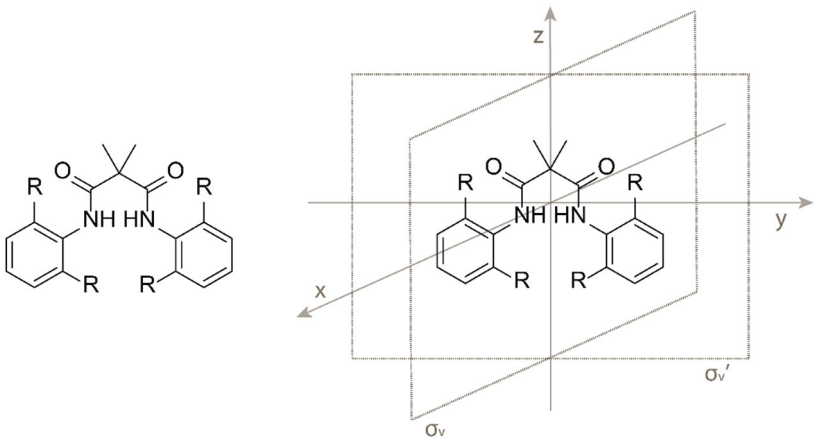

Figure 2.1 – *Left.* Proposed ligand system DMMA^{R} (R = –H, CH_3, $–CH(CH_3)_2$). *Right.* C_{2v} symmetry of DMMA^{R}

Due to the dianionic nature of the two deprotonated amidate functionalities, DMMA^{R} is expected to be a better σ-donor, in comparison with the well-known monoanionic β-diketiminate ligands,[5] enhancing the stabilisation of high valent oxidation state complexes. Moreover, DMMA^{R} has been designed to be oxidatively robust and innocent, through methylation of all the functionalities susceptible of side reactions, such as the α–carbon.

The new DMMA^{R2} ligand platform fulfilled all the required features, representing an ideal candidate for supporting and stabilising high valent metal complexes. In the present chapter we will report and analyse the synthesis and characterisation of this ligand system, focusing in particular on the species with R = –H, CH_3, $–CH(CH_3)_2$.

N.B. In the interest of clarity and consistency, in order to differentiate the chemical species observed in the experimental from the complex analysed in Table 1.1,which are labelled in ascending bold red number, all the new chemical species reported from now on will be reported as ascending bold black numbers.

2.2 Synthesis of DMMA^{R2}

The synthetic pathway of DMMA^{R2} is divided in four separate steps. The starting chemical of choice was the diethylmalonate (**1**), since it was easily accessible, allowing us to work in bulk scale. In the first step, we chose to remove the acidic α-protons, since they could interfere in the following steps of the synthesis and during the complexation. Therefore, we performed the complete methylation of the α–carbon of the molecule, by reaction with iodomethane in presence of sodium ethoxide,[6] giving the dimethyl diethylmalonate (**2**) as product in 65% yield. Subsequently, the dimethyl diethylmalonate was hydrolysed under basic conditions, giving the dimethyl-malonic acid (**3**) in 59% yield. The acid was activated by conversion to the corresponding acyl chloride (**4**, 81%) upon solvolysis with thionyl chloride under reflux. The final ligands (Scheme 2.1) were obtained by reaction of **4** with 2,6-R_2-aniline (R = –H, $–CH_3$, $–CH(CH_3)_2$) in presence of triethylamine. The

three ligands were obtained with the following yields (Scheme 2.1): R = –H (**5**) 45% yield, (overall 14 %); R = –CH_3 (**6**) 32% yield, (overall 10 %); R = –$CH(CH_3)_2$ (**7**) 42% yield, (overall 13 %). Despite the overall yields for each ligand being quite low, the easy access and the safeness of the chemicals required, alongside the ease of the synthetic steps, allowed us to easily scale-up these reactions.

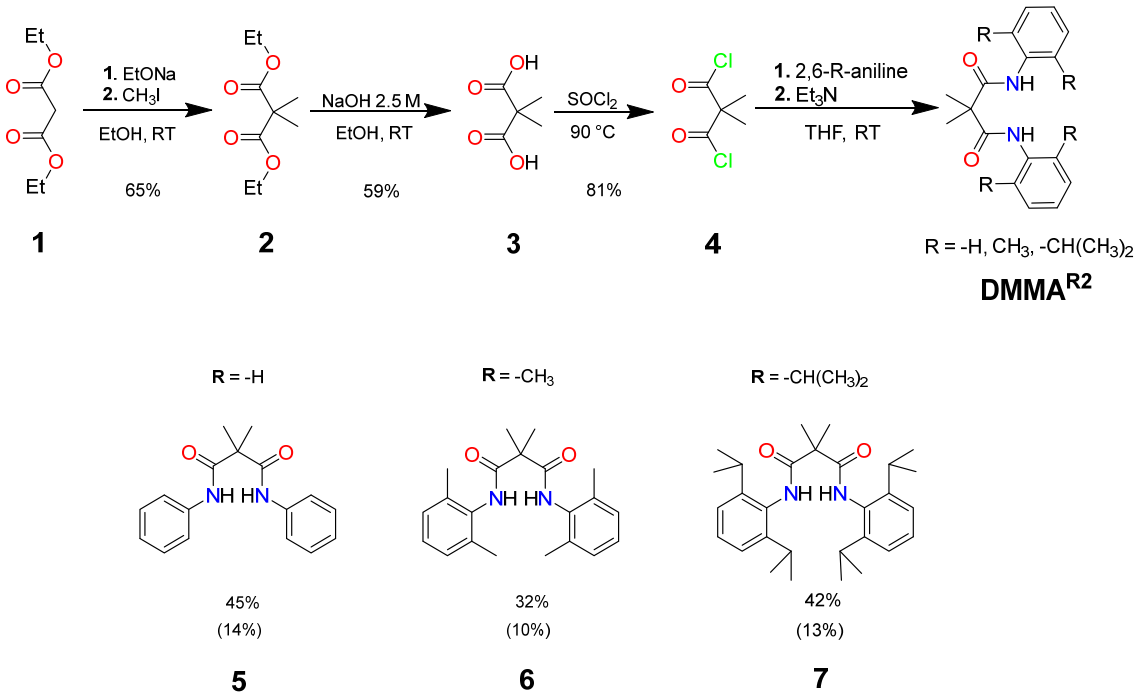

Scheme 2.1 – Synthesis of the malonamidate ligand DMMA^{R2} (R = –H, –CH_3, –$CH(CH_3)_2$). Overall yields reported in brackets.

2.3 Characterization of DMMA^{R2}

The ligands were characterised by ^{1}H-NMR, ^{13}C-NMR (full spectra in Figures A-2.1–A-2.12), FT-IR and ESI-Mass Spectroscopy. Comparison of the ^{1}H-NMR spectra for **5**, **6** and **7** is given in Figure 2.2. Analysis of the aromatic region (~7-8 ppm, Figure 2.2) showed that the different substituents affected the resonance of the phenyl rings hydrogens. In the species **6** and **7**, the shielding effect of the substituents (i.e. –CH_3 for **6**, –$CH(CH_3)_2$ for **7**) resulted in a shift of the aromatic hydrogens in the *meta* position

(multiplet, 7.09 ppm for **6**; doublet, 7.30 ppm for **7**) compared to the unsubstituted species **5** (triplet, 7.34 ppm). Particularly in the case of **6**, the methyl groups cause a high field shift at the *meta* hydrogen atoms at the aryl substituents, overlapping with the peaks of the *para*-hydrogens and resulting in the presence of a multiplet. The presence of substituents affected also the aliphatic region (~1-3 ppm, with an evident shift of the singlet signals correlated to the two methyl groups attached to the α-carbon (1.69 ppm for **5**; 1.78 ppm for **6**; 1.80 ppm for **7**).

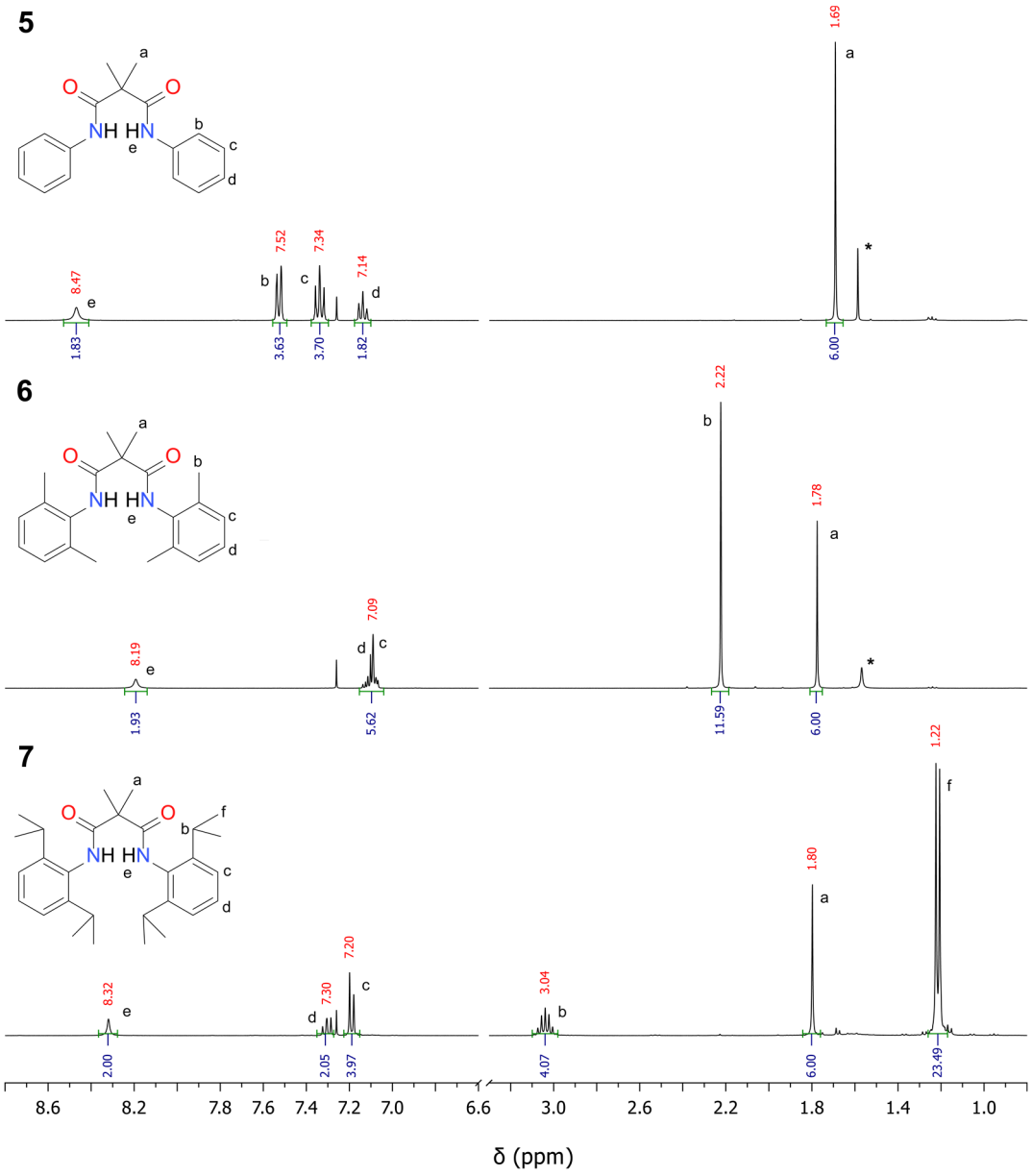

Figure 2.2 – Stacked ^{1}H-NMR spectra of the DMMA^{R2} family of ligands in $CDCl_3$ (*adventitious H_2O present in the deuterated solvent).

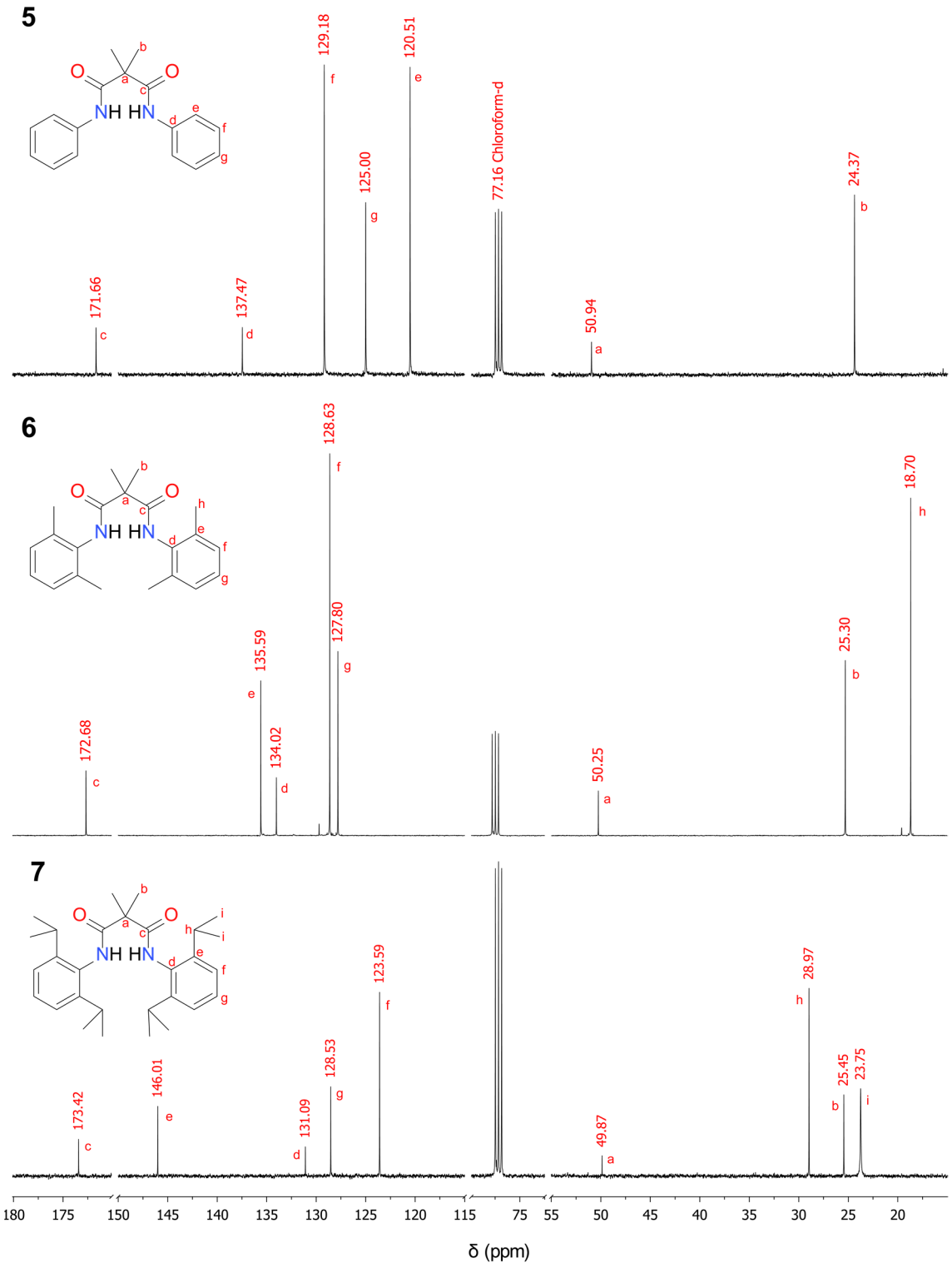

Figure 2.3 – Stacked ^{13}C-NMR spectra of the DMMA^{R2} family of ligands in $CDCl_3$. Assignments were performed on the basis of ^{1}H-^{13}C heteronuclear spectra.

Similar analysis can be extended to the ^{13}C-NMR spectra (Figure 2.3). The carbon atoms st the ligand backbone (*i.e.* the carboxylic carbons c, the quaternary α-carbon a and the corresponding methyls b, see Figure 2.3) were unaffected overall by the change of substituents on the aromatic rings, with negligible differences in their chemical shifts going from **5** to **6**, to **7** (Figure 2.3). However, the carbons on the aromatic rings not directly bound to −R (d, f, g, see Figure 2.3) appeared instead to be greatly affected by the change of substituents. The carbons d (*i.e.* the quaternary carbons attached to the amidic group) and f (the carbons in *meta* position to the amidic group) were progressively more shielded, resonating at lower chemical shifts, going from **5** to **6** to **7**. Oppositely, the carbons g, in *para* positions to the amidic group, appeared to be less shielded, exhibiting an increase in chemical shift going from **5** to **6** to **7**. This change in behaviour is due to the electron donor nature of the substituents on the aromatic rings for **6** and **7** (i.e. −CH_3 for **6**, −$CH(CH_3)_2$, for **7**), which by the inductive effect localise electron density on their *ortho* and *para* positions. Therefore, the carbons d and f (which are in the *ortho* position to the −R groups) displayed an increased electron density (*i.e.* more shielded), resonating at lower ppm as the inductive effect of the substituents increase going from **5** to **6** to **7**. On the opposite, the carbons g, which are in the *meta* position, exhibited a diminished electron density (*i.e.* more deshielded), resonating at higher ppm going from **5** to **6** to **7**.

The ATR-FTIR spectra of the compounds **5**, **6** and **7** are reported in Figures 2.5. Analysis of the spectra allowed us to identify the characteristic stretching of the N–H bond in the region between ν = 3200−3300 cm^{-1} (see Table 2.1) and the stretching of carbonyl groups around ν = 1640 cm^{-1}. The peaks in the range between ν = 3044–2980 cm^{-1}, are due to the asymmetric stretching of the C–H bond of the methyl groups, present in the backbone of the ligands. Interestingly, such vibrations appeared more distinctly in compound **6** and **7**, as a result of the contribution of the methyl and isopropyl substituents. Moreover, **7** exhibited an additional weak peak at ν = 2868 cm^{-1}, generated by the stretching vibration of the tertiary C–H of the isopropyl groups.

The ATR-FTIR data observed for **5**, **6** and particularly **7**, were compared with reported ligands with similar structures (Table 2.1), notably the bidentate **brt^{Ar}** [7] and **H$_2$pyN^{iPr2}** [2] ligands (Figure 2.4). All the systems exhibited close values for the stretching of the N−H bonds, as well as for the stretching of the C=O bonds. A closer comparison was carried out between **7**, **brt^{Ar}** and **H$_2$pyN^{iPr2}**, since they have common isopropyl groups on the

aryl rings. Notably, all the three ligands exhibited almost identical values for the asymmetric stretching of the C–H bonds of the methyl groups and for the stretching of the C–H bonds of the isopropylic tertiary carbons. Such an observation, alongside the aforementioned similarity of the values for the N–H and C=O bond stretching, emphasized once again their structural similarity.

ESI-Mass Spectrometry experiments confirmed the elemental composition of the synthesised compounds **5**, **6** and **7**, displaying the expected molecular peak for each ligand (Figures A-2.13–A-2.15).

Table 2.1 – Selected stretching frequencies for the DMMA^{R} ligands and structurally similar reported ligand. Values reported in wavenumbers (cm^{-1})

Vibrations	5	6	7	brt^{Ar} [7]	H_2pyN^{iPr2} [2]
N-H	3253	3222	3279	3300	3292
C=O	1642	1640	1643	1687	1691
Methyl C-H (asymm)	3044	2980	2964	2962	2963
Tertiary C-H	–	–	2868	2868	2870

brt^{Ar} = bis(2,6-diisopropylphenyl)-N-methyl-biuret; H_2pyN^{iPr2} = N^2,N^6-bis(2,6-diisopropylphenyl)pyridine-2,6-dicarboxamide

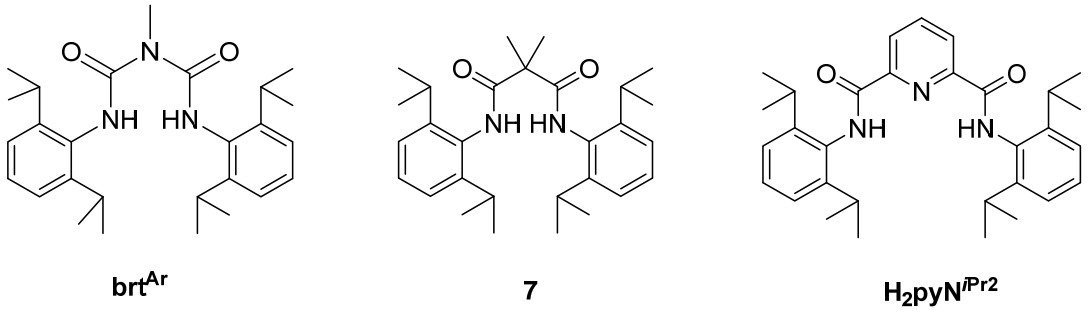

brt^{Ar} 7 H_2pyN^{iPr2}

Figure 2.4 – Structure of the selected ligand reported in Table 2.1

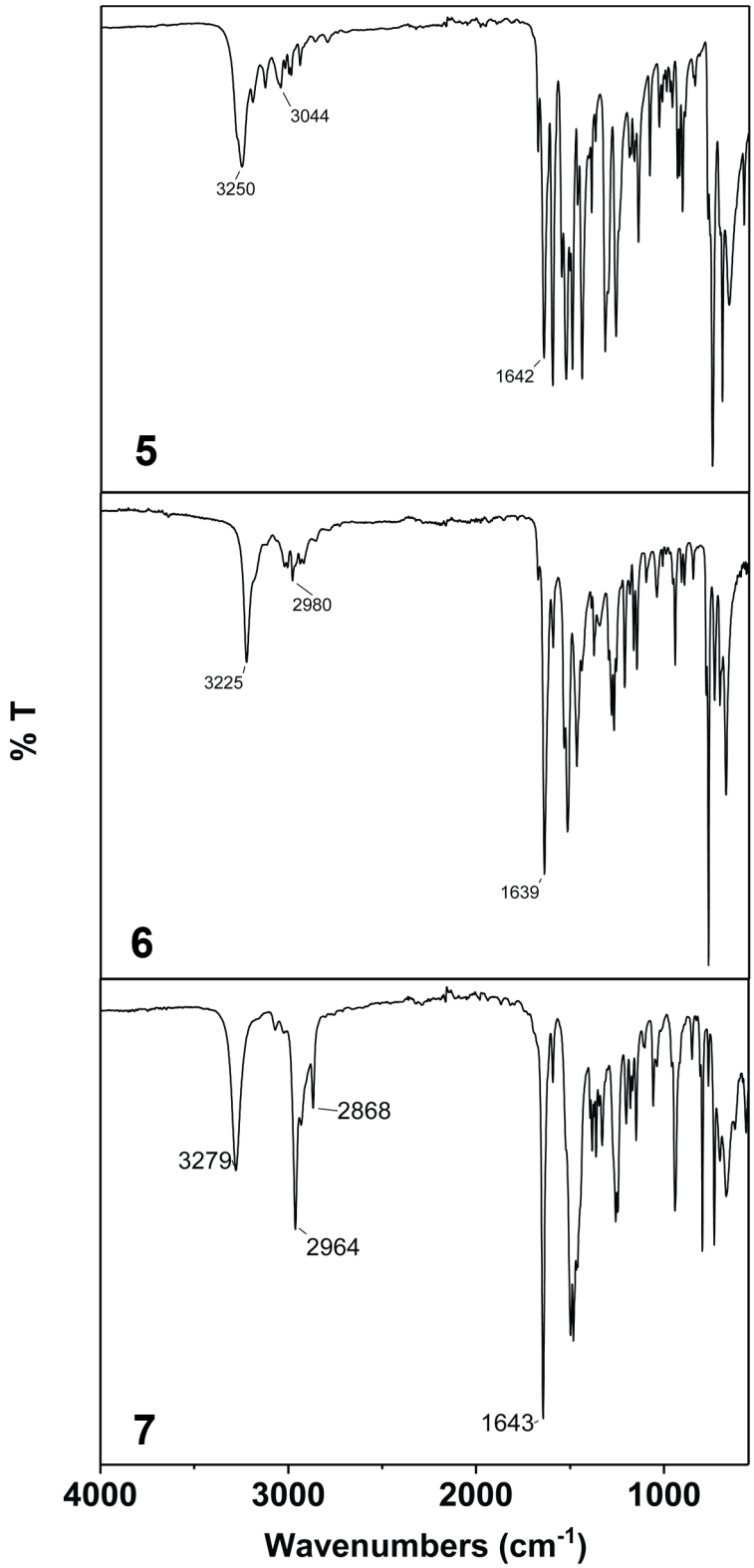

Figure 2.5 – Stacked FT-IR spectra of the DMMA^{R2} family of ligands.

In the case of **6**, upon recrystallization from methanol it was possible to obtain crystals suitable for single-crystal X-ray diffraction. The refinement of the data collected (Table 2.2) gave the crystal structure reported in Figure 2.6 with a R_1 = 4.52% and a GooF = 1.039. The crystal packaging displayed a strong hydrogen bonded network, involving the N–H (donor) and the C=O groups (acceptor), with a refined D···A (O···N) distance of ~2.84 Å (Figure A-2.16, Table A-2.1). Contrary to what was estimated in the introduction of this chapter, the crystal structure showed the presence of a unique rotation axis passing through the α-carbon and no mirror planes. Thus, the molecule can be identified to belong to to the C_2 point group (Figure 2.6), exhibiting a lowering symmetry compared to the expected C_{2v} geometry in the solid state.

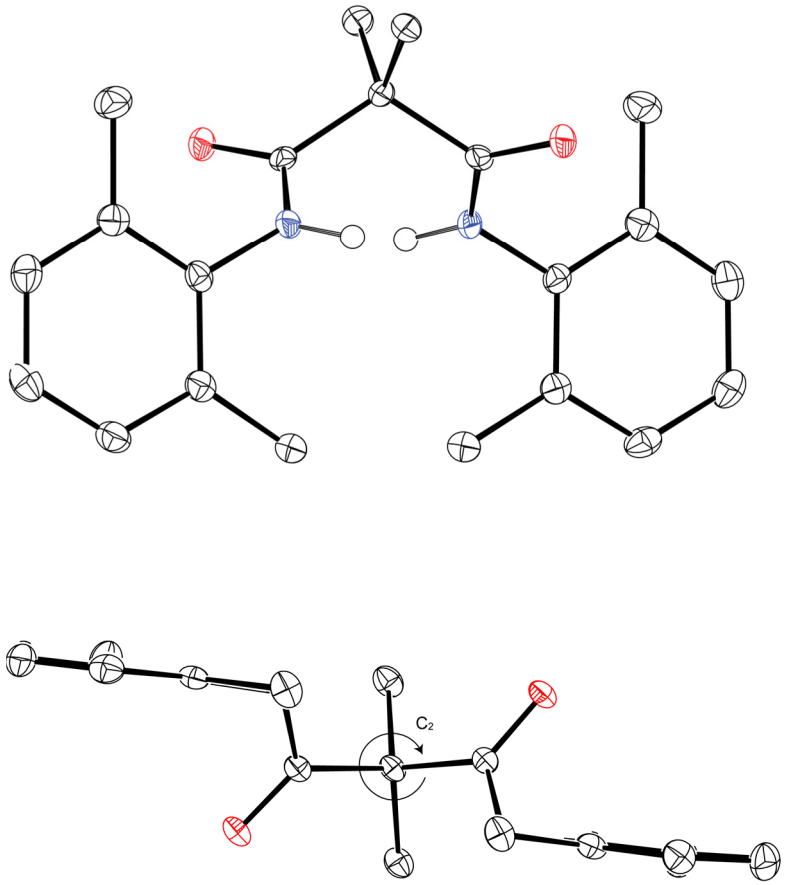

Figure 2.6 - *Top.* Front view of the crystallographic structure obtained for **6**. *Bottom.* Top view of the molecule with indicated the rotation axis. ORTEP at 50% probability level, Hydrogen omitted for clarity, except for those attached to the amide functionalities.

2.4 Conclusions

In conclusion, we successfully designed and synthesised a new family of bidentate ligand, $DMMA^{R2}$ (R = –H, $–CH_3$, $–CH(CH_3)_2$). The ease of the synthetic steps and the relative safety of the reagent employed allowed us to easily scale up these reactions, obtaining the products in bulk quantities. The three obtained ligands, **5** (R = –H), **6** (R = $–CH_3$) and **7** (R = $–CH(CH_3)_2$) were thoroughly characterised by ^1H and ^{13}C NMR and FT-IR spectroscopies, which confirmed their purity and structural features. Moreover, in the case of **6**, crystallographic data were obtained, showing a distorted structure due to the steric repulsion. Such distortion lowered the symmetry of the molecule, which passed from C_{2v} to C_2. Among the three ligands obtained, compound **6** was chosen for the complexation studies, since it exhibited a moderate steric hindrance of the binding site (more significant compared to **5**) combined with an increased robustness to oxidation (contrary to **7**, whose isopropylic tertiary C–H could be subjected to oxidation more easily than the C–H of methyls)[8]

2.5 Experimental Section – Chapter 2

Physical Methods

^1H, ^{13}C, and heteronuclear nuclear magnetic resonance (NMR) analyses were performed on an Agilent MR 400 MHz (400.13 MHz for ^1H-NMR and 100.61 MHz for ^{13}C-NMR). Fourier transform infra-red (FT-IR) spectra were recorded using a Perkin Elmer Spectrum 100 FT-IR/ATR. Electrospray ionisation mass spectrometry (ESI-MS) analyses were performed using a Micromass Time of Flight (ToF), interfaced with a Waters 2690 HPLC.

Synthesis of 2,2-dimethyldiethylmalonate (2)

The synthesis of 2,2-dimethyldiethylmalonate was performed according to a patented procedure.[6]

δ ^{1}*H* (400 MHz, $CDCl_3$): 1.22 (6H, t, *J* = 7.1 Hz, -$CH_2C\mathit{H_3}$), 1.40 (6H, s, -$C\mathit{H_3}$), 4.15 (4H, q, *J* = 7.1 Hz, -$C\mathit{H_2}CH_3$).

Synthesis of 2,2-dimethylmalonic acid (3)

2,2-dimethyldiethylmalonate (9,0 mL, 47.4 mmol) was dissolved in ethanol (80 mL). NaOH (2.5 M in H_2O), 95 mL, 237 mmol, 5 equiv.) was added dropwise at 0 °C and the solution was left stirring at room temperature overnight. Subsequently, the solvent was removed *in vacuo* and the residue was dissolved in H_2O (80 mL). After washing with 40 mL of Et_2O, the solution was acidified to pH 1 with 38% HCl. The product was extracted from the aqueous solution with Et_2O (3 × 70 mL), washed with brine, and dried over magnesium sulphate. The product was obtained as white solid (3.6970 g, 28,0 mmol, 59%).

δ ^{1}*H* (400 MHz, [D_6]-DMSO): 1.27 (6H, s, -$C\mathit{H_3}$), 12.58 (2H, s, -O*H*).

The ^{1}H-NMR data obtained for **3** were compliant with the data reported in the literature.[9]

Synthesis of 2,2-dimethylmalonyldichloride (4)

2,2-dimethylmalonic acid (1.9511 g, 15 mmol) was mixed with thionyl chloride (40 mL, 551 mmol, 37 equiv.). The reaction was stirred at reflux (75 °C) overnight. The excess of thionyl chloride was removed by distillation, yielding the product as a yellow oil (1.6 mL, 12.1 mmol, 81%). The product was used in the next step of the reaction without further purification.

δ ^{1}*H* (400 MHz, $CDCl_3$): 1.68 (6H, s, -$C\mathit{H_3}$).

The ^{1}H-NMR data obtained for **3** were compliant with the data reported in the literature.[10]

Synthesis of N^1, N^3-diphenyl-2,2-dimethyl malonamide (5)

2,2 -dimethyl malonyl dichloride (0.79 mL, 5.97 mmol) was dissolved in THF (20 mL). Separately, triethylamine (1.8 mL, 13 mmol, 2.2 eq) and aniline (1.1 mL, 12 mmol, 2 eq) were dissolved in THF (80 mL). Successively, the two solutions were mixed together, generating a slight colour change from colourless to pale yellow with the formation of a white precipitate of triethylammonium chloride. The solution was left to stir overnight at room temperature. Next, the solid was filtered off and the solvent removed *in vacuo*. The product was purified by recrystallization from MeOH and washed with cold Et_2O. Any trace of co-crystallised water was removed upon addition of absolute EtOH and formation of the corresponding EtOH/H_2O azeotrope. The final product **5** (0.7623 g, 2.70 mmol, 45%) was obtained after evaporation of solvent *in vacuo*.

$\delta_{^1H}$ (400 MHz, $CDCl_3$): 1.69 (6H, s, -C*H*$_3$), 7.14 (2H, t, *J* = 7.4 Hz, Ar-*pH*), 7.34 (4H, t, *J* = 7.9 Hz, Ar-*mH*), 7.52 (2H, d, *J* = 7.8, Hz Ar-*oH*), 8.47 (2H, s, -N*H*-)

$\delta_{^{13}C}$ (100 MHz, $CDCl_3$): 24.37 (*C*H$_3$), 50.94 (*C*q), 120.51 (*oC*H), 125.00 (*pC*H), 129.18 (*mC*H), 137.47 (*C*q), 171.66 (*C*=O).

ν_{max} (ATR-FTIR)/cm^{-1}: 3253 (N-H), 3046m (C-H), 1642 (C=O), 1595, 1524, 1492 (C-H), 1440, 1317, 1260, 1189, 1162, 1141, 1080, 1030, 931, 906, 746, 693, 657, 577

ESI-TOF (m/Z): Found: 281.1291 ([M-H]$^+$. $C_{17}H_{17}N_2O_2^-$ requires 281.1290)

Synthesis of N,N'-bis(2,6-dimethylphenyl)-2,2-dimethylmalonamide (6)

2,2-dimethylmalonyldichloride (1.6 mL, 12.2 mmol) was dissolved in THF (20 mL). Separately, triethylamine (3.4 mL, 24.5 mmol, 2 equiv.) and 2,6-dimethylaniline (3.0 mL, 24.4 mmol, 2 equiv.) were dissolved in THF (80 mL). Combination of the two solutions caused a colour change from colourless to intense yellow and the precipitation of triethylammonium chloride, as a finely dispersed white powder. After stirring overnight

at room temperature, the precipitate was filtered off and the solvent removed *in vacuo*, giving a dark orange residue. The residue was purified by recrystallisation (methanol, -30 °C), giving white crystals that were washed with cold Et_2O and dissolved in absolute ethanol. The product **6** was obtained as a white solid (1.3283 g, 3.92 mmol, 32%) by removing the solvent *in vacuo*.

δ ^{1}*H* (400 MHz, $CDCl_3$): 1.78 (6H, s, -C*H*$_3$), 2.22 (12H, s, Ar-C*H*$_3$), 7.09 (6H, m, Ar-C*H*), 8.19 (2H, s, -N*H*).

δ ^{1}*H* (400 MHz, [D_6]-DMSO): 1.62 (6H, s, -C*H*$_3$), 2.16 (12H, s, Ar-C*H*$_3$), 7.07 (6H, m, Ar-C*H*), 9.01 (2H, s,-N*H*).

δ ^{13}*C* (100 MHz, $CDCl_3$): 18.70 (*C*H$_3$), 25.30 (*C*H$_3$), 50.25 (*C*q), 127.80 (*pC*H), 128.63 (*mC*H), 134.02 (*C*q), 135.59 (Cq), 172.68 (*C*=O).

ν_{max} (FT-IR)/cm^{-1}: 3222 (N-H), 2980m (C-H), 1640 (C=O), 1513, 1465 (C-H), 1375 (C-H), 1269, 1212, 1147, 1098, 1038, 944, 892, 768, 670.

ESI-MS (m/Z): Found: 339.2074 ([M+H]$^+$. $C_{21}H_{27}N_2O_2^+$ requires 339.2067).

Synthesis of *N*^{1},*N*^{3}-bis(2,6-diisopropylphenyl)-2,2-dimethylmalonamide (7)

2,2-dimethylmalonyldichloride (1.1 mL, 8.32 mmol) was dissolved in THF (20 mL). Triethyl amine (2.4 mL, 17.3 mmol, 2.1 eq) and 2,6-diisopropyl aniline (3.2 mL, 17 mmol, 2 eq) were dissolved in THF (80 mL) and mixed with the dichloride solution. The solution immediately turned from colourless to yellow with the formation of triethylammonium chloride as precipitate. The solution was left stirring for 12 hours at toom temperature. The triethylammonium chloride was filtered off, then the product was precipitated by addition of water to the filtrated THF solution. Successively the solid was filtered and dissolved in EtOH. The final product was obtained as a white solid (1.5698 g, 3.49 mmol, 42%) after removing the solvent *in vacuo*.

$\delta_{^1H}$ (400 MHz, $CDCl_3$): 1.22 (24H, d, *J*= 6.9 Hz, Ar-CH(*CH*$_3$)$_2$), 1.80 (6H, s, *J*= 7.1 Hz, -*CH*$_3$), 3.04 (4H, sep, *J*= 6.9 Hz, Ar-*CH*(CH$_3$)$_2$), 7.20 (4H, d, *J*= 7.7 Hz, Ar-*mH*), 7.30 (2H, d, *J* = 7.7 Hz, Ar-*pH*), 8.32 (2H, s, -N*H*-)

$\delta_{^{13}C}$ (100 MHz, $CDCl_3$): 23.75 (-CH(*C*H$_3$)$_2$), 25.45 (-*C*H$_3$), 28.97 (-*C*H(CH$_3$)$_2$), 49.87 (*C*q), 123.59 (*mC*H), 128.53 (*pC*H), 131.09 (*C*q), 146.01 (*C*q), 173.42 (*C*=O)

ν_{max} (ATR-FTIR)/cm^{-1}: 3279 (N-H), 2964 (C-H), 2868 (C-H), 1643 (C=O), 1498, 1482 (C-H), 1384, 1362, 1328, 1255, 1148, 1057, 941, 795, 733, 702, 669, 564.

ESI-TOF (m/Z): Found: 451.3306 ([M+H]$^+$. $C_{29}H_{43}N_2O_2^+$ requires 451.3319); 473.3136 ([M+Na]$^+$. $C_{29}H_{42}N_2NaO_2^+$ requires 473.3138)

X-Ray diffraction experimental data

X-ray structural analysis **6** was performed on a Bruker D8 Quest ECO at 100(2) K with an Oxford Cryostream, with the sample mounted on a MiTeGen microloop using Mo Kα radiation (λ = 0.71073 Å). Bruker APEX[11] software was used to collect and reduce data and determine the space group. Absorption corrections were applied using SADABS.[12] Structures were solved with the shelXT structure solution program[13] using Intrinsic Phasing and refined with the shelXL refinement package[14] using Least Squares minimisation in Olex2.[15] All non-hydrogen atoms were refined anisotropically.

Donor H atoms in **6** were refined with U_{iso} = 1.5 times U_{eq} of riding N atom and refined with restraints (DFIX). All other hydrogen atoms were assigned to calculated positions using a riding model with appropriately fixed isotropic thermal parameters. Crystallographic data for the structure in this thesis has been deposited with the Cambridge Crystallographic Data Centre as supplementary publication #1878991. Copies of the data can be obtained, free of charge, on application to CCDC, 12 Union Road, Cambridge CB2 1EZ, UK, (fax: +44-(0)1223-336033 or e-mail:deposit@ccdc.cam.ac.uk).

Table 2.3. Crystal Data and Structure Refinement for **6**.

Empirical formula	$C_{21}H_{26}N_2O_2$	**μ/mm^{-1}**	0.078
Formula weight	338.44	**F(000)**	1456.0
Temperature/K	100(2)	**Crystal size/mm^3**	0.33 × 0.13 × 0.08
Crystal system	orthorhombic	**Radiation**	MoKα (λ = 0.71073)
Space group	Pbca	**2Θ range for data collection/°**	5.4 to 52.936
a/Å	16.1776(8)	**Index ranges**	-20 ≤ h ≤ 19, -11 ≤ k ≤ 11,
b/Å	9.0607(4)		-31 ≤ l ≤ 31
c/Å	25.2783(12)	**Reflections collected**	37651
α/°	90	**Independent reflections**	3817 [R_{int} = 0.0714, R_{sigma} = 0.0320]
β/°	90	**Data/restraints/parameters**	3817/2/240
γ/°	90	**Goodness-of-fit on F^2**	1.039
Volume/Å^3	3705.3(3)	**Final R indexes [I>=2σ (I)]**	R_1 = 0.0452, wR_2 = 0.1022
Z	8	**Final R indexes [all data]**	R_1 = 0.0716, wR_2 = 0.1155
ρ_{calc}g/cm^3	1.213	**Largest diff. peak/hole / e Å^{-3}**	0.30/-0.22

2.6 References

(1) C. Panda, A. Sarkar and S. Sen Gupta, *Coord. Chem. Rev.*, 2020, **417**.

(2) J.-C. Wasilke, G. Wu, X. Bu, G. Kehr and G. Erker, *Organometallics*, 2005, **24**, 4289-4297.

(3) P. J. Donoghue, J. Tehranchi, C. J. Cramer, R. Sarangi, E. I. Solomon and W. B. Tolman, *J. Am. Chem. Soc.*, 2011, **133**, 17602-17605.

(4) P. Pirovano, E. R. Farquhar, M. Swart and A. R. McDonald, *J. Am. Chem. Soc.*, 2016, **138**, 14362-14370.

(5) L. Bourget-Merle, M. F. Lappert and J. R. Severn, *Chem. Rev.*, 2002, **102**, 3031-3066.

(6) H. Zhang and Y. Dong, WO2012CN01001, KBP BioSciences Co., Ltd., Peop. Rep. China . 2012.

(7) C. Panda, A. Chandra, T. Corona, E. Andris, B. Pandey, S. Garai, N. Lindenmaier, S. Kunstner, E. R. Farquhar, J. Roithova, G. Rajaraman, M. Driess and K. Ray, *Angew. Chem. Int. Ed.*, 2018, **57**, 14883-14887.

(8) Y.-R. Luo, *Handbook of bond dissociation energies in organic compounds*, CRC press, 2002.

(9) C. J. Pouchert and J. R. Campbell, *Aldrich library of NMR spectra*, 1974.

(10) D. A. Evans, G. S. Peterson, J. S. Johnson, D. M. Barnes, K. R. Campos and K. A. Woerpel, *J. Org. Chem.*, 1998, **63**, 4541-4544.

(11) Bruker (2015). APEX3 v2015.9-0, Bruker AXS Inc., Madison, WI, USA.
(12) Bruker (2014/5). SADABS, Bruker AXS Inc., Madison, Wisconsin, USA.
(13) G. Sheldrick, *Acta Cryst. A*, 2015, **71**, 3-8.
(14) G. Sheldrick, *Acta Cryst. A*, 2008, **64**, 112-122.
(15) O. V. Dolomanov, L. J. Bourhis, R. J. Gildea, J. A. K. Howard and H. Puschmann, *J. Appl. Crystallogr.*, 2009, **42**, 339-341.

Chapter 3

Preparation and Characterisation of High valent bis-μ-hydroxo-Ni_2 Complexes

The work described in this chapter has been previously published in an article in Chemistry, A European Journal.[1] The DFT calculations were performed by Dr. Robert Gericke (Trinity College Dublin). The XAS data collection and analysis were done in collaboration with Dr Eric R. Farquahar (Brookhaven National Laboratory, USA); The EPR measurements were performed by Marta Lovisari (Trinity College Dublin); Prof Robert Barkley (School of Physics, TCD) kindly provided access to the EPR spectrometer. The XRD data collection and structure solutions and refinements were done by Dr Brendan Twamley (Trinity College Dublin).

3.1 Introduction

Despite their relevance and the role that they have been postulated to play in several catalytic cycles, such as the tyrosinase[2] and soluble methane monooxygenase (sMMO) cycles,[3] there is a dearth of synthetic hydroxide bridged high-valent oxidants in the literature compared to the widely studied bridging oxo counterparts.[4-9] In addiction, the majority of the existing literature on high valent hydroxide is mainly limited to Fe[10-12] and Cu[13, 14], albeit computational studies proposed Ni–O adducts as better oxidants.[15] To the best of our knowledge no hydroxide-bridged high-valent Ni_2 complexes have been reported to date, and there is limited insight into the reactivity properties of any hydroxide bridged high-valent oxidants. In this chapter, we report the synthesis and characterization of the new $Ni^{II}_2(\mu\text{-}OH)_2$ (**8**) complex and its conversion to the correspondent mixed valent $Ni^{II}Ni^{III}(\mu\text{-}OH)_2$ (**9**) and high valent $Ni^{III}_2(\mu\text{-}OH)_2$ (**10**) complexes. Particular attention will be set on the unambiguous identification of the species **9** and **10** with respect to the oxo/hydroxo possible nature of the bridging ligands.

3.2 Synthesis and characterization of a $Ni^{II}_2(\mu\text{-}OH)_2$ complex (8)

In order to obtain compound **8**, the diamide ligand **6** (**LH_2**) was reacted with *n*-butyllithium (2.5 M in hexane, 2.5 equiv.) in tetrahydrofuran (THF), followed by the addition of $[Ni(DMSO)_6][ClO_4]_2$[16] (1 equiv., DMSO = dimethyl sulfoxide) (Scheme 3.1). The addition of the Ni^{II} salt produced a colour change from pale yellow to purple followed by precipitation of a purple crystalline material. The purple solid was collected by filtration and was identified as the bis-μ-hydroxide complex $Li_2[Ni^{II}(OH)(\mathbf{L})]_2$ (**8**), isolated in 84% yield. The preparation of **8** in high yield relied on the presence of very low concentrations of adventitious H_2O in our THF solutions. However, **8** was unstable in the presence of excess H_2O.

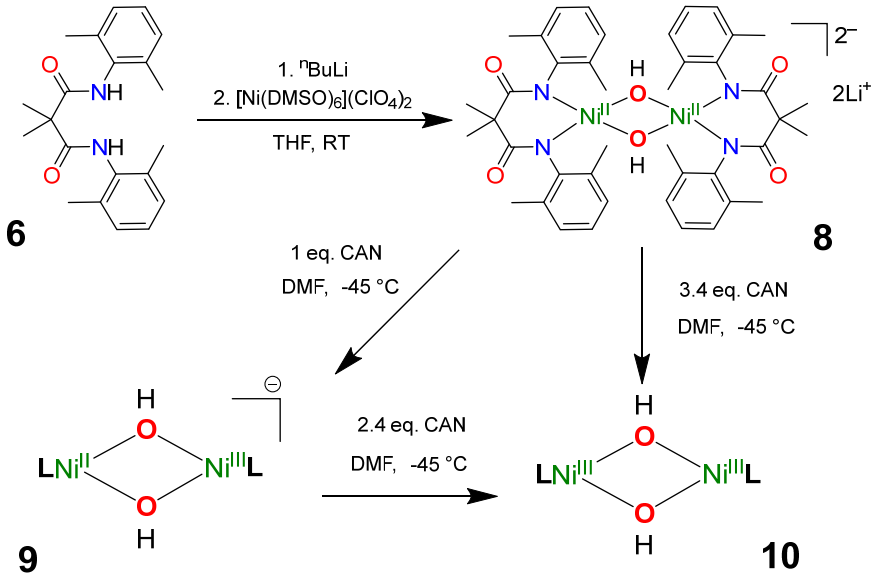

Scheme 3.1 - Synthesis of complex of **8** and oxidation to **9** and **10** by $(NH_4)_2[Ce^{IV}(NO_3)_6]$ (CAN) at -45 °C in N,N-dimethylformamide (DMF).

Diffraction quality crystals were grown from N,N-dimethylformamide (DMF)/diethyl ether (Et_2O) upon metathesis of Li^+ with tetraethylammonium ions (Et_4N^+). **8** exhibited two four-coordinate Ni ions connected by two bridging hydroxide ligands, which were refined in two symmetrical positions with a 50% chemical occupancy (Figure 3.1, Table 3.3). Geometry indexes τ_4 and τ_4'[17] indicated that each Ni centre was in a distorted square-planar geometry ($\tau_4 = 0.22$, $\tau_4' = 0.21$; $\tau = 0$ square planar, $\tau = 1$ tetrahedral, Table A-3.1). This is presumably due to the d^8 ions preference for a square planar geometry (low spin) and to the steric hindrance and rigidity of the backbone of the ligand. The ketone and $-CH_3$ functionalities of the ligand backbone were in and out of the plane containing the core, respectively, while the 2,6-dimethylphenyl groups do not lie exactly perpendicular to the Ni(μ-OH)$_2$Ni plane (Figure 3.1). The average Ni–O bonds length observed in **8** (1.92 Å, Table A-3.1) were longer than structurally analogous $Ni^{II}_2(\mu\text{-OH})_2$ complexes based on the bidentate β-diketiminate ligands (1.86 Å)[18] but shorter than $Ni^{II}_2(\mu\text{-OH})_2$ systems with tri-dentate (1.99 Å)[19] and tetra-dentate (2.01 Å)[20] ligands (Table A-3.2). The increase in the denticity of the ligands in bis-μ-hydroxo-Ni^{II}_2 complexes was thus strictly correlated with a progressive elongation of the Ni–O distances. A similar trend was observed for the Ni···Ni distances (Table A-3.2). In this case **8** displayed the shortest Ni···Ni distances (2.88 Å) between the examples reported above.

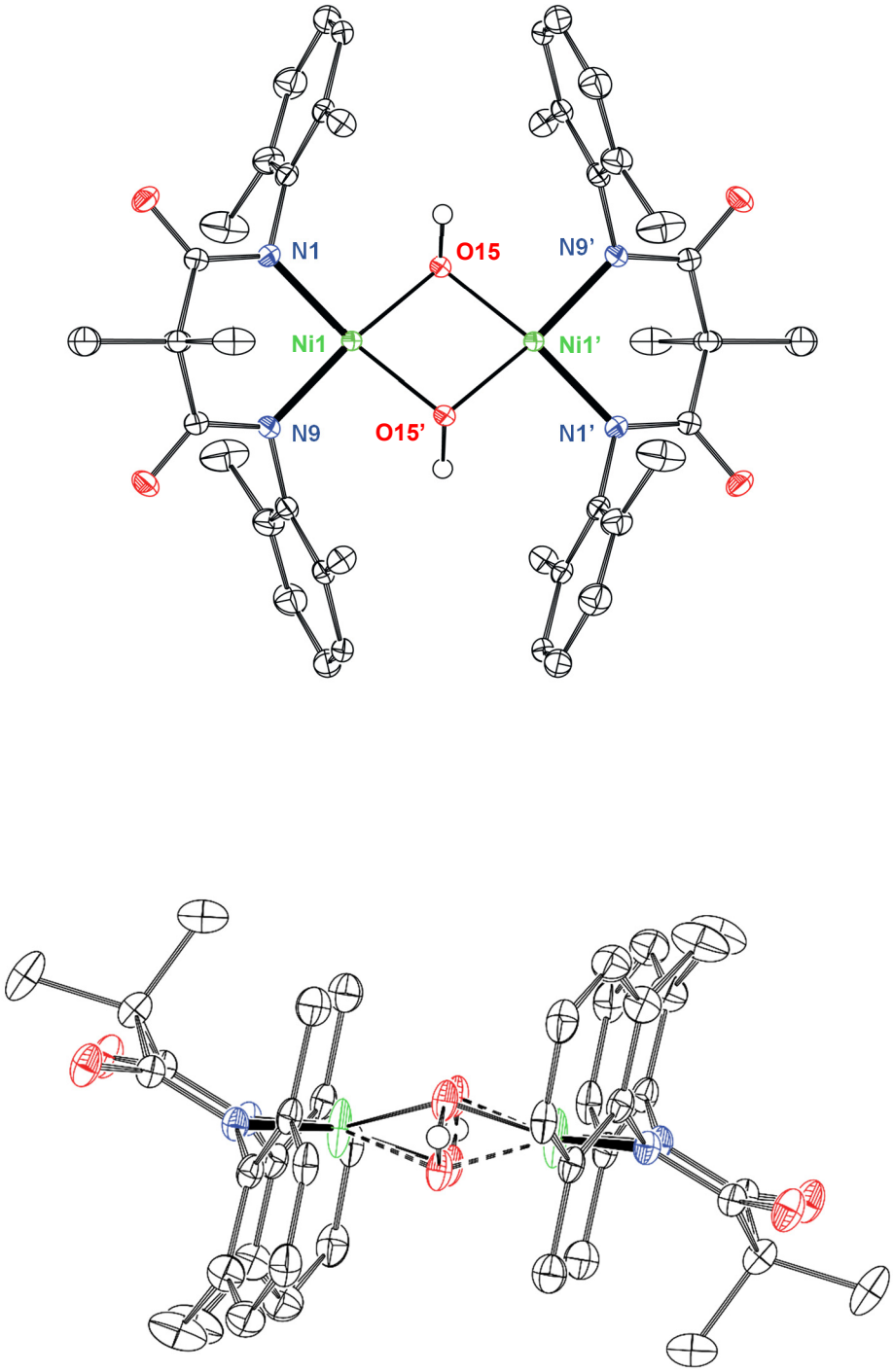

Figure 3.1 - *Top*. Top view of **8** showing one orientation of the bridging hydroxide. *Bottom.* Side on view of **8**. Bridging hydroxide ligands exhibited disorder and were refined in two different positions with 50% probability. Symmetry generated (1-x, 1-y, 1-z) ORTEP plots with atomic displacement at 50%. Counterions and co-crystallised solvent molecules were omitted for clarity as well as H- atoms, except for those associated with the μ-hydroxide ligands.

The ^{1}H-NMR spectrum of complex **8** exhibited an overall shift of all peaks associated with **6** as a result of complexation, and the disappearance of the amide N–H resonances present in **6** (Figures 3.2, A-3.3–A-3.5). The NMR data showed a relatively simple spectrum with two sets of C*H*$_3$ resonances and just two aryl C*H* resonances. This would indicate a high degree of solution fluxionality in **8**, whereas the X-ray crystal structure suggested that signals associated with these protons would be non-equivalent. Moreover, a feature at -9.3 ppm, attributable to the -O*H* resonance of the μ-hydroxide ligands, was identified. The addition of a small amount of D_2O to **8** caused the disappearance of this resonance in the ^{1}H NMR spectrum, presumably as result of hydrogen-deuterium exchange (Figure A-3.2), confirming the identification of this resonance.

Further evidence of μ-hydroxide ligands was provided by ATR/FT-IR (Figure 3.3), which exhibited a sharp feature at ν = 3615 cm^{-1}. Such features are typical of non-hydrogen bonded O–H stretches,[21] as previously observed by Itoh[19] and others[22, 23] in analogous $M^{II}_2(\mu\text{-OH})_2$ complexes (M = Mn, Co, Ni, Cu). Negative mode ESI-MS analysis showed a doubly-charged molecular ion peak at m/z = 411.1225, whose isotopic pattern and mass matched the molecular anion $[(Ni^{II}(OH)(\mathbf{L}))_2]^{2-}$ (Figure A-3.6), confirming the elemental composition of **8**.

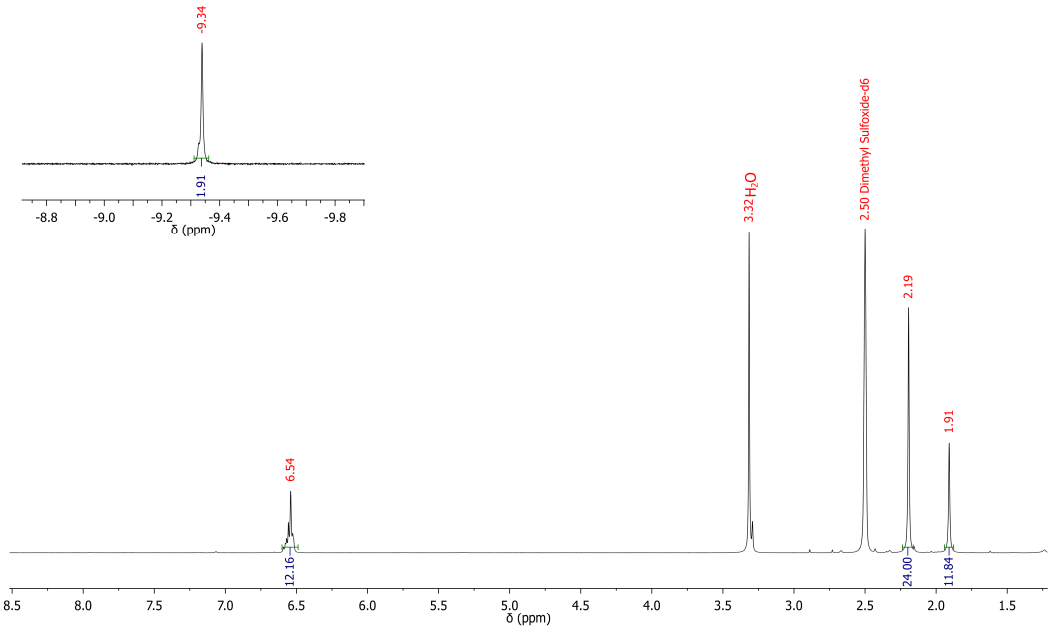

Figure 3.2 - ^{1}H-NMR spectrum of **8** (400 MHz, [D_6]-DMSO).

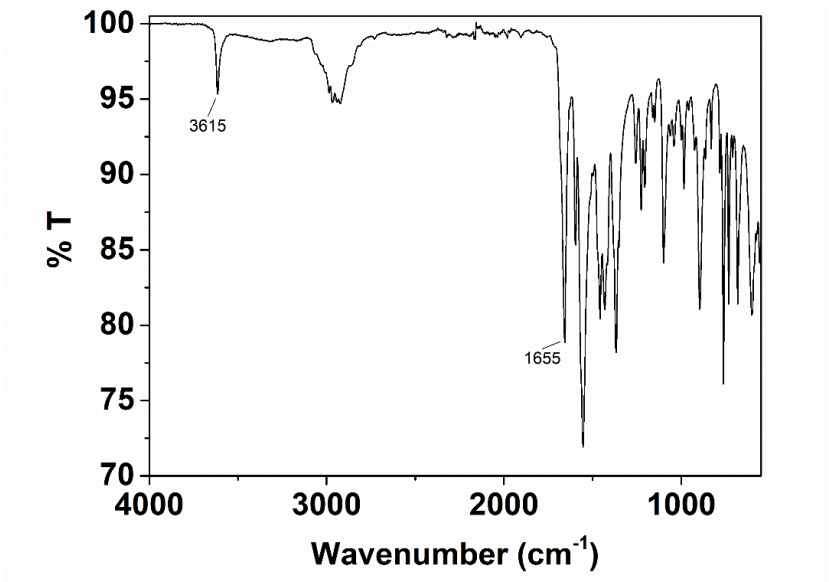

Figure 3.3 – ATR/FT-IR spectrum of **8**

Cyclic voltammetry was performed on a solution of **8** in DMF, showing the presence of two quasi-reversible waves at $E_{1/2}$ = -0.06 V ($\Delta E_{pa,pc}$ = 0.11 V) and $E_{1/2}$ = 0.24 V ($\Delta E_{pa,pc}$ = 0.12 V) vs Fc^+/Fc (Figure 3.4, A-3.7, Fc = ferrocene). The number of electrons involved in each redox event was estimated by comparing the $\Delta E_{pa,pc}$ of each wave to a standard Fc solution (see Table A-3.3), defining this system to be a two e^- oxidation in which every oxidation event occurred stepwise. The first oxidation event was assigned to the $1e^-$ oxidation of **8** (Ni^{II}_2) to a putative mixed-valent $Ni^{II}Ni^{III}$ species (defined as **9**), followed by a subsequent $1e^-$ oxidation to a putative high valent Ni^{III}_2 species (defined as **10**). Zhou and co-workers[24] observed similar multiple $1e^-$ oxidations of a triple *meso*-helicate Ni_2 complex from $Ni^{II}_2 \rightarrow Ni^{II}Ni^{III} \rightarrow Ni^{III}_2$ and, at higher potential, from $Ni^{III}_2 \rightarrow Ni^{III}Ni^{IV} \rightarrow Ni^{IV}_2$. For $Ni^{II}_2(\mu\text{-}OH)_2$ complexes, Itoh and co-workers[19] reported no stepwise oxidation in cyclic voltammetry experiments for **51** (see Table 1.1), observing only a single $1e^-$ oxidation from Ni^{II}_2 to $Ni^{II}Ni^{III}$, presumably due to the instability of the high valent $Ni^{III}_2(\mu\text{-}O)_2$ state, which required low temperature (-90°C) to be observed. The voltammetric observation of a $Ni^{II}Ni^{III} \rightarrow Ni^{III}_2$ (**9** → **10**) oxidation in this work highlights a remarkable accessibility of the high valent Ni^{III}_2 state, presumably as a result of the stabilising contribution of the anionic donors of the ligand.

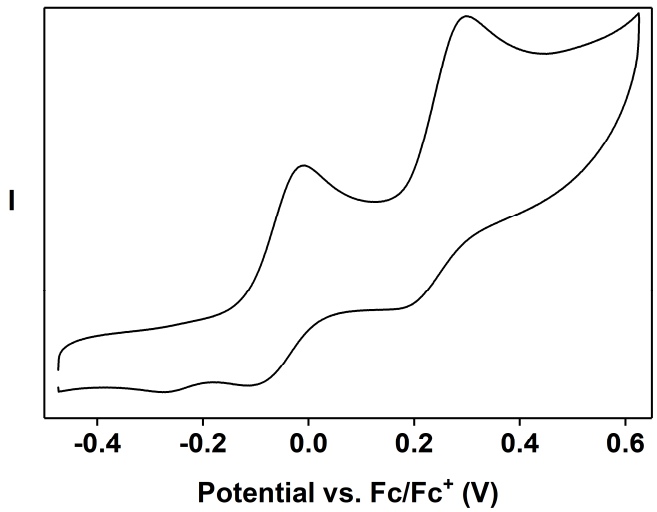

Figure 3.4 - Steady state cyclic voltammograms of **8**. Conditions: 5.5 mM (DMF), 0.1 M Bu_4NPF_6, scan rate 100 mV s^{-1}, room temperature.

3.3 Preparation and characterization of a $Ni^{II}Ni^{III}(\mu\text{-}OH)_2$ (9) and a $Ni^{III}_2(\mu\text{-}OH)_2$ (10) species.

Titration of $(NH_4)_2[Ce^{IV}(NO_3)_6]$ (CAN) into a solution of **8** (0.2 mM, DMF, -45 °C) resulted in an immediate reaction as evidenced by electronic absorption spectroscopy (Figures 3.5, A-3.8). The addition of up to one equivalent of CAN resulted in a new compound, **9** (Scheme 3.1), with a broad absorption feature at λ_{max} = 560 nm and a shoulder at λ_{max} = 430 nm. **9** was relatively stable at -45 °C, demonstrating a half-life of 2700 s. If complex **8** (0.2 mM, DMF, -45 °C) was reacted with one equivalent of CAN, added all at once, the instantaneous formation of **9** was observed in similar yields to that observed under sub-stoichiometric additions (Figure A-3.9). When more than one equivalent of CAN was added to the reaction mixture (Figure 3.5), a second species was identified (**10**, λ_{max} = 600 nm), the maximum yield of which was obtained when 3.4 equivalents of CAN were added. **10** was less stable than **9**, demonstrating a half-life of 1500 s at -45 °C. Furthermore, when more than 3.4 equivalents of CAN were added to the reaction mixture, **10** was observed to display accelerated decay, suggesting it was unstable in the presence of excess CAN. **10** could also be prepared in the same yield by the one-time addition of 3.4 equiv. of CAN to **8** (0.2 mM, DMF, -45 °C,Figure A-3.10).

Electronic absorption features for mono- and di-nuclear Ni^{III}–O compounds are spread over a wide range of values. Mononuclear Ni^{III}–OX complexes (OX = OCO_2H, O_2CCH_3, ONO_2) supported by 2,6-pyridinecarboxamidate ligands exhibited two main features at λ_{max} = 510-560 nm (ϵ = 6000-7000 $M^{-1}cm^{-1}$) and λ_{max} = 760-890 nm (ϵ = 3300-4600 $M^{-1}cm^{-1}$).[25] A putative Ni^{III}–oxyl system based on a bis-carboxamidate macrocyclic ligand showed instead a single band at λ_{max} = 420 nm (ϵ > 7000 $M^{-1}cm^{-1}$) and a weak shoulder at λ_{max} = 580 nm (ϵ > 800 $M^{-1}cm^{-1}$).[26] The spectra obtained for **9** and **10** are thus comparable with high-valent Ni ions supported by carboxamidate donor ligands, leading us to conclude that **9** and **10** contain $Ni^{II}Ni^{III}$ and Ni^{III}_2 cores, respectively. Previously reported $Ni^{III}_2(\mu\text{-}O)_2$ complexes exhibited a common single transition in a narrow range around λ_{max} = 400–410 nm (**61** λ_{max} = 408 nm ϵ = 6000 $M^{-1}cm^{-1}$;[19] **64** λ_{max} = 405 nm ϵ = 5000 $M^{-1}cm^{-1}$;[27] Suzuki *et al.*[5] λ_{max} = 409 nm ϵ = 3800 $M^{-1}cm^{-1}$). Riordan and co-workers reported a $Ni^{III}_2(\mu\text{-}O)_2$ species (**66**) showing two intense features at λ_{max} = 403 nm (ϵ = 12000 $M^{-1}cm^{-1}$) and λ_{max} = 565 nm (ϵ = 12000 $M^{-1}cm^{-1}$).[28] In the light of these reported examples, the lack of any characteristic feature at ~ 405 nm for **9** and **10** indicated the absence of the $Ni^{III}_2(\mu\text{-}O)_2$ core, suggesting the presence of hydroxide ligands.

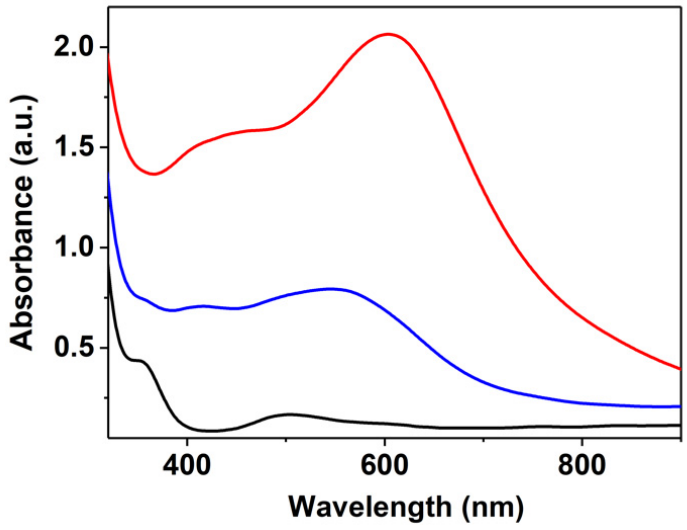

Figure 3.5 - Electronic absorption spectroscopy monitored titration of $(NH_4)_2[Ce^{IV}(NO_3)_6]$ (CAN) with complex **8** (black trace, DMF, -45˚C) to yield **9** (blue trace, 1.0 equiv. CAN) and **10** (red trace, 3.4 equiv. CAN).

Negative-mode ESI-MS performed on a just-thawed solution of **10** detected a doubly-charged species at m/z = 410.1195, whose mass and isotopic pattern were compatible with a doubly charged doubly de-protonated species ($[Ni^{III}(O)(L))_2]^{2-}$, Figure A-3.11). The absence of any pattern related to **8** at m/z = 411.1225 suggested the full conversion of **8** in the oxidation reactions. The observation of the doubly deprotonated ion indicates that deprotonation of the complex allows for its detection by ESI-MS.

3.4 EPR spectroscopy studies

X-band electron paramagnetic resonance (EPR) spectra of frozen-solutions of **8**, **9**, **10**, *and* the titration of **8** with CAN in DMF were measured at 77 K (Figure 3.6). **8** exhibited a silent EPR spectrum, as expected for a Ni^{II}_2 complex in a *pseudo*-square planar geometry. Despite the expected unpaired electrons on each d^7 Ni^{III} ion, the spectrum of **10** was also EPR silent in the X-band EPR (perpendicular mode) at 77 K. This suggests the presence of magnetic coupling between the two Ni^{III} ions. A similar phenomenon was also observed by Itoh and co-workers, that reported the first example of $Ni^{III}_2(\mu\text{-}O)_2$ complex with ferromagnetic coupling between high valent Ni^{III} ions (**64**, $S = 1$, $g \sim 4$ obtained by parallel mode EPR).[27] The EPR spectrum of **9** can be assigned to an $S = ½$ species (Figure 3.6), that we attributed to a mixed-valent $Ni^{II}Ni^{III}$ species. The signal displayed rhombic anisotropy with $g_x = 2.45$, $g_y = 2.34$, and $g_z = 2.00$ (Figure 3.7). The average g value ($g_{av} = 2.26$), alongside the rhombic anisotropy of the signal ($g_x > g_y >> g_z$), suggested the unpaired electron being localized on the metal centres, corroborating the presence of a low-spin d^7 Ni^{III} ion in a square planar or tetragonally distorted *pseudo*-octahedral coordination environment.[29, 30] Therefore, this observation excluded the likelihood of a ligand-based radical. The yield of conversion of **8** into **9** was estimated to be 90 ± 20% by double integration of the signal and comparison with the radical standard (2,2,6,6-tetramethylpiperidin-1-yl)oxyl (TEMPO). Furthermore, the clear conversion of the EPR-active species **9** into the EPR-silent species **10** after addition of more than one equivalent of CAN (Figure 3.6) corroborated our observations made by electronic absorption spectroscopy and cyclic voltammetry. This high-yield formation of **9** with one equivalent of CAN followed by the disappearance of **9** with further addition of equivalents of CAN demonstrates that **9** is a precursor to **10** and that **10** is one oxidising equivalent above **9**.

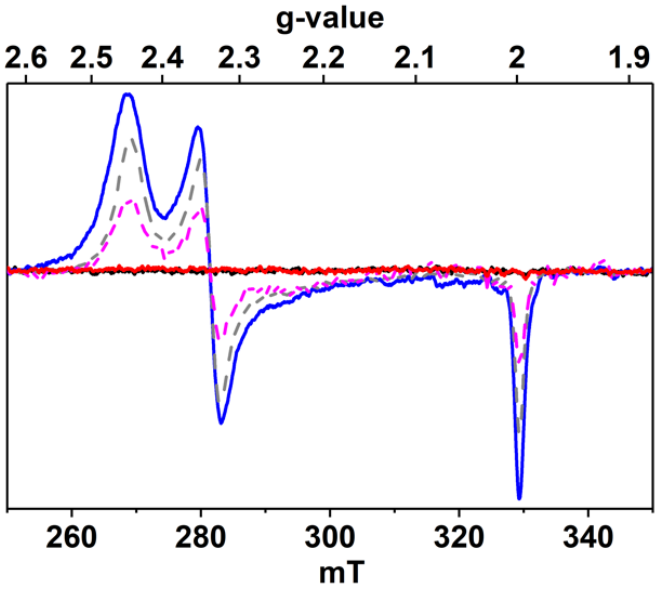

Figure 3.6 - X-band EPR-monitored titration of CAN with **8** (black trace): 1.0 eq (**9**, blue trace), 1.5 eq (grey trace) 2.0 eq (pink trace) and 3.4 eq (**10**, red trace). Each X-band EPR spectrum was acquired from a frozen DMF solution, measured at 77 K, 6.36 mW or 2.01 mW microwave power, with 0.3 mT modulation amplitude.

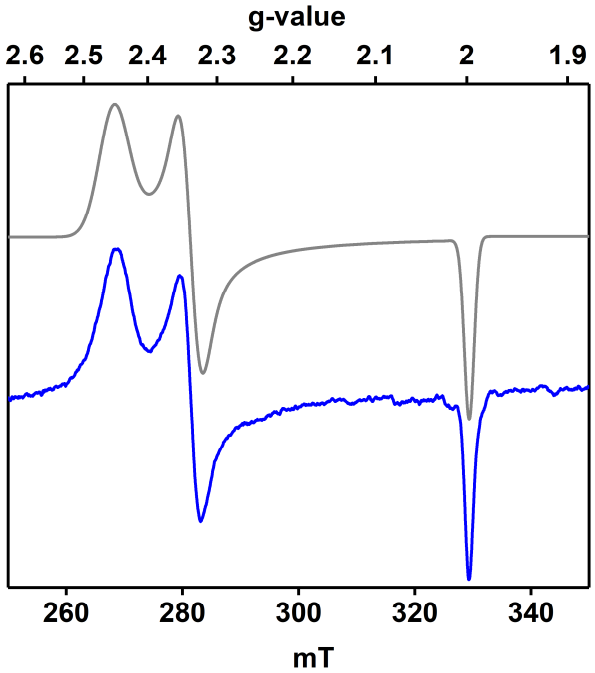

Figure 3.7 - EPR spectrum of **9** (blue trace) and the simulated spectrum (grey trace). EPR spectrum was acquired from a frozen DMF solution, measured at 77 K, 6.36 mW or 2.01 mW microwave power, with 0.3 mT modulation amplitude.

3.5 X-Ray Absorption Spectroscopy

Ni K-edge X-ray absorption spectroscopic studies were performed on frozen samples of **8**, **9**, and **10**. Evaluation of the X-ray absorption near edge structure (XANES) spectra showed that the K-edge energies of the complexes were spread over a narrow range of values (Figure 3.8), similar to those reported for analogous Ni systems.[31-33] With respect to the Ni^{II}_2 precursor **8**, a shift of -0.3 eV for **9** and +0.4 eV for **10** was observed (Figure 3.8, Table 3.1). As reported by Mascharak,[31] these edge energy shifts supply no direct evidence of oxidation state changes, reflecting instead a variation of the effective charge on the Ni centres. The edge can be influenced by core-to-valence transitions that will distort the definition of the edge energy. Indeed, we have observed similarly non-existent or small 'edge' energy shifts for mononuclear Ni complexes upon oxidation from Ni^{II} to Ni^{III}.[25, 32] All three species exhibited a weak pre-edge feature (Figure 3.8-3.9) at 8333.2 eV (**8**), 8333.2 eV (**9**) and 8334.0 eV (**10**), assigned to an electronic-dipole forbidden 1*s*-to-3*d* transition,[31] that in centrosymmetric point groups such as D_{4h} (square planar)[34] gains intensity from *p*/*d* mixing due to deviations from centrosymmetry.[35] Little-to-no difference was observed between the pre-edge energies of this feature for complexes **8** and **9**, while complex **10** exhibited a distinct blue shift of ~0.8 eV. The shift observed reflected a clear change in the ligand field (and possibly oxidation state) between **8**/**9** and **10**.[36]

Pre-edge areas for the compounds were calculated (Table 3.1, Figure A-3.12, Table A-3.4) revealing a ~50% increase of the area for **10** compared to **8**, presumably as a result of an increase in *d*-orbital holes in the higher-valent species **10**. Such differences in areas was reported to be a fingerprint feature of Ni^{II}/Ni^{III} couples, identifying **10** as a fully oxidised Ni^{III}_2 species.[31] No appreciable change in the area was observed for **9**. The broad-double-bump feature approximately 5–8 eV below the edge exhibited by **8** and **9** is distinctive of four-coordinated square planar complexes[25, 31, 37] and has been assigned to a 1*s*-to-4p_z transition.[31] Complex **9** exhibited a less intense feature than **10**, suggesting a partial loss of square planar geometry. The absence of the feature in **10** strongly supports a drastic change in the geometry of the two Ni^{III} centres, suggesting the presence of *pseudo*-octahedral environment.

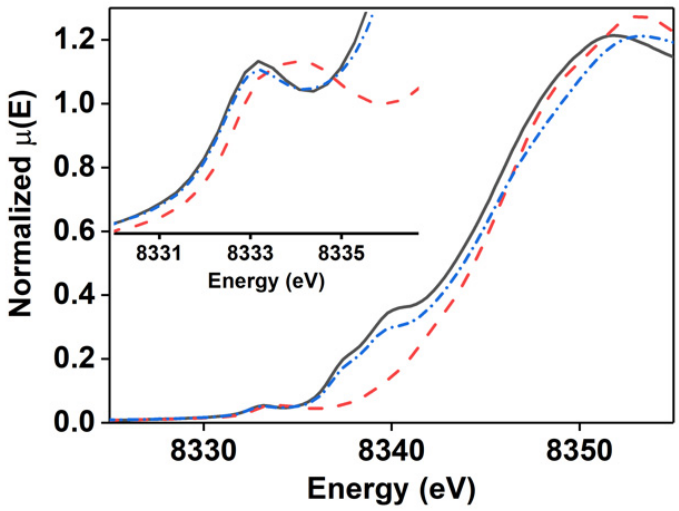

Figure 3.8 - Normalized Ni K-Edge XANES spectra of **8** (solid black line), **9** (dash-dotted blue line), **10** (dashed red line). Inset: Pre-edge region.

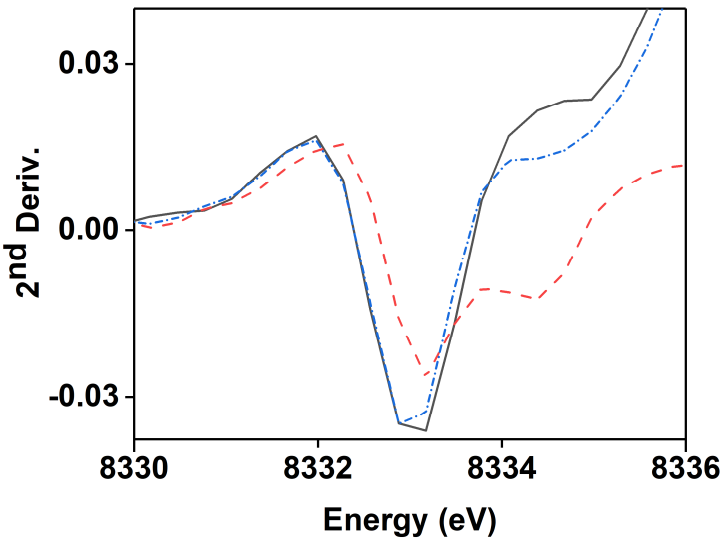

Figure 3.9 - Second derivative of the pre-edge region, showing the asymmetry of **10**.

Table 3.1 - Significant data from Ni K-edge X-ray absorption spectroscopy analysis of complexes **8**, **9**, and **10** and comparison with the predicted distances[a] obtained by DFT calculations[d].

	E_{edge}[b]	$E_{pre\text{-}edge}$[b]	$Area_{pre\text{-}edge}$[c]	Ni–N/O	Ni···O_{DMF}	Ni···Ni
8	8345.7	8333.2	5.65(5)	2 N @ 1.88 2 O @ 2.03		3.09
9	8345.4	8333.2	5.54(29)	4 @ 1.89	-	2.85
9				*4 @ 1.88*	-	*2.86*
9-oxo				*4 @ 1.88*	-	*2.69*
10	8346.1	8334	11.55(36)	4 @ 1.95	2.08	2.97
10				*4 @ 1.92*	*2.07*	*3.00*
10-oxo				*4 @ 1.85*	-	*2.70*

[a] Distances reported in Å. [b] Energy values reported in eV. [c] Areas multiplied by 100 for convenience. [d] DFT predicted models areitalicised.

Extended X-ray absorption fine structure (EXAFS) analysis of **8** demonstrated negligible differences from the crystallographic data (Tables 3.1, A-3.5, Figure 3.10). The best fit showed the presence of a first coordination shell composed of 4 N/O scatterers, divided into subshells of 2 scatterers at 1.88 Å and 2.03 Å each, matching well with X-ray diffraction measurements (Table S8). Several attempts were made to fit the second coordination shell with light atoms, revealing the necessity of a heavier atom to improve the fit. A second Ni atom was refined at 3.09 Å, a value 0.2 Å longer than XRD data reported above (Table A-3.6). The presence of a heavy atom scatterer was also evaluated by the k^5-weighted Fourier transform in EXAFS analysis. The intensity of FT peaks from a heavier scatterer is dependent on *n* (in k^n) and is expected to increase going from k^3 (normally used for EXAFS analysis) to k^5.[38] The k^5-weighted Fourier transform for **8** (Figure 3.11) showed a clear increase in the FT magnitude in the region 2.6-3.0 Å, defining the presence of a heavier scatterer (i.e. the second Ni atom). The shell was completed by 4 C atoms at 2.87 Å from the ligand backbone.

The best fit for the EXAFS analysis of **9** (Tables 3.1, A-3.7, Figure 3.10) showed a first coordination shell composed of 4 N/O atoms, at 1.89 Å (Table A-3.7). The second coordination shell refined the second Ni atom at 2.86 Å, representing a shorter Ni···Ni distance

with respect to **8**. Such a decrease could be ascribed to a formal oxidation state change of +1 when compared to **8**.

EXAFS analysis of **10** initially showed a best fit of six N/O scatterers in the first coordination shell, divided in two sub-shells composed of 3 N/O atoms each at 1.93 Å and 2.05 Å (Tables 3.1, A-3.8, Figure 3.10). DFT calculations performed excluded this possibility because steric crowding around the Ni_2 core prevented two solvent molecules binding to each Ni^{III} atom (*vide infra*). Therefore, EXAFS fitting with penta-coordination was explored, showing a first coordination sphere composed of five N/O scatterers, divided in[to] two sub-shells made by 4 N/O atoms at 1.95 Å and 1 N/O(DMF) atom lying at 2.08 Å. These values were in agreement with the distances gathered by DFT calculations (Tables 3.1–3.2). The calculated metal-ligand bond distances for **10** were longer compared to **8** and **9**, defining a significant expansion of the first shell presumably caused by expanding the coordination number from four to five. A heavy atom scatterer (*i.e.* the second Ni atom, 2.97 Å) was required to improve the fit, as also confirmed by k^5-weighted Fourier transform (Figure 3.11).[38] The EXAFS analysis of **10** nicely corroborates XANES observations, confirming a change in the coordination geometry.

The Ni–O bond length and the Ni···Ni distance are topical parameters to identify the nature of the bridging ligands, allowing us to gauge whether **9** and **10** maintains the bis-μ-hydroxide core or has converted to a bis-μ-oxo core. The presence of a bridging oxo-ligands would be expected to result in shorter Ni–O and Ni···Ni distances. Comparison of the distances in **10** with the few structurally characterised $Ni^{III}_2(\mu\text{-}O)_2$ complexes exhibited stark differences. Even considering the elongation due to the change in coordination number in **10**, the Ni–O bond length of 1.95 Å obtained for **10** was longer than the reported average values for bis-μ-oxo cores of ~1.87 Å, suggesting the presence of hydroxide ligands.[27, 39, 40] Additionally, the refined Ni···Ni distance (**10**, 2.97 Å; $Ni^{III}_2(\mu\text{-}O)_2$, 2.86–2.92 Å[27, 39, 40]) would also suggest a bis-μ-hydroxide core.

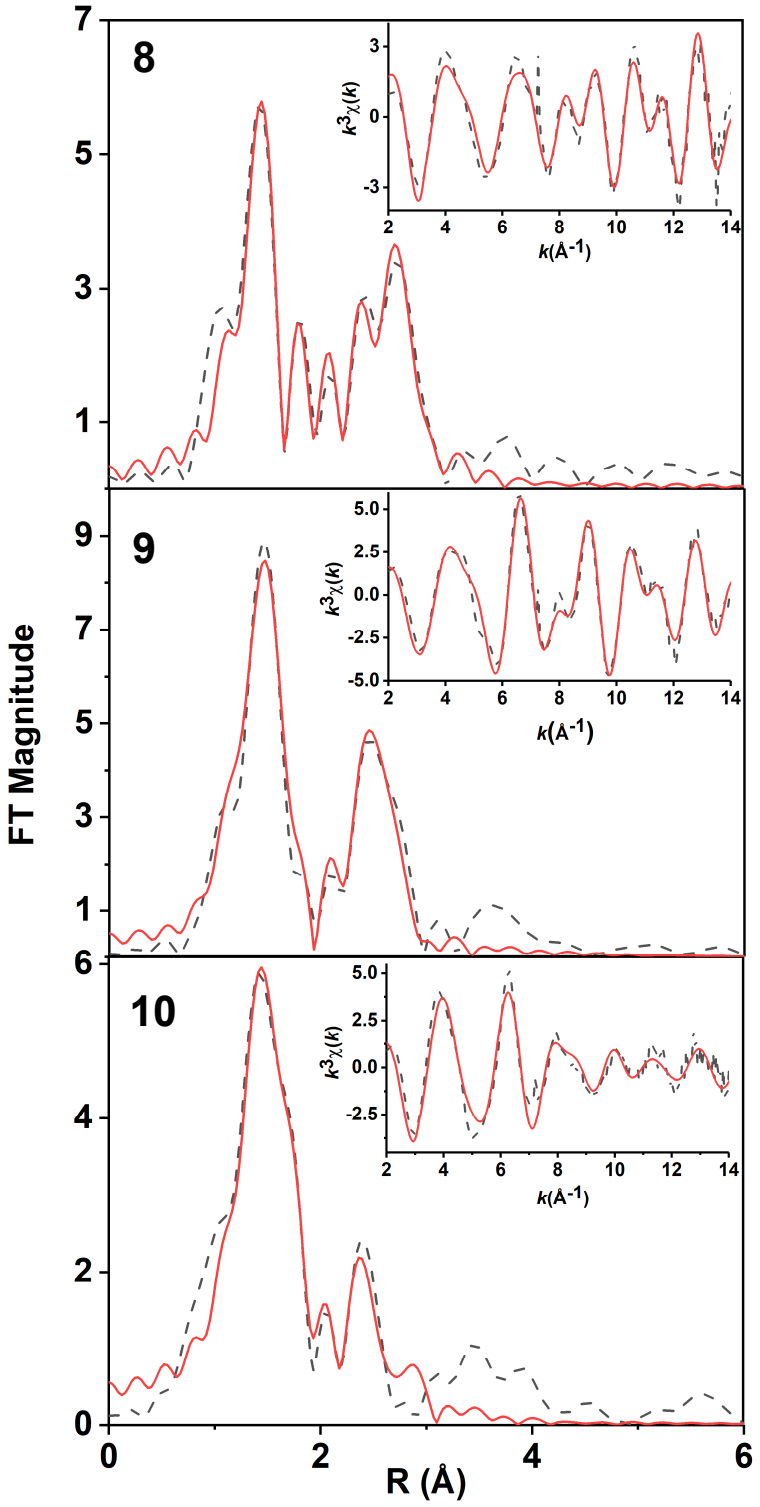

Figure 3.10 - Best fit to k^3-weighted EXAFS of **8** (top), **9** (middle), and **10** (bottom), reported in R-space and k-space (inset). Experimental data are shown as dashed lines, best fits are shown as solid lines.

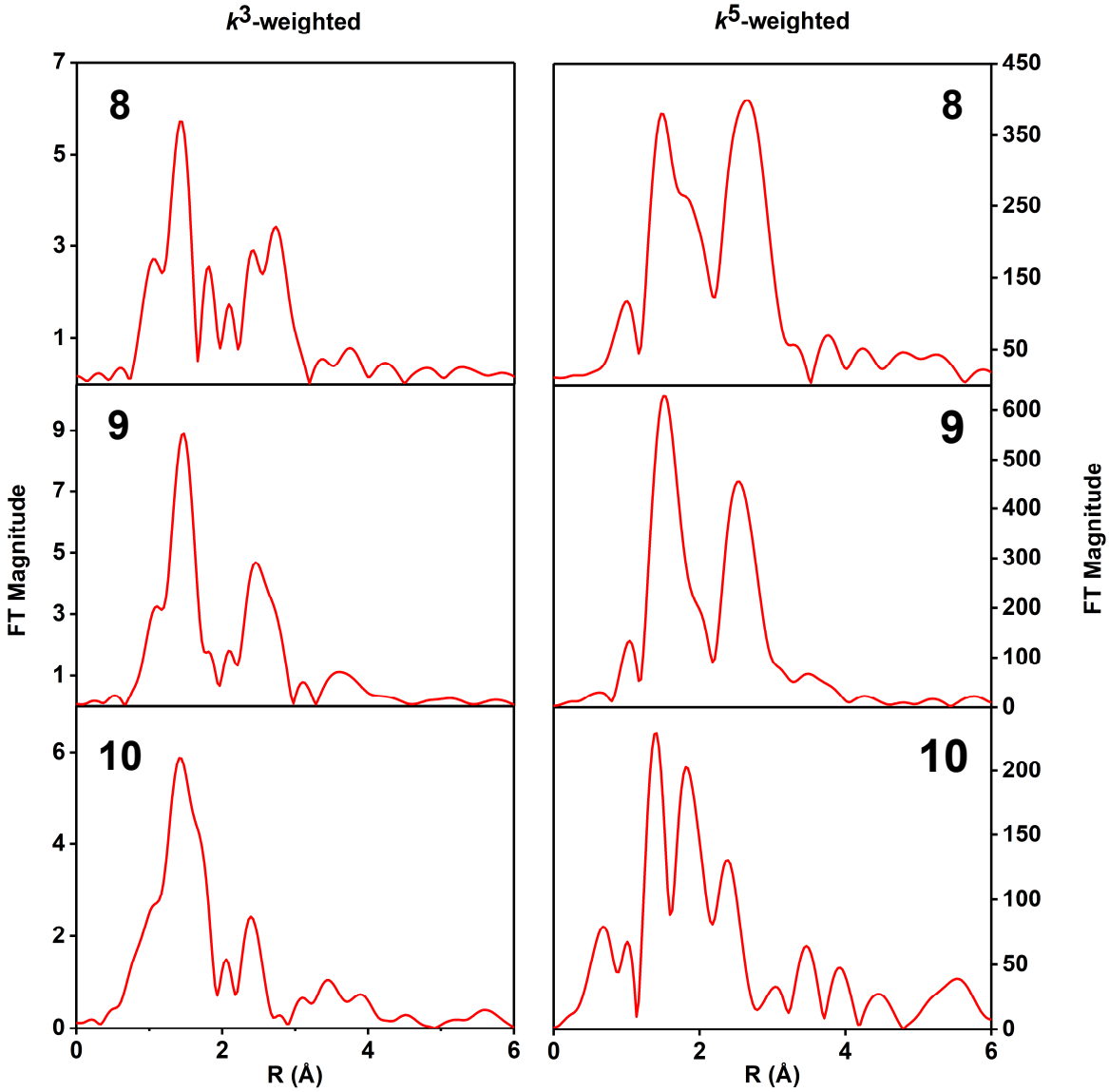

Figure 3.11 - Comparison between the k^3-weighted (left) and k^5-weighted (right) Fourier trasforms in the EXAFS analysis of **8**, **9**, **10.**

3.6 DFT Calculations

Quantum chemical calculations at the DFT uBP86-D3-cc-pVTZ (C, H, N, O) / SDD (Ni) level of theory were performed to give theoretical support for the XAS-measured structures and geometries of complexes **8**, **9**, and **10** and their homologous μ-oxo-bridged complexes **8-oxo**, **9-oxo**, and **10-oxo**. The geometry optimized structures of the μ-oxo complexes **8-oxo**, **9-oxo** and **10-oxo** (Table 3.1, A-3.19–3.21) showed that the average Ni–O bond lengths were 1.79 Å which is shorter (0.08-0.24 Å) than what was measured and computationally predicted for hydroxide complexes **8**, **9**, and **10** (Tables 3.1–3.2, Figure 3.12). Furthermore, the Ni···Ni distances were predicted to be 2.68 (**8-oxo**), 2.69 (**9-oxo**), and 2.70 (**10-oxo**) Å, which are again significantly shorter by about 0.27-0.40 Å compared to those predicted and measured for hydroxide complexes **8**, **9**, and **10** (Table 3.1–3.2). This provides convincing proof that the hydroxide ligand has been maintained in complexes **9** and **10**.

We then used DFT calculations to understand the Ni-ligand coordination number and geometry in complexes **9** and **10**. The single crystal X-ray molecular structure of **8** reveals two possible hydroxide orientations causing a seesaw or planar Ni(μ-OH)$_2$Ni core (Figures A-3.14, A-3.15, Table 3.2). The geometry optimised structures of **8**, **9**, and **10** exhibit the seesaw configuration to be more stable by 2.01 kcal·mol^{-1} for **8**, 1.44 kcal·mol^{-1} for **9**, while for **10** the seesaw configuration was the only structure obtained (Figures A-3.14, A-3.16, A-3.18). The differences in Ni–O and Ni–N bond lengths in the planar or seesaw configurations were small (Table 3.2) indicating that the exact configuration was not consequential for an understanding of the EXAFS results.

Geometry optimizations with or without one DMF coordinated to **9** have been performed (Table 3.2). A better match with the EXAFS results was obtained for the structure without a DMF ligand bound to the complex, which is also consistent with the XANES results that indicated a square planar coordination environment around the Ni ions. DFT thus supports the postulate that the Ni ions remain four-coordinate upon one electron oxidation of **8** to yield **9**. The average Ni–N/O and Ni···Ni distances (Table 3.2) of geometry optimized structures for **10**, without a DMF ligand bound to the Ni ions, were slightly shorter when compared to the results found by EXAFS (Table 3.1). The geometry optimized structure of **10** *with* coordinated DMF molecules (see supporting information for details on Ni/DMF interaction, Table 3.2) was instead in very good agreement with the EXAFS

findings. Overall, DFT confirms the structures of **9** and **10** contain bis-μ-hydroxide cores, and affirms the EXAFS predicted Ni-ligand and Ni···Ni distances (Table 3.1).

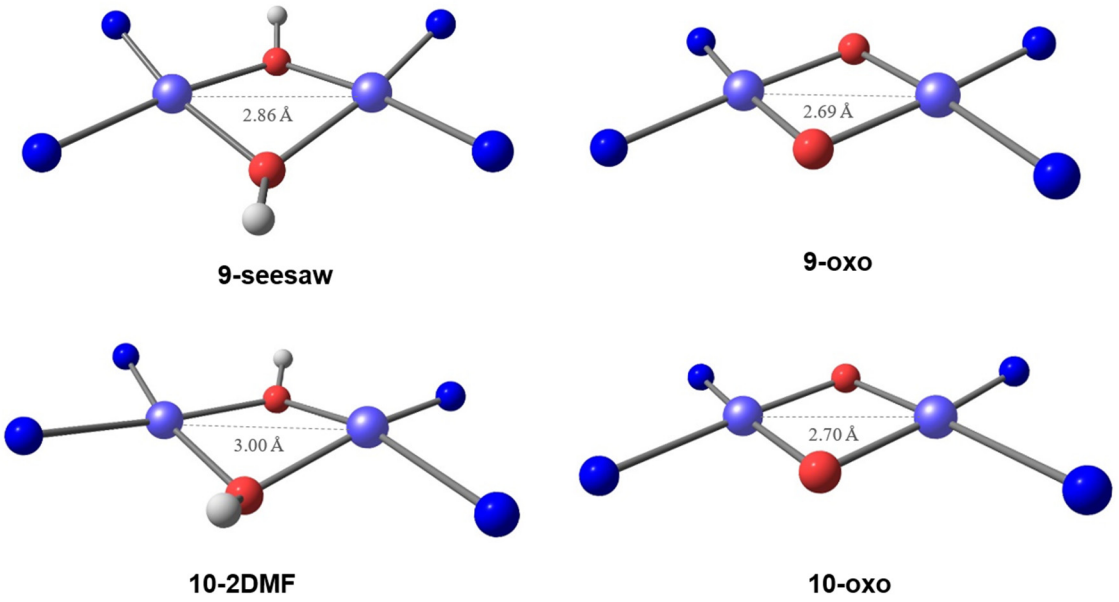

Figure 3.12 - DFT optimised molecular structures for **9-seesaw**, **10-2DMF** and the homologous oxo counterpart **9-oxo** and **10-oxo**. Ligand backbone and coordinating DMF molecules omitted for clarity

Table 3.2 - Average atom-atom distances for the geometry optimized **hydroxide** structures (in Å).

	8-plane	**8-seesaw**	**9-plane**	**9-seesaw**	**9-DMF**	**10-seesaw**	**10-2DMF**
Ni–N	1.895	1.908	1.860	1.865	1.893	1.845	1.897
Ni–O(H)	1.945	1.897	1.877	1.879	1.944	1.880	1.938
Ni–O_{DMF}					2.205		2.072
Ni···Ni	3.012	2.939	2.916	2.861	2.978	2.888	2.999
Ni···C	2.841	2.857	2.839	2.847	2.836	2.810	2.880

Regarding the density of spin, the Mulliken spin density plot for **9** showed spin density located at both Ni cores (0.33, 0.34) with predominant d_{xz} character (Figure A-3.13). For **10** calculations showed that both the $S = 1$ and $S = 0$ states were stable (Figure A-3.23), with neglible difference in energy (0.12 kcal·mol^{-1}). The Mulliken spin density plots for **10** showed two Ni^{III} centers (triplet: 0.909, 0.918; singlet: 0.900, -0.912) with mainly d_{z2} character (Figures 3.13).

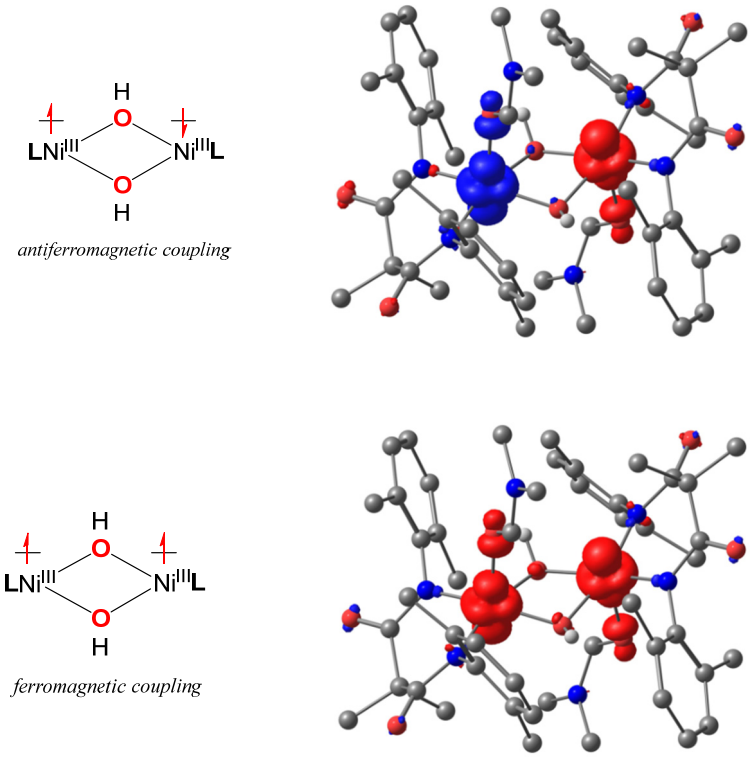

Figure 3.13 - Geometry optimised structures of **10** (anti-ferromagnetic coupled singlet and ferro-magnetic coupled triplet) at an iso-value of 0.01 a.u., with electron spin density plotted. H- atoms omitted for clarity, except those associated with the μ-hydroxide ligands.

3.6.1 Topological analysis of 10-2DMF

In **10-2DMF** (Figure A-3.23), the average Ni–O/N bond length was 1.94 Å and lies at the edge of the sum of the covalent radii (1.90(4) Å),[41] whereas the average Ni-ODMF distance (2.07 Å) was longer, further analysis allowed us to define this Ni/DMF interaction as a bond (see supporting information for details). To gain insight into the nature of the

Ni–ODMF interaction, we performed a topological analysis (atoms in molecules, AIM)[42] of the wave function. This confirms the presence of Ni–O bonds by the identification of bond critical points (BCPs). The relative low electron density at the BCPs (ρ(rb): Ni–OH: 0.089; Ni–ODMF: 0.061 a.u.) together with a positive Laplacian of electron density ($\nabla^2\rho$(rb): Ni–OH: 0.483; Ni–ODMF: 0.353 a.u.) are indicative of a closed shell interaction.[43-45] The similar modulus of the Lagrangian kinetic energy density (G(rb): Ni–OH: 0.131; Ni–ODMF: 0.087 a.u.) and potential energy density (V(rb): Ni–OH: 0.141; Ni–ODMF: 0.085 a.u.) supports a closed shell interaction (G(rb) ≅ |V(rb)|). The electron energy density (H(rb)) for the Ni-OH bonds is negative (-0.010 a.u.), whereas for the Ni-ODMF bond it is slightly positive (0.002 a.u.). This founding is characteristic for a donor-acceptor Ni-OH bond with ionic contribution and a pronounced ionic interaction with a donor-acceptor contribution for Ni···ODMF.[46]

3.7 Conclusions

In this chapter we reported the successful synthesis and characterisation of a new $Ni^{II}_2(\mu\text{-}OH)_2$ (**8**) supported by a novel malonamidate ligand, (**6**). The dinuclear species **8** contained a diamond core structure composed of two Ni atoms and two bridging hydroxide ligands which lie in a distorted square planar environment. Cyclic voltammetry showed the presence of two accessible higher oxidation states that were explored by chemical oxidation, leading to the conversion of **8** to the mixed valent $Ni^{II}Ni^{III}(\mu\text{-}OH)_2$ species **9** and the high valent $Ni^{III}_2(\mu\text{-}OH)_2$ species **10**. EPR, Ni K-edge absorption spectroscopy and DFT calculations supported the proposed oxidation states and the structures of species **9** and **10**, confirming that the bridging hydroxide ligands are maintained despite the increase in oxidation state. In the light of these results, species **9** and **10** represent, to the best of our knowledge, the first examples of mixed valent $Ni^{II}Ni^{III}(\mu\text{-}OH)_2$ and high valent $Ni^{III}(\mu\text{-}OH)_2$ complexes reported to date. The subsequent step will be the study of the reactivity properties of species **9** and **10** towards oxidation of O/C−H, that will be analysed in Chapter 4.

3.8 Experimental Section - Chapter 3

Physical Methods

^{1}H, ^{13}C, and heteronuclear nuclear magnetic resonance (NMR) analyses were performed on an Agilent MR 400 MHz (400.13 MHz for ^{1}H-NMR and 100.61 MHz for ^{13}C-NMR). Fourier transform infra-red (FT-IR) spectra were recorded using a Perkin Elmer Spectrum 100 FT-IR/ATR. Electrospray ionisation mass spectrometry (ESI-MS) analyses were performed using a Micromass Time of Flight (ToF), interfaced with a Waters 2690 HPLC. Cyclic voltammetry (CV) experiments have been conducted with a CH Instrument 600E electrochemical analyser, using a GC working electrode, a Pt wire counter electrode, and an Ag/AgNO$_3$ 0.01 M reference electrode. Electronic absorption spectra were recorded on an Agilent 8453 diode array spectrophotometer (190-1100 nm range) equipped with a cryostat unit from Unisoku Scientific Instruments (Osaka, Japan).

Materials and synthesis

All reactions with air-sensitive or water-sensitive materials were performed under an inert atmosphere. Both Schlenk techniques and a nitrogen atmosphere glovebox have been used. Reagents and solvents were purchased from commercial suppliers and have been used as received, unless otherwise stated. Both anhydrous diethyl ether (Et$_2$O) and anhydrous tetrahydrofuran (THF) were distilled over Na/Benzophenone and stored in a Schlenk bomb prior to use.

Synthesis of [Ni(DMSO)$_6$](ClO$_4$)$_2$

Although no problems were encountered during the syntheses reported herein, perchlorate salts are potentially explosive and should be handled with care.

The synthesis was adapted from the original reported by Cotton.[16] The hydrated perchlorate nickel salt Ni(ClO$_4$)$_2$•6H$_2$O (528.4 mg, 1.44 mmol) was dissolved in dimethyl sulfoxide (DMSO) (25 mL), resulting in a pale green-yellow solution. An excess of Et$_2$O

was added, and the solution was stirred vigorously in order to precipitate the product as a fine pale green powder. The product was filtered and purified by recrystallization in acetone, giving pale green needle-like crystals in 64% yield (667 mg, Figure A-3.1)

ν_{max} (FT-IR)/cm^{-1}: 3007 (C-H), 2920 (C-H) 1440, 1404 (C-H), 1314 (C-H), 1083 (Cl-O), 1001 (C-H), 952 (S-O), 717 (C-S), 622 (Cl-O).

Synthesis of 8

Each step of the synthesis of this complex was performed under an inert atmosphere (Ar) using Schlenk techniques. **6** (251.8 mg, 0.74 mmol) was dissolved in THF (5 mL), ^{n}BuLi (1.2 mL, 1.6 M in hexane, 1.92 mmol, 2.6 equiv., ^{n}Bu = n-butyl) was added to this solution, causing an immediate colour change from colourless to yellow. The subsequent addition of [Ni(DMSO)$_6$](ClO$_4$)$_2$ (540.4 mg, 0.74 mmol, 1 equiv.) caused a slow colour change to dark purple, with the formation of the lithium salt of the complex as a purple precipitate over 12 h. After filtration over a glass frit, the obtained solid was washed with THF (3 × 5 mL) and then acetone (3 × 5 mL) and dried under vacuum. The final product **8** was obtained as a purple powder (223.8 mg, 84%). Crystals suitable for X-ray diffraction were obtained by cation metathesis upon addition of tetraethylammonium perchlorate (Et$_4$NClO$_4$) and recrystallization from DMF/Et$_2$O.

δ ^{1}*H* (400 MHz, [D$_6$]-DMSO): -9.34 (2H, s, -*OH*), 1.91 (12H, s, -C*H*$_3$), 2.19 (24H, s, Ar-C*H*$_3$), 6.54 (12H, m, Ar-C*H*).

δ ^{13}*C* (100 MHz, [D$_6$]-DMSO): 19.25 (*C*H$_3$), 28.47 (*C*H$_3$), 48.92 (*C*q), 121.362 (*p*-*C*H), 127.13 (*m*-*C*H), 133.81 (*o*-*C*q), 146.84 (Cq), 174.64 (*C*=O).

ν_{max} (FT-IR)/cm^{-1}: 3615 (O-H), 2988, 2969, 2922, 1655(C=O), 1596, 1554, 1458, 1431, 1366, 1257, 1226, 1206, 1148, 1100, 1039, 985, 896, 832, 762, 732, 681, 600.

λ_{max} (DMF)/nm: 355 (ε = 1700 dm^{3}mol^{-1}cm^{-1}) 500 (ε = 450 dm^{3}mol^{-1}cm^{-1})

ESI-MS (m/Z): Found: 411.1225 ([Ni^{II}(OH)(**L**)]$_2^{2-}$. C$_{42}$H$_{50}$N$_4$Ni$_2$O$_6^{2-}$ requires 411.1224)

Preparation of 9

To a solution of **8 (**2 mL, 0.2 mM in DMF) cooled to -45 °C in a quartz cuvette was added CAN ($(NH_4)_2[Ce^{IV}(NO_3)_6]$, 40 μL, 0.01 M, CH_3CN) under continuous stirring. An immediate and stark colour change was observed. Monitoring by electronic absorption spectroscopy showed the appearance of two intense bands (λ_{max} = 560 nm, λ_{max} = 430 nm) corresponding to the formation of the mixed-valent species **9**. The reaction reached its maximum yield after 10 s.

Preparation of 10

To a solution of **8** (2 mL, 0.2 mM in DMF) cooled to -45 °C in a quartz cuvette was added CAN ($(NH_4)_2[Ce^{IV}(NO_3)_6]$, 40 μL, 0.034 M, CH_3CN) under continuous stirring. An immediate and stark colour change was observed. Monitoring by electronic absorption spectroscopy showed the appearance of an intense band (λ_{max} = 600 nm) corresponding to the formation of the high-valent species **10**. The reaction reached its maximum yield after 10 s.

X-Ray diffraction experimental data

X-ray structural analysis **8** were performed on a Bruker D8 Quest ECO at 100(2) K with an Oxford Cryostream, with the sample mounted on a MiTeGen microloop using Mo Kα radiation (λ = 0.71073 Å). Bruker APEX[47] software was used to collect and reduce data and determine the space group. Absorption corrections were applied using SADABS.[48] Structures were solved with the XT structure solution program[49] using Intrinsic Phasing and refined with the XL refinement package[50] using Least Squares minimisation in Ole2.[51] All non-hydrogen atoms were refined anisotropically.

The solvent N,N-dimethylformamide (DMF) molecule is disordered over a mirror plane with partial occupancy (1/4). The disordered group was treated with rigid model refinement with restraints (SIMU). Crystallographic data for the structure in this paper have been deposited with the Cambridge Crystallographic Data Centre as supplementary

publication # 1878992. Copies of the data can be obtained, free of charge, on application to CCDC, 12 Union Road,

Cambridge CB2 1EZ, UK, (fax: +44-(0)1223-336033 or e-mail:deposit@ccdc.cam.ac.uk).

Table 3.3 - Crystal Data and Structure Refinement for **8**.

Empirical formula	$C_{61}H_{97}N_7Ni_2O_7$	**μ/mm^{-1}**	0.610
Formula weight	1157.87	**F(000)**	2496
Temperature/K	100(2)	**Crystal size/mm^3**	0.32 × 0.19 × 0.19
Crystal system	Orthorhombic	**Radiation**	MoKα (λ = 0.71073)
Space group	Cmca	**2Θ range for data collection/°**	5.054 to 58.538
a/Å	21.5193(6)	**Index ranges**	-29 ≤ h ≤ 27, -16 ≤ k ≤ 17, -33 ≤ l ≤ 25
b/Å	12.8631(4)		
c/Å	24.3395(7)	**Reflections collected**	61426
α/°	90	**Independent reflections**	4707 [R_{int} = 0.0565]
β/°	90	**Data/restraints/parameters**	4707/ 30/ 227
γ/°	90	**Goodness-of-fit on F^2**	1.069
Volume/Å^3	6737.3(3)	**Final R indexes [I>=2σ (I)]**	R_1 = 0.0532, wR_2 = 0.1459
Z	4	**Final R indexes [all data]**	R_1 = 0.0703, wR_2 = 0.1602
ρ_{calc}g/cm^3	1.142	**Largest diff. peak/hole / e Å^{-3}**	1.203/-1.517

Electron paramagnetic resonance

Electron paramagnetic resonance (EPR) spectra of frozen solutions were acquired on a Bruker EMX X-band EPR, equipped with an Oxford Instruments CE 5396, ESR9 Continuous Flow Cryostat, a precision Temperature Controller and an Oxford Instruments

TTL20.0/13 Transfer Tube. EPR samples were prepared by freezing the EPR tubes containing the analyte solutions, previously prepared at the cryostat as listed below, in liquid nitrogen. EPR-monitored titration spectra were recorded at 77 K, 9.2 GHz, 6.36 mW microwave power, with a 120 mT field sweep in 168 s, and 0.3 mT field modulation amplitude. The EPR spectrum of **9** was recorded at 77 K, 9.2 GHz, 2.01 mW microwave power, with a 100 mT field sweep in 84 s, and 0.3 mT field modulation amplitude. Integration, simulation, and fitting were performed with Matlab and the easySpin computational package.[52] The simulation was modelled as $S = ½$ electron spin with axial g tensor with inhomogeneous line broadening. The oxidation yield of sample **9** was calculated by quantification of the concentration of spin in the samples. This was obtained by comparison of the double integral of the signals to that of a reference frozen 0.8 mM DMF solution of (2,2,6,6-tetramethyl-piperidin-1-yl)oxyl (TEMPO), measured under the same conditions.

X-ray Absorption Spectroscopy

The Ni-K-edge X-ray absorption data were collected on beam line 7-3 at SSRL (*Stanford Synchrotron Radiation Lightsource*, SLAC National Accelerator Lab, Menlo Park, CA, USA). Data were collected with the storage ring operating at ca. 3 GeV and 500 mA, using a LN_2 cooled Si (220), $\phi = 0^\circ$ double-crystal monochromator, calibrated by using the first inflection point of a Ni foil (8333.0 eV). The monochromator was detuned by ~30% for higher harmonic rejection. The fluorescence detector used was a Canberra 30-element Ge solid state detector. All the measurements were performed at ambient pressure at ~17 K, gained by an Oxford Helium cryostat, cooled by closed-cycle He gas loop. The parameters used for the scans were the following: 10 eV steps/1 second integration time in the pre-edge region, 0.3 eV steps/2 second integration time in the edge, and 0.05 k steps in the EXAFS, with integration time increasing in a k^2-weighted fashion from 2 to 9 s over the energy range (k_{max} = 15.1 k). The total detector counts were in the range between 20 k - 35 k, well within the linear range of the detector electronics. Each sample was monitored for radiation damage, using different spots where required to expose fresh sample. The samples were measured as frozen solutions using a Delrin® Mössbauer/XAS cups with a sample window of 4 mm x 10 mm. In the case of **9** and **10**, the samples were prepared by transferring the solution (~3 mM in DMF) from the cryostat (-45 °C) to a

XAS sample cup pre-cooled in a liquid nitrogen bath. For **8**, a dispersion of the complex in Nujol (13.5 mg in 1 mL) was prepared, then transferred into an XAS cup and frozen in a liquid nitrogen bath.

Elaboration of the XAS data, including averaging, background removal and normalization, was performed using Athena.[53] Edge energies were determined as the half-height of the white-line intensity. Peak fitting of the pre-edge regions was performed using one or more *pseudo*-Voigt functions with a fixed 50:50 Gaussian:Lorentzian ratio. EXAFS analysis was carried out using Artemis,[53] which incorporates the IFEFFIT fitting engine and FEFF6 for *ab initio* EXAFS phase and amplitude parameters. Crystal structures (either as-is or modified slightly to test different structural models) were used for FEFF6 input to identify significant paths. Fits of **8**, **9**, and **10** are reported in the following tables. For a given shell in all simulations, the coordination number n was fixed, while r and σ^2 were allowed to float. The amplitude reduction factor S_0^2 was fixed at 0.9, while the edge shift parameter ΔE_0 was allowed to float at a single common value for all shells. The fit was evaluated in k^3-weighted R-space, and fit quality was judged by the reported R-factor and reduced χ^2. Significant fits are highlighted in bold and reported in k^3-weighted R-space.

Electrochemistry

Cyclic voltammetry experiments were conducted on a 5.5 mM solution of **8** in DMF at room temperature. n-Bu_4NPF_6 (0.1 M) was used as the supporting electrolyte. Glassy carbon was used as the working electrode and 0.01 M Ag/$AgNO_3$ was used as the reference electrode. Platinum wire was used as the counter electrode. Scan rates of 25 mV/s – 100 mV/s were used. Potentials were referenced against the Fc^+/Fc couple (Fc = ferrocene). The voltammograms of Fc were acquired under the same solvent and scan rate conditions.

DFT Calculations

For the computational analyses of compounds **8**, **9**, and **10**, the atomic coordinates from the crystallographically determined molecular structure of **8** were used as the starting geometry. According to the crystal structure, two different starting geometries were possible

(planar or seesaw Ni(μ-O_2)Ni core). The geometry optimization was carried out with Gaussian16[54] using a DFT-unrestricted BP86 functional and cc-pVTZ basis set for C, H, N, and O atoms and SDD for the Ni atoms including Grimme's dispersion with the original D3 damping function.[55] The antiferromagnetic coupling singlet state at **10-2DMF** was modulated by fragmentation of the molecule into four fragments (2: $[(L)Ni^{III}]^+$, 2: OH^-) and assigning duplet states to $[(L)Ni^{III}]^+$ with alpha or beta spin, respectively. A final stability calculation gave proof of a stable wave function. Spin population calculations and topological analysis (atoms in molecules, AIM) were performed using Multiwfn.[56] The graphical representations were created using ChemCraft.[57]

3.9 References

(1) G. Spedalotto, R. Gericke, M. Lovisari, E. R. Farquhar, B. Twamley and A. R. McDonald, *Chem. Eur. J.*, 2019, **25**, 11983-11990.
(2) Y. Matoba, T. Kumagai, A. Yamamoto, H. Yoshitsu and M. Sugiyama, *J. Biol. Chem.*, 2006, **281**, 8981-8990.
(3) G. E. Cutsail, 3rd, R. Banerjee, A. Zhou, L. Que, Jr., J. D. Lipscomb and S. DeBeer, *J. Am. Chem. Soc.*, 2018, **140**, 16807-16820.
(4) S. Itoh, H. Bandoh, S. Nagatomo, T. Kitagawa and S. Fukuzumi, *J. Am. Chem. Soc.*, 1999, **121**, 8945-8946.
(5) K. Honda, J. Cho, T. Matsumoto, J. Roh, H. Furutachi, T. Tosha, M. Kubo, S. Fujinami, T. Ogura, T. Kitagawa and M. Suzuki, *Angew. Chem. Int. Ed.*, 2009, **48**, 3304-3307.
(6) S. Mahapatra, J. A. Halfen, E. C. Wilkinson, G. Pan, X. Wang, V. G. Young, C. J. Cramer, L. Que and W. B. Tolman, *J. Am. Chem. Soc.*, 1996, **118**, 11555-11574.
(7) P. L. Holland, C. J. Cramer, E. C. Wilkinson, S. Mahapatra, K. R. Rodgers, S. Itoh, M. Taki, S. Fukuzumi, L. Que and W. B. Tolman, *J. Am. Chem. Soc.*, 2000, **122**, 792-802.
(8) L. Que Jr and W. B. Tolman, *Angew. Chem. Int. Ed.*, 2002, **41**, 1114-1137.
(9) A. Kochem, F. Gennarini, M. Yemloul, M. Orio, N. Le Poul, E. Rivière, M. Giorgi, B. Faure, Y. Le Mest, M. Réglier and A. J. Simaan, *ChemPlusChem*, 2017, **82**, 615-624.
(10) D. Lee and S. J. Lippard, *J. Am. Chem. Soc.*, 2001, **123**, 4611-4612.
(11) D. Lee and S. J. Lippard, *J. Am. Chem. Soc.*, 1998, **120**, 12153-12154.
(12) C.-C. Ou, R. A. Lalancette, J. A. Potenza and H. J. Schugar, *J. Am. Chem. Soc.*, 1978, **100**, 2053-2057.
(13) M. R. Halvagar, P. V. Solntsev, H. Lim, B. Hedman, K. O. Hodgson, E. I. Solomon, C. J. Cramer and W. B. Tolman, *J. Am. Chem. Soc.*, 2014, **136**, 7269-7272.
(14) J. A. Isaac, A. Thibon-Pourret, A. Durand, C. Philouze, N. Le Poul and C. Belle, *Chem. Commun.*, 2019, **55**, 12711-12714.
(15) A. W. Pierpont and T. R. Cundari, *Inorg. Chem.*, 2010, **49**, 2038-2046.
(16) F. Cotton and R. Francis, *J. Am. Chem. Soc.*, 1960, **82**, 2986-2991.
(17) L. Yang, D. R. Powell and R. P. Houser, *Dalton Trans.*, 2007, 955-964.

(18) Y. Li, L. Jiang, L. Wang, H. Gao, F. Zhu and Q. Wu, *Appl. Organomet. Chem.*, 2006, **20**, 181-186.
(19) S. Itoh, H. Bandoh, M. Nakagawa, S. Nagatomo, T. Kitagawa, K. D. Karlin and S. Fukuzumi, *J. Am. Chem. Soc.*, 2001, **123**, 11168-11178.
(20) C. Jaeheung, F. Hideki, F. Shuhei and S. Masatatsu, *Angew. Chem. Int. Ed.*, 2004, **43**, 3300-3303.
(21) R. M. Silverstein, F. X. Webster, D. J. Kiemle and D. L. Bryce, *Spectrometric identification of organic compounds*, John Wiley & Sons, 8th edn., 2014.
(22) E. Carmona, J. M. Marin, P. Palma, M. Paneque and M. L. Poveda, *Inorg. Chem.*, 1989, **28**, 1895-1900.
(23) N. Kitajima, S. Hikichi, M. Tanaka and Y. Morooka, *J. Am. Chem. Soc.*, 1993, **115**, 5496-5508.
(24) J. Ferrando-Soria, O. Fabelo, M. Castellano, J. Cano, S. Fordham and H. C. Zhou, *Chem. Commun.*, 2015, **51**, 13381-13384.
(25) P. Pirovano, E. R. Farquhar, M. Swart and A. R. McDonald, *J. Am. Chem. Soc.*, 2016, **138**, 14362-14370.
(26) T. Corona, F. F. Pfaff, F. Acuna-Pares, A. Draksharapu, C. J. Whiteoak, V. Martin-Diaconescu, J. Lloret-Fillol, W. R. Browne, K. Ray and A. Company, *Chem. Eur. J.*, 2015, **21**, 15029-15038.
(27) Y. Morimoto, Y. Takagi, T. Saito, T. Ohta, T. Ogura, N. Tohnai, M. Nakano and S. Itoh, *Angew. Chem. Int. Ed.*, 2018, **57**, 7640-7643.
(28) R. Schenker, B. S. Mandimutsira, C. G. Riordan and T. C. Brunold, *J. Am. Chem. Soc.*, 2002, **124**, 13842-13855.
(29) R. I. Haines and A. McAuley, *Coord. Chem. Rev.*, 1981, **39**, 77-119.
(30) S. A. Jacobs and D. W. Margerum, *Inorg. Chem.*, 1984, **23**, 1195-1201.
(31) G. J. Colpas, M. J. Maroney, C. Bagyinka, M. Kumar, W. S. Willis, S. L. Suib, P. K. Mascharak and N. Baidya, *Inorg. Chem.*, 1991, **30**, 920-928.
(32) P. Mondal, P. Pirovano, A. Das, E. R. Farquhar and A. R. McDonald, *J. Am. Chem. Soc.*, 2018, **140**, 1834-1841.
(33) S. Kundu, F. F. Pfaff, E. Miceli, I. Zaharieva, C. Herwig, S. Yao, E. R. Farquhar, U. Kuhlmann, E. Bill, P. Hildebrandt, H. Dau, M. Driess, C. Limberg and K. Ray, *Angew. Chem. Int. Ed.*, 2013, **52**, 5622-5626.
(34) A. Roe, D. Schneider, R. Mayer, J. Pyrz, J. Widom and L. Que Jr, *J. Am. Chem. Soc.*, 1984, **106**, 1676-1681.
(35) G. Shulman, Y. Yafet, P. Eisenberger and W. Blumberg, *Proc. Natl. Acad. Sci.*, 1976, **73**, 1384-1388.
(36) J. Cho, R. Sarangi, J. Annaraj, S. Y. Kim, M. Kubo, T. Ogura, E. I. Solomon and W. Nam, *Nat. Chem.*, 2009, **1**, 568.
(37) L. R. Furenlid, M. W. Renner and E. Fujita, *Physica B Condens. Matter*, 1995, **208**, 739-742.
(38) R. A. Scott and M. K. Eidsness, *Comments Inorg. Chem.*, 1988, **7**, 235-267.
(39) K. Shiren, S. Ogo, S. Fujinami, H. Hayashi, M. Suzuki, A. Uehara, Y. Watanabe and Y. Moro-oka, *J. Am. Chem. Soc.*, 2000, **122**, 254-262.
(40) S. Hikichi, M. Yoshizawa, Y. Sasakura, M. Akita and Y. Moro-oka, *J. Am. Chem. Soc.*, 1998, **120**, 10567-10568.
(41) B. Cordero, V. Gómez, A. E. Platero-Prats, M. Revés, J. Echeverría, E. Cremades, F. Barragán and S. Alvarez, *Dalton Trans.*, 2008, 2832-2838.
(42) R. F. W. Bader, *Atoms in Molecules*, Clarendon Press, Oxford, 1994.
(43) R. Bianchi, G. Gervasio and D. Marabello, *Inorg. Chem.*, 2000, **39**, 2360-2366.
(44) R. Bianchi, G. Gervasio and D. Marabello, *C. R. Chim.*, 2005, **8**, 1392-1399.
(45) L. Ehrlich, R. Gericke, E. Brendler and J. Wagler, *Inorganics*, 2018, **6**, 119.
(46) E. Espinosa, I. Alkorta, J. Elguero and E. Molins, *J. Chem. Phys.*, 2002, **117**, 5529-5542.
(47) Bruker (2015). APEX3 v2015.9-0, Bruker AXS Inc., Madison, WI, USA.
(48) Bruker (2014/5). SADABS, Bruker AXS Inc., Madison, Wisconsin, USA.

(49) G. Sheldrick, *Acta Cryst. A*, 2015, **71**, 3-8.
(50) G. Sheldrick, *Acta Cryst. A*, 2008, **64**, 112-122.
(51) O. V. Dolomanov, L. J. Bourhis, R. J. Gildea, J. A. K. Howard and H. Puschmann, *J. Appl. Crystallogr.*, 2009, **42**, 339-341.
(52) S. Stoll and A. Schweiger, *J. Magn. Reson., Ser A*, 2006, **178**, 42-55.
(53) B. Ravel and M. Newville, *J. Synchrotron Radiat.*, 2005, **12**, 537-541.
(54) Gaussian 16 Rev. B.01
(55) S. Grimme, J. Antony, S. Ehrlich and H. Krieg, *J. Chem. Phys.*, 2010, **132**, 154104.
(56) T. Lu and F. Chen, *J. Comput. Chem.*, 2012, **33**, 580-592.
(57) Chemcraft ver.1.8 (Build164) 2016. Available online: http://www.chemcraftprog.com.

Chapter 4

Reactivity studies of mixed $Ni^{II}Ni^{III}$ and high valent Ni_2^{III} bis-μ-hydroxo species

The EPR measurements were performed by Marta Lovisari (Trinity College Dublin)

4.1 Introduction

In the previous chapter we reported the synthesis of the hydroxide bridged $Ni^{II}Ni^{III}$ (**9**) and Ni_2^{III} complexes (**10**, Scheme 3.1) starting from the precursor **8**. Thorough characterization of the two species were performed, confirming that the bridging hydroxide groups are retained in **9** and **10** despite the change in oxidation state. In particular, species **10** represents, at the best of our knowledge, the first example of high valent Ni_2^{III} bis(μ-hydroxide) complex reported so far.

In this chapter, we will explore the reactivity of **9** and **10** testing their capability to activate O–H and C–H bonds, alongside their oxygen atom transfer properties. Emphasis will be put on elucidation of the mechanism involved in the reactivity pathways of the above-mentioned species, investigating the identity of the possible intermediates through chemical and spectroscopic means.

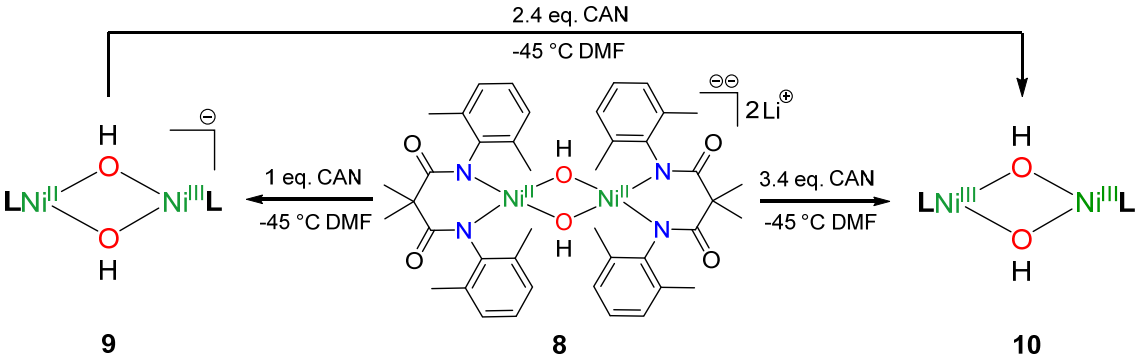

Scheme 4.1. Preparation of **9** and **10** by oxidation of **8** with CAN at -45 °C.

4.2 Reactivity towards O–H bonds

4.2.1 Preliminary Studies

The oxidation reactivity of both species **10** and **9** towards substrates containing weak O–H bonds was preliminarily tested by reaction of the two species with 2,4-di-*tert*-butyl phenol (2,4-DTBP) at -45 °C in N,N-dimethylformamide (DMF). The kinetics of the reactions were studied by electronic absorption spectroscopy, monitoring the feature at λ_{max} = 600 nm for **10** (Figure 4.1) and λ_{max} = 560 nm for **9** (Figure 4.3). The decay of each species upon reaction with the substrate was fitted as *pseudo*-first order, yielding a k_{obs} value. A plot of k_{obs} against the concentration of substrate resulted in the second order rate constant (k_2). An important observation was that upon reaction of **10** with an external substrate, the formation of a species with similar spectral features of **9**, called **9'**, was observed (Figure 4.2). **9'** decayed further at a significantly lower rate, after **10** had decayed. Such behaviour of **10** resulted in a biphasic decay curve (Figure 4.3). We measured the kinetics of substrate oxidation of **10** and **9** independently, by preparing them separately. The data reported as **10** refers to the first phase of decay only, correlated with a one electron process. The decay of **9'** (*i.e.* the second phase of the decay of **10**, see Figure 4.3) was also analysed, in order to fully understand the reaction mechanism involved.

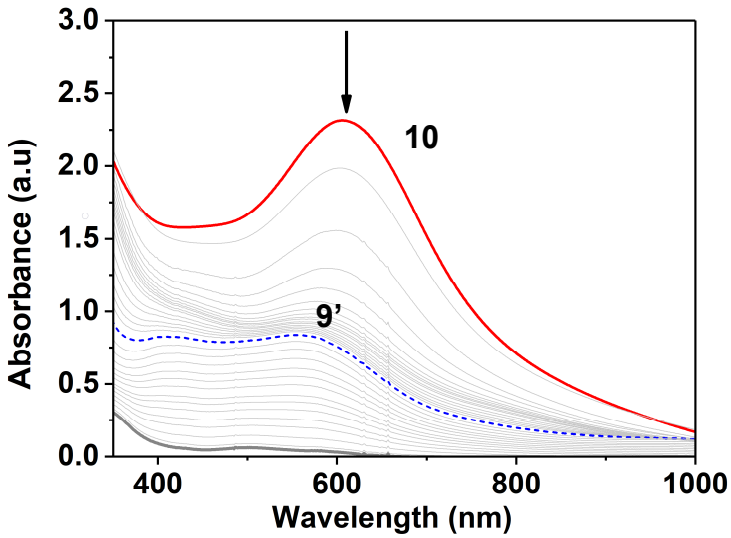

Figure 4.1 - Electronic absorption spectrum showing the decay of **10** (red trace) upon reaction with 2,4-DTBP (100 equiv.) and the formation of **9'** (blue dashed trace)**.** Reaction performed at -45 °C in DMF.

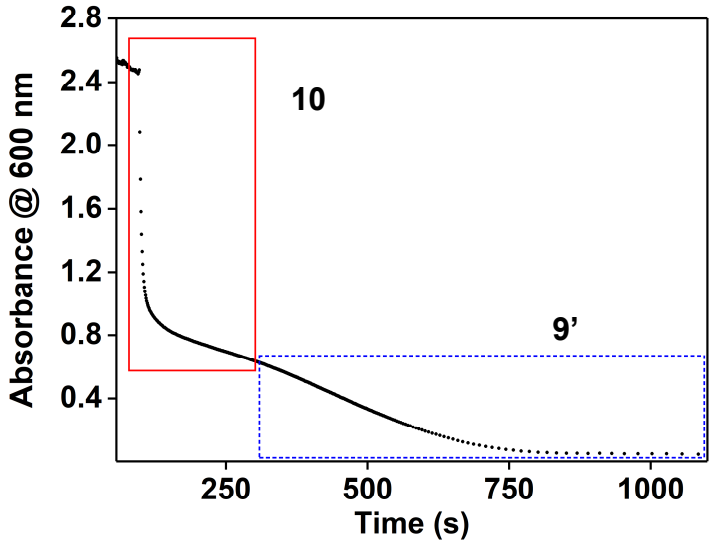

Figure 4.2 – Absorbance decay of the λ_{max} = 600 nm feature against the time for the reaction of **10** with the substrate (*i.e.* 2,4-DTBP, -45 °C in DMF), showing the biphasic behaviour.

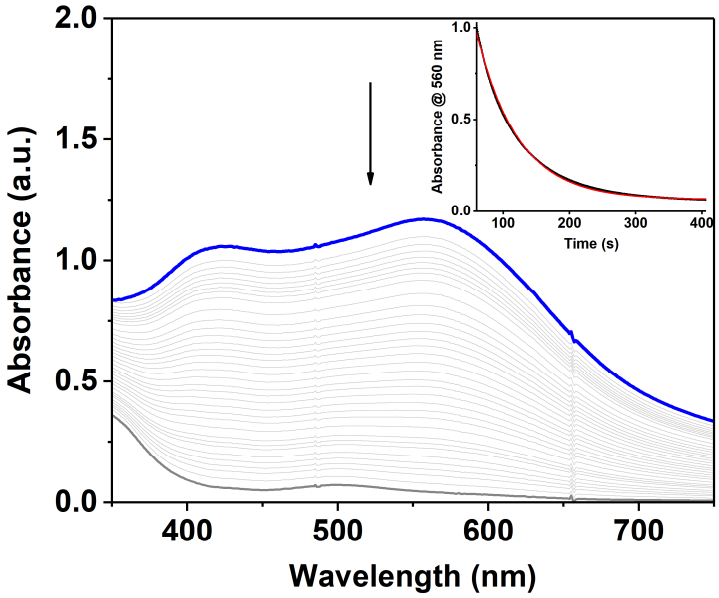

Figure 4.3 - Electronic absorption spectrum showing the decay of **9** (blue trace) upon reaction with 2,4-DTBP (100 equiv.) at -45 °C in DMF. Inset: Decay of λ_{max} = 560 nm feature against time.

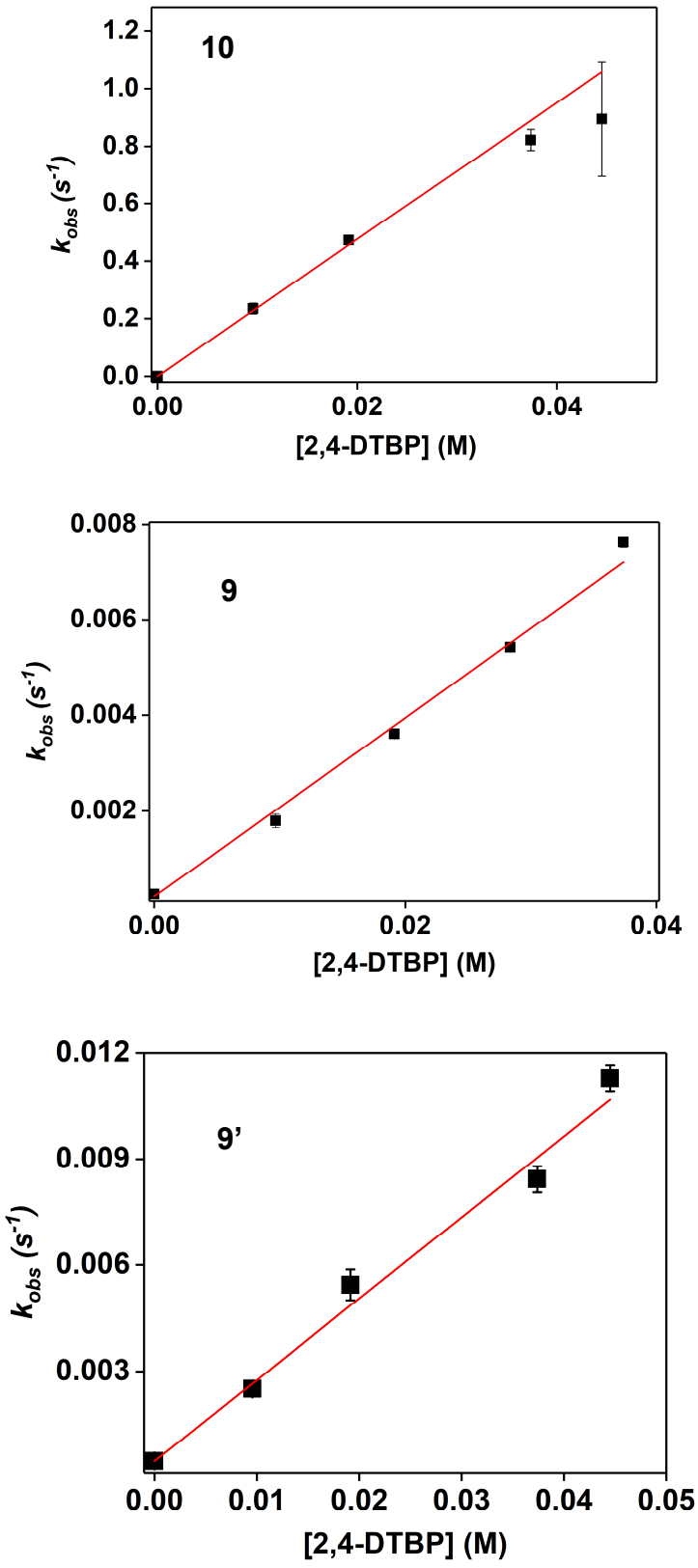

Figure 4.4 – Plots k_{obs} vs. [2,4-DTBP], for the reaction between the species **10** (*top*, k_2 = 23.8(6) $M^{-1}s^{-1}$), **9** (*centre*, k_2 = 0.18(1) $M^{-1}s^{-1}$) and **9'** (*bottom*, k_2 = 0.23(1) $M^{-1}s^{-1}$) and 2,4-DTBP, at -45 °C in DMF.

For the reaction between **10** and 2,4-DTBP at -45 °C, a k_2 = 23.8(6) $M^{-1}s^{-1}$ (Figure 4.4, *top*) was calculated. In the reaction of **9** and 2,4-DTBP, under the same conditions, a k_2 = 0.18(1) $M^{-1}s^{-1}$ was obtained (Figure 4.4, *centre*), while a value of k_2 = 0.23(1) $M^{-1}s^{-1}$ was observed in the case of **9'** (Figure 4.4, *bottom*). Comparing the k_2 for both high-valent oxidants showed that **10** was more than 100-fold more reactive than **9** and **9'**, suggesting that the higher oxidation state of **10** imbued it with higher rates of reaction. Notably, the reaction rate of **9** and **9'** for the reaction with 2,4-DTBP can be considered the same, within the experimental error. This evidence suggested that, in the first approximation, **9** and **9'** may be considered the same species from a kinetic point of view. However, a full analysis of their reactivity needs to be performed in order to validate this statement.

Finally, the k_2 values obtained for the studied complexes were compared with previously reported $Ni^{III}_2(\mu\text{-}O)_2$ complexes (Table 4.1), showing that **10** was an extraordinarily reactive species, comparable, if not superior, to any $Ni^{III}_2(\mu\text{-}O)_2$complex reported to date.

The remarkable reactivity of **9, 10** and **9'** towards the oxidation of 2,4-DTBP encouraged us to explore deeper the reactivity of these species, in order to have a clear insight of the mechanism through which these high-valent hydroxide-bridged species can perform oxidation. Therefore, species **9** and **10** were reacted with a series of *para*-substituted 2,6-di-*tert*-butyl-phenols, which are a widely used mechanistic probe for oxidation process, especially for proton coupled electron transfer reaction.[1-4]

Table 4.1 - Comparison of reactivity of **9**, **10** and **9'** with 2,4 di-*tert*-butylphenol against bis-μ-oxo-Ni^{III}_2 complexes.

	T (°C)	k_2 ($M^{-1}s^{-1}$)
9	-45	0.18(1)
10	-45	23.8(6)
9'	-45	0.23(1)
61	-50	1.08 [5]
64	-60	13 [6]

4.2.2 Reaction of 10 and with 4-X-2,6-di-*tert*-butyl phenols

Compound **10** was reacted with a series of *para*-X-2,6-di-*tert*-butylphenols (4-X-2,6-DTBP, X = −OCH_3, −CH_2CH_3, −CH_3, −$C(CH_3)_3$, −H, −Br, −CN, −NO_2) at -45 °C in DMF (0.2 mM, see Experimental Section at the end of the chapter for details). Addition of the substrates caused the rapid decay of the characteristic electronic absorption feature of **10** (λ = 600 nm, Figure 4.1) which was monitored by electronic absorption spectroscopy. As explained above, **10** decayed over time resulting in the formation of **9'** (Figure 4.1), which further decayed at a slower rate generating a biphasic decay curve (Figure 4.2). For this reason, in the determination of rate constants for the reaction of **10** with 4-X-2,6-DTBP, only the first part of the decay was considered for the kinetic studies (Figure 4.2, red rectangle). The second phase of the decay, that corresponds to the decay of **9'** upon reaction with excess substrate (Figure 4.2, dashed blue rectangle), was analysed to determine the rate constants of the reaction of **9'** with 4-X-2,6-DTBP (section 4.2.4, see below).

The decay curves for the reaction of each substrate with **10** were fitted with a *pseudo*-first order kinetic model (substrates were added in > 10 equiv. excess), allowing for determination of *pseudo*-first order rate constants (k_{obs}) for each reaction. The k_{obs} obtained were found showing a linear dependency on the substrate concentration, allowing for determination of the second order rate constant (k_2) as the slope of the plot k_{obs} vs. [substrate] (Table 4.2, Figures A-4.1–A-4.7). However, the reaction between **10** and 4-CN-2,6-DTBP exhibited an unexpected trend, (Figure A-4.8), with an initial increase of the absorbance at λ_{max} = 600 nm, followed by a partial exponential decay. This unexpected behaviour, displayed only by this specific substrate, prevented us from interpreting the decay with a *pseudo*-first order kinetic model. Although these observations will be subject to future studies, for the purpose of the present thesis the reactivity of **10** with 4-CN-2,6-DTBP will be considered as an outlier and therefore will not be further discussed in the next sections.

Comparison of the reactivity of compound **10** towards both 2,6-DTBP and 2,4-DTBP (see section 4.2.1) was carried out, showing that **10** reacted with 2,4-DTBP (k_2 = 23.8(6) $M^{-1}s^{-1}$) nearly 20 times faster than 2,6-DTBP (k_2 = 1.16(3) $M^{-1}s^{-1}$, Figure 4.5). Analysis of the reactivity of this couple of substrates, which display an identical $BDE_{O–H}$ (82.8 kcal/mol[7, 8]) but a starkly different steric hindrance around the O−H group, suggested the

Table 4.2 - k_2-values and end reaction products for the reactions of **10**, **9** and **9'** with different 4-X-2,6-DTBP at -45 °C in DMF.

X	**10**			**9**			**9'**		
	k_2 ($M^{-1}s^{-1}$)	**Products**	**Yield[a] %**	k_2 ($M^{-1}s^{-1}$)	**Products**	**Yield[a] %**	k_2 ($M^{-1}s^{-1}$)	**Products**	**Yield[a] %**
-OCH_3	520(11)	phenoxyl radical	35 ± 10[c]	84.6(3)	phenoxyl radical	66 ± 6 (*49 ± 20*)[b]	41(1)	-	-
-CH_2CH_3	29(1)	*p*-C_2H_4-CD	-	0.84(2)	*p*-C_2H_4-CD	-	0.553(3)	-	-
-CH_3	24.7(11)	*p*-CH_2-CD	-	0.76(4)	*p*-CH_2-CD	-	0.67(1)	-	-
-$C(CH_3)_3$	22(1)	phenoxyl radical	52 ± 27[c]	0.45(1)	phenoxyl radical	88 ± 14 (*64 ± 20*)[b]	0.42(1)	-	-
-H	1.16(3)	DPQ	10 ± 2[d]	0.045(2)	DPQ	11 ± 2	0.042(2)	-	-
-Br	1.28(4)	DPQ	6 ± 1[d]	0.031(3)	DPQ	15 ± 2	0.08(1)	-	-
-CN	-	-	-	0.99(1)	DPQ	18 ± 2	-	-	-
-NO_2	52.0(24)	4-NO_2-2,6-DTB phenoxide	-	0.65(3)	4-NO_2-2,6-DTB phenoxide	-	0.45(2)	-	-

[a] Yields estimated by UV-Vis considering the 1e^- oxidation of the substrate by **9** and **10**, respectively. [b] Radical yield estimated by double integration of the EPR spectrum. [c] Estimated as difference between the moles of radical obtained in the 2e^- oxidation of the substrate by **10** and the moles of radical obtained by the reaction of the substrate with **9**. [d] Yield of formation of DPQ was estimated quenching the complex with TFA in correspondence with the end of the first exponential decay. [e] k_2 values obtained for **9'** where calculated by fitting with a *pseudo*-first order model the second phase of the reaction between **10** and each substrate. Time traces were plotted using absorbance at λ = 560 nm. Abbreviation: *p*-C_2H_4-CD = 2,6-di-tert-butyl-4-ethylidene-2,5-cyclohexadienone; *p*-CH_2-CD = 2,6-di-tert-butyl-4-methylene-2,5-cyclohexadienone; DPQ = 3,3',5,5'-tetra-tert-butyl-4,4'-diphenoquinone.

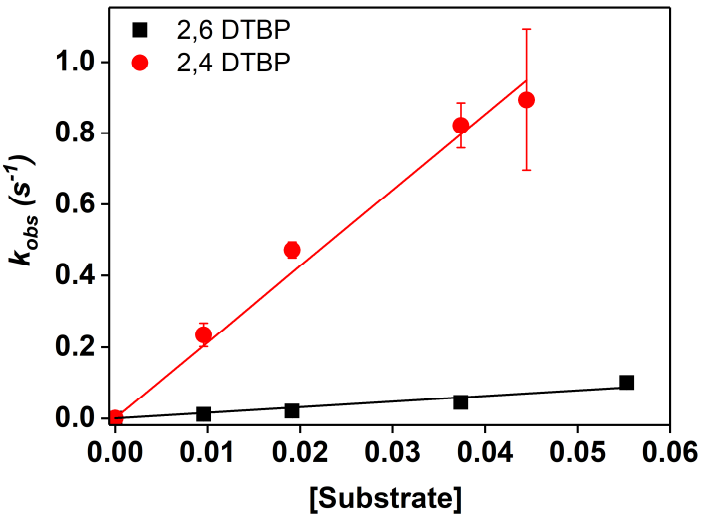

Figure 4.5– Plot of the k_{obs} against [substrate] for the reaction of **10** with 2,4-DTBP and 2,6-DTBP in DMF at -45 °C.

presence of a hydrogen atom abstraction mechanism, that will be discussed in details in section 4.3.

For all the other aforementioned phenols, analysis of the end reaction products for their reaction with **10** was carried out (Figure 4.6, Table 4.2). Reaction of the latter with the 4-X-2,6-DTBP substrates X = –OCH_3, –$C(CH_3)_3$ led to the formation of the corresponding stable phenoxyl radicals (X = –OCH_3, λ = 408, 390 nm; X = –$C(CH_3)_3$, λ = 403, 384 nm Figure 4.6).[9-11] The identity of these species was confirmed by electron paramagnetic resonance (Figures A-4.9–A-4.10) and comparison with the electronic absorption spectra of the corresponding phenoxyl radicals (4-X-2,6-di-*tert*-butyl phenoxyl radical: for X = –OCH_3, λ = 407, 390 nm, Figure A-4.11; for X = –$C(CH_3)_3$, λ = 402, 384 nm, Figure A-4.12). Reaction of **10** with substrates X = –CH_2CH_3, –CH_3 resulted in UV-Vis featureless species (Figure 4.6). Therefore, the end reaction products for these substrates were detected by electron-spray ionization (ESI) mass spectrometry (Figure A-4.13) and identified as 2,6-di-*tert*-butyl-4-ethylidene-2,5-cyclohexadienone (X = –CH_2CH_3) and 2,6-di-*tert*-butyl-4-methylene-2,5-cyclohexadienone (X = –CH_3). Reaction of **10** with substrates X = –H and X = –Br resulted in a common spectrum with features at λ = 430, 408 nm, consistent with the formation of the coupled product 3,3',5,5'-tetra-*tert*-butyl-4,4'-diphenoquinone (DPQ, control experiment in Figure 4.14). The formation of the diphenyl-quinone is a widely reported outcome in case of hydrogen atom abstraction for X = –H.[12, 13] However, the presence of this product for X = –Br could be assigned to the formation of

an unstable phenoxy radical upon an hydrogen abstraction event and resulting dimerization to form the diphenyl quinone.

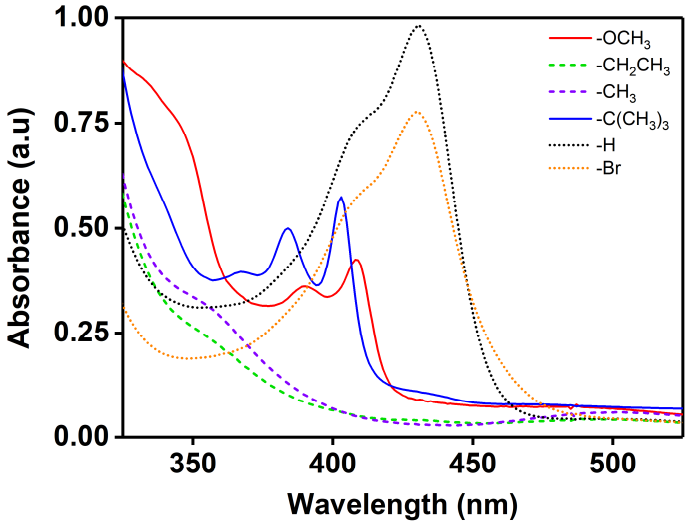

Figure 4.6 - End reaction products for the reaction between **10** and 4-X-2,6-DTBP (X = –OCH_3, –CH_3CH_2, –CH_3, –$C(CH_3)_3$, –H, –Br).

For X = –NO_2, the end reaction product rapidly saturated the spectrum (Figure A-4.15) making its identification not trivial. However, considering the growing band features (λ = 452, 466 nm) present before saturation, it was possible to identify the end reaction product as the 4-NO_2-2,6-di-*tert*-butyl-phenolate by comparison with a solution of 4-NO_2-2,6-di-tert-butyl sodium phenoxide (Figure A-4.16).

Partial quantification of the end reaction products was also performed by UV-Vis. As stated above, species **10** can perform $1e^-$ oxidation of the substrates giving **9'** as product, which further reacted with excess substrate. Therefore, to have a reliable quantification of the species generated by **10**, we focused on each reaction individually. In order to achieve this, the reactions of **10** with X = –H and X = –Br were interrupted after the first decay phase (see Figure 4.2), quenching the just formed species **9'** by addition of an acid (*i.e.* trifluoracetic acid, TFA) and quantifying the amount of DPQ formed. The estimated oxidation yield for the formation of DPQ was 10 ± 2% for X = –H and 6 ± 1% for X = –Br (Table 4.2). In the case of substrates generating stable radicals (X = –OCH_3, –$C(CH_3)_3$), it was not possible to use the same approach, since the addition of TFA to the reaction mixture caused the quenching of both metal complex and radical. For this reason,

the oxidation yields of these substrates were estimated as the difference between the overall moles of phenoxyl radical detected at the end of the reaction of **10** and the moles of radical due to **9'**. Considering the transient nature of **9'**, we postulated that the amount of radical generated by reaction with **9'** would match the one obtained for **9** (see section 4.2.3). The estimated yields for X = –OCH_3 and –$C(CH_3)_3$ were 35 ± 10% and 52 ± 27%, respectively. The featureless end reaction products observed for X = –CH_2CH_3, –CH_3 and the saturating 4-NO_2-2,6-di-*tert*-butyl-phenolate obtained for X = –NO_2 were not quantified.

4.2.3 Reaction of 9 with 4-X-2,6-di-*tert*-butyl phenols

The reactivity of **9** was explored in the same way as for species **10**. **9** was reacted at -45 °C in DMF (0.2 mM, see Experimental Section) with the same series of 4-X-2,6-DTBP (X = −OCH_3, −CH_2CH_3, −CH_3, −$C(CH_3)_3$, −H, −Br, −CN, −NO_2) used for **10**. Addition of the substrates to **9** resulted in an immediate reaction, reflected by the decay of the characteristic spectral feature at λ = 560 nm (Figure 4.3). As for **10**, each reaction was monitored by electronic absorption spectroscopy and the decay curves of each substrate were fitted with a *pseudo*-first order kinetic model, obtaining the second order rate constants k_2 (Table 4.2, Figures A-4.17–A-4.24).

As reported for **10**, the reactivity of **9** towards the two sterically disparate 2,6-DTBP and 2,4-DTBP (see section 4.2.1) substrates was compared. Notably, **9** reacted with 2,6-DTBP (k_2 = 0.045(2) $M^{-1}s^{-1}$) nearly 4 times slower than 2,4-DTBP (k_2 = 0.18(1) $M^{-1}s^{-1}$, Figure 4.7), suggesting the involvement of an hydrogen atom abstraction mechanism.

The outcome for the reaction between **9** and each substrate was analysed, identifying the products of each reaction (Figure 4.8, Table 4.2). Analogous to what was observed for **10**, substrates with X = –H, –Br, and also X = –CN displayed a common spectrum with features at λ = 430, 406 nm, suggesting the formation of the coupled product 3,3',5,5'-tetra-*tert*-butyl-4,4'-diphenoquinone (DPQ). The identity of the latter was unequivocally confirmed by comparison with the corresponding control experiment (Figure 4.14).

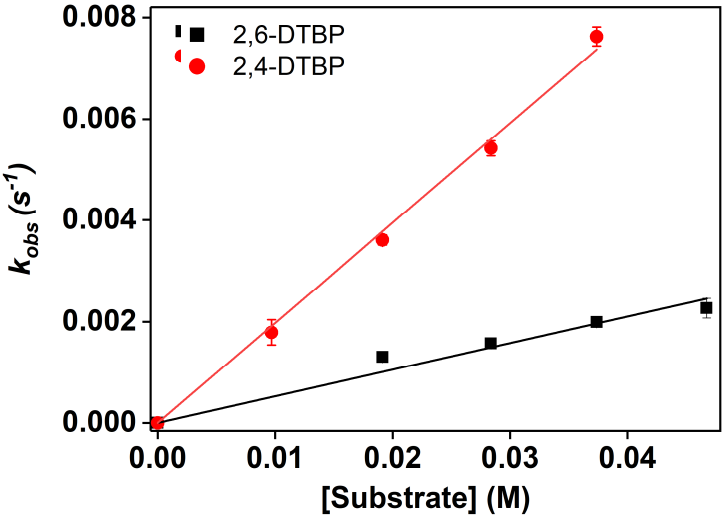

Figure 4.7 – Plot of the k_{obs} against [substrate] for the reaction of **9** with 2,4-DTBP and 2,6-DTBP in DMF at -45 °C.

The formation of the diphenyl-quinone suggested that a radical mechanism such HAT might be involved,[12, 13] with formation of an unstable phenoxy radical and subsequent dimerization to form the diphenyl quinone. The post-reaction mixtures for the reaction between **9** and electron rich phenols such as X = $–OCH_3$, $–C(CH_3)_3$, $–CH_2CH_3$, $–CH_3$ (Figure 4.8), did not exhibit any feature attributable to the formation of the diphenyl quinone dimer and led us to exclude its presence. The reaction between **9** and X = $–OCH_3$, $–C(CH_3)_3$, showed the formation of the corresponding stable phenoxyl radicals (Figure 4.8),[9-11] as confirmed by comparison with the electronic absorption spectra of the corresponding control experiments (4-X-2,6-di-*tert*-butyl phenoxyl radical: for X = $–OCH_3$, λ = 407, 390 nm, Figure A-4.11; for X = $–C(CH_3)_3$, λ = 402, 384 nm, Figure A-4.12) and by electron paramagnetic resonance (Figure A-4.25−A-4.26). The post-reaction mixtures for X = $–CH_2CH_3$, $–CH_3$ displayed mainly featureless spectra (Figure 4.8), requiring different techniques, such a mass spectrometry, to identify the end reaction products. ESI mass spectrometry analysis resulted in the detection of 2,6-di-*tert*-butyl-4-methylene-2,5-cyclohexadienone for X = $–CH_3$ and 2,6-di-*tert*-butyl-4-ethylidene-2,5-cyclohexadienone for X = $–CH_2CH_3$ (Figure A-4.27). As observed for **10**, reaction of **9** with X = $–NO_2$ resulted in the formation of an intense chromophore that saturated the spectrum (Figure A-4.28). Comparison of the growing band features (λ = 452, 466 nm) present before saturation with a solution of 4-NO_2-2,6-di-*tert*-butyl sodium phenoxide

(Figure A-4.16), allowed for the identification of the end reaction product as 4-NO_2-2,6-di-*tert*-butyl-phenolate.

Partial quantification of the end reaction products was performed using electron absorption spectroscopy (Table 4.2). The yield of formation of the DPQ for X = –H, –Br, –CN was calculated to be 11 ± 2%, 15 ± 2% and 18 ± 2%, respectively. Such a low yield was not unexpected, since the observed product was the result of dimerization of the metastable phenoxyl radical, that could easily undergo over oxidation to generate the 2,6-di-*tert*-butyl-1,4-benzoquinone.[14-16] In the case of the species that undergo the formation of stable radicals (*i.e.* X = $–OCH_3$, $–C(CH_3)_3$), the yield of the radical species was determined both by electron absorption spectroscopy and electron paramagnetic resonance. For X = $–OCH_3$, the corresponding radical species was obtained in 66 ± 6% yield (49 ± 20% by EPR, Table 4.2). In the case of X = $–C(CH_3)_3$, the experimental yield of conversion to the radical species was 88 ± 14% (64 ± 20 % by EPR, Table 4.2). The end reaction product for X = $–CH_2CH_3$, $–CH_3$ were not quantified due to their featureless spectra. In the case of X = $–NO_2$, the rapid saturation of the UV-Vis upon reaction of the phenol with **9** did not allow a reliable quantification.

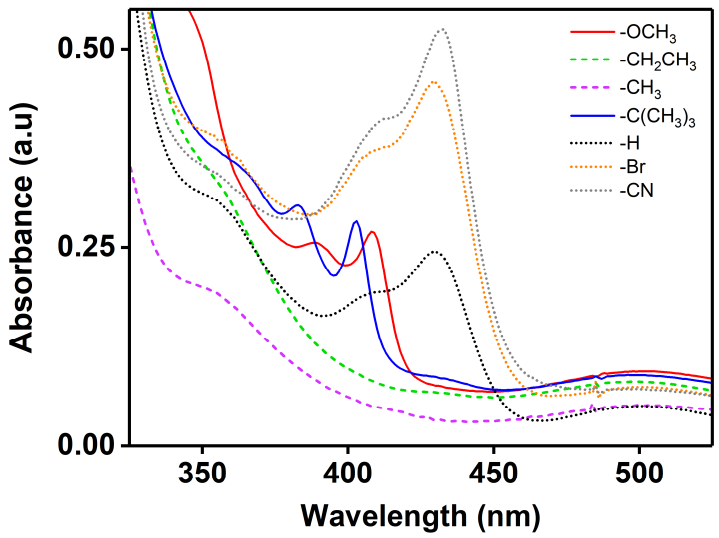

Figure 4.8 - End reaction products for the reaction between **9** and 4-X-2,6-DTBP (X = $–OCH_3$, $–CH_3CH_2$, $–CH_3$, $–C(CH_3)_3$, –H, –Br, –CN).

4.2.4 Reaction of 9' with 4-2,6-di-*tert*-butyl phenols

As explained in section 4.2.1, species **9'** is strictly correlated with **10**, from which it is generated upon reaction of **10** with a substrate (Figure 4.1). Once formed, the intermediate species **9'** reacted with excess substrate leading to the biphasic decay behaviour observed in Figure 4.2. The first phase of the decay curve was assigned to the reaction of **10** with the substrate (Figure 4.2, red rectangle) and has been analysed in section 4.2.2. The second phase of the decay curve (Figure 4.2, dashed blue rectangle) was identified by correlating the reaction of **9'** with the substrate. The absorbance decay of the feature at λ = 560 nm in the second phase of the decay curve was fitted with a *pseudo*-first order kinetic model, allowing for the determination of k_{obs} for each substrate. Plot of the obtained k_{obs} against the concentration of the corresponding substrate resulted in the determination of the second order rate constant k_2 as slope.

Comparison of the reactivity of compound **9'** towards both 2,6-DTBP and 2,4-DTBP (see section 4.2.1) was carried out, as previously reported for **10** and **9**. Reaction of **9'** with 2,4-DTBP (k_2 = 0.23(1) $M^{-1}s^{-1}$) appeared to be nearly 5 times faster than the reaction with 2,6-DTBP (k_2 = 0.042(2) $M^{-1}s^{-1}$, Figure 4.9). Such a stark difference in reactivity suggested the presence of a hydrogen atom abstraction mechanism, that will be discussed in detailed in section 4.3.

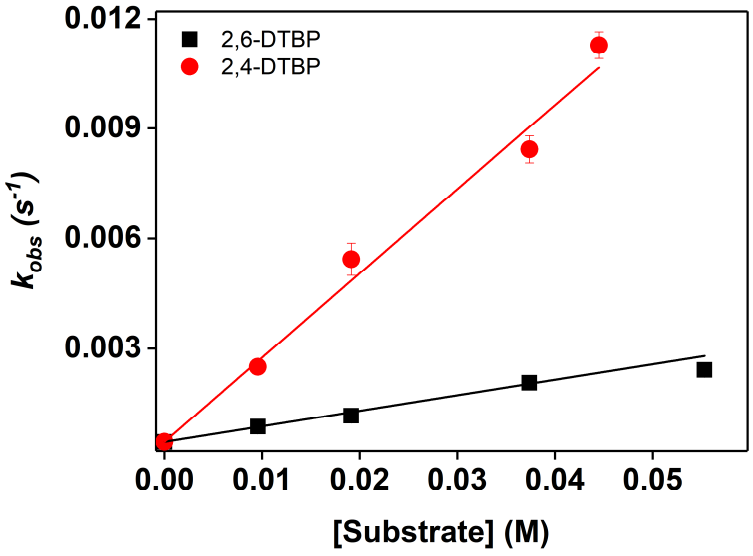

Figure 4.9 – Plot of the k_{obs} against [substrate] for the reaction of **9'** with 2,4-DTBP and 2,6-DTBP in DMF at -45 °C.

As mentioned above, due to the nature of the active species, the reactivity studies of **9'** were performed contextually to the reactivity of **10** with the series of 4-X-2,6-DTBP (X = −OCH_3, −CH_2CH_3, −CH_3, −$C(CH_3)_3$, −H, −Br, −CN, −NO_2). Therefore, substrates and conditions (-45 °C in DMF) are the same for both species **10** and **9'**. The k_2 values obtained for the reaction of **9'** with the series of 4-X-2,6-DTBP (Figures A-4.29−A-4.35) are reported in Table 4.2. Unfortunately, due to its transient nature, species **9'** cannot be obtained independently from **10**. Therefore, the contemporary presence in solution of the products of the reaction of **10** with the substrates prevented us to perform a proper analysis and quantification of the end reaction products. However, the lack of new spectral features and the results obtained for **9**, we proposed that **9'** could achieve the same end reaction product observed for **9** and **10**.

4.2.5 Kinetic isotopic effect experiments

In order to further understand the oxidation mechanism of the species **9**, **10** and **9'**, the kinetic isotopic effect (KIE) for all species were measured. In particular, we analysed the reaction of the three species (i.e. **10**, **9** and **9'**) with the deuterated substrate 4-CH_3-[D]-2,6-DTBP (Figure A-4.36–A-4.38). The corresponding k_2 values (**9**: k_2 = 0.36(2) $M^{-1}s^{-1}$; **10**: k_2 = 5.9(8) $M^{-1}s^{-1}$; **9'**: k_2 = 0.140(4) $M^{-1}s^{-1}$) were compared with the previously measured k_2 value for 4-CH_3-[H]-2,6-DTBP (Table 4.2, Figure A-4.3, A-4.19, A-4.31). The KIE values consequently calculated showed a KIE ~ 4 for **10** (Figure 4.10) and a KIE ~ 2 for **9** (Figure 4.11) defining the cleavage of the phenolic O–H bond as the rate determining step. Critically, the KIE values obtained for **9'** was higher than the previous two species (KIE ~ 4.8, Figure 4.12) suggesting that the isotopic labelling had a stronger influence on its reactivity.

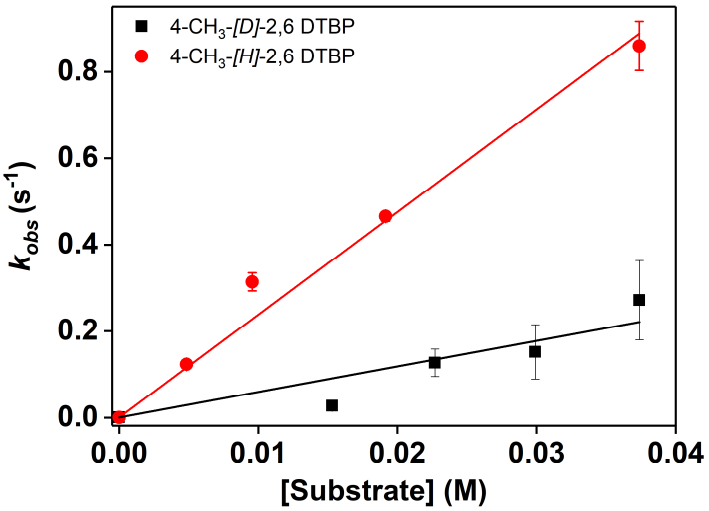

Figure 4.10 - Plots of k_{obs} versus [substrate] for the reaction of **10** with 4-CH_3-[*H*]-2,6 DTBP and 4-CH_3-[*D*]-2,6 DTBP, in DMF at -45 °C.

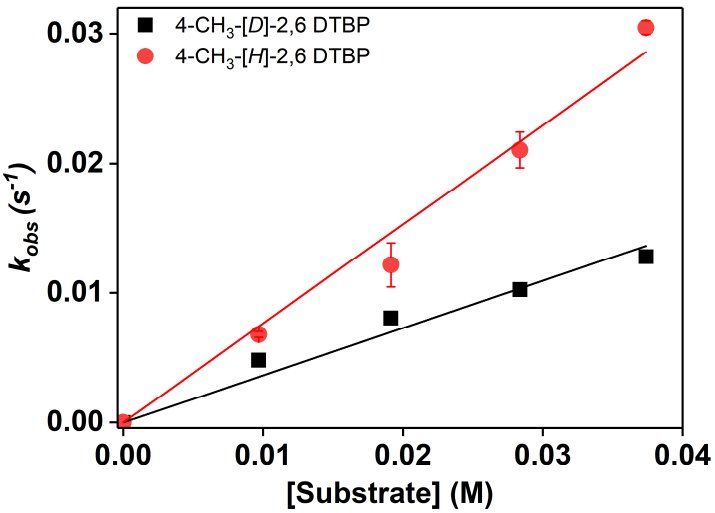

Figure 4.11 - Plots of k_{obs} versus [substrate] for the reaction of **9** with 4-CH_3-[*H*]-2,6 DTBP and 4-CH_3-[*D*]-2,6 DTBP, in DMF at -45 °C.

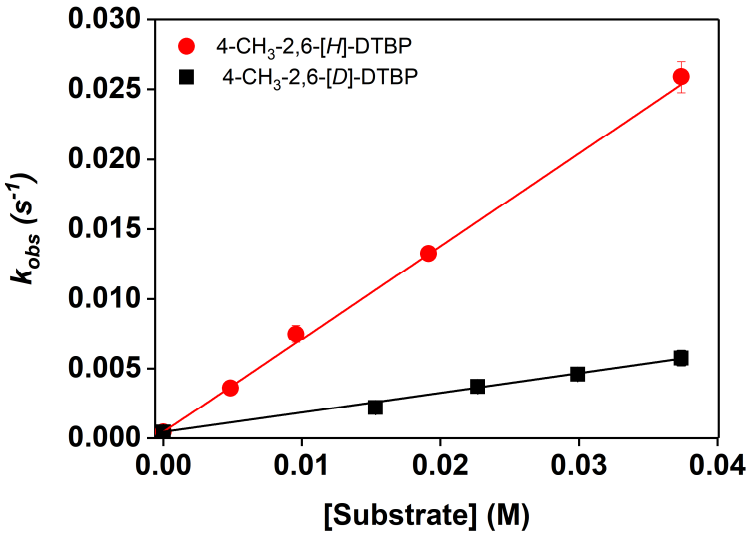

Figure 4.12 - Plots of k_{obs} versus [substrate] for the reaction of **9'** with 4-CH_3-[*H*]-2,6 DTBP and 4-CH_3-[*D*]-2,6 DTBP, in DMF at -45 °C.

4.2.6 Discussion about the reactivity of 9, 10 and 9' towards O–H oxidation

The comparison of the measured k_2 values identified **10** as a stronger oxidant reacting nearly 100-fold faster than **9** and **9'** for all the substrates analysed. Such a stark difference in reactivity rate can be easily attributed to the presence of a higher oxidation state in **10**, that imbues it with higher rates of reaction. Analysis of the kinetic results for **9** (Table 4.2) showed that the phenol bearing the most electron rich substituent (*i.e.* 4-OCH_3-2,6-DTBP) reacted most rapidly, exhibiting a k_2 value two orders of magnitude higher than the unsubstituted 2,6-DTBP (k_2 = 85 $M^{-1}s^{-1}$ and 0.045 $M^{-1}s^{-1}$, respectively). Almost identical behaviour was observed for **9'** and **10**, with the more electron rich phenols reacting at considerably higher rates than the electron-poor phenols (**9'**: X = –OCH_3 k_2 = 41(1) $M^{-1}s^{-1}$, X = –Br k_2 = 0.08(1) $M^{-1}s^{-1}$; **10**: X = –OCH_3 k_2 = 520 $M^{-1}s^{-1}$; X = –Br k_2 = 1.28 $M^{-1}s^{-1}$, Table 4.2). Such behaviour, strictly related to the low O–H bond dissociation energy of 4-OCH_3-2,6-DTBP (BDE_{O-H} = 78.3 kcal/mol[20]), was ascribed to a more general trend that also included other analysed substrates (X = –CH_3, –CH_2CH_3 –$C(CH_3)_3$, –H, –Br). A linear correlation between the magnitude of the O–H bond dissociation energy

($BDE_{O–H}$, Table A-4.1) and the measured second order rate constants k_2 was observed for all the oxidant species (Figures 4.13–4.15).

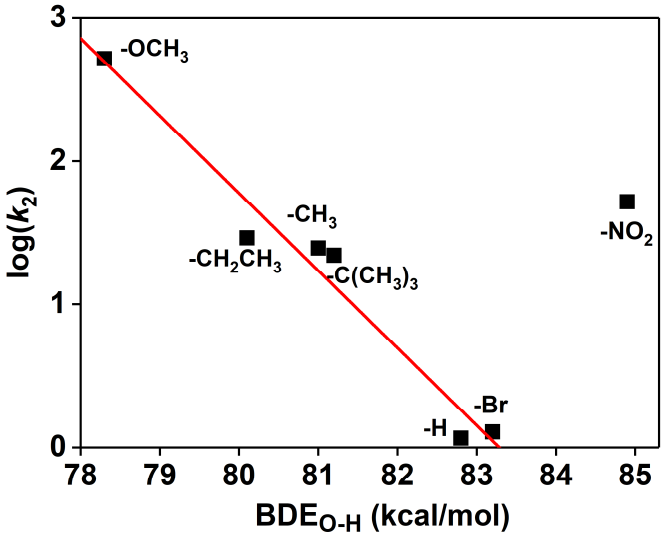

Figure 4.13 – Plot of log(k_2) against $BDE_{O–H}$ for the reaction of **10** with a series of 4-X-2,6-DTBP in DMF at -45 °C. Slope = -0.54(5).

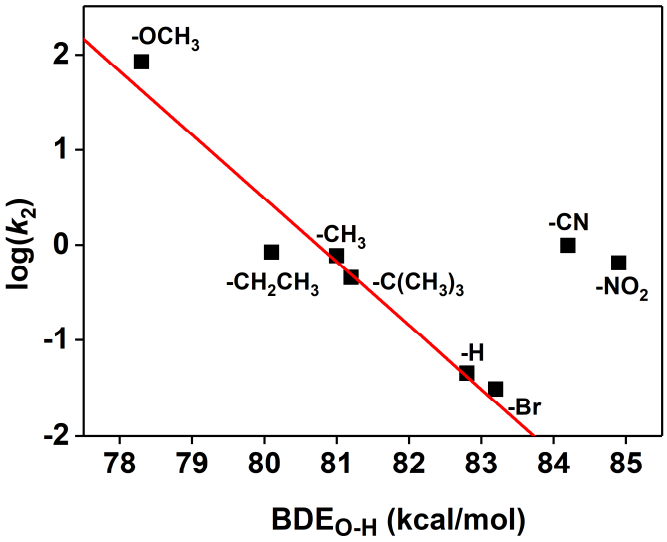

Figure 4.14 – Plot of log(k_2) against $BDE_{O–H}$ for the reaction of **9** with a series of 4-X-2,6-DTBP in DMF at -45 °C. Slope = -0.67(8).

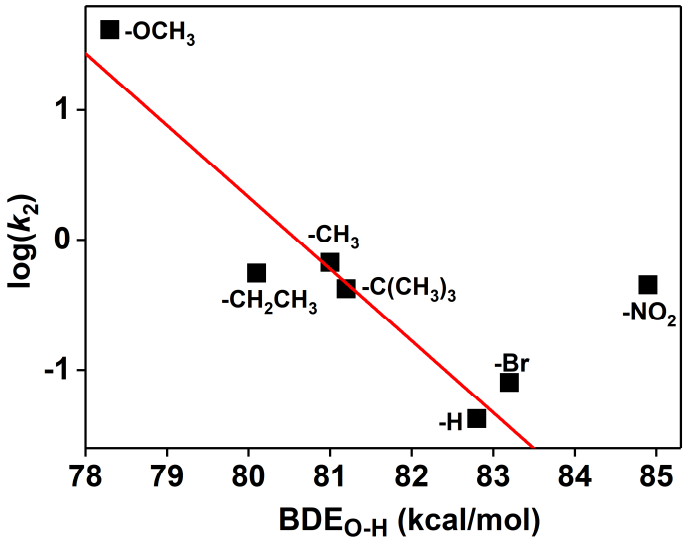

Figure 4.15 – Plot of log(k_2) against $BDE_{O–H}$ for the reaction of **9'** with a series of 4-X-2,6-DTBP in DMF at -45 °C. Slope = -0.55(9).

Such a linear trend strongly suggested the presence of a proton couple electron transfer event.[2, 4, 21] However, the 4-X-2,6-DTBP bearing strong electron-withdrawing substituents (X = –CN, $–NO_2$) exhibited unexpectally high k_2 values, considerably higher than expected on the basis of the trend observed and for this reason are considered outliers.

Comparison of the reactivity of **10**, **9** and **9'** towards both 2,6-DTBP and 2,4-DTBP, which display an identical $BDE_{O–H}$ (82.8 kcal/mol[7, 8]) but a starkly different steric hindrance around the O–H group, gave us more information about the mechanism involved. The stark difference in reactivity between the two sterically disparate substrates and, in particular, the higher reactivity of the less hindered 2,4-DTBP compared to 2,6-DTBP displayed by all the three active species, identified the hydrogen atom abstraction as the rate determining step. This observation implies that the oxidation mechanism could proceed through an hydrogen atom transfer (HAT) mechanism, as reported in previous study.[13, 22, 23]

Polanyi and co-workers defined that in an HAT reaction, a linear correlation between the Eyring barrier, $\Delta G^{\ddagger}$[30-32] and the ΔG° (*i.e.* Evans-Polanyi plot) is expected, with a slope close to 1/2.[2, 30, 33] Since in an organic HAT reaction, the entropy component of the reaction is almost null ($\Delta S^{\circ} \cong 0$), the ΔG° is effectively equal to ΔH°(thus BDEs). However, Meyer demonstrated that in transition metal complexes, this assumption (*i.e.* the negligible nature of the entropic term) is not always correct, and therefore bond dissociation free energies, (BDFE) that include both enthalpic and entropic contributions, must be used.[1, 2, 27] The Eyring barrier $\Delta G^{\ddagger}$ for the reaction of **9** , **10** and **9'** with the substrates (calculated from the k_2 values using the Eyring equation[30-32]) was plotted against the O–H bond dissociation free energies of the phenols (Table A-4.1, Figure 4.16–4.18), displaying good linear correlation, except for X = –CN, $–NO_2$ that were outside the trend and considered outliers. Linear regression calculations gave a slope of 0.56(6) for **10**, 0.70(8) for **9** and 0.58(10) for **9'** (Table 4.3). The value obtained for **10** and **9'** were very close to the theoretical value of 0.5 expected for a formal HAT mechanism (see above), suggesting that a hydrogen atom transfer mechanism occurred in the phenol oxidation. With regards to **9**, the slope value obtained appears to be relatively high but, within the experimental error, is still indicative of a HAT mechanism.

Table 4.3 – Correlation plots slopes for the reactivity of **9**, **9'** and **10.**

	Evans-Polanyi plot	**Hammett plot**	**Marcus plot**
10	0.56(6)	-2.9(3)	-0.21(3)
9	0.70(8)	-3.6(5)	-0.27(1)
9'	0.58(10)	-2.9(6)	-0.23(2)

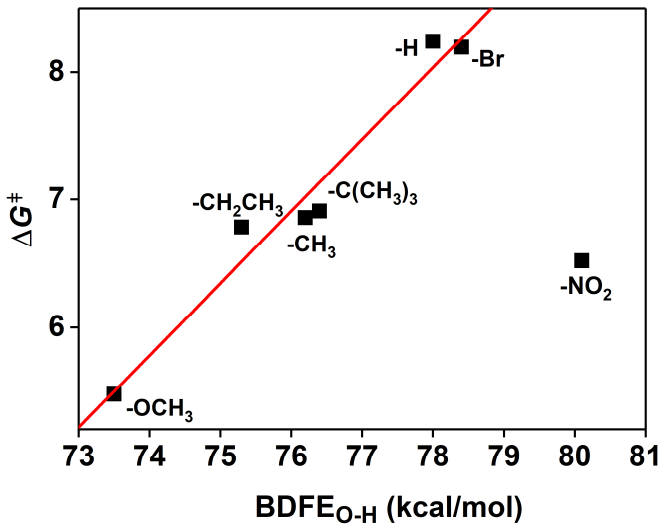

Figure 4.16 – Evans-Polanyi plot ($\Delta G^{\ddagger}$ vs. $BDFE_{O-H}$) for the reaction of **10** with a series of 4-X-2,6-DTBP in DMF at -45 °C.

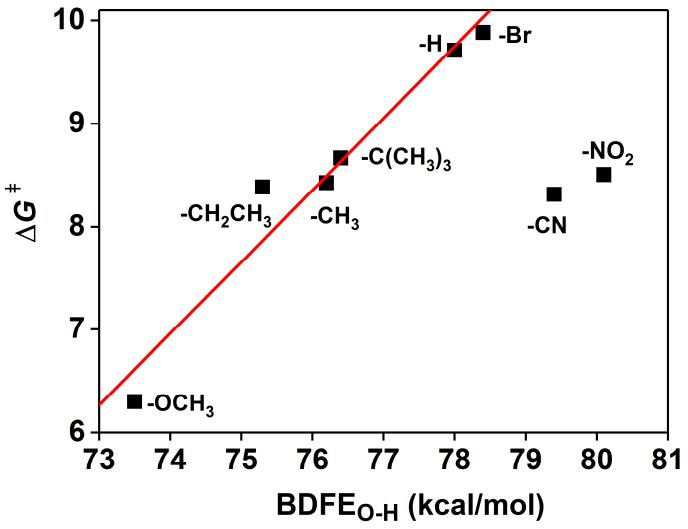

Figure 4.17 – Evans-Polanyi plot ($\Delta G^{\ddagger}$ vs. $BDFE_{O-H}$) for the reaction of **9** with a series of 4-X-2,6-DTBP in DMF at -45 °C.

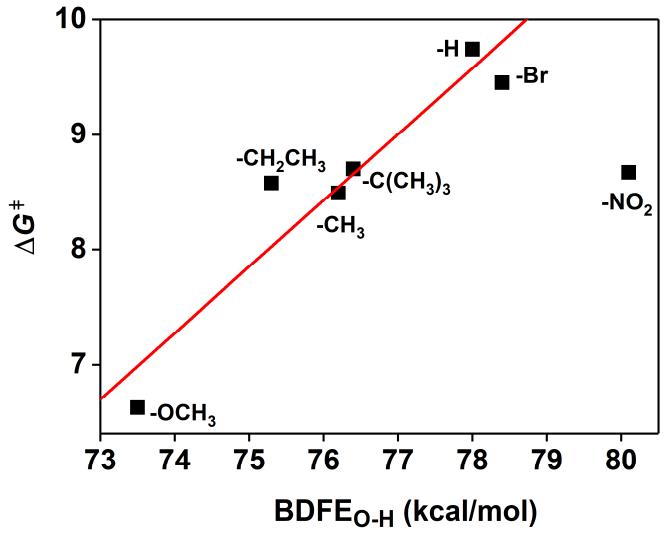

Figure 4.18 – Evans-Polanyi plot ($\Delta G^{\ddagger}$ vs. $BDFE_{O-H}$) for the reaction of **9'** with a series of 4-X-2,6-DTBP in DMF at -45 °C.

The log ($^{X}k_2/^{H}k_2$) for **10**, **9** and **9'** were plotted as function of the Hammett parameter σ^{+}_{p} (Figures 4.19–4.21), giving an insight of the electronic effect of the *para* substituents on the reactivity. All the high valent complexes displayed a linear dependency of the k_2 values from the nature of the *para* substituent on the 4-X-2,6-DTBP. As previously observed, due to their unusual high k_2 values, the electron-poor phenols bearing –CN and $–NO_2$ substituents were outliers with respect to this trend. Linear fits of the three plots resulted in negative Hammett slopes, ρ = -2.9(3) for **10,** ρ = -3.6(5) for **9** and ρ = -2.9(6) for **9'**, respectively (Table 4.3). These negative values suggested that the reactions involve the loss of a negative charge (*i.e.* the protonation of the negatively charged hydroxide ligand upon the HAT event).[34, 35] This evidence, along with the linear relationship of the k_2 values, are consistent with a HAT mechanism, as previously observed in literature.[22, 36-38]

Another incredibly powerful tool to understand the mechanism in PCET reaction is the Marcus theory. Despite being originally developed for electron-transfer processes[39, 40] it has been quite successfully adapted to understand PCET reactions, thanks to the work of Mayer and co-workers.[2, 24, 25, 33] Marcus theory, applied to PCET reactions predicts a linear correlation between the rate constants (as $(RT/F)\ln(k_2)$) and the one e^- oxidation potentials of the phenols. The slope of such a plot (*i.e.* Marcus plot) is considered a critical parameter capable of differentiating between different proton and electron transfer mechanisms. The slope can vary between -1.0 and -0.5 in the presence of nonconcerted

PCET reaction with proton transfer (PT) and electron transfer (ET) with similar rates. In the case in which the rate-determining step is the proton transfer (followed by a fast ET), a slope of -1.0 is expected. In the opposite way, if the electron transfer is the rate determining step (followed this time by a fast PT) the slope will be close to -0.5.[21, 33, 36, 41] In the case of concerted reaction in which proton and electron are transferred simultaneously (*i.e.* HAT), the slope is instead predicted to be close to 0.0.[12, 42, 43] The Marcus plot for **10**, **9** and **9'** are reported in Figures 4.22–4.24. All the high valent species exhibited a very good linear correlation, (except for X = – CN, $–NO_2$) resulting in slope values of -0.21(3) for **10**, -0.27(1) for **9** and -0.23(2) for **9'** (Table 4.3). In light of the aforementioned parameters and considering the experimental error, such values can be considered indicative of a HAT mechanism, as already depicted by the previously reported correlation plots. The unusual high reactivity rate of the electron poor phenols with X = –CN, $–NO_2$ (Table 4.2) determined their nature as outliers in all the correlation plots calculated (see above). As recently reported by Tolman,[4] such anomalies could be addressed as a change of mechanism from a possible CPET to a stepwise proton transfer in which the relatively lower pK_a of this electron-poor substrates[44] would be the driving force. Such an outcome is consistent with the phenolate species observed in the end reaction mixture for X = $–NO_2$. As there is a lack of further information about such a mechanism, the k_2 values obtained for X = –CN, $–NO_2$ have been considered outliers and werethus excluded from any fit calculation.

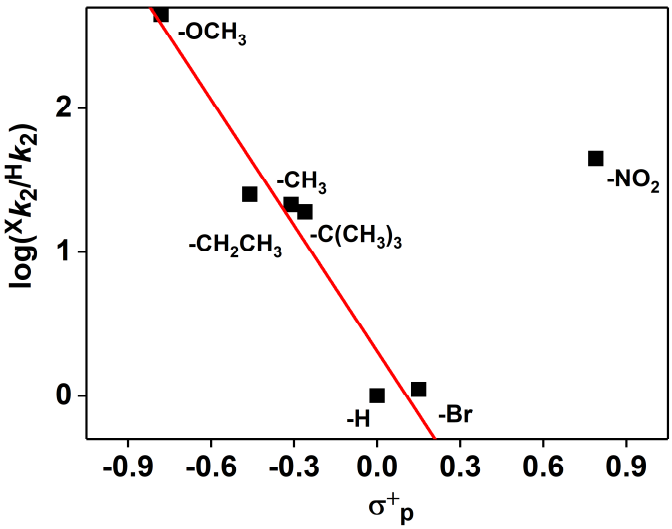

Figure 4.19 – Hammett correlation plot (log ($^{X}k_2/^{H}k_2$) vs. σ^+) for the reaction of **10** with a series of 4-X-2,6-DTBP in DMF at -45 °C.

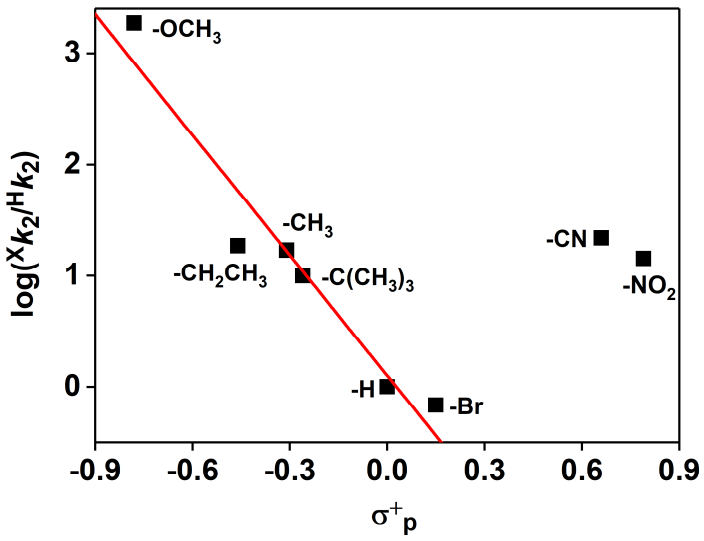

Figure 4.20 – Hammett correlation plot (log ($^{X}k_2/^{H}k_2$) vs. σ^+) for the reaction of **9** with a series of 4-X-2,6-DTBP in DMF at -45 °C.

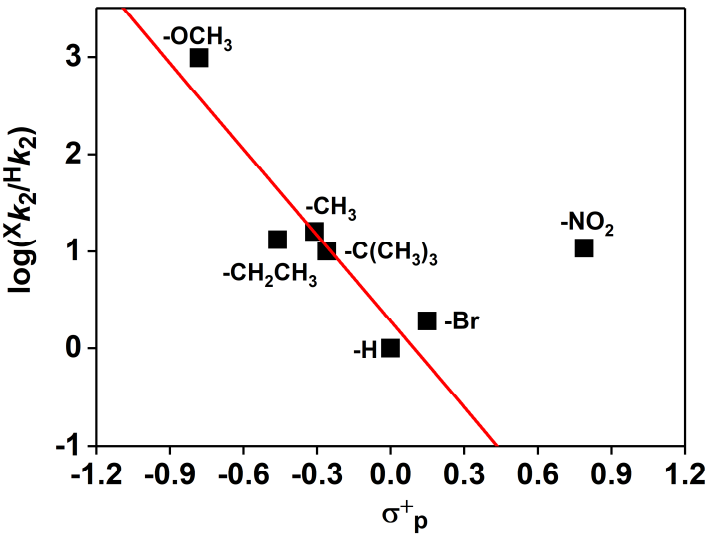

Figure 4.21 – Hammett correlation plot (log ($^{X}k_2/^{H}k_2$) vs. σ^+) for the reaction of **9'** with a series of 4-X-2,6-DTBP in DMF at -45 °C.

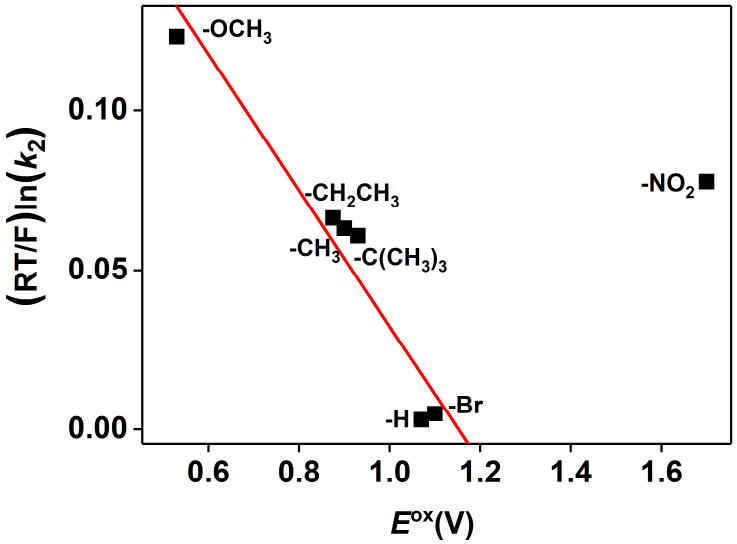

Figure 4.22 – Marcus correlation plot ((RT/F) ln(k_2) vs. E^{ox}) for the reaction of **10** with a series of of 4-X-2,6-DTBP in DMF at -45 °C.

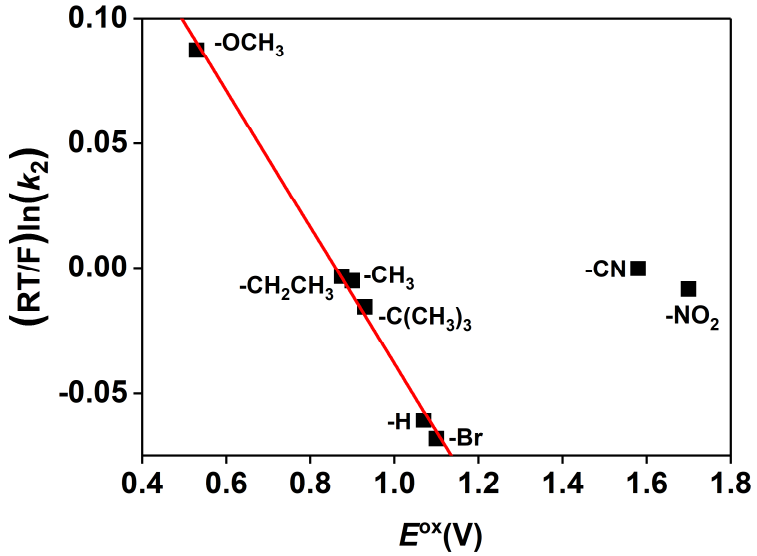

Figure 4.23 – Marcus correlation plot ((RT/F) ln(k_2) vs. E^{ox}) for the reaction of **9** with a series of 4-X-2,6-DTBP in DMF at -45 °C.

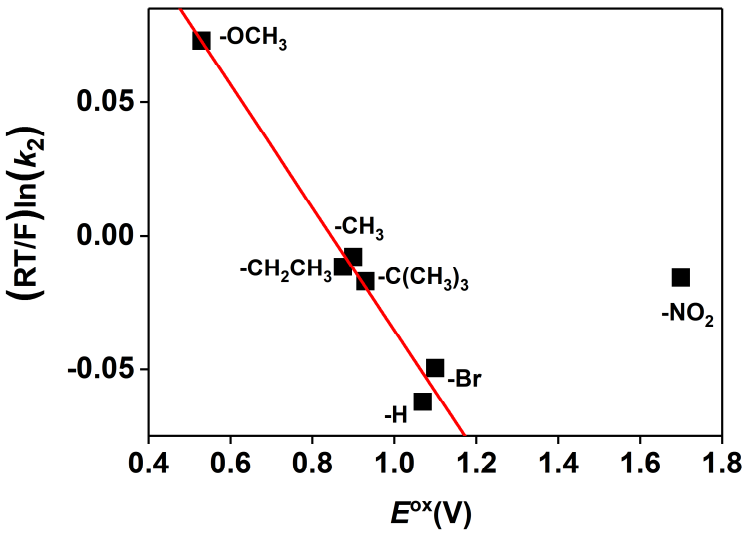

Figure 4.24 – Marcus correlation plot ((RT/F) ln(k_2) vs. E^{ox}) for the reaction of **9'** with a series of of 4-X-2,6-DTBP in DMF at -45 °C.

The KIE values calculated for **10** (KIE ~4), **9** (KIE ~2) , and **9'** (KIE ~4.8) clearly identified the hydrogen abstraction event as rate determining. Critically, **9'** exhibited the highest KIE value among the species analysed suggesting that the isotopic labelling had a stronger influence on its reactivity. This might be assigned to the nature of **9'**: since the latter is generated by formal transfer of a deuterium atom in the reaction of **10** with the labelled substrate, it can be more accurately identified as $Ni^{II}Ni^{III}$(μ-OH-μ-OHD). Thus, the further reaction of the partially deuterated species **9'** with the labelled substrate would exhibit a more distinct dependency from the isotopic substitution, resulting in a higher KIE. The values above reported for the reactive species **10**, **9** and **9'** were all within the classical limit of 7, as widely observed for M–O–X oxidants.[45] This observation rules out the presence of a tunnelling mechanism, as reported instead for analogues oxo-ligated complexes such as $Ni^{III}_2(\mu\text{-}O)_2$ (**61**, KIE = 21.4),[5] $Cu^{III}_2(\mu\text{-}O)_2$ (**91**, KIE = 26-40)[46] and $Fe^{III}Fe^{IV}(\mu\text{-}O)_2$ (KIE = 20)[47].

The reactivity studies reported above outlined a close relationship between species **9** and **9'**. In light of the information achieved regarding the mechanism of the analysed reactive species, we identified species **9'** as the HAT product of the reaction of **10** with the substrate, namely a $Ni^{II}Ni^{III}$(μ-OH-μ-OH_2) (Figure 4.25). Therefore, although both of them exhibit the same oxidation state for the Ni centres and share almost identical UV-

Vis features (Figure A-4.39), **9'** and **9** are structurally different (Figure 4.29) and, moreover, **9'** can be formally considered as the protonated version of **9**.

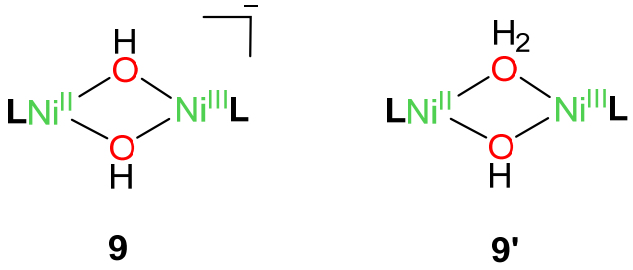

9 **9'**

Figure 4.25 – Comparison between **9** and the proposed structure for **9'**

A comparison of the rate constants related to the reactivity of **9** and **9'** against the series of phenols reported above was carried out (Table 4.2, Table 4.4). All the calculated k_2 values for **9'** were comparable and often quite close to the values measured for **9**, such as in the case of X = $–CH_2CH_3$, $–CH_3$, $–C(CH_3)_3$, –H and –Br. For the remaining substrates, namely the "extreme" X = $–OCH_3$ (electron-richest) and X = $–NO_2$ (electron-poorest), **9'** appeared to be slower than **9**. However, it is noteworthy highlight that, being **9'** obtained as product of **10** and not as an independent species as **9**, it will inevitably be affected by a larger error in the k_{obs} measurements for extremely reactive substrates such as X = $–OCH_3$ and X = $–NO_2$. Comparison of the correlation plots slope (Table 4.3) showed insignificant differences between the two species, indicating, within the experimental error, the HAT as a common oxidation mechanism.

Despite being two structurally different but similar species, a closer relationship between **9** and **9'** was proposed: since **9'** was the formally protonated version of **9**, so as not to exclude that the two species could be part of an equilibrium, albeit no conclusions can be drawn from the actual data. However, in light of the observation made above and due to the actual limits in a more detailed analysis of **9'**, **9** can be reasonably considered as a reliable model system for **9'**.

Table 4.4 – Comparison of the reactivity towards 4-X-2,6-DTBP between **9** and **9'**.

	4-X-2,6-DTBP							Correlation plots				
	-OCH_3	**-CH_2CH_3**	**-CH_3[a]**	**-$C(CH_3)_3$**	**-H**	**-Br**	**-NO_2**	**BDE Plot**	**E-P Plot**	**Hammett plot**	**Marcus plot**	**KIE**
9	84.6(3)	0.84(2)	0.76(4) **0.36(2)**	0.45(1)	0.045(2)	0.031(3)	0.65(3)	-0.67(8)	0.70(8)	-3.6(5)	-0.27(1)	2
9'	41(1)	0.553(3)	0.67(1) **0.140(4)**	0.42(1)	0.042(2)	0.08(1)	0.45(2)	-0.55(9)	0.58(10)	-2.9(6)	-0.23(2)	4.8

[a] k_2 values in bold are referred to the reaction with 4-CH_3-[D]-2,6-DTBP

4.2.7 Comparison of the reactivity of 9, 10 and 9' towards 2,6 DTBP with reported complexes

The reactivity of **9**, **10** and **9'** were compared with some selected mono- and di-nuclear reported late transition metal complexes, using the oxidation of the 2,6-DTBP as comparative probe (Table 4.5). **9** and **9'** were considerably less reactive than the most of the mono-nuclear $pyN_2^{Me2}Ni^{III}$–X complexes (X = –OCO_2H, –OAc, –ONO_2, –Cl, entries 4-7),[12, 13] and $pyN_2^{iPr2}M^{III}$–OAc (M = Ni, Cu, entries 9-10) while comparable rates where observed in the case of $pyN_2^{Me2}Ni^{III}$–terpy (entry 8).[48] Homo-bimetallic $Ni^{III}Ni^{III}$-oxo and hetero-bimetallic $Cu^{III}Ni^{III}$-oxo complexes (entries 11-12)[5, 49] displayed k_2 values comparable with **9** and **9'**, while the Nam Co^{II} iminoiodane complexes (formally isoelectronic with Ni^{III}, entries 13-14) showed a substantially diminished reactivity rate.

The high valent species **10** showed an overall more reactive behaviour, with a k_2 value nearly 10 times higher than $pyN_2^{Me2}Ni^{III}$–X (X = –OCO_2H, –OAc, –Cl, -terpy, entries 4-5,7-8) [12, 13, 48] and $pyN_2^{iPr2}M^{III}$–OAc (M = Ni, Cu, entries 9-10).[50] **10** reacted almost 100 times faster than the di-nuclear oxo complexes reported (entries 11-12),[5, 49] demonstrating its ability as one of the most reactive Ni^{III} complexes reported so far regarding to O–H activation. A 1000-fold reactivity was displayed in comparison with the Co^{II} iminoiodane complexes (entries 13-14). Only the $pyN_2^{Me2}Ni^{III}$–ONO_2 complex (entry 6)[13] appeared to

be more reactive, even if it displayed a higher but comparable k_2 value. For the sake of completeness, the room temperature stable $Ni^{III}(pyalk)_2^+$ complex (entry 15) was also reported. However, it is important to highlight that the incredibly high oxidation rate towards 2,6 DTBP (k_2 = 189.3 $M^{-1}s^{-1}$) observed for $Ni^{III}(pyalk)_2^+$ are measured at 25˚C, so any comparison with the previously reported examples (measured between -20˚C and -50˚C) have to take into account the huge role of the temperature on the reaction rate.

Table 4.5 - Comparison between k_2 values for the oxidation of 2,6-DTBP by **9**, **10** and **9'** and some selected complexes.

#	Complex	k_2 ($M^{-1}s^{-1}$)	T(˚C)	solvent	Ref.
1	**10**	1.16(3)	-45	DMF	this work
2	**9**	0.045(2)	-45	DMF	this work
3	**9'**	0.042(2)	-45	DMF	this work
4	$[pyN_2^{Me2}Ni^{III}(OCO_2H)]$	0.104	-40	acetone	[13]
5	$[pyN_2^{Me2}Ni^{III}(OAc)]$	0.125	-40	acetone	[13]
6	$[pyN_2^{Me2}Ni^{III}(ONO_2)]$	1.96	-40	acetone	[13]
7	$pyN_2^{Me2}Ni^{III}Cl$	0.176	-40	acetone	[12]
8	$pyN_2^{Me2}Ni^{III}(^{tBu}terpy)$	0.06	-40	acetone	[48]
9	$pyN_2^{iPr2}Ni^{III}(OAc)$	0.24	-40	acetone	[50]
10	$pyN_2^{iPr2}Cu^{III}(OAc)$	0.10	-40	acetone	[50]
11	**61**	0.0166	-50	acetone	[5]
12	$[(MeAN)Cu^{III}(\mu\text{-}O)_2Ni^{III}L]^+$	0.03	-50	CH_2Cl_2	[49]
13	$[(TMG_3tren)Co^{II}\text{–}(^sPhINTs)]^{2+}$	0.0043	-20	acetone	[7]
14	$[(TMG_3tren)Co^{II}\text{–}^sPhINTs(Sc(OTf)_3)]^{2+}$	0.0005	-20	acetone	[7]
15	$Ni^{III}(pyalk)_2^+$	189.3	25	CH_2Cl_2	[51]

pyN_2^{Me2} = N,N'-bis(2,6-dimethylphenyl)2,6-pyridinedicarboxamidate;MeAN = N,N,N′,N′,N′-pentamethyl-dipropylenetriamine; L = $[HC(CMeNC_6H_3(iPr)_2)_2]$; ^{s}PhINTs = N-(p-toluenesulfonyl)imino(2-tert-butylsulfonyl)phenyliodinane; pyalk = 2-pyridinyl-2-propanoate

4.3 Determination of the reaction mechanism for 10, 9 and 9'

4.3.1 ^{1}H-NMR analysis of the reaction of 9 and 10 with 4-OCH_3-2,6-DTBP

^{1}H-NMR analysis of the final reaction mixture from the reaction of **9** and **10** with 4-OCH_3-2,6-DTBP in deuterated DMF was performed (Figure 4.26) in order to have more information regarding the fate of the complexes after the reaction. Notably, both the **9** and **10** were prepared in situ using exclusively deuterated solvents. The measurements were performed on end reaction mixtures warmed to room temperature, because a low temperature ^{1}H-NMR experiments were not possible at our facilities. Since no ^{1}H-NMR spectra for the species **9** and **10** were available due to their thermal instability, the features of **8** were monitored instead (purple trace). In both end reaction mixtures, the resonance of the bridging -OH ligands expected at δ = -9.22 ppm for **8** was absent, while the two other main feature of the ligand backbone at δ = 2.08 ppm and δ = 2.36 were shifted to the values typical of the free ligand, δ = 1.78 ppm and δ = 2.24 ppm, respectively. Moreover, both end reaction mixtures exhibited a peak at δ = 9.14 ppm corresponding to the resonance of the -NH groups of **6**. Such observations suggested a total consumption of the two high valent species and their quantitative conversion to **6**. A broadening and a shift of the H_2O peak from δ = 3.47 ppm to δ = 3.28 ppm (for **9)** and δ = 3.12 ppm (for **10)** was also observed, suggesting a change of pH in solution and/or the establishment of a hydrogen bond interaction. Such observations pointed towards the formation of a metastable aquo-ligated complex at the end of the reactions, which has been hypothesized to correspond to a bis-aquo-ligated Ni^{II}_2 species. Such metastable complexes rapidly decayed at room temperature through re-protonation of the diamidate ligand by the previously ligated H_2O molecule, resulting in the formation of **6** and formally OH^- in solution. The OH^- ion generated will affect the resonance of the H_2O in solution justifying the broadening and the shift observed at ^{1}H-NMR for **9** and **10**.

For what concerns the other products of the two reactions, the presence of the characteristic set of peaks of 2,6-di-tert-butyl-1,4-benzoquinone (orange trace) at δ = 1.29 ppm and δ = 6.58 ppm confirmed its formation as product. The presence of a further set of peaks (δ = 1.43 ppm, 3.77 ppm, 6.57 ppm and 6.74 ppm), corresponding to 4-OCH_3-

2,6-DTBP (dark green trace) was observed. Such an observation suggested that the metastable phenoxyl radical previously observed (Table 4.2) underwent overoxidation to form the quinone in both systems.

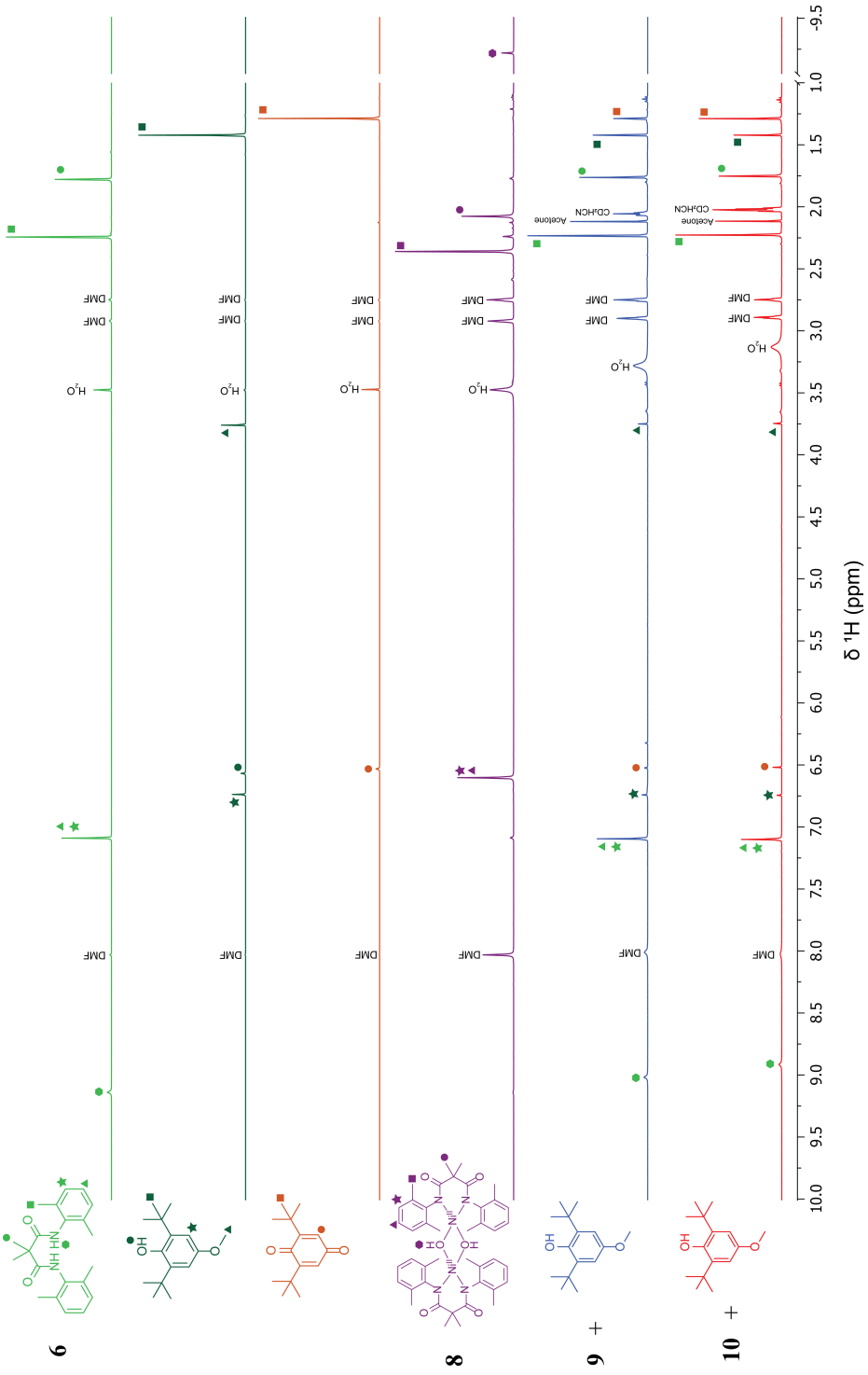

Figure 4.26 – End reaction mixture ^{1}H-NMR for the reaction of **9** and **10** with 4-OCH_3-2,6-DTBP in DMF-D_7 at – 45 °C.

4.3.2 Reactivity of 8 with acids

In light of the results obtained in the previously reported ^{1}H-NMR experiment, we suggested that a putative metastable $Ni^{II}_2(\mu\text{-}OH_2)_2$ species, **8-2H** (Figure 4.27) was formed at the end of the reaction of **10** and **9** with the substrate. This metastable complex was proposed to rapidly decay at room temperature through re-protonation of the diamide ligand by the previously ligated H_2O molecule, resulting in the formation of the detected free ligand **6** and OH^- anions.

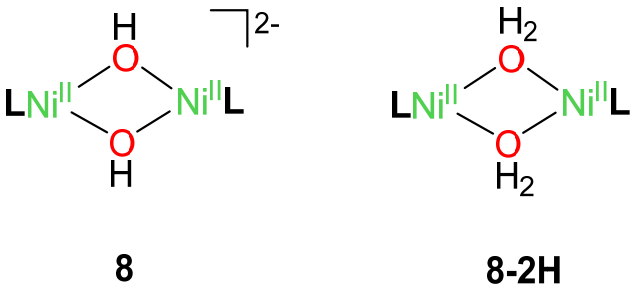

8 **8-2H**

Figure 4.27 – Comparison between **8** and the bis aquo-ligated complexes **8-2H**.

Since the $Ni^{II}_2(\mu\text{-}OH_2)_2$ species **8-2H** was identified as the formally protonated version of the low valent Ni^{II}_2 species **8**, we attempted to isolate the aquo complexes simply by reaction of **8** with an acid at -45 °C in DMF. We decided to use a weak organic acid, since a strong acid would re-protonated immediately by the highly basic diamide ligand causing demetallation. Different weak organic acids were preliminarily screened (Table 4.6, Figures A-4.40–A-4.41) in order to find the best conditions and identify a range of pK_a suitable for the experiment, finding the best candidates in variously substituted benzoic acids.

Compound **8** was then treated with a series of substituted benzoic acids (pK_a 9.37–11.21, Table 4.6) showing an immediate reaction, accompanied by a 8–38 nm range red shift (Figure 4.28). Despite the significant shift caused by some of these acids (*e.g.* 3-Cl benzoic acid), the majority of them led to an unstable species that decayed in few seconds. Acetic acid (pK_a = 11.94) was tested as a comparison, and despite observing a minimal shift, it brought about immediate decay of the complex. Critically, only the 2,6-dimethyl-benzoic acid resulted in a stable species.

Table 4.6 – Screened acids and relative outcomes.

	pK_a in DMSO[a]	**Outcome**
Pyridinium triflate	4.25	quenching
Picolinic acid	8.46	quenching
2-NO_2-benzoic acid	9.37	reaction + shift
2-Br-benzoic acid	10.05	reaction + shift
2,6-dimethyl-benzoic acid	10.40	reaction + shift
3-Cl-benzoic acid	11.04	reaction + shift
Benzoic acid	11.21	reaction + shift
Acetic acid	11.94	reaction
Phenylboronic acid	15.9	No reaction
Boric acid (1st diss.)	16.43	No reaction
H_2O	31.4[18]	No reaction

[a]pK_a in DMSO estimated from the corresponding value in water using the empirical method reported by Knapp et al.[19]

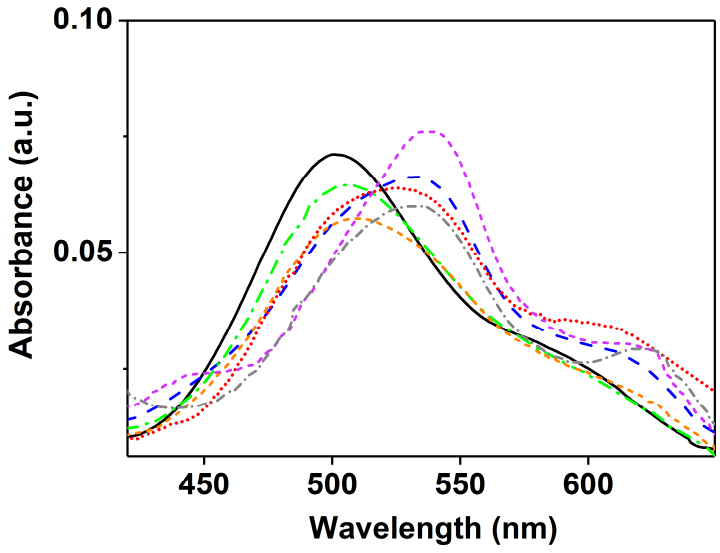

Figure 4.28 – UV-Vis of **8** (502nm feature, black trace) after addiction of benzoic acid (blue trace), acetic acid, (green trace), 2-Br-benzoic acid (orange trace), 3-Cl-benzoic acid (purple trace), 2-NO_2-benzoic acid (grey trace) and 2,6-dimethyl-benzoic acid (red trace). Each trace corresponds to the addition of 4 equiv. of acid at -45 °C in DMF.

In order to test the nature of such interactions, we used the conversion of **8** to **10** as mechanistic probe. A solution containing **8** was treated with 4 equiv. of 2,6-dimethyl-benzoic acid, causing the shift of the feature of **8** at λ = 502 nm (Figure 4.29, red trace). Addition of 3.4 equivalents of CAN resulted in decreased yield of **10** (Figure 4.29, inset, red trace) compared to the control experiment in absence of acid (Figure 4.29, black trace), suggesting a decrease of the amount of **8** in solution. Subsequently, a solution containing **8** and 4 equiv. of 2,6-dimethyl-benzoic acid was treated with 4 equiv. of 1,8-diazabicyclo(5.4.0)undec-7-ene (DBU, Figure 4.27, blue trace), causing the partial restoration of the feature of **8** at λ = 502nm (Figure 4.29). Addition of 3.4 CAN to this solution led to the formation of **10** in similar yield to the control experiment. (Figure 4.29, inset, blue trace), indicated that the concentration of **8** was reverted to its initial extent. Such observations indicated the presence of an equilibrium between **8** and the protonated species (Scheme 4.2) in the presence of 2,6-dimethyl-benzoic acid .

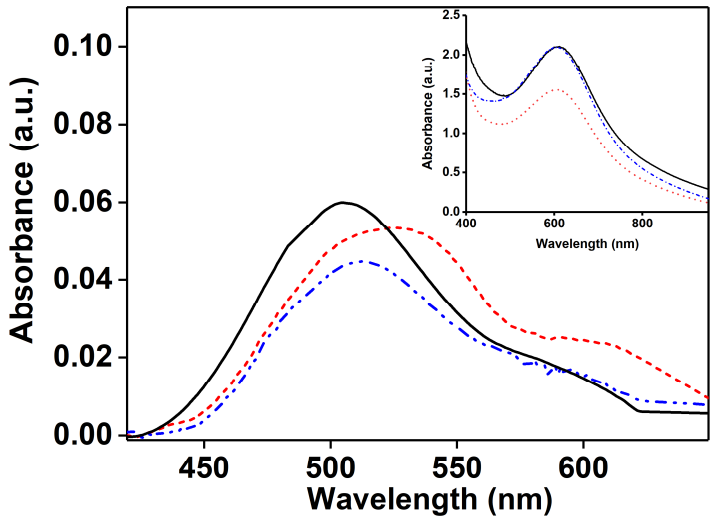

Figure 4.29 – UV-Vis of **8** (black trace) in the presence of 4 equiv. of 2,6-dimethyl-benzoic acid (red trace) and subsequent addition of 4 equiv. of DBU (blue trace). Inset: comparison of the oxidation yield of **10** (black trace) in the presence of 2,6-dimethyl-benzoic acid (red trace) and subsequent addition of DBU (blue trace).

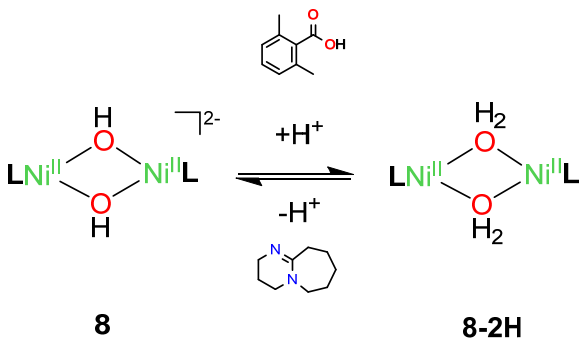

8 **8-2H**

Scheme 4.2 – Proposed equilibrium for the protonation of **8** by 2,6-dimethyl benzoic acid and possible de-protonation by DBU.

In light of such results a proper UV-monitored titration of **8** with sub-stoichiometric amounts (0.25 equiv.) of 2,6-dimethyl-benzoic acid was performed (Figure 4.30, A-4.43). Upon addition of a maximum of 2.5 equiv. of acid, we observed a clear conversion of **8** to a different species with λ_{max} = 535 nm, as observed previously (Figure 4.30). Addition of further equivalents of acid (Figure A-4.43) caused the decay of such a feature, albeit no change in λ_{max} was observed. Such an observation suggested a decrease of the concentration of the protonated species (*i.e.* **8-2H**) as a result of a further conversion of the latter to a featureless compound.

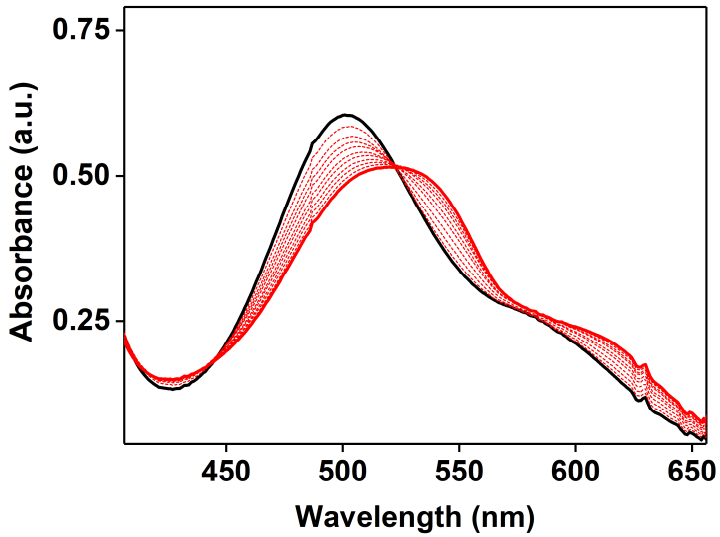

Figure 4.30 – UV-Vis monitored titration of **8** (black trace) with sub-stoichiometric amount of 2.6 dimethyl benzoic acid at -45˚C in DMF. Each dashed line corresponds to an increment of 0.25 equiv, till a maximum of 2.50 equiv.

The plot of [**8-2H**][2,6 $DMBA^-]^2$/[**8**] vs. $[2,6\ DMBAH]^2$ is reported in Figure 4.31. This plot has been drawn considering the protonation of **8** by the 2,6-dimethyl-benzoic acid to led to **8-2H**, therefore a two proton equilibrium. The obtained plot is better fitted with two separate linear trends (Figure 4.31). The slope of the fits, which correspond to the equilibrium constants of the two reactions, have been calculated to be $K_1 = 1.0\times 10^{-10}$ (Figure 4.31, red straight line) and $K_2 = 2.1\times 10^{-10}$ (Figure 4.31, blue straight line).

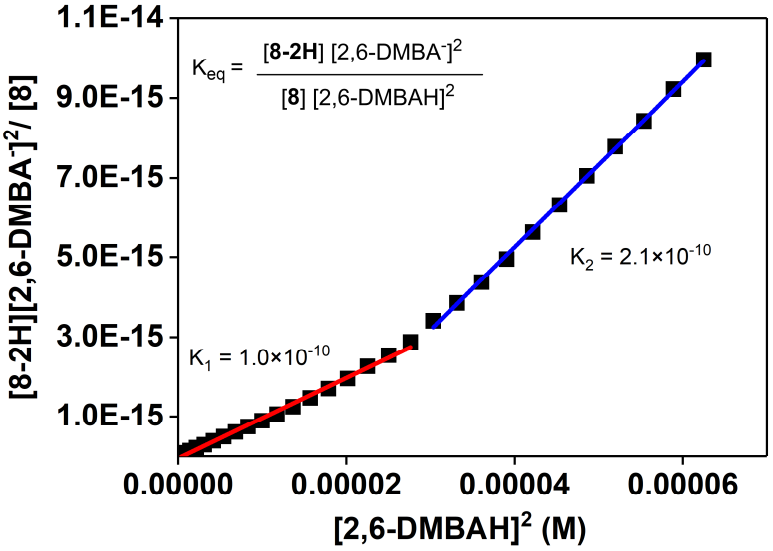

Figure 4.31 – Plot of $[2,6\ DMBAH]^2$ vs. [**8-2H**][2,6 $DMBA^-]^2$/[**8**]. 2,6 DMBAH = 2,6-dimethyl benzoic acid; 2,6 $DMBA^-$ = 2,6-dimethyl-benzoate.

4.3.3 Discussion about the reaction mechanism for 10, 9 and 9'

In order to elucidate the oxidation mechanism for the reaction of **10**, **9** and **9'** with the substrates, we performed ^{1}H-NMR experiments on the post-reaction mixture for the reaction of **10** and **9** with 4-OCH_3-2,6-DTBP (see section 4.3.1). The detection of free ligand **6** and of OH^- anion in the end reaction solutions suggested the formation of metastable aquo-ligated complexes as products of the reaction with the substrate. Moreover, the ligated H_2O has been proposed to be responsible for the re-protonation of the basic diamidate ligand, thus resulting in the formation of the detected products in solution (**6** and formally OH^-). Such evidences are consistent and coherent with the HAT mechanism suggested by the kinetic analysis discussed above.

The aquo-ligated species was proposed to correspond to the $Ni^{II}_2(\mu\text{-}OH_2)_2$ species **8-2H**, formally the double protonated analogue of **8**. Further information was obtained upon UV-monitored titration of **8** with 2,6-dimethyl-benzoic acid. The obtained [**8-2H**][2,6 $DMBA^-]^2$/[**8**] vs. [2,6 DMBAH]^2 plot (Figure 4.31) was fitted with two separate linear trends, suggesting that the protonation reaction was not a simple A-to-B conversion,[48] but a stepwise A-to-B-to-C reaction. These observations suggested a stepwise protonation of the hydroxide groups on **8**, to form the mono-protonated **8-H** and subsequently the di-protonated **8-2H** (Scheme 4.3). The slope of the fits, which correspond to the equilibrium constants of the two reactions, have been calculated to be $K_1 = 1.0\times 10^{-10}$ and K_2 2.1×10^{-10} (Figure 4.31, blue straight line). Therefore, we derived the pK_a values of the two protonated species, which correspond to pK_a = 9.7 for **8-2H** and pK_a = 10 for **8-H**.

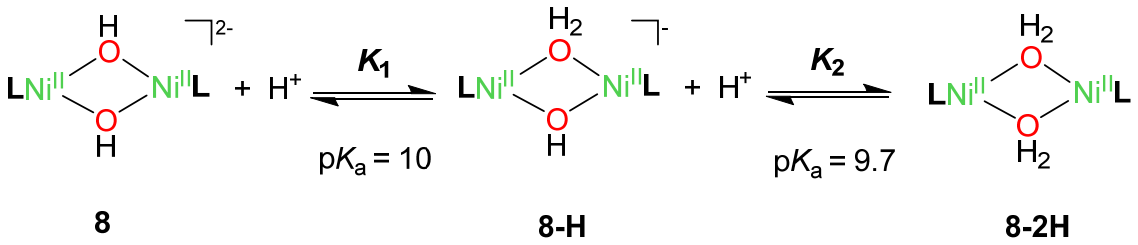

Scheme 4.3 – Stepwise protonation of **8** to achieve **8-H** (K_1=1.0×10^{-10}) and **8-2H** (K_2=2.1×10^{-10}).

In light of the result obtained in this chapter, we proposed a possible reaction mechanism for the active species herein reported. The reaction mechanism proposed for **9** (Scheme 4.4) suggests that **9** reacts with the substrates through a hydrogen atom transfer mechanism, leading to the formation of the phenoxyl radical (which undergoes different successive oxidation pathways according to the influence of the *para* substituent, see 4.2.3). The compound **9** decayed through the formation of the postulated species **8-H**, which further decayed at room temperature leading to the re-protonation of the ligand and OH^- in solution, as observed in the ^{1}H-NMR experiment.

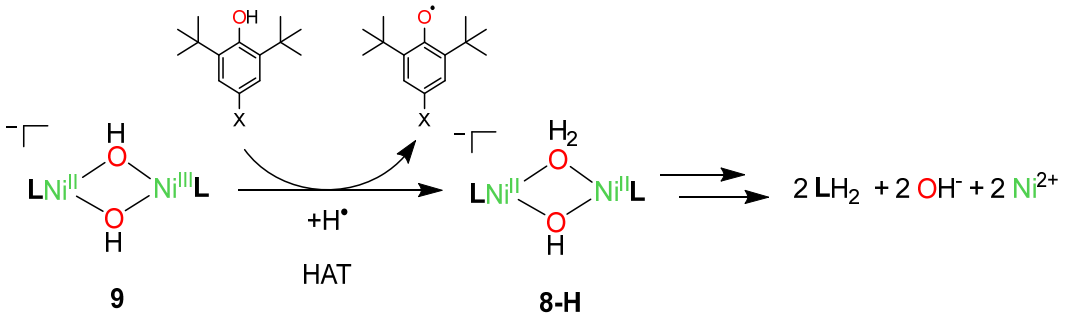

Scheme 4.4 – Proposed reaction mechanism for the reaction of **9** with substrate

A similar mechanism was proposed for the species **10** (Scheme 4.5). Species **10** is proposed to oxidise the phenol substrate by HAT leading to the formation of the phenoxyl radical and species **9'**. The latter continued reacting with excess substrate at slower rate through a hydrogen atom transfer mechanism, forming an additional equivalent of phenoxyl radical and the unstable species **8-2H**. As proposed in the previous chapter, the aquo-ligated species was unstable and decays through re-protonation of the ligand and probable formation of OH^-, coherently with the ^{1}H-NMR results reported in chapter 4.3.1.

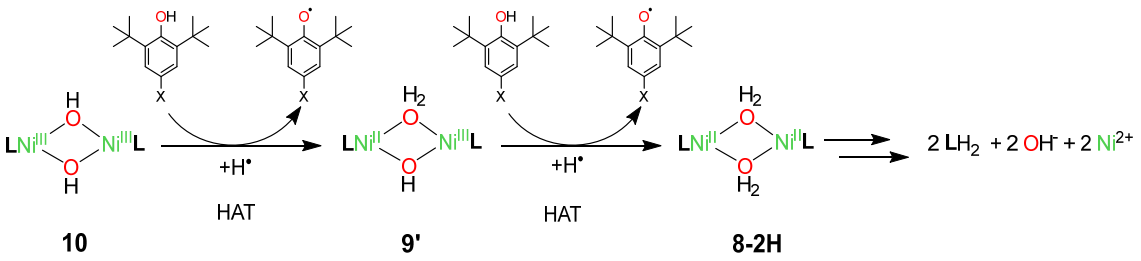

Scheme 4.5 – Proposed reaction mechanism for the reaction of **10** and **9'** with substrate.

4.4 Additional reactivity studies

4.4.1 Reactivity towards C–H bonds

Once the reactivity towards O–H was fully analysed, we studied the reactivity of **9**, **10** towards C–H activation. The two species **9** and **10** were preliminarily reacted with a weak C–H bond substrate, 9,10-dihydroanthracene (DHA, BDE_{C-H} = 78 kcal/mol),[8] at -45 °C in DMF, monitoring the reaction by electronic absorption spectroscopy. Surprisingly, no reaction was observed for **9** at the operative conditions. However, **10** reacted very slowly with DHA leading to the formation of **9'** and anthracene (Figure 4.32). The oxidised product was successfully identified by GC-MS (Figure A-4.44) and electronic absorption spectroscopy (Figure 4.32, λ = 360, 379 nm).[52 53] Attempts to measure k_{obs} by *pseudo-first order* kinetic model were performed, leading however to values very close to the self-decay rate of the complex (4.59×10^{-4} s^{-1}), making the calculation of a k_2 value innacurate under the experimental conditions. In the interest of completeness, the amount of anthracene produced in the reaction between **10** and DHA was quantified by flame ionization detector gas chromatography (GC-FID). After proper calibration and method setup (Figure A-4.45) GC analysis allowed us to identify anthracene in the post-reaction mixture obtained in ~80% yield with respect of **10** (Table 4.7). This observation allowed us to demonstrate that, even though a proper kinetic study was not possible, **10** was however capable of activating weak C–H bonds at -45 °C, converting DHA to anthracene.

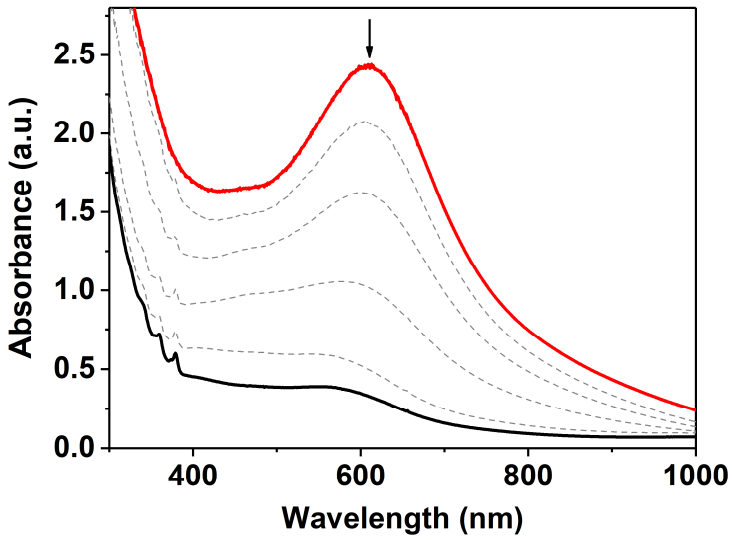

Figure 4.32 – UV-Vis spectra for the reaction of **10** (red trace) with DHA at -45 °C in DMF.

Table 4.7 – Quantification of anthracene found for the reaction between **10** and DHA upon GC-FID analysis of post-reaction mixture

	200 equiv. DHA	**100 equiv. DHA**
Overall amount detected	7.06×10^{-7} mol	5.41×10^{-7} mol
Blank	3.85×10^{-7} mol	2.30×10^{-7} mol
Oxidation product	3.21×10^{-7} mol	3.12×10^{-7} mol
Yield	80%	78%

Reactions of **10** with other weak C–H substrates, such as xanthene ($BDE_{C–H}$ = 75.5 kcal/mol, Figure A-4.46),[8] and 1,4 cyclohexadiene ($BDE_{C–H}$ = 74 kcal/mol, Figure A-4.47) were also conducted. Despite the GC-MS evidence for the formation of the oxidised products (respectively xanthone and benzene, Figure A-4.48), analysis of the data led to the same k_{obs} observed for the reaction with DHA. Such observations suggested that the oxidation of these weak C–H bonds hydrocarbons was kinetically competitive with the self-decay of the complex and the observed k_{obs} values were relative to the complex decay and independent from the substrate used. Therefore, since no other suitable substrate with lower $BDE_{C–H}$ were available, no further kinetic studies were performed about C–H oxidation.

4.4.2 Reactivity of 10 with bases

In the previous sections we analysed the reactivity properties towards O/C–H activation by the bis-μ-hydroxo species **9** and **10**. We observed that, despite the presence of the hydroxo moieties, such complexes were better oxidants than several $Ni^{III}_2(\mu\text{-}O)_2$ complexes.[5, 6, 49] However, such an observation raised the question about the possibility of converting **9** and **10** to their μ-oxo analogues in order to perform a proper comparison. Since the μ-oxo analogues are formally de-protonated versions of **9** and **10,** we opted for a simple approach, attempting to de-protonate them with a base. Therefore, compound **10** was preliminarily reacted with a series of different bases (Table 4.8, Figure 4.33, A-4.50–A-4.54), with the aim of observing the possible formation of analogue bis-μ-oxo complexes that, according to literature examples, should exhibit an intense feature around 400nm.[5, 6, 54]

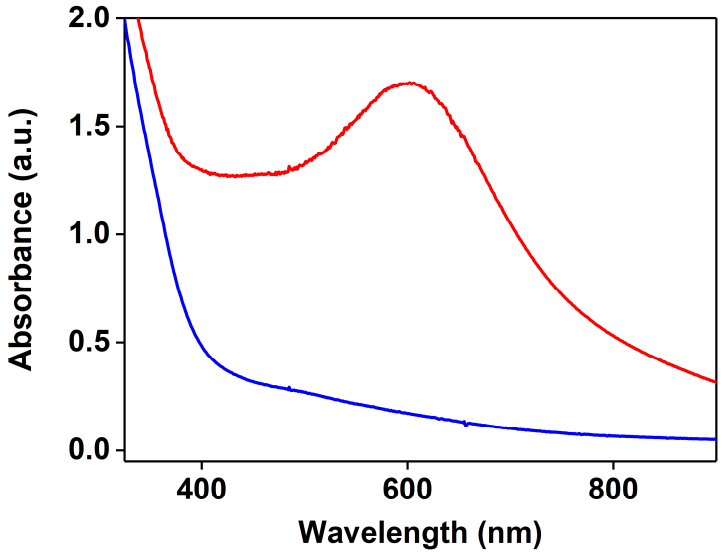

Figure 4.33 – UV-Vis spectra for the reaction of **10** (red trace) with 2 equiv. of tetrabutylammonium hydroxide (methanol solution, blue trace) at -45 °C in DMF.

Upon addition of each base (Figure 4.33, A-4.50–A-4.54), rapid decay of **10** was observed. For the bases in methanol solution (*i.e.* tetrabutylammonium hydroxide and KOH) a control experiment was performed adding pure methanol to **10** (Figure A-4.49), showing a 50% quench of high valent species features. However, in the presence of 2–4 equiv. of tetrabutylammonium hydroxide or KOH, complete quenching was observed (Figures

4.34, A-4.51), suggesting that the decay of **10** was caused by both solvent and base. Complete quenching was observed also in the presence of few equivalents of two other strong bases such as potassium *tert*-butoxide (Figure A-4.50) and DBU (Figure 4.54). We also analysed the reaction with pyridine and 2,6-lutidine, that exhibited lower pK_a (Table 4.8). Even in these cases, complete or partial quenching of **10** was observed (Figure A-4.52–A-4.53), albeit a higher number of equivalents was required. In all cases no formation of new features was observed, excluding the formation of a visible bis-μ-oxo species. However, the hypothesis regarding formation of a transient unstable bis-μ-oxo species, that decayed immediately after its formation was not completely ruled out, albeit no conclusions can be draw at this stage. Considering the characteristics of the supporting ligand **6,** it is reasonable to think that it will push electron density on the metal, thanks to its anionic amido functionalities, making a hypothetical oxido complex quite unstable. Therefore, a possible interpretation of the decay observed for all the bases used could be the complete or partial deprotonation of **10**, which leads to the formation of a transient, highly unstable μ-oxo complex. Such a complex would immediate decay, on a time scale that does not allow us to observe any significative change on the electronic absorption spectra.

Table 4.8 – Bases tested for the reaction with **10**

Base (solvent)	pK_a in DMSO[a]	Reaction
Tetrabutylammonium hydroxide (methanol)	31.4	Decay
Potassium *tert*-butoxide (THF)	32.2[55]	Decay
Potassium hydroxide (methanol)	31.4	Decay
Pyridine	4.25	Decay
2,6 lutidine	5.6	Decay
DBU	17.8	Decay

[a] pK_a in DMSO estimated from the correspondent value in water using the empirical method reported by Knapp et al.[19]

4.4.3 Reactivity with triphenylphosphine (PPh_3)

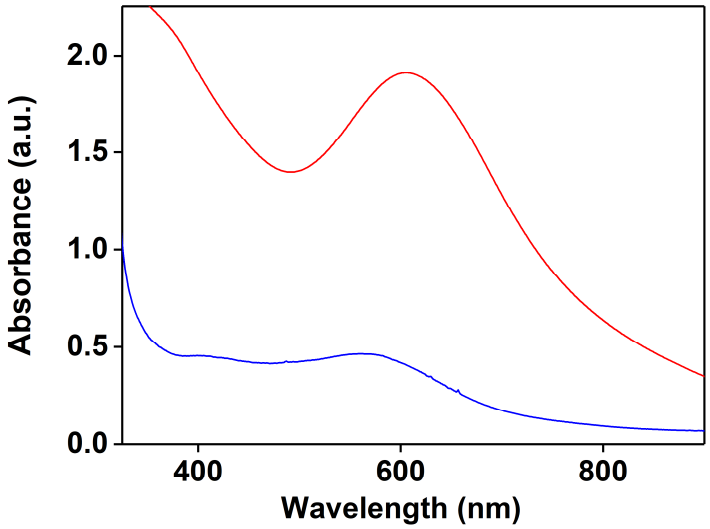

Figure 4.34 – UV-Vis spectra for the reaction of **10** (red trace) with 50 equiv. of PPh_3 at -45 °C in DMF.

In the previous sections of this chapter we analysed the reactivity properties of species **9** and **10**, showing their ability to oxidise different O/C–H substrate by hydrogen atom transfer mechanism. However, the established presence of the O–H ligand in the high valent species (see Chapter 3) raised the question regarding the possible oxygen atom transfer (OAT) reactivity by **9** and **10**. Therefore, we decided to react the high valent species with PPh_3, which is a widely use OAT probe.[56, 57] Preliminary reaction of **10** with PPh_3 at -45 °C in DMF (Figure 4.34) showed a rapid decay of the feature associated the complex, highlighting the formation of **9'** and suggesting a decay pathway similar to what observed for HAT. However, in order to gain evidence regarding the occurrence of an OAT process, the end reaction mixture was required to be analysed for the presence of the oxygen atom transfer product of PPh_3, namely $O{=}PPh_3$ (triphenylphosphine oxide). Therefore, the end reaction mixtures of the reaction of **9** and **10** with PPh_3 in DMF-D_7 were analysed by room temperature ^1H and ^{31}P NMR. Comparison of the end reaction mixture ^1H-NMR spectra for **9** (blue trace) and **10** (red trace) with control experiments spectra of PPh_3(orange trace), $O{=}PPh_3$ (dark green trace), **6** (green trace) and **8** (purple trace) is shown in Figure 4.35. Analysing the reaction of **9** with PPh_3, a clear conversion of the complex to the free ligand was observed, together with a broadening of the H_2O

resonance peak. Such observations were observed also in section 4.3.1 suggesting a similar outcome.

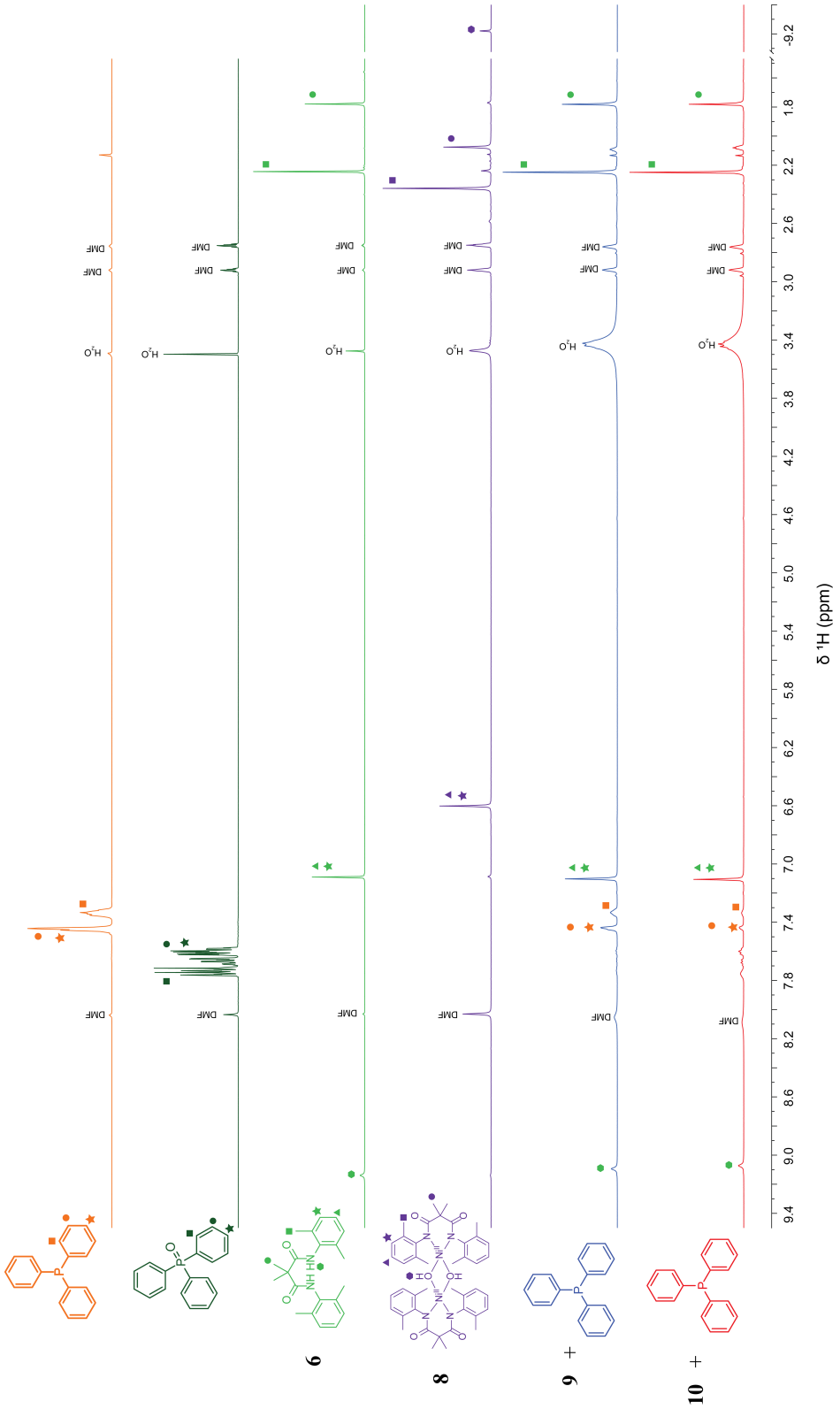

Figure 4.35 – End reaction mixture ^{1}H-NMR for the reaction of **9** and **10** with PPh_3 in DMF-d7 at – 45 °C.

Peaks related to residual of PPh_3 were detected (δ = 7.33−7.44 ppm), but no clear evidence for formation of $O{=}PPh_3$ was observed. Similar behaviour was observed for the reaction of **10** with PPh_3. Even in this case, complete conversion of **10** to free ligand, along with broadening of H_2O peak was observed. Analysis of the aromatic region showed instead a less intense peak for the residual PPh_3 at δ = 7.33−7.44 ppm, and the presence of new broad weak peaks at δ = 7.58 and δ = 7.68 ppm, compatible with $O{=}PPh_3$ formation.

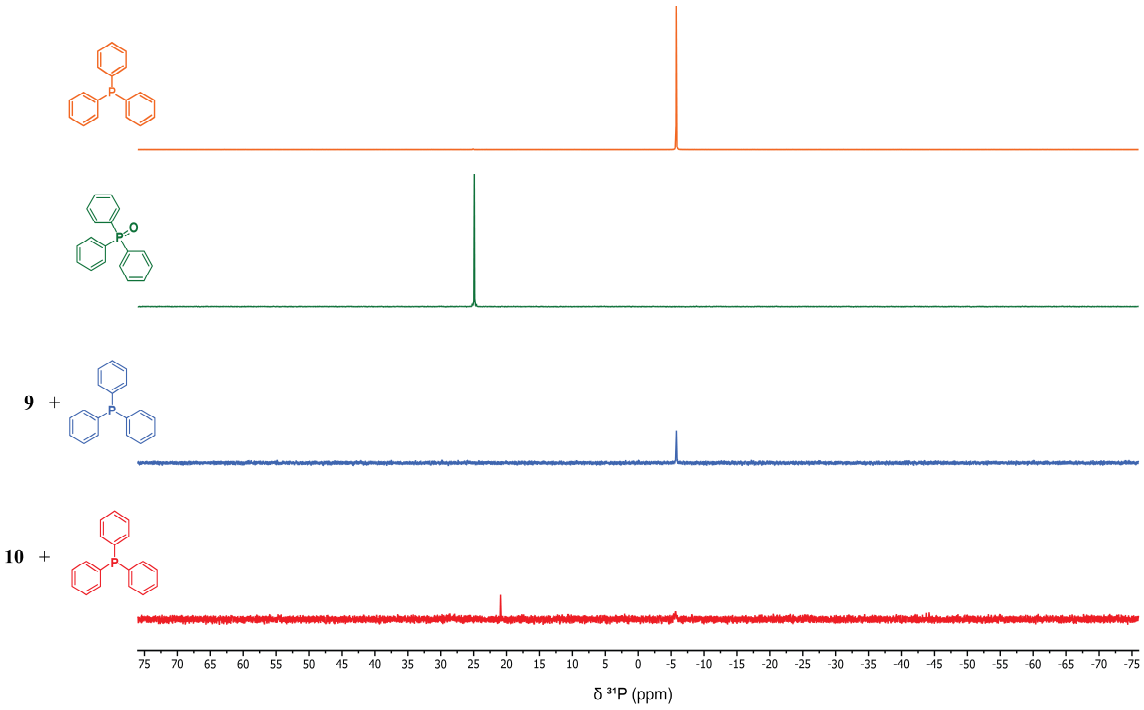

Figure 4.36 – End reaction mixture ^{31}P-NMR for the reaction of **9** (blue trace) and **10** (red trace) with PPh_3 (purple trace) in DMF-D_7 at -45 °C and comparison with $O{=}PPh_3$ (green trace).

^{31}P-NMR spectra are reported in Figure 4.36. As observed for the ^{1}H-NMR, in the case of the reaction of **9**, only the peak of the residual triphenylphosphine was observed at δ = -5.90 ppm. Post-reaction for **10** showed instead the presence of a very weak peak for PPh_3 and a new peak at δ = 20.90 ppm. Such a value, however, was ~ 4 ppm downshifted compared to $O{=}PPh_3$ (δ = 24.83 ppm) ruling out the formation of the triphenylphosphine oxide product.

This unexpected outcome will require more analysis for its identification in future works. Although no conclusive results can be drawn at the moment, some hypotheses can be proposed. Formation of $O{=}PPh_3$ as OAT product of PPh_3 was observed mainly in M=O

and M–O–M complexes.[56, 57] Therefore, the presence of the hydroxo ligand instead of the oxo in **9** and **10** could prevent the OAT from occurring. However, the evidence observed in the ^{1}H and ^{31}P-NMR spectra for the reaction of **10**, could be related to some form of phosphorus-based adduct, either with hydroxide to form some kind of phosphonium ion, or with the free Ni^{2+} generated by the decay of the complex.

4.5 Conclusions

In conclusion, we analysed and discussed in detail the reactivity of **10** and **9** towards phenolic O−H oxidation. Critically, upon reaction of **10** with the substrates, we observed the formation of a new transient species, **9'** which has been demonstrated to react with substrates in a very similar fashion to **9**. In order to have a deeper insight in the oxidation mechanism involved, the reactivity of the three species with a series of 4-X-2,6-DTBP (X = $-OCH_3$, $-CH_2CH_3$, $-CH_3$, $-C(CH_3)_3$, −H, −Br, −CN, $-NO_2$) was analysed. The analysis and study of the obtained kinetic data indicated that all three species performed the oxidation of the analysed substrates through a HAT mechanism. The KIE values were calculated for **10** (KIE ~4), **9** (KIE ~2) , and **9'** (KIE ~4.8) identifying the hydrogen abstraction event as the rate determining step. Moreover, the KIE values obtained were all within the classical limit of 7, ruling out any tunnelling mechanism. Analysis of the post-reaction mixtures allowed us to outline a coherent mechanism for the oxidation of phenolic O−H bond by species **10**, **9** and **9'**. Finally, the reactivity of **10**, **9** and **9'** were compared with mono and dinuclear high valent Ni complexes reported in literature. Critically, **10** displayed k_2 values higher than any reported $Ni^{III}_2(\mu\text{-}O)_2$ complex reported to date and was demonstrated to be capable of activating weak C–H bonds. These results demonstrate that high-valent hydroxide-bridged dinuclear clusters are capable oxidants and match the kinetic reactivity of the most reactive comparable oxo-bridged entities, turning the tables in the current understanding of the activity of several metallo-enzymes.

4.6 Experimental Section – Chapter 4

Physical Methods

Electronic absorption spectra were recorded on a Agilent 8453 diode array spectrophotometer (190-1100 nm range) equipped with a cryostat unit from Unisoku Scientific Instruments (Osaka, Japan). Gas Chromatography/mass spectrometry (GC/MS) was performed using a GCT Premier Micromass Time of Flight (ToF) mass spectrometer. ^{1}H, ^{31}P nuclear magnetic resonance (NMR) analyses were performed on an Agilent MR 400 MHz (400.13 MHz for ^{1}H-NMR and 162.05 MHz for ^{31}P-NMR). Gas chromatography experiments have been performed using a ThermoFisher TRACE™ 1300 Gas Chromatograph equipped with a Flame Ionisation Detector. Hydrogen was provided by a Parker Hydrogen Gas Generator 20H-MD. Air was provided by Parker Zero Air Generator UHP-10ZA-S. The column used is a ThermoFisher TraceGOLD TG-1MS GC column.

Materials

All reactions were performed under atmospheric conditions. Reagents and solvents were purchased from commercial suppliers and have been used as received, unless otherwise stated.

Preparation of complexes 9 and 10

The complexes 9 and 10 were prepared according to the procedure reported in Chapter 3[58]

Preparation of 4-NO_2-2,6-di-*tert*-butyl-phenol

The 4-NO_2-2,6-di-*tert*-butyl-phenol was synthesised according the reported procedure.[59]

Preparation of 4-X-2,6-di-tert-butyl phenoxy radicals (X = –OCH_3, –$C(CH_3)_3$)

The 4-X-2,6-di-tert-butyl phenoxy radicals (X = –OCH_3, –$C(CH_3)_3$) were synthesised according the reported procedures.[10, 11]

Kinetic experiments

Different amounts of substrate, as a DMF solution, were added to a 0.2 mM solution in N,N' dimethylformamide (DMF) of **9** or **10** at -45 °C (prepared in situ according to the procedure reported in Chapter 3)[58] causing the immediate decay of the spectral features of the oxidant species. For species **9**, the monitored wavelength was λ_{max} = 560nm (Figure 4.3), while in the case of species **10** was monitored λ_{max} = 600nm (Figure 4.1). The decay of these features upon addition of substrates was fitted using a *pseudo-first order* kinetic model, obtaining a k_{obs} for each reaction. For complex **9**, the decay pattern was composed of single exponential curve (Figure 4.3, inset). In the case of the reaction of **10** with the substrates, a biphasic decay pattern was observed (Figure 4.2). The first exponential decay, corresponding to the reaction between **10** and the substrate to give **9'** and the $1e^-$ oxidised substrate was considered for the kinetic studies relative to **10**. The second phase, relative to the reaction of **9'** with excess substrates, was instead considered for the kinetic studies of **9'**. Reporting the k_{obs} values obtained against the concentrations of the correspondent substrate allowed the determination of the *second order* rate constant (k_2) for the examined substrate as the slope of the resulting k_{obs} vs. [substrate] plot.

Gas chromatography-Flame Ionisation Detector (GC-FID) analysis:

Solution of **10** were prepared at -45 °C in situ as described in Chapter 3.[58] Different amounts of 9,10-dihydroanthracene were added as DMF solutions under continuous stirring until complete decay of **10** was achieved. Once the reaction was complete, the reaction mixture was allowed to reach room temperature and then analysed by GC-FID. All the solutions were kept strictly in the dark, to avoid any photochemical oxidation of

excess DHA. A reference standard solution was prepared by adding 100 μL (200 equiv.,) or 50 μL (100 equiv.,) of a 9,10-dihydroanthracene solution (0.8 M in DMF) to 2.04 mL of pure DMF. The instrument method was based on a temperature ramp (2 min at 175 °C, 10 °C/min to 250 °C, 2 min at 250 °C) with injections of 1 μL each. Under these conditions, the retention time for anthracene was between 6.3−6.4 min. The quantitative analysis was based on a calibration curve showed in Figure A-4.45.

NMR experiments in DMF-D_7

Compound **6**

δ ^{1}*H* (400 MHz, [D_7]-DMF): 1.78 (6H, s, -C*H*$_3$), 2.24 (12H, s, Ar-C*H*$_3$), 7.09 (6H, m, Ar-C*H*), 9.14 (2H, s,-N*H*).

Compound **8**

δ ^{1}*H* (400 MHz, [D_7]-DMF): -9.22 (2H, s, -*OH*), 2.08 (12H, s, -C*H*$_3$), 2.36 (24H, s, Ar-C*H*$_3$), 6.60 (12H, m, Ar-C*H*).

4-OCH_3-2,6-di-*tert*-butyl-phenol

δ ^{1}*H* (400 MHz, [D_7]-DMF): 1.43 (18H, s, -C(C*H*$_3$)$_3$), 3.77 (3H, s, -OC*H*$_3$), 6.57 (1H, s, -O*H*), 6.74 (2H, s, Ar-C*H*)

2,6-di-tert-butyl-1,4-benzoquinone

δ ^{1}*H* (400 MHz, [D_7]-DMF): 1.29 (18H, s, -C(C*H*$_3$)$_3$), 6.58 (2H, s, Ar-C*H*)

Triphenylphosphine (PPh_3)

δ ^{1}*H* (400 MHz, [D_7]-DMF): 7.32–7.35 (6H, m, Ar-C*H*), 7.44–7.48 (9H, m, Ar-C*H*)

δ ^{31}*P* (162 MHz, [D_7]-DMF): -5.78 ppm

Triphenylphosphine oxide ($O=PPh_3$)

δ ^{1}*H* (400 MHz, [D_7]-DMF): 7.41 (6H, m, Ar-C*H*), 7.47 (3H, m, Ar-C*H*), 7.54 (6H, m, Ar-C*H*)

δ ^{31}*P* (162 MHz, [D_7]-DMF): 24.9 ppm

4.7 References

(1) J. J. Warren, T. A. Tronic and J. M. Mayer, *Chem. Rev.*, 2010, **110**, 6961-7001.
(2) J. M. Mayer, *Acc. Chem. Res.*, 2011, **44**, 36-46.
(3) J. M. Mayer, *Acc. Chem. Res.*, 1998, **31**, 441-450.
(4) W. D. Bailey, D. Dhar, A. C. Cramblitt and W. B. Tolman, *J. Am. Chem. Soc.*, 2019, **141**, 5470-5480.
(5) S. Itoh, H. Bandoh, M. Nakagawa, S. Nagatomo, T. Kitagawa, K. D. Karlin and S. Fukuzumi, *J. Am. Chem. Soc.*, 2001, **123**, 11168-11178.
(6) Y. Morimoto, Y. Takagi, T. Saito, T. Ohta, T. Ogura, N. Tohnai, M. Nakano and S. Itoh, *Angew. Chem. Int. Ed.*, 2018, **57**, 7640-7643.
(7) S. Kundu, P. Chernev, X. Engelmann, C. S. Chung, H. Dau, E. Bill, J. England, W. Nam and K. Ray, *Dalton Trans.*, 2016, **45**, 14538-14543.
(8) Y.-R. Luo, *Handbook of bond dissociation energies in organic compounds*, CRC press, 2002.
(9) E. R. Altwicker, *Chem. Rev.*, 1967, **67**, 475-531.
(10) J. M. Wittman, R. Hayoun, W. Kaminsky, M. K. Coggins and J. M. Mayer, *J. Am. Chem. Soc.*, 2013, **135**, 12956-12959.
(11) V. W. Manner, A. G. DiPasquale and J. M. Mayer, *J. Am. Chem. Soc.*, 2008, **130**, 7210-7211.
(12) P. Mondal, P. Pirovano, A. Das, E. R. Farquhar and A. R. McDonald, *J. Am. Chem. Soc.*, 2018, **140**, 1834-1841.
(13) P. Pirovano, E. R. Farquhar, M. Swart and A. R. McDonald, *J. Am. Chem. Soc.*, 2016, **138**, 14362-14370.
(14) S. Srivastava, A. Ali, A. Tyagi and R. Gupta, *Eur. J. Inorg. Chem.*, 2014, **2014**, 2113-2123.
(15) H. Nishino, H. Satoh, M. Yamashita and K. Kurosawa, *J. Chem. Soc. Perk. Trans. 2*, 1999, 1919-1924.
(16) S. Muto and T. C. Bruice, *J. Am. Chem. Soc.*, 1982, **104**, 2284-2290.
(17) The pKa value are in DMSO. The values have been estimated from the correspondent values in water according the procedure reported by Knapp et al. Ref. (46).
(18) W. N. Olmstead, Z. Margolin and F. G. Bordwell, *J. Org. Chem.*, 1980, **45**, 3295-3299.
(19) E. Rossini, A. D. Bochevarov and E. W. Knapp, *ACS Omega*, 2018, **3**, 1653-1662.
(20) M. Lucarini, P. Pedrielli, G. F. Pedulli, S. Cabiddu and C. Fattuoni, *J. Org. Chem.*, 1996, **61**, 9259-9263.
(21) S. Kundu, E. Miceli, E. R. Farquhar and K. Ray, *Dalton Trans.*, 2014, **43**, 4264-4267.
(22) D. T. Yiu, M. F. Lee, W. W. Lam and T.-C. Lau, *Inorg. Chem.*, 2003, **42**, 1225-1232.
(23) S. Kundu, F. F. Pfaff, E. Miceli, I. Zaharieva, C. Herwig, S. Yao, E. R. Farquhar, U. Kuhlmann, E. Bill, P. Hildebrandt, H. Dau, M. Driess, C. Limberg and K. Ray, *Angew. Chem. Int. Ed.*, 2013, **52**, 5622-5626.

(24) J. P. Roth, J. C. Yoder, T.-J. Won and J. M. Mayer, *Science*, 2001, **294**, 2524-2526.
(25) J. M. Mayer, *J. Phys. Chem. Lett*, 2011, **2**, 1481-1489.
(26) J. W. Darcy, B. Koronkiewicz, G. A. Parada and J. M. Mayer, *Acc. Chem. Res.*, 2018, **51**, 2391-2399.
(27) J. J. Warren and J. M. Mayer, *Biochemistry*, 2015, **54**, 1863-1878.
(28) D. R. Weinberg, C. J. Gagliardi, J. F. Hull, C. F. Murphy, C. A. Kent, B. C. Westlake, A. Paul, D. H. Ess, D. G. McCafferty and T. J. Meyer, *Chem. Rev.*, 2012, **112**, 4016-4093.
(29) A. Sirjoosingh and S. Hammes-Schiffer, *J. Phys. Chem. A*, 2011, **115**, 2367-2377.
(30) M. G. Evans and M. Polanyi, *Trans. Faraday Soc.*, 1938, **34**, 11-24.
(31) M. G. Evans and M. Polanyi, *Trans. Faraday Soc.*, 1935, **31**, 875-894.
(32) H. Eyring, *J. Chem. Phys.*, 1935, **3**, 107-115.
(33) J. M. Mayer, *Annu. Rev. Phys. Chem.*, 2004, **55**, 363-390.
(34) L. P. Hammett, *J. Am. Chem. Soc.*, 1937, **59**, 96-103.
(35) P. Muller, *Pure Appl. Chem.*, 1994, **66**, 1077-1184.
(36) T. Osako, K. Ohkubo, M. Taki, Y. Tachi, S. Fukuzumi and S. Itoh, *J. Am. Chem. Soc.*, 2003, **125**, 11027-11033.
(37) M.-C. Kafentzi, M. Orio, M. Réglier, S. Yao, U. Kuhlmann, P. Hildebrandt, M. Driess, A. J. Simaan and K. Ray, *Dalton Trans.*, 2016, **45**, 15994-16000.
(38) L. R. Mahoney and M. A. DaRooge, *J. Am. Chem. Soc.*, 1970, **92**, 890-899.
(39) R. A. Marcus and N. Sutin, *BBA-Bioenergetics*, 1985, **811**, 265-322.
(40) R. A. Marcus, *J. Chem. Phys.*, 1956, **24**, 966-978.
(41) M. S. Ram and J. T. Hupp, *The Journal of Physical Chemistry A* 1990, **94**, 2378-2380.
(42) J. Y. Lee, R. L. Peterson, K. Ohkubo, I. Garcia-Bosch, R. A. Himes, J. Woertink, C. D. Moore, E. I. Solomon, S. Fukuzumi and K. D. Karlin, *J. Am. Chem. Soc.*, 2014, **136**, 9925-9937.
(43) I. Garcia-Bosch, R. E. Cowley, D. E. Díaz, R. L. Peterson, E. I. Solomon and K. D. Karlin, *J. Am. Chem. Soc.*, 2017, **139**, 3186-3195.
(44) C. H. Rochester and B. Rossall, *Phys. Org.*, 1967, 743-748.
(45) P. Pirovano and A. R. McDonald, *Eur. J. Inorg. Chem.*, 2018, **2018**, 547-560.
(46) S. Mahapatra, J. A. Halfen, E. C. Wilkinson, G. Pan, X. Wang, V. G. Young, C. J. Cramer, L. Que and W. B. Tolman, *J. Am. Chem. Soc.*, 1996, **118**, 11555-11574.
(47) C. Kim, Y. Dong and L. Que, *J. Am. Chem. Soc.*, 1997, **119**, 3635-3636.
(48) C. McManus, P. Mondal, M. Lovisari, B. Twamley and A. R. McDonald, *Inorg. Chem.*, 2019, **58**, 4515-4523.
(49) S. Kundu, E. Miceli, E. R. Farquhar and K. Ray, *Dalton Trans.*, 2014, **43**, 4264-4267.
(50) D. Unjaroen, R. Gericke, M. Lovisari, D. Nelis, P. Mondal, P. Pirovano, B. Twamley, E. R. Farquhar and A. R. McDonald, *Inorg. Chem.*, 2019, **58**, 16838-16848.
(51) K. J. Fisher, M. L. Feuer, H. M. C. Lant, B. Q. Mercado, R. H. Crabtree and G. W. Brudvig, *Chem. Sci.*, 2020, **11**, 1683-1690.
(52) B. Sun, C.-Q. Ye, Z.-Q. Liang, P. Ding, X.-M. Wang, Z.-G. Chen, X.-T. Tao and Q.-H. Wang, *Asian J. Chem.*, 2014, **26**, 1413-1416.
(53) A. Ohta, K. Hattori, Y. Kusumoto, T. Kawase, T. Kobayashi, H. Naito and C. Kitamura, *Chem. Lett.*, 2012, **41**, 674-676.
(54) K. Shiren, S. Ogo, S. Fujinami, H. Hayashi, M. Suzuki, A. Uehara, Y. Watanabe and Y. Moro-oka, *J. Am. Chem. Soc.*, 2000, **122**, 254-262.
(55) L. M. Huffman, A. Casitas, M. Font, M. Canta, M. Costas, X. Ribas and S. S. Stahl, *Chem. Eur. J.*, 2011, **17**, 10643-10650.
(56) J. Cho, J. Woo and W. Nam, *J. Am. Chem. Soc.*, 2012, **134**, 11112-11115.
(57) J.-U. Rohde, J.-H. In, M. H. Lim, W. W. Brennessel, M. R. Bukowski, A. Stubna, E. Münck, W. Nam and L. Que, *Science*, 2003, **299**, 1037-1039.
(58) G. Spedalotto, R. Gericke, M. Lovisari, E. R. Farquhar, B. Twamley and A. R. McDonald, *Chem. Eur. J.*, 2019, **25**, 11983-11990.
(59) C. D. Selassie, R. P. Verma, S. Kapur, A. J. Shusterman and C. Hansch, *J. Chem. Soc. Perk. Trans. 2*, 2002, 1112-1117.

Chapter 5

Preparation, characterization and reactivity of a bis-μ-hydroxo-Cu_2 complex

The XAS data collection and analysis were done in collaboration with Dr Eric R. Farquahar (Brookhaven National Laboratory, USA); The EPR measurements were performed by Marta Lovisari (Trinity College Dublin); The XRD data collection and structure solutions and refinements were done by Dr Brendan Twamley (Trinity College Dublin) and Dr Robert Gericke (Trinity College Dublin).

5.1 Introduction

In the previous chapters we reported the synthesis and characterisation of a $Ni^{II}_2(\mu\text{-}OH)_2$ (**8**) complex and its chemical oxidation to the corresponding mixed and high valent species $Ni^{II}Ni^{III}(\mu\text{-}OH)_2$ (**9**) and $Ni^{III}_2(\mu\text{-}OH)_2$ (**10**), proving the unprecedented capability of this system to retain the μ-hydroxo moiety in the high oxidation state.[1] Furthermore, reactivity studies demonstrated that **9** and **10** are capable of oxidising O−H bonds of phenolic systems.

In the present chapter we want to extend the study from Ni^{II} (d^8) to Cu^{II} (d^9), with the aim of analysing how the structure and the properties change after increasing the *d-electron* count. Therefore, herein we report the synthesis and characterisation of a $Cu^{II}_2(\mu\text{-}OH)_2$ (**11**) complex supported by the same malonamide ligand **6** (see Chapter 2) used for **8**, and its chemical conversion to a proposed mixed valent species $Cu^{II}Cu^{III}(\mu\text{-}OH)_2$ (**12**).

5.2 Synthesis and characterisation of a $Cu^{II}_2(\mu\text{-}OH)_2$ complex (11)

Compound **11** was synthesised starting from the malonamide ligand **6** (**H_2L**), which was reacted with dry potassium hydride (KH, 2.5 equiv.) in N,N-dimethylformamide (DMF) at room temperature (Scheme 5.1). The deprotonation reaction resulted in a vigorous bubbling, due to the evolution of H_2 gas from the solution. The copper source, $[Cu(OAc)_2]$ (1 equiv.) was added to the solution immediately after the gas evolution ceased (Scheme 5.1). Addition of the metal salt resulted in a slow colour change of the solution from off-white to dark green brown over a period of ~6h. After this time, the solution was filtered twice under inert atmosphere over Celite® on a glass frit. Double filtration and the use of Celite® was necessary to remove the by-product potassium acetate, which is not soluble in DMF, alongside any trace of unreacted material. Compound **11** was then collected as crystalline material (67% yield) upon purification by DMF/Et_2O (Et_2O = diethyl ether) vapour diffusion re-crystallization. Analogous to what was observed for **8** (see Chapter

3), the preparation of **11** relied on the presence of adventitious H_2O in the DMF solutions, although **11** appeared to be unstable in the presence of excess water.

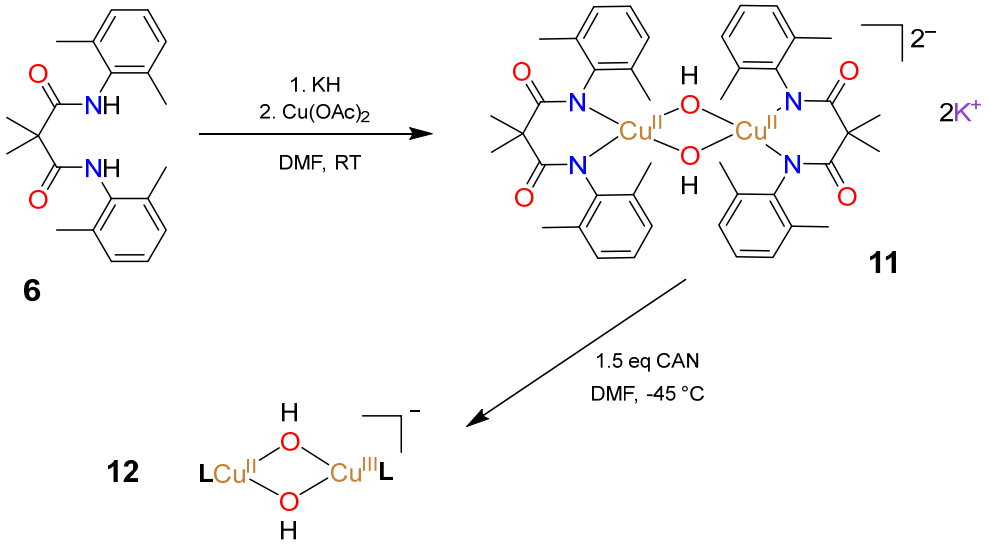

Scheme 5.1 - Synthesis of complex of **11** and oxidation to **12** by $(NH_4)_2[Ce^{IV}(NO_3)_6]$ (CAN) at -45 °C in N,N-dimethylformamide (DMF).

The aforementioned crystalline material contained diffraction quality crystals that were used for X-ray diffraction analysis. Compound **11** exhibited a dinuclear structure with two hydroxide ligands bridging the Cu^{2+} ions in a closed diamond core structure (Figure 5.1). Such a structural motif is quite common for copper complexes, as observed in section 1.5.5. The asymmetric unit of the potassium salt contained two almost identical structures with different degrees of distortion, generated by the strain introduced by the K^+ ions, which created a complex network interacting with the aromatic rings and the molecule of solvent (*i.e.* DMF) co-crystallised into the structure. The two tetracoordinated Cu^{2+} atoms adopted a distorted square planar geometry with $\tau_4 = 0.17$, $\tau_4' = 0.16$ (less distorted species) and $\tau_4 = 0.32$, $\tau_4' = 0.31$ (more distorted structure, $\tau = 0$ square planar, $\tau = 1$ tetrahedral). The distortion of the square planar geometry, which is energetically favoured for d^9 ions in a four-coordinated environment, resulted in the two μ-OH ligands lying in a plane that is tilted compared to the plane formed by the two copper atoms and the nitrogen ligands by an angle range between 12° and 30° (Figure A-5.1).

XRD analysis of **11** after metathesis of K^+ with Me_4N^+ was performed, resulting in crystals exhibiting a single asymmetric unit. The different packaging, due to the presence

of differently hindered counterions, affected the distortion of the Cu centres, which exhibited a distorted square planar geometry with τ_4 = 0.24, τ_4' = 0.23. However, comparison of selected bond distances and angles for the asymmetric units of the K^+ and Me_4N^+ salt of **11** (Table 5.1) showed that the asymmetric unit obtained in the presence of Me_4N^+ can be considered, within the experimental error, an average of the two asymmetric units obtained in the presence of K^+ as counterion. Therefore, in the interest of clarity, we will consider only the crystal structure of the tetramethylammonium salt of **11**.

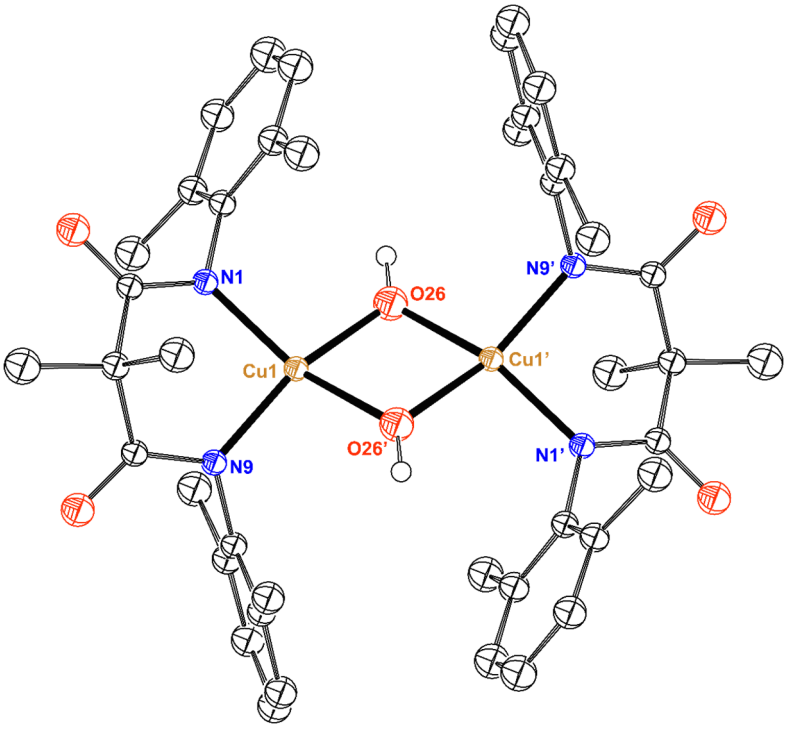

Figure 5.1 - Molecular structure of **11**·DMF·0.5Et_2O obtained by single-crystal X-ray diffraction. Counter ions, solvent molecules and H atoms, except for those associated with the μ-hydroxide ligands, were omitted for clarity. Symmetry generated (‘ = -x,-y+2,-z+1) ORTEP with atomic displacement at 50%.

Table 5.1 – Comparison between selected distances and angles for the structure of **11** in the presence of different counterions.

	Me_4N^+	K^+	K^+
N1–Cu	1.95 Å	1.95 Å	1.94 Å
N9–Cu	1.95 Å	1.94 Å	1.94 Å
Cu1-O26	1.94 Å	1.93 Å	1.93 Å
Cu1–O26'	1.95 Å	1.94 Å	1.93 Å
Cu1···Cu1'	3.06 Å	3.02 Å	3.07 Å
∠ N1-Cu1-O26'	162.15 °	156.78 °	165.92 °
∠ N9-Cu1-O26	164.30 °	158.19 °	169.24 °
τ_4	0.24	0.32	0.17
τ_4'	0.23	0.31	0.16

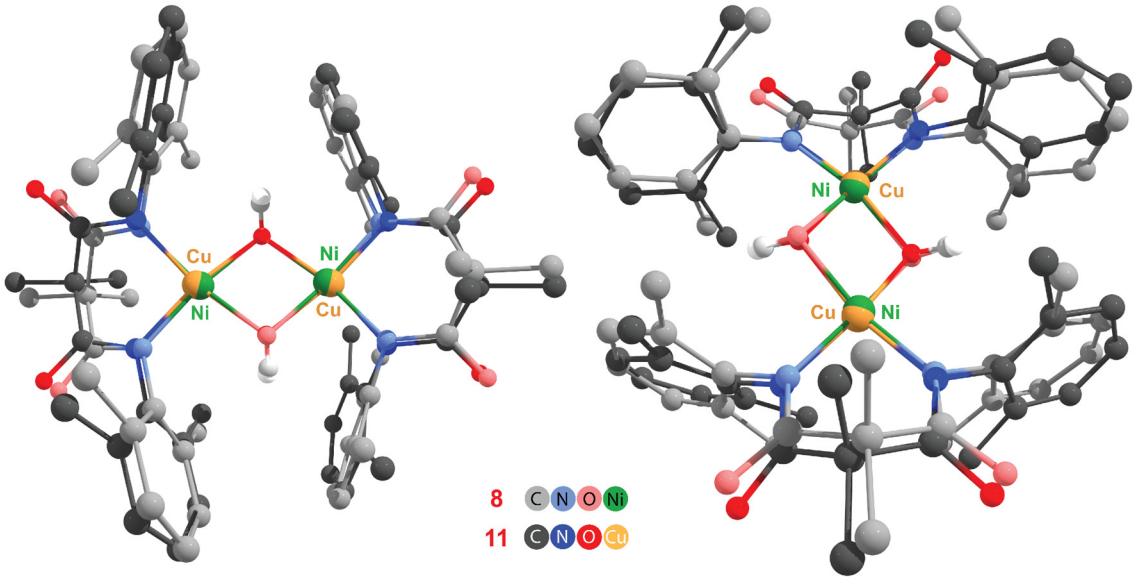

Figure 5.2 – Overlap of the crystal structures of **8** (lighter colours) and **11** (darker colours), top and longitudinal views. Root-mean-square deviation of atomic positions for the $M^{II}_2(\mu\text{-}OH)_2$ core RMSD = 0.147 Å.

The structure of **11** displayed several analogies with the structure of its Ni counterpart **8**. An overlap of the two crystal structures, exhibiting a root-mean-square deviation of atomic positions (RMSD) of 0.147 Å, is reported in Figure 5.2. Such a small value for RMSD is quite indicative of the structural similarities between **11** and **8**.

Table 5.2 – Selected distances (Å) and geometry index for **11** and comparison with **8**.

11		**8**	
N1–Cu	1.95	**N1–Ni1**	1.88
N9–Cu	1.95	**N9-Ni1**	1.88
Cu1-O26	1.94	**Ni1-O15**	1.93
Cu1–O26'	1.95	**Ni1-O15'**	1.90
Cu1···Cu1'	3.06	**Ni1···Ni1'**	2.88
τ_4	0.24	**τ_4**	0.22
τ_4'	0.23	**τ_4'**	0.21

In Table 5.2 are reported selected bond distances for **11** alongside its analogues for **8**. The Cu–N distances in **11** appears to be longer than the corresponding Ni–N observed in **8**, as a result of the increase in covalent radius[2] and *d*-electron count going from Ni^{2+} (d^8) to Cu^{2+} (d^9). Notably, we observe an increase of the M···M distance going from Ni (2.88 Å) to Cu (3.06 Å), albeit the Cu–O(H) distances in **11** and **8** have little-to-no-differences. The Cu···Cu distance observed for **11** is one of the longest reported for anionic diamond core $Cu^{II}_2(\mu\text{-}OH)_2$ complexes, whose distances fall in the range between 2.98–3.06 Å.[3]

The high relaxation time of Cu^{II} (t_s = 1–5 × 10^{-9} s),[4] almost three orders of magnitude larger compared to other late transition metals such as Ni^{II} (t_s = ~ 10^{-12} s),[4] alongside the paramagnetic nature of the d^9 ion, negatively influenced the quality and resolution of the NMR spectra. Several attempts to acquire ^{1}H-NMR data of **11** have been performed, but well resolved data was never obtained.

Additional evidence for the presence of the bridging μ-hydroxide ligands were obtained by ATR/FT-IR spectroscopy (Figure 5.3) which exhibited a sharp feature at ν = 3644 cm^{-1}, typical of a non-hydrogen bonded O–H stretch.[5] Such a distinct feature, present also in

8 (ν = 3615 cm^{-1}), has been observed for several Cu^{II}_2(μ-OH) complexes, such as compound **70** (ν = 3622 cm^{-1})[6, 7] and **72** (ν = 3404 cm^{-1}) reported in Table 1.1.[3] The composition of **11** was further confirmed by negative mode ESI-MS analysis, which detected a single charged ion peak at m/z = 871.1825, whose isotopic pattern and mass corresponded the adduct $[(Cu^{II}(OH)(\mathbf{L}))_2 + K^+]^-$ (Figure A-5.2).

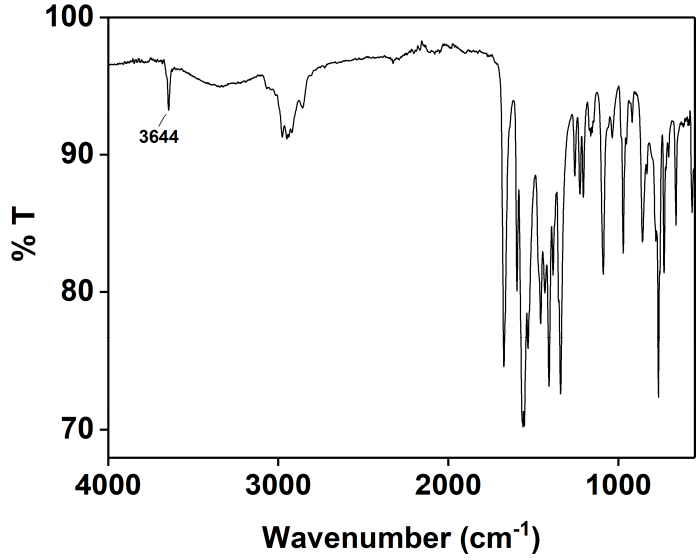

Figure 5.3 – ATR/FT-IR spectrum of **11**

Cyclic Voltammetry was performed on a DMF solution of **11**, in order to probe its electrochemical properties. Compound **11** cyclic voltammetry (Figures 5.4, A-5.3) exhibited a reversible wave at $E_{1/2}$ = -0.35 V ($\Delta E_{pa,pc}$ = 0.07 V) vs. Fc^+/Fc (Figure 5.5, Fc = ferrocene) and a second broad irreversible wave in the range ~0.4-0.5 V vs. Fc^+/Fc (Figure 5.3). The first wave with $E_{1/2}$ = -0.35 V (Figure 5.5, Table A-5.1) was assigned to the $1e^-$ reversible oxidation of **11** to a putative $Cu^{II}Cu^{III}$ species, **12**. The extent of the negative redox potential of the couple $Cu^{II}_2/Cu^{II}Cu^{III}$ was unexpected: although values up to $E_{1/2}$ = -0.26 V have been reported for mononuclear Cu^{II}/Cu^{III} couples,[8] no examples of a such negative potential are reported to date for the dinuclear $Cu^{II}_2/Cu^{II}Cu^{III}$ couple. The extent of the value obtained for **11** can be justified considering the combined electron donating contributions of both amide and hydroxide ligands, which significantly decreased the oxidation potential of the Cu^{II}_2 core enhancing the accessibility of the $Cu^{II}Cu^{III}$ state.

The second irreversible wave at higher potential have been tentatively assigned to the irreversible oxidation of **12** to its Cu^{III}_2 counterpart (~0.4–0.5 V vs. Fc/Fc^+). The irreversibility of such oxidation wave can be addressed to the instability of the proposed highly reactive Cu^{III}_2 species at the experimental conditions. A similar value for the redox potential of the couple $Cu^{II}Cu^{III}/Cu^{III}_2$ was observed for the Cu^{II}_2(μ-OH) complex **75** reported by Tolman,[9] albeit in this case both the oxidations waves, corresponding to $Cu^{II}_2 \rightarrow Cu^{II}Cu^{III} \rightarrow Cu^{III}_2$, appeared to be semi-reversible, probably due to the stabilising effect given by the macrocyclic ligand system used.

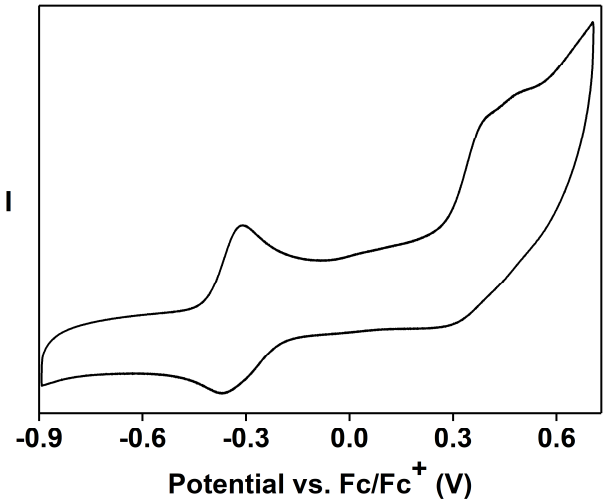

Figure 5.4 - Steady state cyclic voltammograms of **11**. Conditions: 0.33 mM (DMF), 0.1 M Bu_4NPF_6, scan rate 100 mV s^{-1}, room temperature.

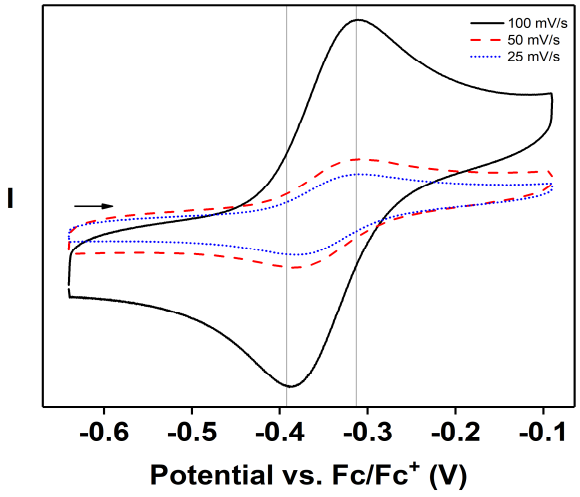

Figure 5.5 – Cyclic voltammograms of **11** (first wave). Conditions: 0.33 mM (DMF), 0.1 M Bu_4NPF_6, scan rate 25 mV/s –100 mV/, room temperature.

5.3 Preparation of a mixed valent $Cu^{II}Cu^{III}$ species (12)

UV-Vis monitored chemical oxidation of **11** to higher oxidation states was probed. Titration of $(NH_4)_2[Ce^{IV}(NO_3)_6]$ (CAN) into a solution of **11** (0.2 mM, DMF, -45 °C), resulted in the immediate formation of a new species, **12**, characterised by an intense absorption feature at λ_{max} = 525 nm (Scheme 5.1, Figure 5.6), with an estimated a half-life of 4260 s at -45 °C. Although sub-stoichiometric additions of oxidant suggested that the maximum yield of **12** was achieved in the presence of 1 equiv. of CAN (Figure 5.7), one-time additions revealed that the maximum yield required up to 1.5 equiv. of oxidant (Figure A-5.5). Notably, the complete disappearance of the feature of **11** at λ_{max} = 398 nm (Figure 5.6) upon addition of CAN suggested a clear conversion from **11** → **12**. It is important to highlight that when more than 1.5 equiv. of CAN were added to **11**, no new features were observed but compound **12** showed an accelerated decay instead.

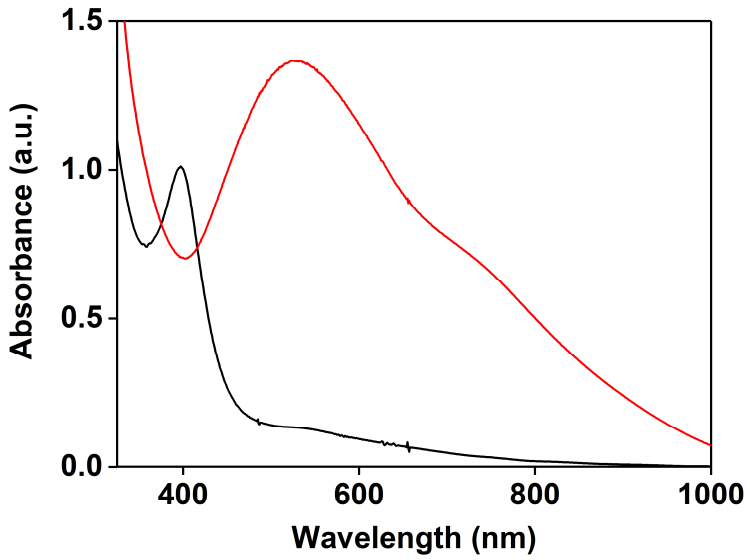

Figure 5.6 - Electronic absorption spectra of species **11** (black trace, 0.2 mM, DMF, -45 °C) and species **12** (red trace), obtained by addition of 1.5 equiv. of $(NH_4)_2[Ce^{IV}(NO_3)_6]$ (CAN).

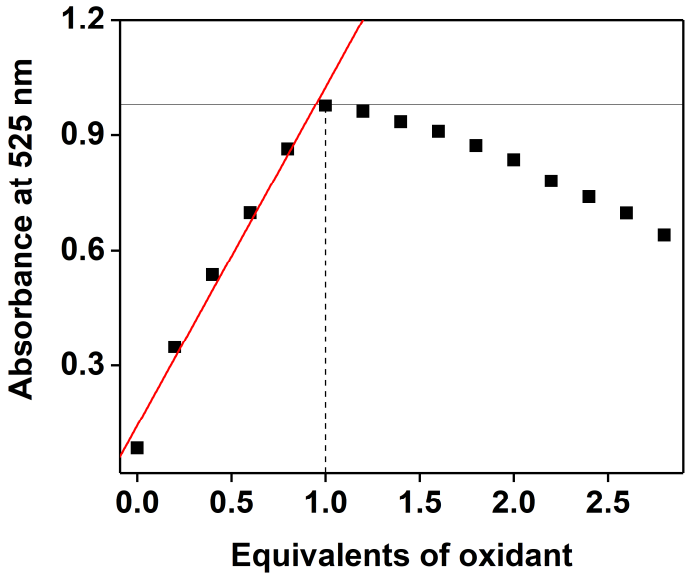

Figure 5.7 - Plot of equiv. of CAN versus absorption intensity at λ = 525 nm for the reaction between **11** and CAN in DMF at -45 °C

In order to get a better insight of the hypothetical structure of **12**, its electronic absorption features were compared with analogous dicopper-oxygen systems reported in literature (Table 1.1). The $Cu^{III}_2(\mu\text{-}O)_2$ complexes generally exhibit an intense LMCT transition between 378 and 430 nm, albeit additional features at lower wavelength are also reported (**91**, λ_{max} = 320 nm ϵ = 12000 $M^{-1}cm^{-1}$, 430 nm ϵ = 14000 $M^{-1}cm^{-1}$; **94**, λ_{max} = 378 nm ϵ = 22000 $M^{-1}cm^{-1}$; **95**, λ_{max} = 402 nm ϵ = 17700 $M^{-1}cm^{-1}$).[10-12] The widely studied side-on $Cu^{II}_2(\mu\text{-}\eta^2\text{:}\eta^2\text{-}O_2)$ complexes exhibit a characteristic LMCT feature around 350 nm (**84**, λ_{max} = 366 nm; **85**, λ_{max} = 350 nm, **88**, λ_{max} = 364 nm),[13-15] starkly different from the less common end-on $Cu^{II}_2(\mu\text{-}\eta^1\text{:}\eta^1\text{-}O_2)$ systems, which show a main feature close to 510 nm with an additional band between 590 nm and 630 nm (**78**, λ_{max} = 525 nm, 590 nm; **79**, λ_{max} = 500 nm, 630 nm; **80**, λ_{max} = 508 nm, 630 nm).[16-18] Only two examples of $Cu^{II}Cu^{III}(\mu\text{-}OH)$ species have been reported to our knowledge, **74**[19] and **76**[9], which displayed a main feature at λ_{max} = 424 nm and λ_{max} = 525 nm, respectively. Although no conclusions can be drawn at this stage, the comparison of **12** with previously reported dicopper-oxygen adducts seems to exclude, in initial analysis, the presence of oxo or side-on peroxo ligands. The end-on peroxo complexes reported have similar features, but

the conversion of the low valent $Cu^{II}_2(\mu\text{-}OH)_2$ species into a $Cu^{II}_2(\mu\text{-}\eta^1\text{:}\eta^1\text{-}O_2)$ appears to be unlikely and energetically disfavoured considering the operative conditions. The results reported by Tolman for their well characterised $Cu^{II}Cu^{III}(\mu\text{-}OH)$ (**76**) and comparison with the behaviour of the Ni analogue complexes (see Chapter 3), suggest that the hydroxide ligands could be retained in **12**. In the light of the experimental observations, the comparison with the reported dicopper-oxygen adducts and the cyclic voltammetry data, we tentatively propose that compound **12** can be identified as a $Cu^{II}Cu^{III}(\mu\text{-}OH)_2$ species.

5.4 EPR Spectroscopy studies

X-band electron paramagnetic resonance (EPR) spectroscopy studies were performed on frozen DMF solutions of **11** and **12** at 77 K (Figure 5.8). As widely reported for Cu^{II}_2 systems,[20] compound **11** was silent in perpendicular mode EPR, due to the strong magnetic coupling ($S = 0$ or $S = 1$) present between the unpaired electrons on the two d^9 ions. The residual signal observed could be ascribed to a distortion in the coordination geometry of the copper centres, which interferes with the coupling of the unpaired spins. **12** exhibited an $S = 1/2$ axial EPR signal with $g_{\|} \sim 2.39$ and $g_{\perp} \sim 2.07$, consistent with a tetragonal Cu^{2+} ion (Figure 5.8). Hyperfine splitting due to the coupling with the ^{63}Cu or ^{65}Cu nucleus ($I = 3/2$) was observed in the $g_{\|}$ component, with a measured $A_{\|} = 120.7$ G. In contrast, no ^{14}N ($I = 1$) superhyperfine coupling was resolved in the EPR spectrum. The simulation of the spectrum was not achieved yet and the reported g and A values were estimated from analysis of the spectral data.

The EPR spectrum of **12** was consistent with the breaking of the magnetic coupling observed for **11**, suggesting the conversion of one of the low spin Cu^{II} centre (d^9, $S = 1/2$) to Cu^{III} (d^8, $S = 0$), with the remaining Cu^{II} centre being responsible for the observed EPR signal. The EPR analysis appeared to support the identification of **12** as a $Cu^{II}Cu^{III}$ and a similar behaviour has been previously reported by Tolman and co-worker[9] for the conversion of the $Cu^{II}_2(\mu\text{-}OH)$ species **75** ($S = 1$ or $S = 0$, silent in parallel mode EPR) into the $S = 1/2$ mixed valent $Cu^{II}Cu^{III}(\mu\text{-}OH)$ **76**. However, it is noteworthy that, in our

case, EPR gave no direct evidence regarding the retention of the dinuclear structure of **12**: thus the formation of a $S = 0$ mononuclear Cu^{III} species alongside a $S = 1/2$ mononuclear Cu^{II} species cannot be excluded at first glance.

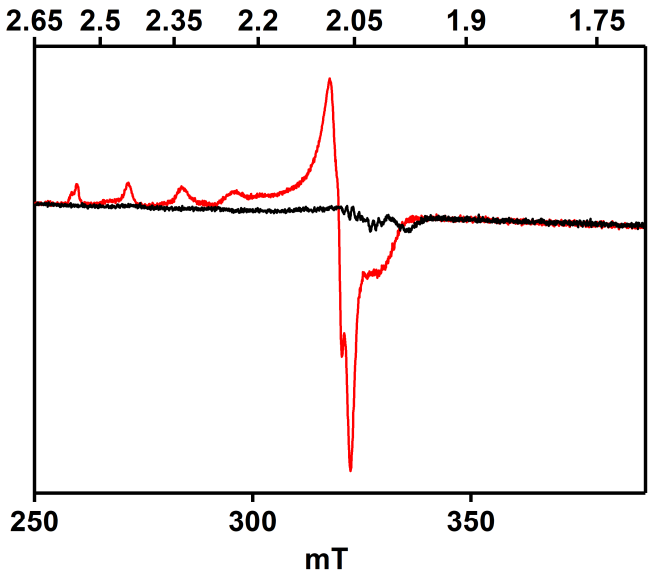

Figure 5.8 - EPR spectrum of **11** (black trace) and **12** (red trace). EPR spectra were acquired from a frozen DMF solution, measured at 77 K, 6.36 mW or 2.01 mW microwave power, with 0.3 mT modulation amplitude.

5.5 X-Ray Absorption Spectroscopy

Cu K-edge X-ray absorption spectroscopic studies on frozen samples of metastable compounds **12** and **11** were also performed (Figure 5.9). The X-ray absorption near edge structure (XANES) spectra of compound **11** exhibited a spectrum analogous to those reported for other Cu^{II} systems, with a weak pre-edge feature centred at 8978.0 eV (Table 5.2). Such a feature, which falls in the expected range reported for Cu^{II} systems,[21] has been assigned to an electric-dipole forbidden but electric-quadrupole allowed 1s-to-3d transition, which in centrosymmetric environment (*e.g.* square planar geometry, D_{4h}) gains intensity through p/d orbital mixing in the presence of deviation from centrosymmetry.[21, 22] Such a feature is therefore strongly affected by the ligand field

strength and the effective nuclear charge of the Cu centre.[21] **11** also displays two additional features along the rising edge (Figure 5.9), assigned to the electric-dipole allowed 1s-to-4p "main" transition (8991.5 eV) and a 1s-to-4p with concurrent ligand-to-metal-charge-transfer (LMCT) "shakedown" transition (8984.9 eV).[21, 23, 24]

12 Cu K-edge spectrum (Figure 5.9), displayed a pre-edge 1s-to-3d transition centred at 8977.5 eV, quite out of the range reported for Cu^{III} (8981 ± 0.5 eV)[21] and closer to the values reported for Cu^{II} systems (8978.8 ± 0.4 eV),[21] with an red-shift of 0.5 eV compared to **11**. Critically, no 1s-to-4p transitions were present along the rising edge, whereas the maximum edge energy exhibited a stark red-shift (2.5 eV). Contrary to the well-studied Cu^{II}_2 and Cu^{III}_2 systems,[21] examples of mixed valent $Cu^{II}Cu^{III}$ are rare, and therefore a direct comparison of our data with previously reported examples is not possible. However, from the study performed on trinuclear complexes such as $Cu^{II}_2Cu^{III}$,[21] the spectrum of a mixed valent system such as $Cu^{II}Cu^{III}$ can be approximated to the sum of the edges of the dimeric species Cu^{II}_2 and Cu^{III}_2 in 1:1 ratio,[21] albeit the edge shape will be highly dependent on the local environment of the absorbing metal. The peculiar characteristics of the XANES spectrum of **12** are subjected to interpretation. According to the aforementioned studies on the trinuclear mixed valent species,[21] a little-to-no shift of the 1s-to-3d transition, alongside a broadening of the pre-edge feature, is expected. Such features are observed both in **9** (Section 3.5) and **12**, albeit only the latter exhibited a redshift, probably due to a partial decomposition of the complex. The coordination of a solvent molecule, as observed for species **10**, could cause a change in coordination geometry affecting the energy of the 1s-to-3d transition. However, this hypothesis has no support from the EXAFS data (see below). The lack of the 1s-to-4p transitions observed for **12** finds correspondence in the mixed valent trinuclear species $Cu^{II}_2Cu^{III}$ [21] and can be tentatively addressed to the destructive overlap of the features present in the corresponding Cu^{II}_2 and Cu^{III}_2 dimeric species. Although these considerations are consistent with the proposed $Cu^{II}Cu^{III}$ oxidation state, because of the lack of similar reported complexes and the peculiarity of the features exhibited by **12**, the complete absence of Cu^{III} species cannot be excluded at this stage. More studies are ongoing to shed the light on the oxidation state of **12**.

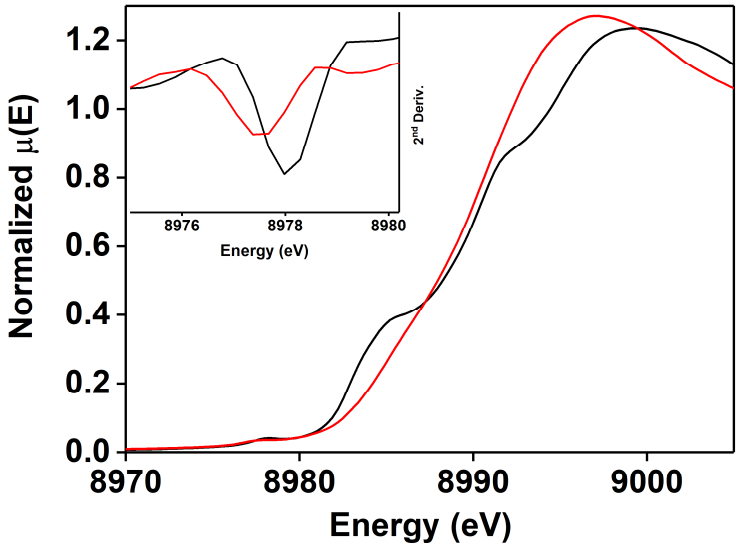

Figure 5.9 - Normalized Cu K-Edge XANES spectra of **11** (black trace) and **12** (red trace). Inset: Second derivative of the pre-edge region.

Table 5.3 - Significant data from Cu K-edge X-ray absorption spectroscopy analysis of complexes **11** and **12**.

	$E_{pre\text{-}edge}$[a]	$E_{edge\ max}$[a]	$Area_{pre\text{-}edge}$[b]	Cu–N/O[c]	Cu···Cu[c]
11	8978.0	8999.4	3.86(2)	4 @ 1.95	3.03
12	8977.5	8996.9	3.24(16)	4 @ 1.98	2.82

[a] Energy values reported in eV. [b] Areas multiplied by 100 for convenience. [c] Distances reported in Å.

Analysis of the extended X-ray absorption fine structure (EXAFS) data for **11** was also performed (Figure 5.10, Tables 5.3, A-5.4). The best fit obtained for **11** showed a first coordination shell composed of 4 N/O scatterers at 1.95 Å. Although the second coordination shell was tentatively fitted with light atoms, the presence of a heavier atom was required and therefore the second Cu atom was refined at 3.03 Å. As reported for Ni complexes in Chapter 3, for **11** the presence of a heavier scatterer was confirmed by

evaluation of the the k^5-weighted Fourier transform (Figure A-5.6), which showed a discrete increase in the FT magnitude in the region 2.7-3.0 Å. The refined values for the Cu−N/O and Cu···Cu distances obtained by EXAFS analysis of **11** were perfectly in agreement (within the experimental error) with the crystallographic data (Table A-5.3).

In spite of the peculiar XANES features reported above, analysis of the EXAFS region of **12** (Tables 5.3, A-5.5, Figure 5.10) was performed. The best fit obtained for **12** showed a first coordination shell composed by 4 N/O scatterers at 1.98 Å. The retention of the tetracoordinated geometry suggested that no solvent molecules were coordinated to proposed Cu^{III} centre, contrary to what was observed for **10**. The second coordination shell was tentatively fitted with light atoms, revealing the necessity of a heavier atom to improve the fit. A second Cu atom was refined at 2.82 Å. However, evaluation of the the k^5-weighted Fourier transform (Figure A-5.8) was not conclusive as in the case of Ni (section 3.5) and a clear and unequivocal increase in the region 2.6-3.0 Å is missing. Such an observation can be addressed to a destructive overlap of the Cu feature with the nearby lighter C atoms, although the lack of dimeric structure in **12** cannot be definitively excluded. It is important to underline that the quality of the data acquired forced us to a *k*-range (k = 2−13), defining a resolution of the atomic distances of fit of ~ 0.14 Å. The decay of **12** or experimental errors in sample preparation were considered as a hypothesis for the quality of the data. As stated above, more analyses are ongoing to confirm or deny these considerations.

Although the Cu K-edge data of **12** have to be considered as provisional, it is noteworthy to highlight some parallels with that observed for Ni based species **9**. In both the complexes we observed a substantial contraction of the M···M distances going from the low valent species (**8**, Ni···Ni =3.09 Å; **11**, Cu···Cu = 3.03 Å) to the mixed valent species (**9**, Ni···Ni = 2.85 Å; **11**, Cu···Cu = 2.82 Å), as a result of the asymmetric change in oxidation state.

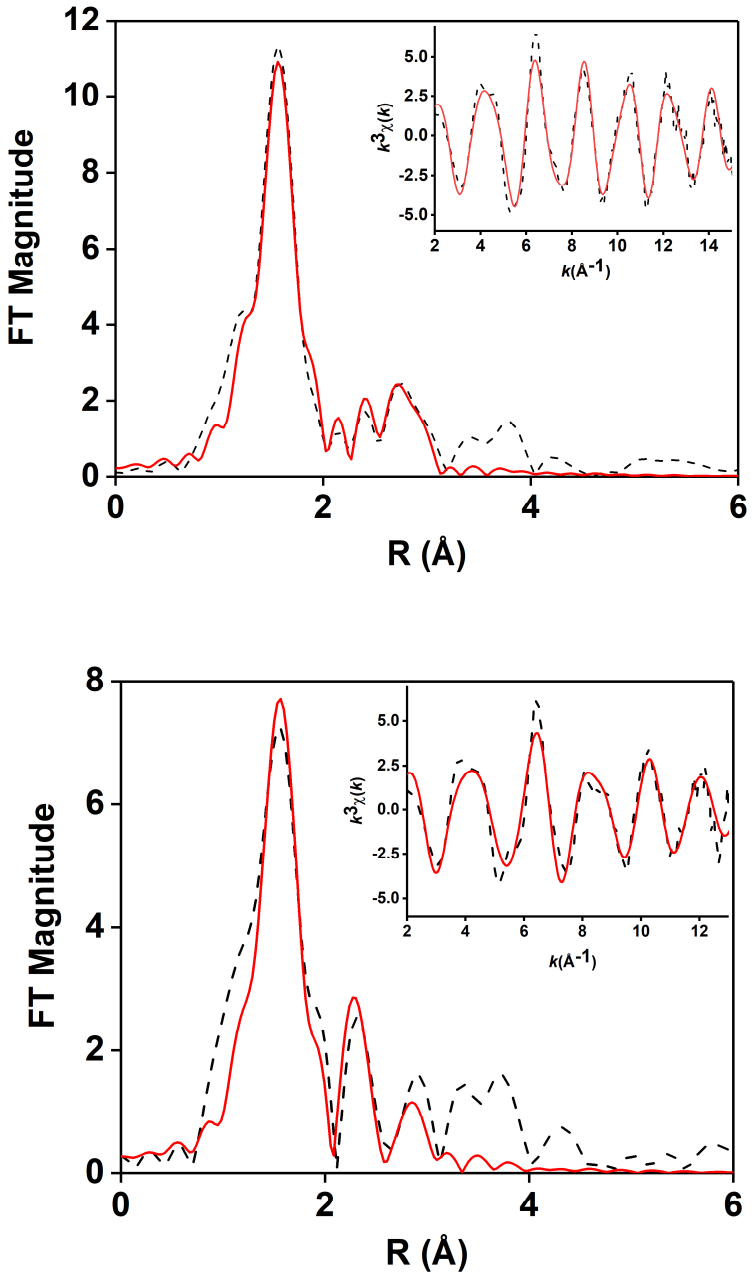

Figure 5.10 - Best fit to k^3-weighted EXAFS of **11** (*top*) and **12** (*bottom*), reported in R-space and *k*-space (inset). Experimental data are shown as dashed lines, best fits are shown as solid lines.

5.6 Reactivity toward O–H bonds

5.6.1 Reaction of 12 with a series of 4-2,6-di-*tert*-butyl phenols

Analogous to what was previously reported for **9** and **10**, the reactivity of **12** towards oxidation of substrates containing weak O–H was probed. Species **12** was therefore reacted with a series of *para*-X-2,6-di-*tert*-butylphenols (4-X-2,6-DTBP, X = $-OCH_3$, $-CH_2CH_3$, $-CH_3$, $-C(CH_3)_3$, $-H$, $-NO_2$) at -45 °C in N,N-dimethylformamide (DMF, 0.2 mM, see Experimental Section at the end of the chapter for details), monitoring the reaction by electronic absorption spectroscopy. Upon addition of the substrate to **12**, rapid decay of the electronic absorption feature at λ = 525 nm was observed (Figure 5.11). It is noteworthy that a single-phase exponential event was observed, similar to what was observed for the mixed valent $Ni^{II}Ni^{III}$ species **9**. The decay curves for each substrate were fitted with a *pseudo*-first order kinetic model, allowing the determination of the pseudo-first order rate constants (k_{obs}) for each reaction, which exhibited a linear dependency on the substrate concentration. The second order rate constant (k_2) was obtained as the slope of the corresponding k_{obs} vs. [substrate] plot. (Figures A-5.8–A-5.13).

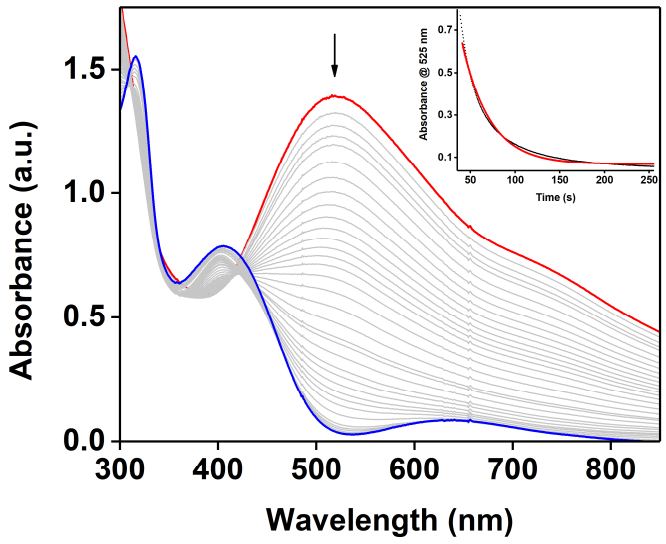

Figure 5.11 - Electronic absorption spectrum showing the decay of **12** (red trace) upon reaction with 4-CH_3-2,6-DTBP (100 equiv.) at -45 °C in DMF. Inset: Decay of λ_{max} = 525 nm feature against the time.

The post reaction mixtures for the reaction of **12** with each substrate was analysed, in order to identify the corresponding end reaction products (Figure 5.12, A-5.15, Table 5.4). The reaction between **12** and X = $–OCH_3$, $–C(CH_3)_3$, exhibited the formation of the corresponding stable phenoxyl radicals (Figure 5.9),[25-27] whose characteristic features (X = $–OCH_3$: λ = 407, 390 nm; X = $–C(CH_3)_3$: λ = 402, 384 nm) are clearly visible despite the overlap with an intense band at ~405 nm deriving from the decayed metal complex (Figure A-5.14). Unfortunately, such overlap prevented us from any quantification of the end reaction products by electronic absorption spectroscopy for these substrates. As experienced for the analogous Ni-based systems in Chapter 4, the post reaction mixtures for X = $–CH_2CH_3$, $–CH_3$ (Figure 5.12) displayed no additional features compared to the natural self-decay spectrum of the complex (Figure A-5.14). Therefore, the end reaction products were identified by mass spectrometry, which detected the presence of 2,6-di-*tert*-butyl-4-methylene-2,5-cyclohexadienone for X = $–CH_3$ and 2,6-di-*tert*-butyl-4-ethylidene-2,5-cyclohexadienone for X = $–CH_2CH_3$ (Figure A-5.16). Analogous to what was observed for **9** and **10**, reaction between **12** and X = −H resulted in the formation of the coupled product 3,3',5,5'-tetra-*tert*-butyl-4,4'-diphenoquinone (DPQ, λ = 430, 406 nm), whereas reaction with X = $–NO_2$ showed a rapid saturation of the spectrum (Figure A-5.17). Analysis of the growing band features (λ = 452, 466 nm) visible before saturation allowed the identification of the end reaction product as the 4-NO_2-2,6-di-*tert*-butyl-phenolate by comparison with the reference UV-Vis spectrum reported in Figure A-4.18.

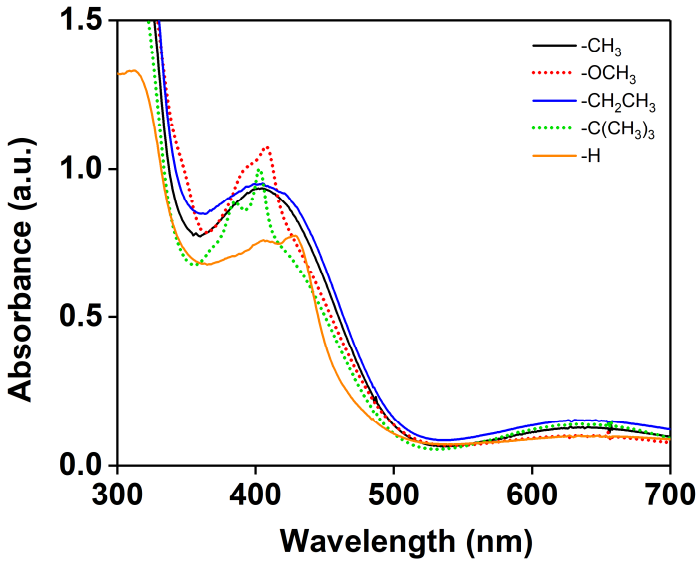

Figure 5.12 – UV-Vis spectra of the post reaction mixtures for the reaction between **12** and 4-X-2,6-DTBP (X = $–OCH_3$, $–CH_3CH_2$, $–CH_3$, $–C(CH_3)_3$, −H) at -45 °C in DMF.

Table 5.4 - k_2-values and products for the reaction of **12** with different 4-X-2,6 DTBP at -45 °C in DMF.

X	**12**		**10**	**9**	**9'**
	k_2 ($M^{-1}s^{-1}$)	**Products**	k_2 ($M^{-1}s^{-1}$)	k_2 ($M^{-1}s^{-1}$)	k_2 ($M^{-1}s^{-1}$)
-OCH_3	232(2)	phenoxyl radical	520(11)	84.6(3)	41(1)
-CH_2CH_3	2.8(1)	*p*-C_2H_4-CD	29(1)	0.84(2)	0.553(3)
-CH_3	5.7(1)	*p*-CH_2-CD	24.7(11)	0.76(4)	0.67(1)
-$C(CH_3)_3$	2.28(1)	phenoxyl radical	22(1)	0.45(1)	0.42(1)
-H	0.23(1)	DPQ	1.16(3)	0.045(2)	0.042(2)
-NO_2	12.4(7)	4-NO_2-2,6-DTB phenoxide	52.0(24)	0.65(3)	0.45(2)

Abbreviation: *p*-C_2H_4-CD = 2,6-di-tert-butyl-4-ethylidene-2,5-cyclohexadienone; *p*-CH_2-CD = 2,6-di-tert-butyl-4-methylene-2,5-cyclohexadienone; DPQ = 3,3',5,5'-tetra-tert-butyl-4,4'-diphenoquinone.

The kinetic results for **12** (Table 5.4) showed a reactivity pattern quite similar to the analogous Ni complexes in Chapter 4, with high reaction rates concomitant with the presence of electron rich substituents such as 4-OCH_3-2,6-DTBP (k_2 = 232(2) $M^{-1}s^{-1}$), which was the fastest substrate of the series. As mentioned in the previous chapter, such behaviour is correlated to the low O−H bond dissociation energy of 4-OCH_3-2,6-DTBP (BDE_{O-H} = 78.3 kcal/mol)[28] and belongs to a trend that included the majority of the substrate analysed (X = $-CH_3$, $-CH_2CH_3$ $-C(CH_3)_3$,−H), with a linear correlation between the magnitude of the O–H bond dissociation energy (BDE_{O-H}, Table A-4.1) and the measured second order rate constants k_2 (Figure 5.13). The linear trend observed in Figure 5.13 is consistent with the presence of a proton coupled electron transfer event.[29-31] The electron-poor phenol X = $-NO_2$ exhibited an unexpectedly high k_2 values with respect to the observed trend, and therefore will be considered as an outlier.

Notably, the k_2 values observed for **12** were one order of magnitude faster compared to the species **9** and **9'**, which are proposed to share the same mixed valent II/III oxidation state, suggesting that the increase in *d*-electron count from Ni to Cu had an huge impact on the reactivity. However, **12** is also one order of magnitude slower of the Ni^{III}_2 species **10**. Following the depicted trend, an hypothetical Cu^{III}_2 supported by the herein reported malonamide ligand **6**, is expected to be a powerful oxidant.

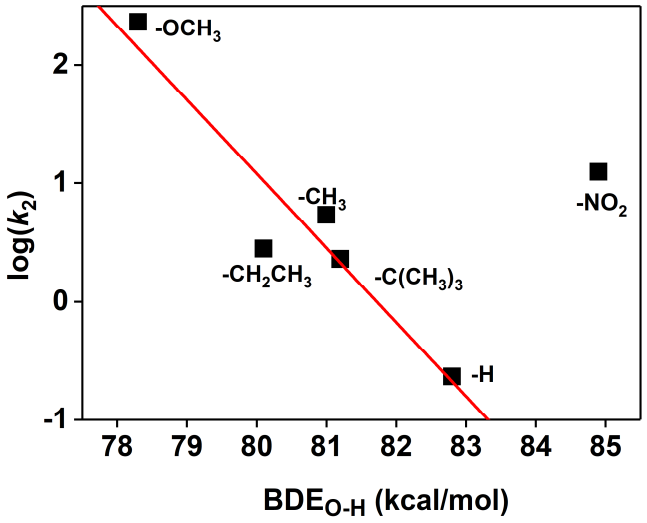

Figure 5.13 – Plot of log(k_2) against BDE_{O-H} for the reaction of **12** with a series of 4-X-2,6 DTBP in DMF at -45 °C.

The Evans-Polanyi plot for **12**, namely the correlation between the Eyring barrier energy $\Delta G^{\ddagger}$ (calculated from experimental k_2 values using the Eyring equation)[32-34] against the O–H bond dissociation free energy of the chosen phenols (Table A-4.1), is reported in Figure 5.14. The Evans-Polanyi plot for **12** showed a linear correlation, with the exception of the aforementioned outlier X = $–NO_2$. Linear regression of the data resulted in a slope of 0.65(12), a value which, albeit higher than the ideal value of 0.5,[29, 32, 35] can still be considered consistent, within the experimental error, with the presence of a HAT mechanism.

The $\log({}^{X}k_2/{}^{H}k_2)$ for **12** was plotted as a function of the Hammett parameter σ^{+}_{p} (Figure 5.15), giving insight into the electronic effect of the *para* substituents on the reactivity. Compound **12** exhibited a linear dependency of the k_2 values from the nature of the *para* substituent on the 4-X-2,6-DTBP. As previously observed, due its unusual high k_2 values, the $–NO_2$ substituent appeared to be an outlier with respect to this trend. Linear regression of the plot resulted in a negative Hammett slope, ρ = -3.6(7) These negative values suggested that the reactions involve the loss of a negative charge (*i.e.* the protonation of the negatively charged hydroxide ligand upon the HAT event).[36, 37] This evidence, in conjuction with the linear relationship of the k_2 values, are consistent with a HAT mechanism, as previously observed in literature.[15, 38-40]

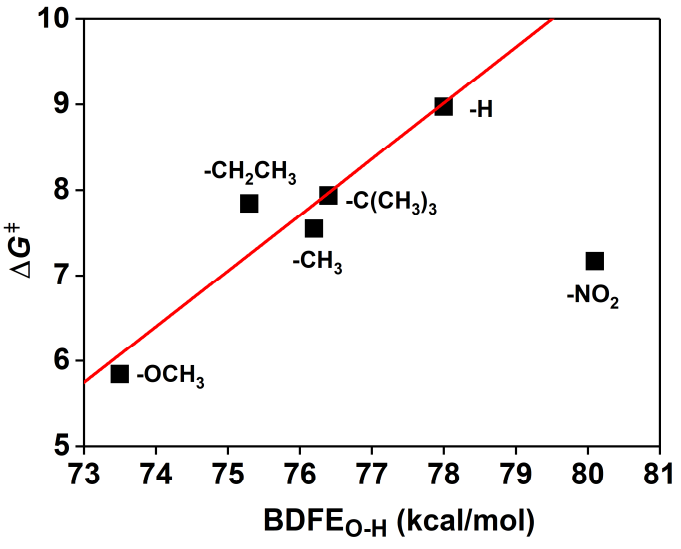

Figure 5.14 – Evans-Polanyi plot ($\Delta G^{\ddagger}$ vs. $BDFE_{O–H}$) for the reaction of **12** with a series of 4-X-2,6-DTBP in DMF at -45 °C.

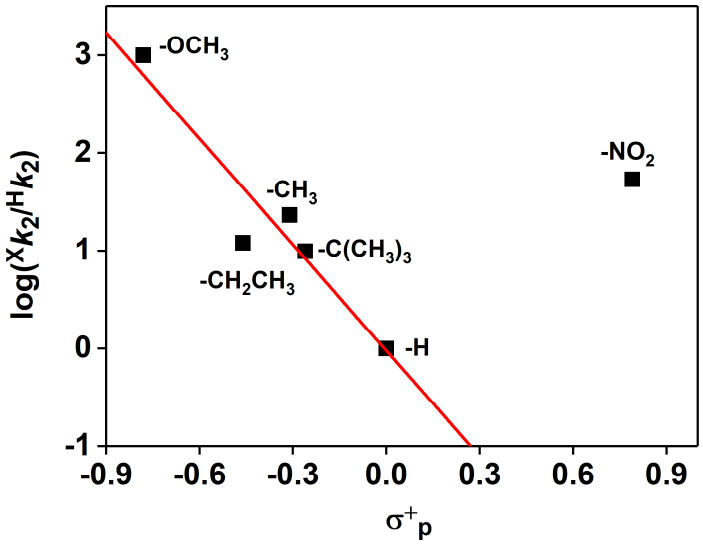

Figure 5.15 – Hammett correlation plot (log ($^{X}k_2/^{H}k_2$) vs. σ^+) for the reaction of **12** with a series of 4-X-2,6-DTBP in DMF at -45 °C.

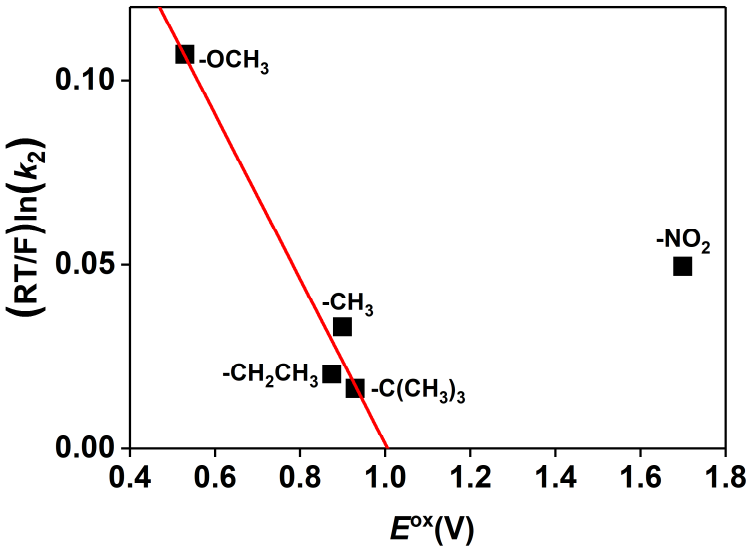

Figure 5.16 – Marcus correlation plot ($(RT/F)\ \ln(k_2)$ vs. E^{ox}) for the reaction of **12** with a series of 4-X-2,6-DTBP in DMF at -45 °C.

As experienced with complexes **9**, **9'** and **10**, Marcus theory is a powerful tool to understand the mechanism involved in PCET reaction.[29, 35, 41, 42] The plot of the k_2 values obtained for **12** (reported as (RT/F) ln(k_2)), against the $1e^-$ oxidation potential of the phenols (Table A-4.1), namely the Marcus plot for **12**, is reported in Figure 5.16. Even in this case, a good linear correlation is observed (except for X = $–NO_2$), with a calculated slope of -0.24(2). This value, similar to the one obtained for the Ni-based analogous species, is close, within the experimental error, to the ideal value of 0.0 expect for HAT.[43-45] In light of the results obtained by all the correlation plots (Marcus, Evans-Polanyi and Hammett plots), we can conclude that **12** is capable of oxidising phenolic O–H bonds through a HAT mechanism, corresponding to the detected end reaction products.

Concerning the outlier X = $–NO_2$, its unexpectedly high rate constant can be addressed as a change in reaction mechanism from a possible CPET to a stepwise proton transfer, as proposed in the previous chapter and recently reported by Tolman.[31] Such a proposed change in mechanism could be due to the relatively low pK_a of 4-NO_2-2,6 DTBP,[46] which would act as a driving force.

5.6.2 Comparison of the reactivity of 12 towards 4-$C(CH_3)_3$-2,6-DTBP with reported systems

The reactivity of **12** was compared with selected mono and di-nuclear Ni and Cu complex using the oxidation of 4-$C(CH_3)_3$-2,6-DTBP as a comparative standard. In the first place, **12** was compared with the analogous Ni-based complexes **9**, **9'** and **10.** As mentioned in the previous section, **12** was capable of oxidising 4-$C(CH_3)_3$-2,6-DTBP five time faster than **9** and **9'** (entries 2, 4), which are proposed to have the same mixed valent oxidation state. This observation suggests that in going from Ni to Cu, a distinct impact on the reactivity is observed, despite being equal ligand system, oxidation state and experimental conditions. However, **12** was an order of magnitude slower compared to **10** (entry 3) which is a high valent Ni^{III}_2 species. **12** displayed a reactivity almost twice as fast than the mononuclear [$pyN_2^{iPr2}Cu^{III}$(OAc)] (entry 5) reported by Unjaoren et al.,[47] and an order of

magnitude faster than the heterobimetallic $Cu^{III}Ni^{III}(\mu\text{-}O)_2$ reported by Ray and co-workers.[48]

Unfortunately, the majority if the Cu^{III} chemistry is performed at a temperature below -80 °C, making a direct comparison with our data, acquired at -45 °C inappropriate. However, approximating that a two-fold increase in k_2 will occur every 10 K as a rule of thumb, allows us to do some general considerations. In the light of this approximation, **12** results in a valid oxidant compared to more reactive Cu species: $L^{Py2}Cu^{II}_2(\mu\text{-}\eta^2\text{:}\eta^2\text{-}O_2)$ (entry 7),[49] exhibited an estimated k_2 at -40 °C approximately an order of magnitude lower (~ 0.3 M^{-1} s^{-1}) than **12**, whereas the high valent $L^{Py1Bz}Cu^{III}_2(\mu\text{-}O)_2$ complex (entry 8)[49] exhibited an approximated k_2 value at -40 °C of ~ 7.5 M^{-1} s^{-1}, higher but still comparable with the value obtained for **12**.

Table 5.5 - Comparison between k_2 values for the oxidation of 4-$C(CH_3)_3$-2,6 DTBP by **12** and some selected complexes.

#	Complex	k_2 ($M^{-1}s^{-1}$)	T(°C)	solvent	Ref.
1	**12**	2.28(1)	-45	DMF	this work
2	**9**	0.45(1)	-45	DMF	this work
3	**10**	22(1)	-45	DMF	this work
4	**9'**	0.42(1)	-45	DMF	this work
5	$[pyN_2^{iPr2}Cu^{III}(OAc)]$	1.19	-40	acetone	ref. [47]
6	$[(MeAN)Cu^{III}(\mu\text{-}O)_2Ni^{III}L]^+$	0.18	-50	CH_2Cl_2	ref. [48]
7	L^{Py2} $Cu^{II}_2(\mu\text{-}\eta^2\text{:}\eta^2\text{-}O_2)$	0.015	-80	acetone	ref.[49]
8	$L^{Py1Bz}Cu^{III}_2(\mu\text{-}O)_2$	0.47	-80	acetone	ref.[49]

pyN_2^{Me2} = N,N'-bis(2,6-dimethylphenyl)2,6-pyridinedicarboxamidate; DMM-tmpa = tris((4-methoxy-3,5-dimethylpyridin-2-yl)methyl)amine; L^{Py2} = 1-phenyl-N,N-bis(pyridin-2-ylmethyl)methanamine-d2; L^{Py1Bz} = N-(phenylmethyl-d2)-N-(pyridin-2-ylmethyl)ethanamine; MeAN = N,N,N′,N′,N′-pentamethyl-dipropylenetriamine;

5.7 Conclusions

In this chapter we successfully reported the synthesis and characterization of a new $Cu^{II}_2(\mu\text{-}OH)_2$ (**11**) complex, based on the malonamide ligand **6** reported in Chapter 2 of this thesis. Species **11** exhibited a diamond core composed by two Cu atoms and two bridging hydroxide ligands. The structure of **11** appeared to be quite similar to **8** and overlap of the two structures showed only subtle difference between the two complexes. Cyclic voltammetry experiment showed the presence of an accessible higher oxidation state, that was probed by UV-Vis monitored chemical oxidation. Such experiments led to the formation of **12**, which being one oxidising equivalent above **11**, was tentatively assigned to a $Cu^{II}Cu^{III}(\mu\text{-}OH)_2$, in line to what was observed for Ni in chapter 3. Both EPR and Cu K-edge absorption spectroscopy experiment were consistent with the hypothesised structure, although none of them confirmed it unequivocally. Further investigations are ongoing to prove the correct structure of **12**.

Nevertheless, reactivity of **12** towards phenolic O−H bonds was studied through a series of reactions involving 4-X-2,6-DTBP (X = $-OCH_3$, $-CH_2CH_3$, $-CH_3$, $-C(CH_3)_3$, −H, $-NO_2$). Analysis of the post reaction mixtures and the obtained kinetic data (particularly the second order rate constants k_2) indicated that equal to **10**, **9** and **9'**, species **12** was capable of performing the oxidation of the phenolic O−H bonds through a HAT mechanism. Finally, reactivity of **12** towards 4-$C(CH_3)_3$-2,6-DTBP was compared to reported mono and dinuclear Cu^{III} complexes showing comparable oxidation rates, which identified **12** as a valid oxidant for O−H bond activation.

5.8 Experimental Section – Chapter 5

Physical Methods

Fourier transform infra-red (FT-IR) spectra were recorded using a Perkin Elmer Spectrum 100 FT-IR/ATR. Electrospray ionisation mass spectrometry (ESI-MS) analyses were performed using a Micromass Time of Flight (ToF), interfaced with a Waters 2690 HPLC. Cyclic voltammetry (CV) experiments have been conducted with a CH Instrument 600E

electrochemical analyser, using a GC working electrode, a Pt wire counter electrode, and an $Ag/AgNO_3$ 0.01 M reference electrode. Electronic absorption spectra were recorded on an Agilent 8453 diode array spectrophotometer (190-1100 nm range) equipped with a cryostat unit from Unisoku Scientific Instruments (Osaka, Japan).

Materials and synthesis

All reactions with air-sensitive or water-sensitive materials were performed under an inert atmosphere. Both Schlenk techniques and a nitrogen atmosphere glovebox have been used. Reagents and solvents were purchased from commercial suppliers and have been used as received, unless otherwise stated. Dry potassium hydride (KH) was obtained from the commercially available paraffin dispersion by washing it several times with anhydrous hexane inside the glovebox. Dry KH is extremely pyrophoric and require to be stored under inert atmosphere. Anhydrous diethyl ether (Et_2O) was distilled over Na/Benzophenone and stored in a Schlenk bomb prior to use.

Synthesis of 11

Each step of the synthesis of this complex was performed under an inert atmosphere (Ar) using Schlenk techniques. To a solution of **6** (128 mg, 0.38 mmol) in DMF (3 mL), dry KH (38 mg, 0.95 mmol, 2.5 equiv.) was added to this solution, causing the evolution of H_2 (bubbling of the solution). When the gas evolution ceased, $Cu(OAc)_2$ (69 mg, 0.38 mmol, 1 equiv.) was added, causing a slow colour change from white to dark green-brown over a period of 6h, with formation of whitish precipitate (potassium acetate, KOAc). The dispersion was at first filtered over a fritted glass filter (porosity 4) and then further filtered over Celite® to remove any by-product or unreacted material. All the filtration operations were performed in an inert atmosphere. Compound **11** (113 mg, 0.12 mmol, 63%) was then obtained as crystals by slow vapour diffusion of Et_2O into the DMF solution.

ν_{max} (FT-IR)/cm^{-1}: 3644 (O−H), 2974, 2950, 2916 (C−H), 1672(C=O), 1593, 1564, 1450, 1408, 1343, 1090, 873, 762, 661, 566.

λ_{max} (DMF)/nm: 398 (ε = 4100 $dm^3mol^{-1}cm^{-1}$) 544 (sh)

ESI-MS (m/Z): Found: 871.1825 m/z ($[(Cu^{II}(OH)\mathbf{L})_2 + K]^-$. $C_{42}H_{50}Cu_2KN_4O_6^-$ requires 871.1965 m/z).

Preparation of 12

To a solution of **11** (2 mL, 0.2 mM in DMF) cooled to -45 °C in a quartz cuvette was added CAN ($(NH_4)_2[Ce^{IV}(NO_3)_6]$, 40 μL, 0.015 M, CH_3CN) under continuous stirring. An immediate and stark colour change was observed. Monitoring by electronic absorption spectroscopy showed the appearance of an intense band (λ_{max} = 525 nm) corresponding to the formation of the mixed-valent species **12**. The reaction reached its maximum yield after 15 s.

X-Ray diffraction experimental data

X-ray structural analyses of **11** were performed on a Bruker D8 Quest ECO at 100(2) K with an Oxford Cryostream, with the sample mounted on a MiTeGen microloop using Cu Kα radiation (λ = 0.71073 Å). Bruker APEX[50] software was used to collect and reduce data and determine the space group. Absorption corrections were applied using SADABS.[51] Structures were solved with the XT structure solution program[52] using Intrinsic Phasing and refined with the XL refinement package[53] using Least Squares minimisation in Olex2.[54] All non-hydrogen atoms were refined anisotropically.

Table 5-6 – Crystal Data and Structure Refinement for **11** in the presence of K^+ as counterion.

Empirical formula	$C_{48}H_{64}Cu_2K_2N_6O_8$	**μ/mm^{-1}**	1.072
Formula weight	1058.33	**F(000)**	1108
Temperature/K	100(2)	**Crystal size/mm^3**	0.21 × 0.16 × 0.08
Crystal system	Triclinic	**Radiation**	MoKα (λ = 0.71073)
Space group	$P\bar{1}$	**2Θ range for data collection/°**	2.614 to 26.232
a/Å	10.8316(5)	**Index ranges**	-13 ≤ h ≤ 13, -16 ≤ k ≤ 16, -22 ≤ l ≤ 22
b/Å	13.6061(7)		
c/Å	17.8202(9)	**Reflections collected**	49316
α/°	92.8750(18)	**Independent reflections**	10033 [R_{int} = 0.0440]
β/°	105.2806(17)	**Data/restraints/parameters**	10033/ 144/ 641
γ/°	96.9736(18)	**Goodness-of-fit on F^2**	1.063
Volume/Å^3	2505.4(2)	**Final R indexes [I>=2σ (I)]**	R_1 = 0.0418, wR_2 = 0.1072
Z	2	**Final R indexes [all data]**	R_1 = 0.0573, wR_2 = 0.1163
ρ_{calc}g/cm^3	1.403	**Largest diff. peak/hole / e Å^{-3}**	0.932/-0.489

Table 5-7 – Crystal Data and Structure Refinement for **11** in the presence of Me_4N^+ as counterion.

Empirical formula	$C_{60}H_{98}Cu_2N_8O_9$	**μ/mm^{-1}**	0.724
Formula weight	1202.54	**F(000)**	2576
Temperature/K	100(2)	**Crystal size/mm^3**	0.295 × 0.234 × 0.178
Crystal system	Monoclinic	**Radiation**	MoKα (λ = 0.71073)
Space group	C 2/c	**2Θ range for data collection/°**	1.935 to 29.999
a/Å	28.9693(11)	**Index ranges**	-40 ≤ h ≤ 38, 0 ≤ k ≤ 16, 0 ≤ l ≤ 28
b/Å	11.4088(4)		
c/Å	20.5429(8)	**Reflections collected**	9297
α/°	90	**Independent reflections**	9297 [R_{int} = 0.0577]
β/°	109.912(2)	**Data/restraints/parameters**	9297/ 3/ 391
γ/°	90	**Goodness-of-fit on F^2**	1.043
Volume/Å^3	6383.6(4)	**Final R indexes [I>=2σ (I)]**	R_1 = 0.0472, wR_2 = 0.1230
Z	4	**Final R indexes [all data]**	R_1 = 0.0731, wR_2 = 0.1339
ρ_{calc}g/cm^3	1.251	**Largest diff. peak/hole / e Å^{-3}**	0.635/-0.474

Electron paramagnetic resonance

Electron paramagnetic resonance (EPR) spectra of frozen solutions were acquired on a Bruker EMX X-band EPR, equipped with an Oxford Instruments CE 5396, ESR9 Continuous Flow Cryostat, a precision Temperature Controller and an Oxford Instruments TTL20.0/13 Transfer Tube. EPR samples were prepared by freezing the EPR tubes containing the complex solutions, previously prepared at the cryostat as listed below, in liquid nitrogen. Both EPR spectra were recorded at 77 K, 9.3 GHz, 2.02 mW microwave power, with a 140 mT field sweep, 0.3 mT field modulation amplitude and attenuation of 20 dB.

X-ray Absorption Spectroscopy

The Cu-K-edge X-ray absorption data were collected on beam line 7-3 at SSRL (*Stanford Synchrotron Radiation Lightsource*, SLAC National Accelerator Lab, Menlo Park, CA, USA). Data were collected with the storage ring operating at ca. 3 GeV and 500 mA, using a LN_2 cooled Si (220), $\phi = 0°$ double-crystal monochromator, calibrated by using the first inflection point of a Cu foil (8979.0 eV). The monochromator was detuned by ~50% for higher harmonic rejection. The fluorescence detector used was a Canberra 30-element Ge solid state detector. All the measurements were performed at ambient pressure at ~10 K, gained by an Oxford Helium cryostat, cooled by closed cycle He gas loop. The parameters used for the scans were the following: 10 eV steps/1 second integration time in the pre-edge region, 0.3 eV steps/2 second integration time in the edge, and 0.05 *k* steps in the EXAFS, with integration time increasing in a k^2-weighted fashion from 2 to 9 s over the energy range (k_{max} = 15.1 *k*). The total detector counts were in the range between 25k−35k, well within the linear range of the detector electronics. Each sample was monitored for radiation damage, using different spots where required to expose fresh sample. The samples were measured as frozen solutions using a Delrin® Mössbauer/XAS cups with a sample window of 4 mm x 10 mm. In the case of **12**, the samples were prepared by transferring the solution (~3 mM in DMF) from the cryostat (-45 °C) to a XAS sample cup pre-cooled in a liquid nitrogen bath. For **11**, a dispersion of the complex

in Nujol (8.5 mg in 1 mL) was prepared, then transferred into an XAS cup and frozen in a liquid nitrogen bath.

Elaboration of the XAS data, including averaging, background removal and normalization, was performed using Athena.[55] Edge energies were determined as the half-height of the white-line intensity. Peak fitting was performed using Fityk.[56] Peak fitting of the pre-edge regions was performed using one or more *pseudo*-Voigt functions with a fixed 50:50 Gaussian:Lorentzian ratio. EXAFS analysis was carried out using Artemis,[55] which incorporates the IFEFFIT fitting engine and FEFF6 for *ab initio* EXAFS phase and amplitude parameters. Crystal structures (either as-is or modified slightly to test different structural models) were used for FEFF6 input to identify significant paths. For a given shell in all simulations, the coordination number n was fixed, while r and σ^2 were allowed to float. The amplitude reduction factor S_0^2 was fixed at 0.9, while the edge shift parameter ΔE_0 was allowed to float at a single common value for all shells. The fit was evaluated in k^3-weighted R-space, and fit quality was judged by the reported R-factor and reduced χ^2. Significant fits are highlighted in bold and reported in k^3-weighted R-space and reported in Tables A-5.4, A-5.5 in the appendix.

Electrochemistry

Cyclic voltammetry experiments were conducted on a 0.33 mM solution of **11** in DMF at room temperature. As the supporting electrolyte, *n*-Bu_4NPF_6 (0.1 M) was used. Glassy carbon was used as the working electrode and 0.01 M $Ag/AgNO_3$ was used as the reference electrode. Platinum wire was used as the counter electrode. Scan rates of 25 mV/s – 100 mV/s were used. Potentials were referenced against the Fc^+/Fc couple (Fc = ferrocene). The voltammograms of Fc were acquired under the same solvent and scan rate conditions.

Kinetic experiments

Different amount of substrate, as a N,N' dimethylformamide (DMF) solution, were added to a 0.2 mM solution in DMF of **12** at -45 °C (prepared in situ according to the procedure reported above) causing the immediate decay of the spectral features of the oxidant species. For species **12**, the monitored wavelength was λ_{max} = 525 nm (Figure 5.11). The decay of this feature upon addition of substrates were fitted using a *pseudo-first order* kinetic model, obtaining a k_{obs} for each reaction. The k_{obs} values were then plotted the concentrations of the correspondent substrate allowed for the determination of the *second order* rate constant (k_2) for the examined substrate as the slope of the resulting k_{obs} vs. [substrate] plot.

5.9 References

(1) G. Spedalotto, R. Gericke, M. Lovisari, E. R. Farquhar, B. Twamley and A. R. McDonald, *Chem. Eur. J.*, 2019, **25**, 11983-11990.

(2) B. Cordero, V. Gómez, A. E. Platero-Prats, M. Revés, J. Echeverría, E. Cremades, F. Barragán and S. Alvarez, *Dalton Trans.*, 2008, 2832-2838.

(3) R. Haase, T. Beschnitt, U. Flörke and S. Herres-Pawlis, *Inorg. Chim. Acta*, 2011, **374**, 546-557.

(4) I. Bertini and C. Luchinat, *Coord. Chem. Rev.*, 1996, **150**, 77-110.

(5) R. M. Silverstein, F. X. Webster, D. J. Kiemle and D. L. Bryce, *Spectrometric identification of organic compounds*, John Wiley & Sons, 8th edn., 2014.

(6) N. Kitajima, K. Fujisawa, C. Fujimoto, Y. Morooka, S. Hashimoto, T. Kitagawa, K. Toriumi, K. Tatsumi and A. Nakamura, *J. Am. Chem. Soc.*, 1992, **114**, 1277-1291.

(7) N. Kitajima, K. Fujisawa, Y. Morooka and K. Toriumi, *J. Am. Chem. Soc.*, 1989, **111**, 8975-8976.

(8) D. Dhar, G. M. Yee, A. D. Spaeth, D. W. Boyce, H. Zhang, B. Dereli, C. J. Cramer and W. B. Tolman, *J. Am. Chem. Soc.*, 2016, **138**, 356-368.

(9) M. R. Halvagar, P. V. Solntsev, H. Lim, B. Hedman, K. O. Hodgson, E. I. Solomon, C. J. Cramer and W. B. Tolman, *J. Am. Chem. Soc.*, 2014, **136**, 7269-7272.

(10) S. Mahapatra, J. A. Halfen, E. C. Wilkinson, G. Pan, X. Wang, V. G. Young, C. J. Cramer, L. Que and W. B. Tolman, *J. Am. Chem. Soc.*, 1996, **118**, 11555-11574.

(11) H. Hayashi, S. Fujinami, S. Nagatomo, S. Ogo, M. Suzuki, A. Uehara, Y. Watanabe and T. Kitagawa, *J. Am. Chem. Soc.*, 2000, **122**, 2124-2125.

(12) S. Itoh, M. Taki, H. Nakao, P. L. Holland, W. B. Tolman, J. Que, Lawrence and S. Fukuzumi, *Angew. Chem. Int. Ed.*, 2000, **39**, 398-400.

(13) J. A. Halfen, S. Mahapatra, E. C. Wilkinson, S. Kaderli, V. G. Young, L. Que, A. D. Zuberbuhler and W. B. Tolman, *Science*, 1996, **271**, 1397-1400.
(14) L. M. Mirica, M. Vance, D. J. Rudd, B. Hedman, K. O. Hodgson, E. I. Solomon and T. D. P. Stack, *J. Am. Chem. Soc.*, 2002, **124**, 9332-9333.
(15) T. Osako, K. Ohkubo, M. Taki, Y. Tachi, S. Fukuzumi and S. Itoh, *J. Am. Chem. Soc.*, 2003, **125**, 11027-11033.
(16) R. R. Jacobson, Z. Tyeklar, A. Farooq, K. D. Karlin, S. Liu and J. Zubieta, *J. Am. Chem. Soc.*, 1988, **110**, 3690-3692.
(17) K. E. Dalle, T. Gruene, S. Dechert, S. Demeshko and F. Meyer, *J. Am. Chem. Soc.*, 2014, **136**, 7428-7434.
(18) H. R. Lucas, L. Li, A. A. N. Sarjeant, M. A. Vance, E. I. Solomon and K. D. Karlin, *J. Am. Chem. Soc.*, 2009, **131**, 3230-3245.
(19) J. A. Isaac, F. Gennarini, I. Lopez, A. Thibon-Pourret, R. David, G. Gellon, B. Gennaro, C. Philouze, F. Meyer, S. Demeshko, Y. Le Mest, M. Reglier, H. Jamet, N. Le Poul and C. Belle, *Inorg. Chem.*, 2016, **55**, 8263-8266.
(20) L. M. Mirica, X. Ottenwaelder and T. D. P. Stack, *Chem. Rev.*, 2004, **104**, 1013-1046.
(21) J. L. DuBois, P. Mukherjee, T. D. P. Stack, B. Hedman, E. I. Solomon and K. O. Hodgson, *J. Am. Chem. Soc.*, 2000, **122**, 5775-5787.
(22) J. E. Hahn, R. A. Scott, K. O. Hodgson, S. Doniach, S. R. Desjardins and E. I. Solomon, *Chem. Phys. Lett.*, 1982, **88**, 595-598.
(23) N. Kosugi, T. Yokoyama, K. Asakura and H. Kuroda, *Chem. Phys.*, 1984, **91**, 249-256.
(24) R. A. Bair and W. A. Goddard, *Phys. Rev. B*, 1980, **22**, 2767-2776.
(25) E. R. Altwicker, *Chem. Rev.*, 1967, **67**, 475-531.
(26) J. M. Wittman, R. Hayoun, W. Kaminsky, M. K. Coggins and J. M. Mayer, *J. Am. Chem. Soc.*, 2013, **135**, 12956-12959.
(27) V. W. Manner, A. G. DiPasquale and J. M. Mayer, *J. Am. Chem. Soc.*, 2008, **130**, 7210-7211.
(28) M. Lucarini, P. Pedrielli, G. F. Pedulli, S. Cabiddu and C. Fattuoni, *J. Org. Chem.*, 1996, **61**, 9259-9263.
(29) J. M. Mayer, *Acc. Chem. Res.*, 2011, **44**, 36-46.
(30) S. Kundu, E. Miceli, E. R. Farquhar and K. Ray, *Dalton Trans.*, 2014, **43**, 4264-4267.
(31) W. D. Bailey, D. Dhar, A. C. Cramblitt and W. B. Tolman, *J. Am. Chem. Soc.*, 2019, **141**, 5470-5480.
(32) M. G. Evans and M. Polanyi, *Trans. Faraday Soc.*, 1938, **34**, 11-24.
(33) M. G. Evans and M. Polanyi, *Trans. Faraday Soc.*, 1935, **31**, 875-894.
(34) H. Eyring, *J. Chem. Phys.*, 1935, **3**, 107-115.
(35) J. M. Mayer, *Annu. Rev. Phys. Chem.*, 2004, **55**, 363-390.
(36) L. P. Hammett, *J. Am. Chem. Soc.*, 1937, **59**, 96-103.
(37) P. Muller, *Pure Appl. Chem.*, 1994, **66**, 1077-1184.
(38) D. T. Yiu, M. F. Lee, W. W. Lam and T.-C. Lau, *Inorg. Chem.*, 2003, **42**, 1225-1232.
(39) M.-C. Kafentzi, M. Orio, M. Réglier, S. Yao, U. Kuhlmann, P. Hildebrandt, M. Driess, A. J. Simaan and K. Ray, *Dalton Trans.*, 2016, **45**, 15994-16000.
(40) L. R. Mahoney and M. A. DaRooge, *J. Am. Chem. Soc.*, 1970, **92**, 890-899.
(41) J. M. Mayer, *J. Phys. Chem. Lett*, 2011, **2**, 1481-1489.
(42) J. P. Roth, J. C. Yoder, T.-J. Won and J. M. Mayer, *Science*, 2001, **294**, 2524-2526.

(43) J. Y. Lee, R. L. Peterson, K. Ohkubo, I. Garcia-Bosch, R. A. Himes, J. Woertink, C. D. Moore, E. I. Solomon, S. Fukuzumi and K. D. Karlin, *J. Am. Chem. Soc.*, 2014, **136**, 9925-9937.
(44) P. Mondal, P. Pirovano, A. Das, E. R. Farquhar and A. R. McDonald, *J. Am. Chem. Soc.*, 2018, **140**, 1834-1841.
(45) I. Garcia-Bosch, R. E. Cowley, D. E. Díaz, R. L. Peterson, E. I. Solomon and K. D. Karlin, *J. Am. Chem. Soc.*, 2017, **139**, 3186-3195.
(46) C. H. Rochester and B. Rossall, *Phys. Org.*, 1967, 743-748.
(47) D. Unjaroen, R. Gericke, M. Lovisari, D. Nelis, P. Mondal, P. Pirovano, B. Twamley, E. R. Farquhar and A. R. McDonald, *Inorg. Chem.*, 2019, **58**, 16838-16848.
(48) S. Kundu, E. Miceli, E. R. Farquhar and K. Ray, *Dalton Trans.*, 2014, **43**, 4264-4267.
(49) T. Osako, K. Ohkubo, M. Taki, Y. Tachi, S. Fukuzumi and S. Itoh, *J. Am. Chem. Soc.*, 2003, **125**, 11027-11033.
(50) Bruker (2015). APEX3 v2015.9-0, Bruker AXS Inc., Madison, WI, USA.
(51) Bruker (2014/5). SADABS, Bruker AXS Inc., Madison, Wisconsin, USA.
(52) G. Sheldrick, *Acta Cryst. A*, 2015, **71**, 3-8.
(53) G. Sheldrick, *Acta Cryst. A*, 2008, **64**, 112-122.
(54) O. V. Dolomanov, L. J. Bourhis, R. J. Gildea, J. A. K. Howard and H. Puschmann, *J. Appl. Crystallogr.*, 2009, **42**, 339-341.
(55) B. Ravel and M. Newville, *J. Synchrotron Radiat.*, 2005, **12**, 537-541.
(56) M. Wojdyr, *J. Appl. Crystallogr.*, 2010, **43**, 1126-1128.

Chapter 6

Conclusions and future work

6.1 Summary and conclusions

As previously outlined in section 1.6, the main subject of the present thesis was the preparation of high valent bis(μ-hydroxo) late transition metals (Ni and Cu) complexes and the study of their reactivity towards O/C–H activation. As there is an overall dearth of high-valent late transition metal μ-hydroxo species in the literature, the herein reported study had the aim to partially shed light on the role of this class of metastable species, which have been proposed as intermediates in the catalytic cycle of some monooxygenase systems such as sMMO and tyrosinase (see section 1.3).

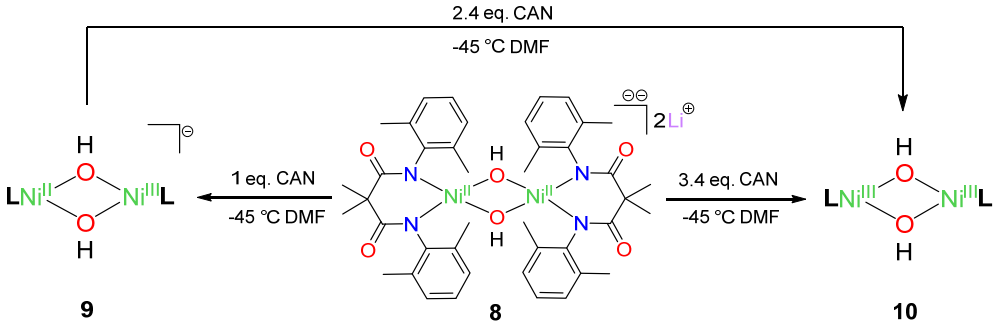

Scheme 6.1. Preparation of **9** and **10** by oxidation of **8** with CAN at -45 °C.

As a first step, the bidentate *N*,*N*'-bis(2,6-dimethyl-phenyl)-2,2-dimethylmalonamide ligand ($DMMA^{Me_2}$, **6**) was identified as a suitable platform for the synthesis of the desired complexes (Chapter 2). The ligand has been designed to be oxidatively robust and bear anionic nitrogen donor functionalities, in order to stabilise high valent oxidants. Starting from **6**, the dinuclear $[\mathbf{L}Ni^{II}(\mu\text{-}OH)]_2$ (**8**, Chapter 3, **L** = $DMMA^{Me_2}$) has been successfully synthesised and characterised by a series of techniques, such as XRD, FT-IR, NMR, cyclic voltammetry, mass spectrometry and electronic absorption spectroscopy. **8** exhibited a diamond core structure with two hydroxide ligands bridging the Ni^{II} ions, lying in a distorted square planar environment. Notably, cyclic voltammetry showed the presence of two accessible higher oxidation states that were explored by chemical oxidation. The low valent complex **8** was therefore reacted with a one electron oxidant (CAN) at low temperature (-45 °C), leading to the formation of the metastable mixed valent $Ni^{II}Ni^{III}$ (**9**) and high valent Ni^{III}_2 species (**10**) upon addition of 1 equiv. and 3.4 equiv. of oxidant respectively (Scheme 6.1, Figure 6.1). X-band EPR monitored titration of CAN with **8**

(Figure 6.1) showed the clear conversion of the $S = 0$ species **8** to the $S = 1/2$ species **9**, confirming its assignment as $Ni^{II}Ni^{III}$.

Further addition of oxidant led to **10**, which exhibited a silent spectrum in perpendicular mode EPR, revealing an antiferromagnetic ($S = 0$) or ferromagnetic coupling ($S = 1$) between the unpaired electrons on the Ni^{III} centres. The possibility of such a coupling was confirmed by DFT calculations, which found that both configurations are possible under the experimental conditions, with negligible differences in energy. X-ray absorption spectroscopy and DFT calculations were consistent with the assigned oxidation states and confirmed that the bridging hydroxide ligands are maintained in **9** and **10** despite the increase in oxidation state.

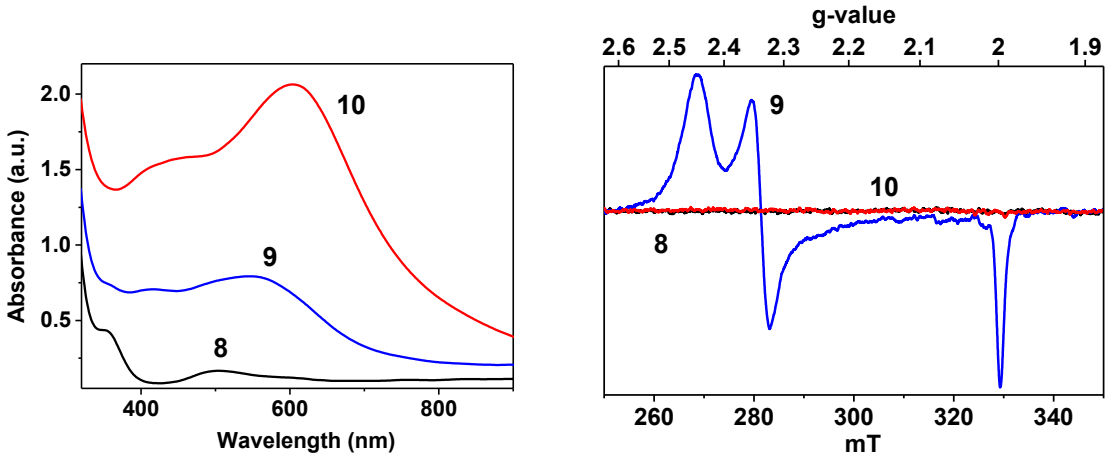

Figure 6.1 – Electronic absorption (*left*) and X-band EPR (*right*) spectroscopy of **8** (black trace), **9** (blue trace) and **10** (red trace).

Species **9** and **10** were demonstrated to be competent in the oxidation of phenolic O–H bonds using a series of *para*-X-2,6-di-*tert*-butylphenols (X = $-OCH_3$, $-CH_3CH_2$, $-CH_3$, $-C(CH_3)_3$, –H, –Br, –CN, $-NO_2$) as probe substrates. Analysis of the kinetic data showed that for both species, the oxidation of the substrates followed a hydrogen atom transfer (HAT) mechanism. Moreover, in the case of the $Ni^{III}_2(\mu\text{-}OH)_2$ species **10** a biphasic decay was observed, with formation of the intermediate species **9'** (Scheme 6.2) in the first step. This species, which was capable of further reaction with the substrates through a HAT mechanism, exhibited similar reactivity and electronic absorption features with **9** and was identified as the formal product of the HAT reaction of **10** on the substrate, namely $Ni^{II}Ni^{III}(\mu\text{-}OH\text{-}\mu\text{-}OH_2)$. All the three active species displayed relatively high oxidation

rates towards phenolic O–H bonds: however, the oxidation rates displayed by **10** surpassed those of many among the most known mononuclear Ni^{III}–O–X and dinuclear $Ni^{III}_2(\mu\text{-}O)_2$ complexes.

Analysis of the post reaction mixtures for both **9** and **10** by ESI and ^{1}H-NMR allowed for the proposal of an overall reaction mechanism for these species (Scheme 6.2). The presence of the free pristine ligand at the end of the reaction, in addition to emphasise the innocence of the ligand, suggested the formation of an intermediate unstable $Ni^{II}_2(\mu\text{-}OH_2)$ species (**8-2H**), which would release **6** upon decay. This hypothesis was corroborated by the reaction of the low valent species **8** with a weak acid (*i.e.* 2,6-dimethylbenzoic acid), which led to the formation of a double protonated species (formally **8-2H**) with pK_a values of 9.7 and 10 in DMF. Species **10** also demonstrated the ability to oxidise 9,10-dihydroanthracene (BDE_{C-H} = 78 kcal/mol) to yield anthracene in ≈ 80% yield (GC-FID), albeit a proper kinetic study was not possible as this reaction occurred at comparable rates with the self-decay of the complex.

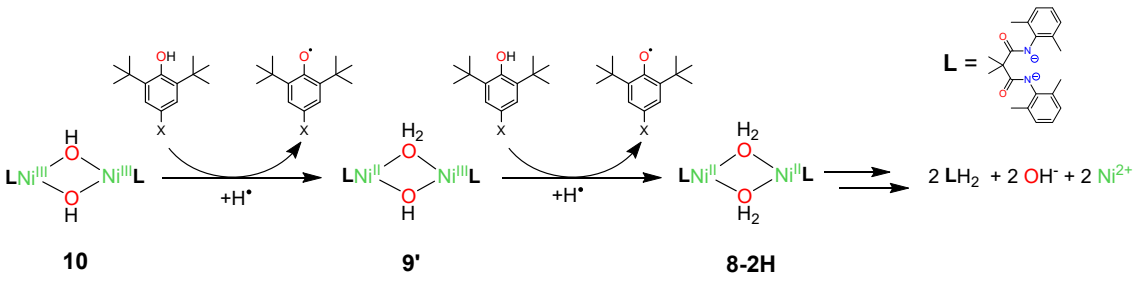

Scheme 6.2 – Proposed reaction mechanism for the reaction of **10** and **9'** with substrate.

In the last chapter of this thesis, applying the acquired knowledge on the $DMMA^{Me2}$ based complexes, the $[\mathbf{L}Cu^{II}(\mu\text{-}OH)]_2$ (**11**, Chapter 5) complex was synthesised, in order to understand how the structural and reactivity properties observed for **8**, **9** and **10** were influenced by changing the metal centre. Structural characterisation by XRD identified **11** as characterized by a diamond core structure almost identical to **8** (Figure 6.2), suggesting that the dinuclear geometry was driven by the ligand structure. Following cyclic voltammetry results, which assessed the presence of only one accessible oxidation state, **11** was demonstrated to react with a one electron oxidant (CAN, 1.5 equiv.) at low temperature (-45 °C) in DMF to lead the formation of a new species **12**, tentatively

identified as the $Cu^{II}Cu^{III}(\mu\text{-}OH)_2$ species, in parallel to what has been observed for the Ni complex. Both EPR and Cu K-edge absorption spectroscopy experiments were consistent with the proposed structure of **12**, although none of them confirmed it unequivocally. Nevertheless, reactivity of **12** towards phenolic O–H bonds was analysed by reaction with a series of *para*-X-2,6-di-*tert*-butylphenols (X = $-OCH_3$, $-CH_2CH_3$, $-CH_3$, $-C(CH_3)_3$, –H, $-NO_2$). Analysis of the kinetic data identified species **12** as capable of performing the oxidation of phenolic O–H bonds through a hydrogen atom transfer mechanism, displaying reactivity rates comparable with previously reported mono and dinuclear Cu^{III} species. Moving from Ni to Cu caused a stark enhancement of the reactivity properties of the complex: the $Cu^{II}Cu^{III}$ species **12** was more reactive than the analogue $Ni^{II}Ni^{III}$ complex **9**, although less reactive than the Ni^{III}_2 complex **10**. According to these results, a hypothetical Cu^{III}_2 species based on the herein reported ligand system would actually be a superior oxidant capable of competing with most reactive high valent bis-μ-oxo species reported to date.

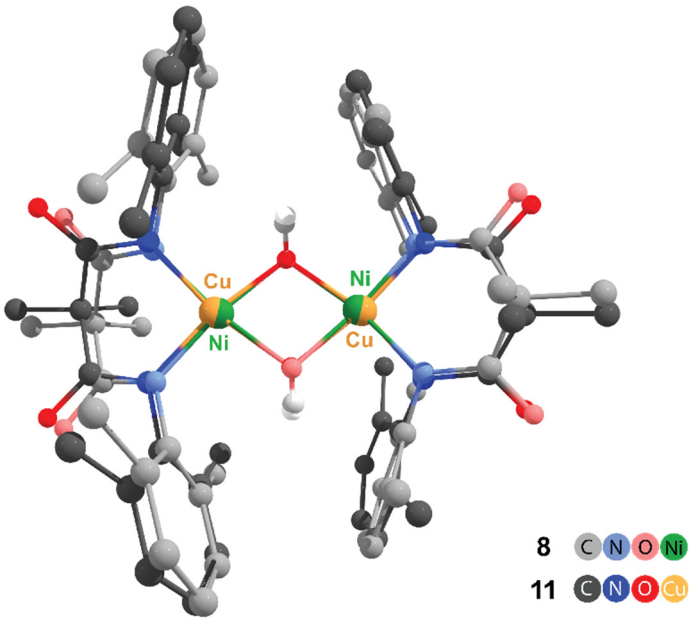

Figure 6.2 – Overlap of the crystal structures of **8** (lighter colours) and **11** (darker colours), top and longitudinal views. Root-mean-square deviation of atomic positions for the $M^{II}_2(\mu\text{-}OH)_2$ core RMSD = 0.147 Å.

The results obtained in this thesis identified species **9** and **10** as the first examples of high-valent bis-μ-hydroxo-Ni_2 reported to date and **12** as one of the few mixed valent dinuclear bis-μ-hydroxo late transition metal complexes observed. The unprecedented synthesis of such elusive species, which could play a fundamental role in the understanding of several dinuclear monooxygenases, relied on the tailored features of the chosen ligand system. The enhanced σ-donation of the amidic nitrogen atoms on **6** highly stabilised the high valent ions, moving electron density on to the metal centres and decreasing the acidity of the HO^- functionalities. Such a decreased acidity of the hydroxide moieties resulted in an enhancement of the stability of the high valent bis-μ-hydroxide complexes.

Moreover, the experimental kinetic results extensively proved that herein reported high-valent hydroxide-bridged dinuclear late transition metal complexes are powerful oxidants that can even match, such in the case of **10**, the kinetic reactivity of the most reactive comparable oxo-bridged entities.

In conclusion, we experimentally proved the effectiveness of the high-valent hydroxide-bridged dinuclear complexes in performing oxidation reactions with the same mechanism and similar rates of the postulated high valent bis-μ-oxo dinuclear active sites of several metalloenzymes. Such strong evidence corroborated the hypothesis that, according to the local pH, an equilibrium between the bis-μ-oxo and the bis-μ-OH could exist, with the latter a possible species responsible for enzymatic activity, therefore turning the tables in the current understanding of the activity of several monooxygenase enzymes.

6.2 Future works

The results presented in this thesis open several avenues to expand the current knowledge regarding the potential of the high valent dinuclear bis-μ-hydroxo complexes supported by the reported malonamide ligand.

1) Although the ligand system fulfilled the proposed aims, several improvements could be made. Both for the complex **8** and **11**, their poor solubility in apolar solvents limited the oxidation studies to the use of DMF, which, other than being a coordinating solvent, has a relatively high melting point (-61 °C) which did not allowed the testing of the behaviour of the studied systems below -45 °C, due to a rapid increase of solution viscosity. Since metathesis of the cations with phase transfer agents such as ammonium salts was not effective, a possible solution will be improving the solubility of the complexes in apolar low melting point solvents, bringing some modification to the ligand backbone. In particular, the α-carbon of the $DMMA^{Me_2}$ ligand could be functionalised with aliphatic chains, which should increase the solubility without interfering with the reactivity of the metal centres. Moreover, the introduction of different substituents on the aromatic rings will be evaluated, in order to understand how they will affect the solubility and the overall chemistry properties of these systems.

2) The synthesis of a high-valent bis-μ-hydroxo reactive species such as **10** strongly supported the hypothesis of a more important role of the μ-hydroxo species in enzymatic processes. This hypothesis could be strongly supported finding evidences of the proposed equilibrium between the species **10** and its high valent bis-μ-oxo counterpart. Therefore, a critically important avenue to pursue would be the synthesis of a $Ni^{III}_2(\mu\text{-}O)_2$ based on the $DMMA^{Me2}$ ligand. The preliminary work conducted treating **10** with different bases showed no direct evidences of formation bis-μ-oxo species at the experimental conditions. An alternative approach could be the synthesis of the $Ni^{III}_2(\mu\text{-}O)_2$ species by reaction of **8** with two electrons oxidant such as *m*-CPBA (*m*-chloroperoxybenzoic acid) or H_2O_2, followed by conversion of the obtained species to **10** in presence of a weak proton source.

3) An interesting question is whether high valent mononuclear complexes could be accessed by using the herein reported $DMMA^{Me2}$ ligand, focusing on mononuclear M–O–X and M=O systems (M = Co, Ni, Cu). These systems could have reactivity

comparable to the most powerful late transition metal-based oxidant reported to date. In order to achieve this aim, a crucial point will be adapting the ligand structure to force a trigonal planar geometry of the metal centre, allowing for the stabilisation of the elusive M=O complexes (M = Co, Ni, Cu). The molecular orbitals arrangement in a trigonal planar geometry should allow the allocation of the *d*-electrons > 6 without destabilising the oxo ligand, thus overcoming the "oxo wall" limit theorised by Gray and Winkler for late first-row transition metal in a pseudo-octahedral environment.

4) One of the main reasons driving our research on nickel and copper complexes was the hypothesis that late first-row transition metal (Co, Ni and Cu) oxidants would exhibit a greater oxidising power than the corresponding iron and manganese complexes. Therefore, it will be fundamental to explore these metals, synthesising the corresponding dinuclear μ-hydroxo complexes, in order to have a clear understanding of how the different metal centres can affect the structure, reactivity and oxidising power. We plan to ideally use the same approach seen for Ni and Cu, thus obtaining the high valent bis-μ-hydroxo species starting from the corresponding low valent bis-μ-hydroxide precursor. Initially, particular efforts will be put on Co, in order to complete the late first-row transition metal series with Ni and Cu. Then, once the corresponding Mn and Fe species are also prepared, we will perform a comparative study, using the same methods observed for Ni and Cu. This will include analysis of the high valent species through advanced spectroscopic techniques, such as EPR and X-ray absorption spectroscopy, and analysis of their reactivity through the use of probe substrates such as phenols and hydrocarbons.

Appendix

Appendix A

Appendix to Chapter 2

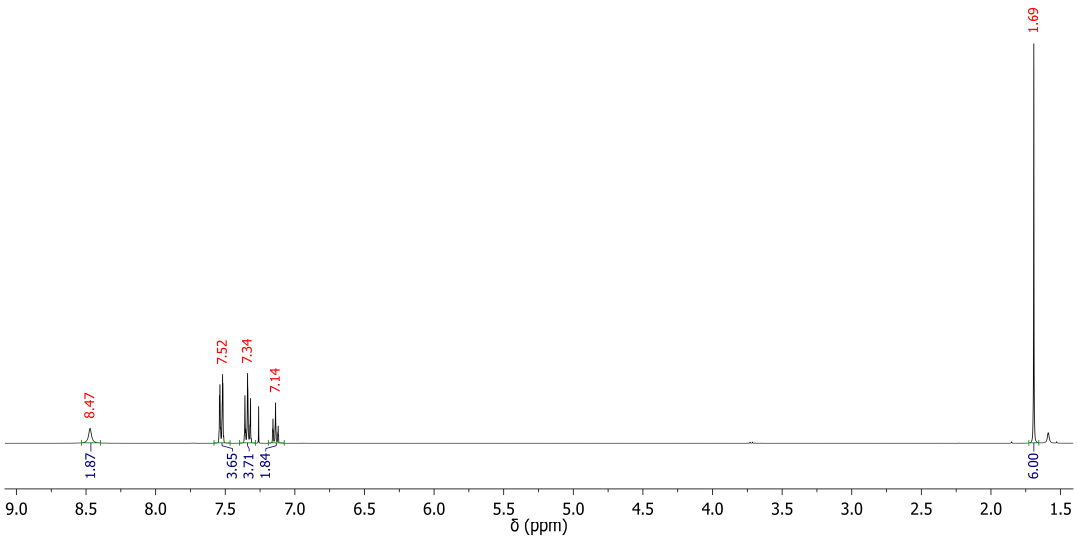

Figure A-2.1 - ^{1}H-NMR spectrum of **5** (400 MHz, $CDCl_3$).

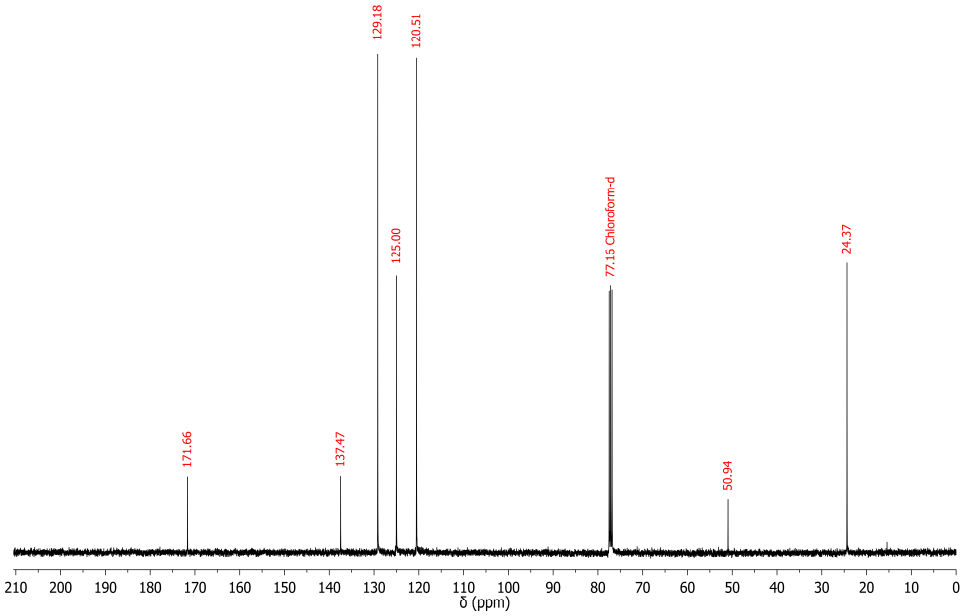

Figure A-2.2 - ^{13}C-NMR spectrum of **5** (100 MHz, $CDCl_3$).

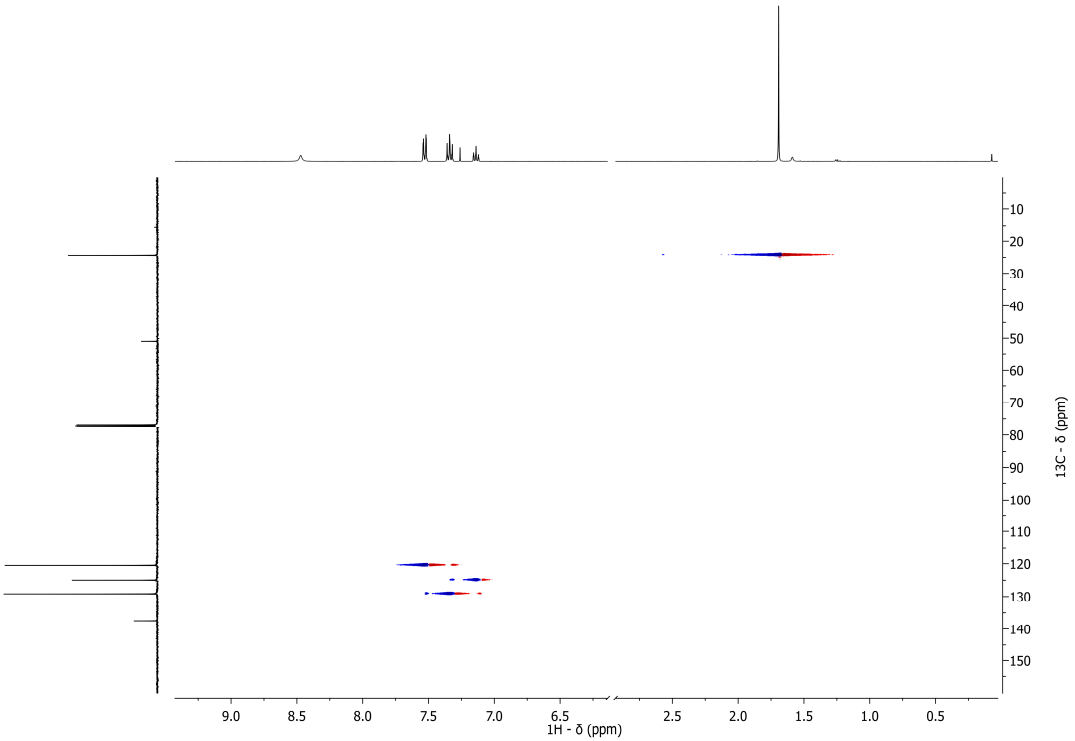

Figure A-2.3 - ^{1}H-^{13}C heteronuclear single quantum correlation spectrum of **5** (CDCl3).

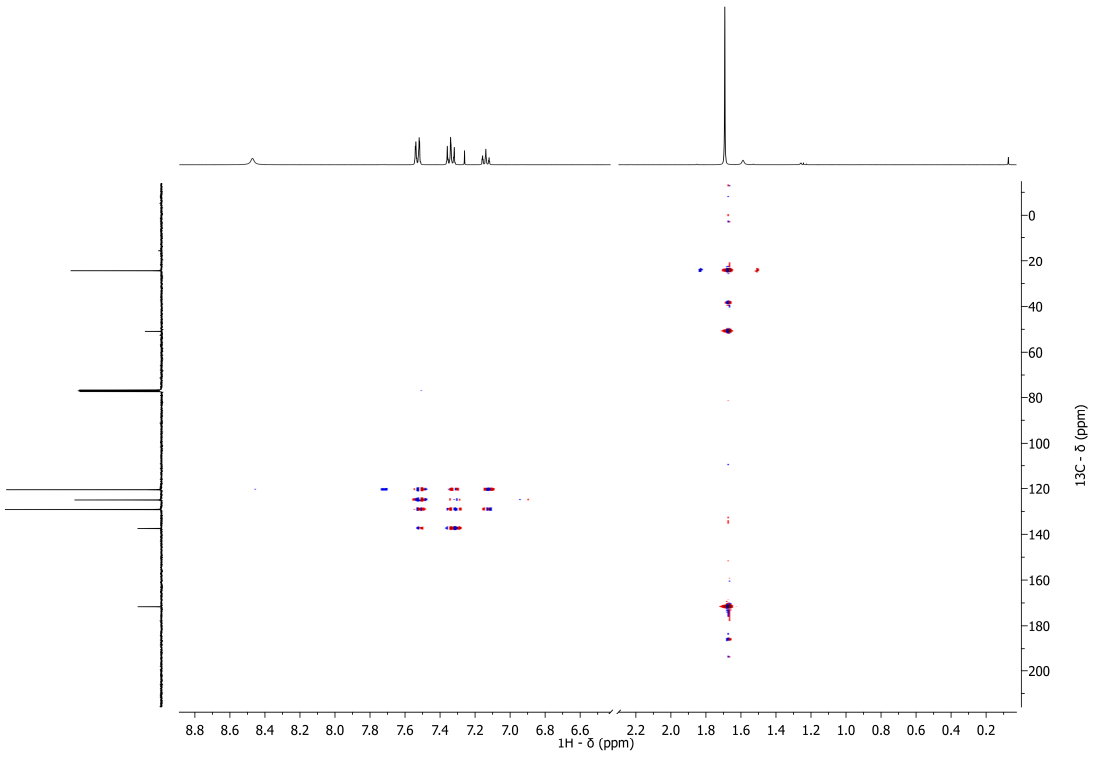

Figure A-2.4 - ^{1}H-^{13}C heteronuclear multiple bonds correlation spectrum of **5** ($CDCl_3$).

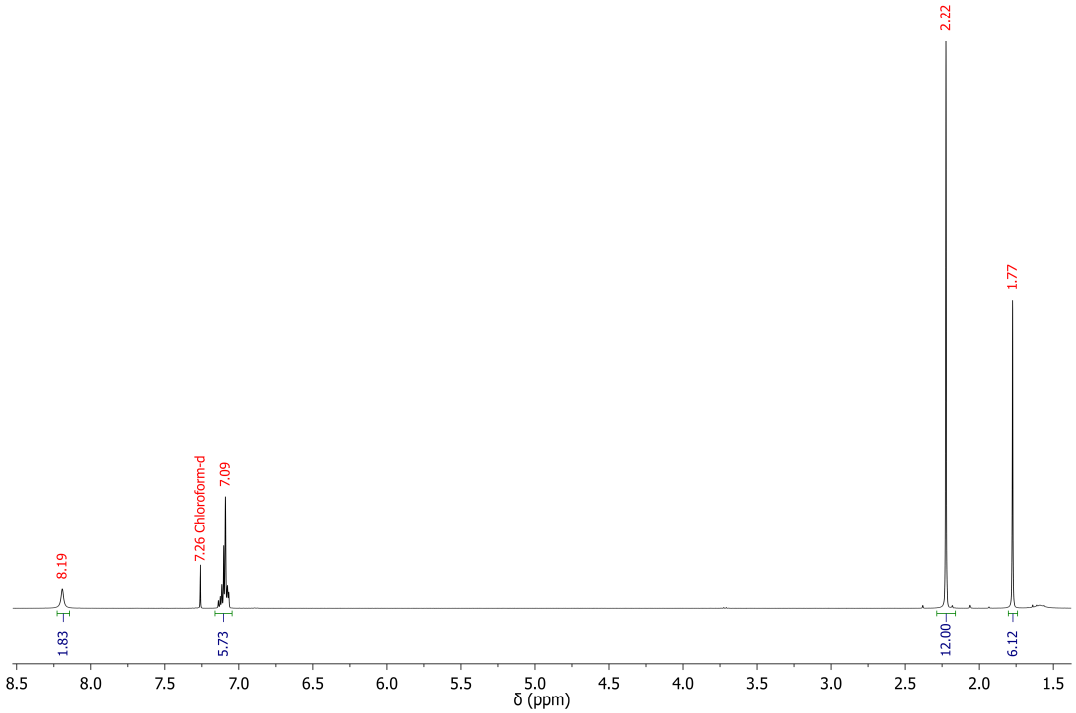

Figure A-2.5 - ^{1}H-NMR spectrum of **6** (400 MHz, $CDCl_3$).

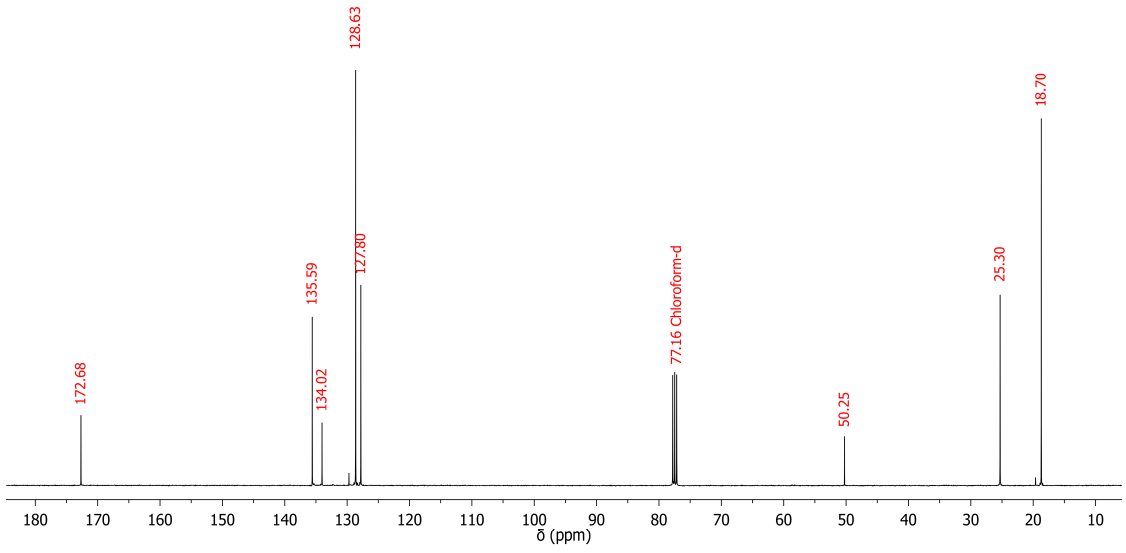

Figure A-2.6 -^{13}C-NMR spectrum of **6** (100 MHz, $CDCl_3$).

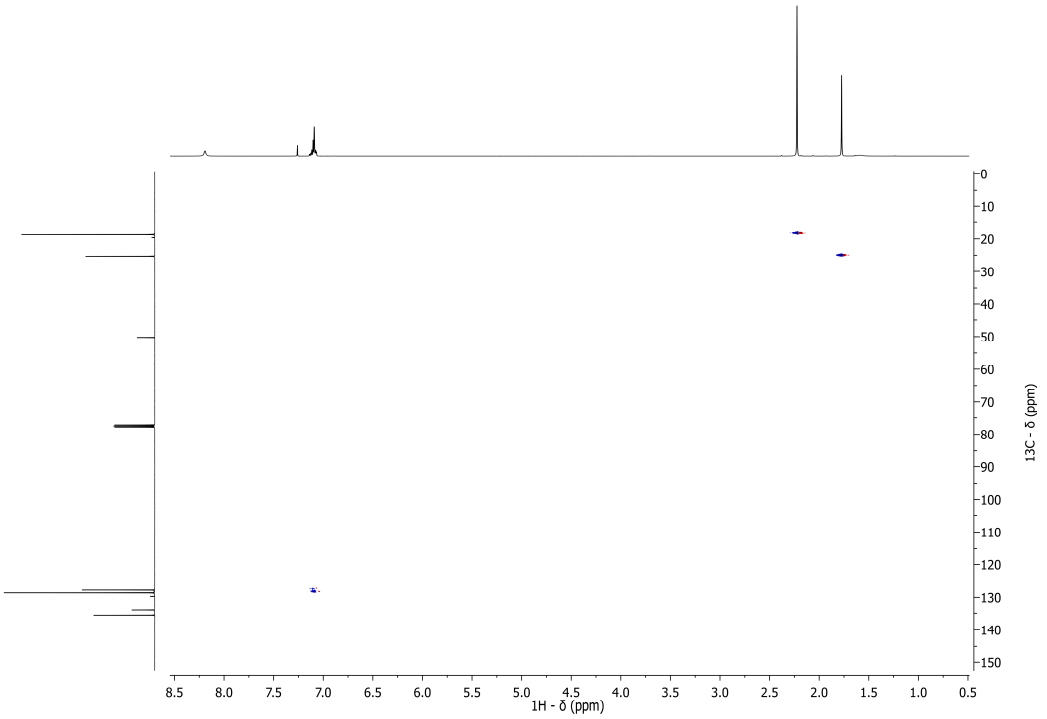

Figure A-2.7 - ^{1}H-^{13}C heteronuclear single quantum correlation spectrum of **6** (CDCl3).

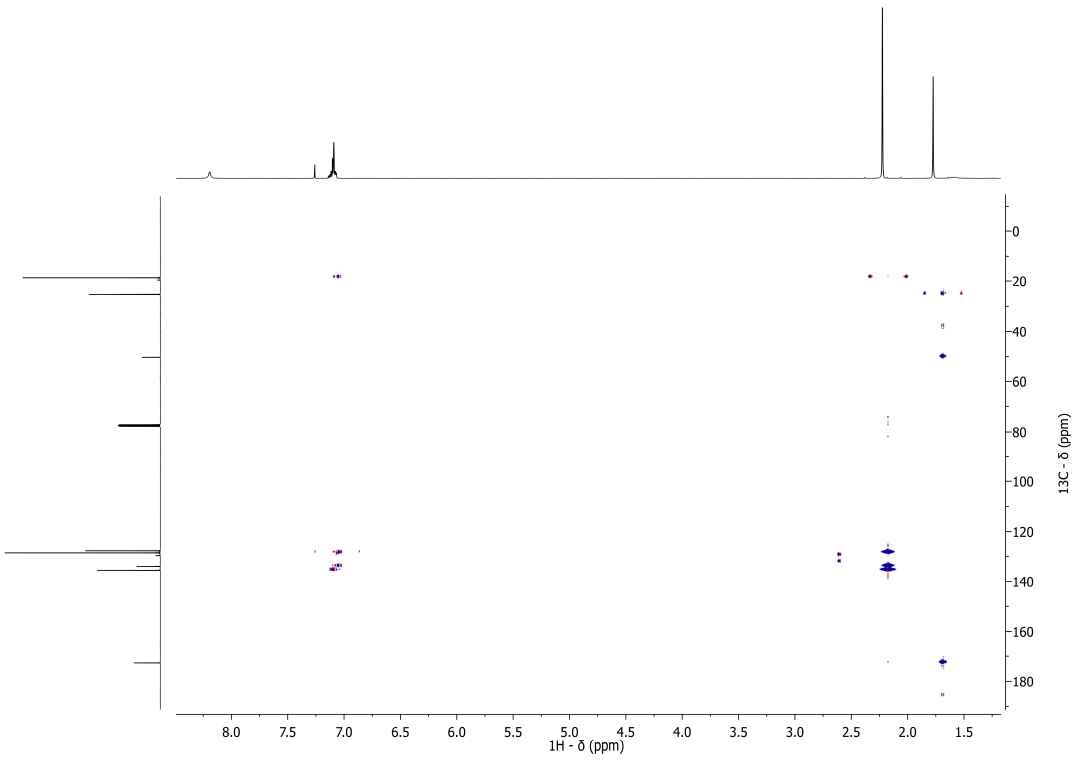

Figure A-2.8 - ^{1}H-^{13}C heteronuclear multiple bonds correlation spectrum of **6** ($CDCl_3$).

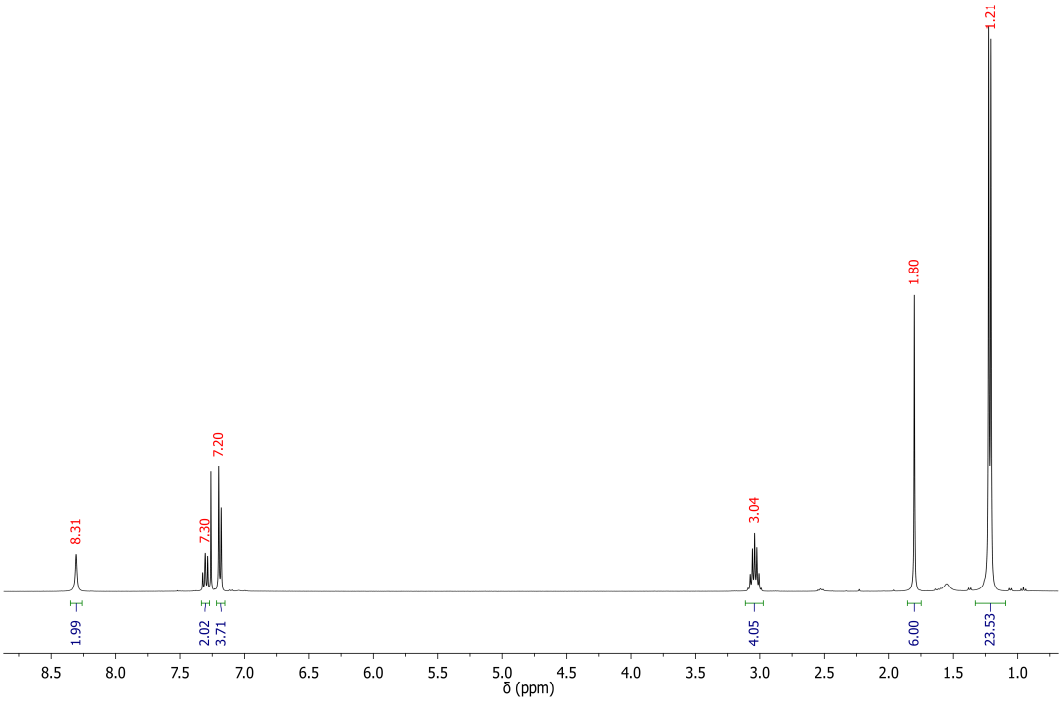

Figure A-2.9 - ^{1}H-NMR spectrum of **7** (400 MHz, $CDCl_3$).

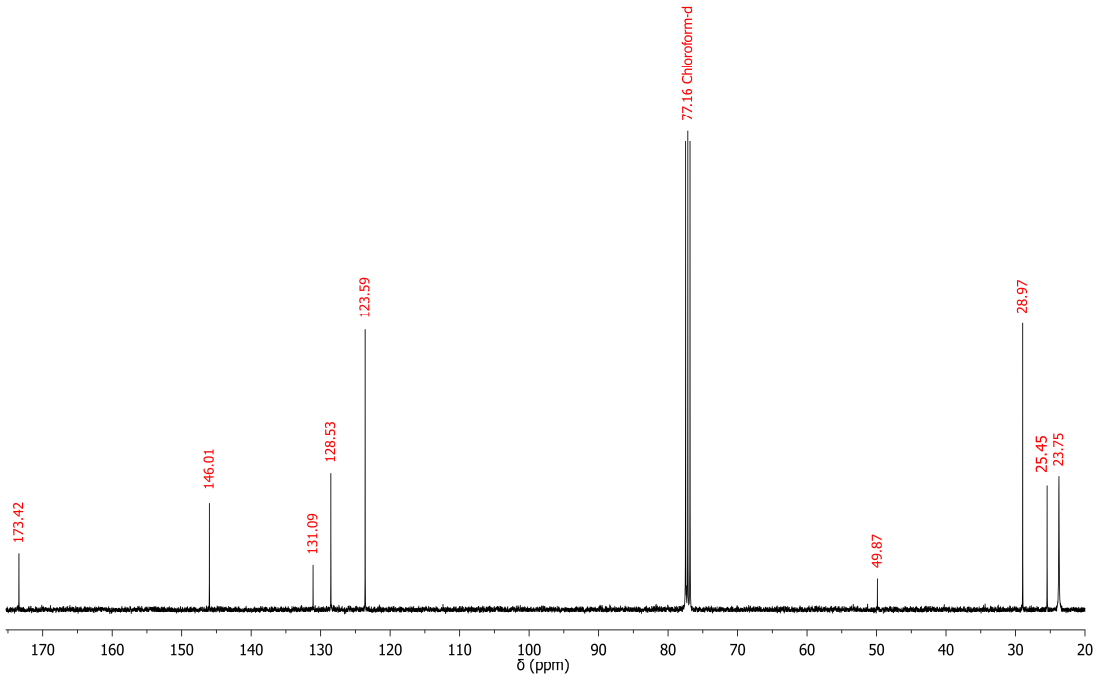

Figure A-2.10 -^{13}C-NMR spectrum of **7** (100 MHz, $CDCl_3$).

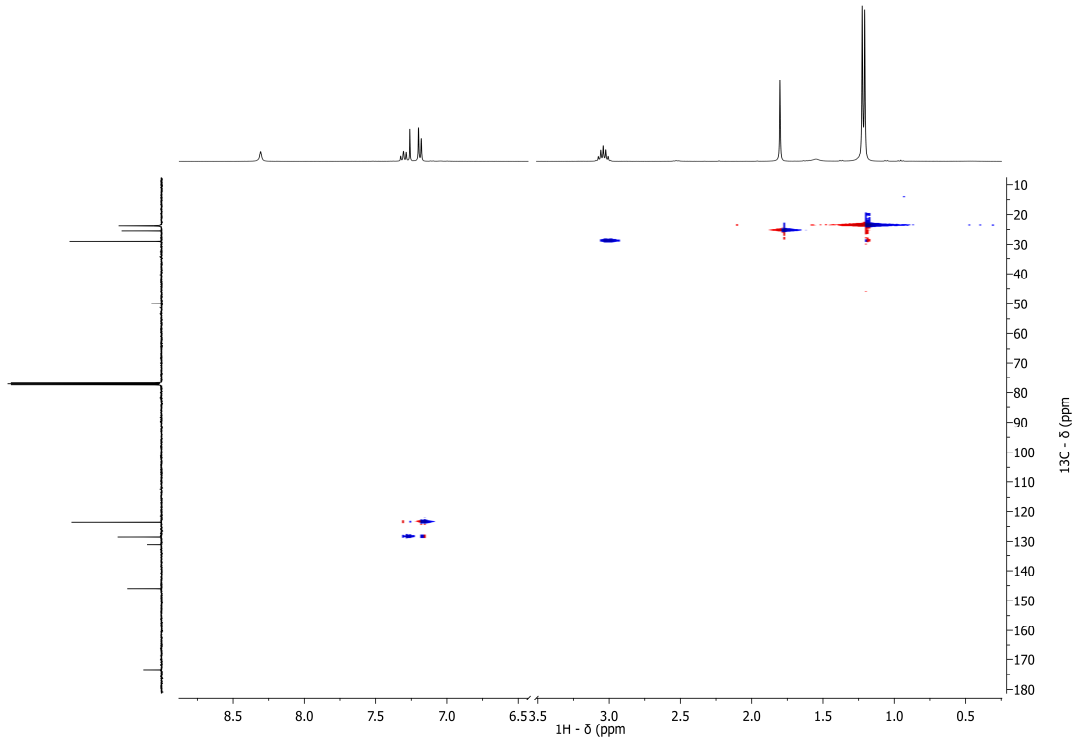

Figure A-2.11 - ^{1}H-^{13}C heteronuclear single quantum correlation spectrum of **7** (CDCl3).

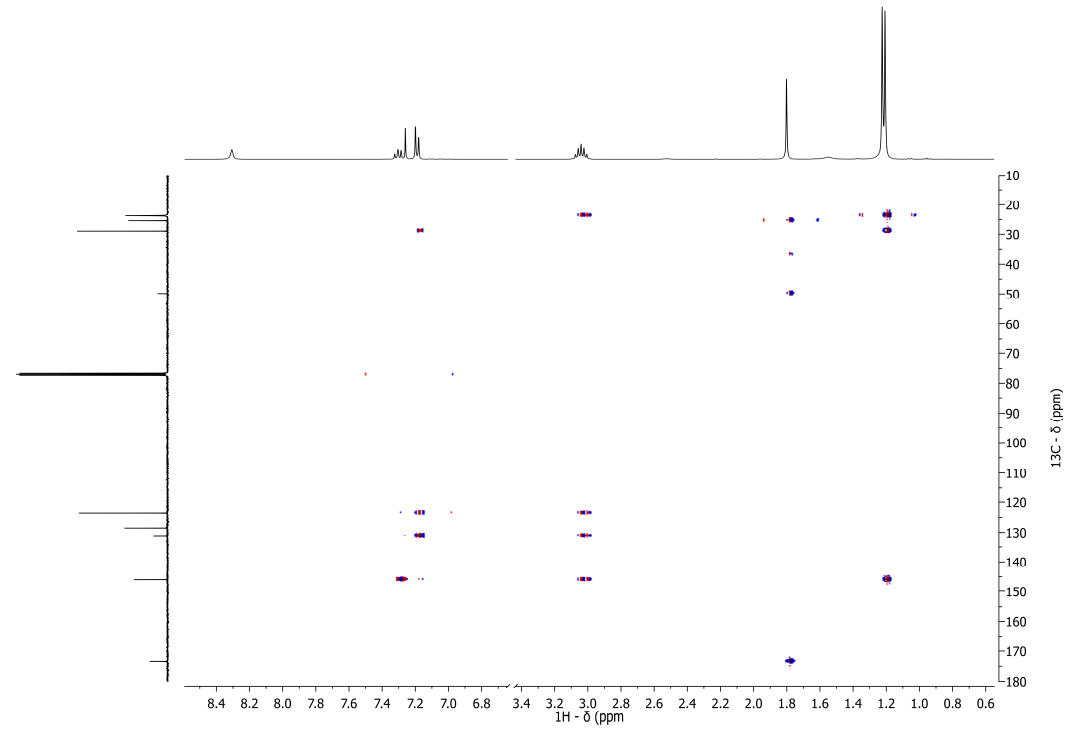

Figure A-2.12 - ^{1}H-^{13}C heteronuclear multiple bonds correlation spectrum of **7** ($CDCl_3$).

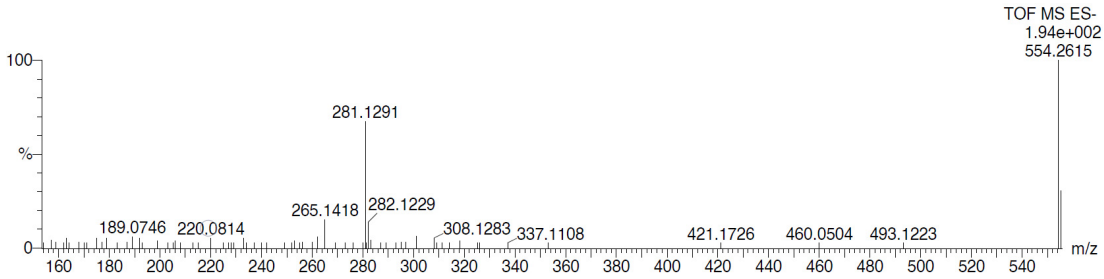

Figure A-2.13 – ESI spectra for **5**. Found: 281.1291 ($[M-H]^+$. $C_{17}H_{17}N_2O_2^-$ requires 281.1290).

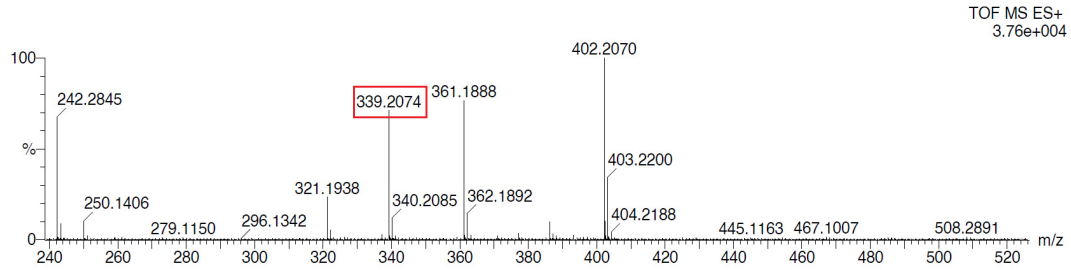

Figure A-2.14 – ESI spectra for **6**. Found: 339.2074 ($[M+H]^+$. $C_{21}H_{27}N_2O_2^+$ requires 339.2067).

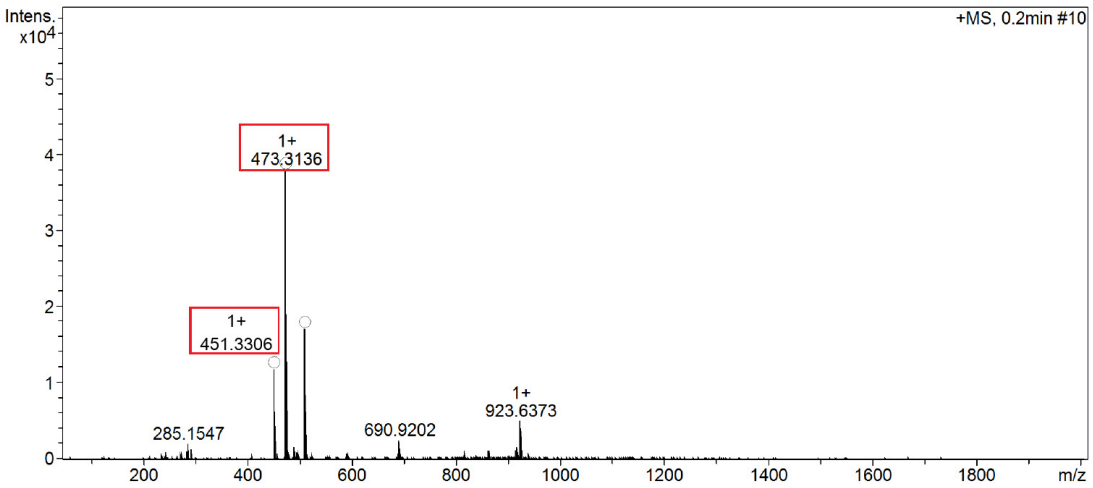

Figure A-2.15 - ESI spectra for **7**. Found: 451.3306 ($[M+H]^+$. $C_{29}H_{43}N_2O_2^+$ requires 451.3319); 473.3136 ($[M+Na]^+$. $C_{29}H_{42}N_2NaO_2^+$ requires 473.3138)

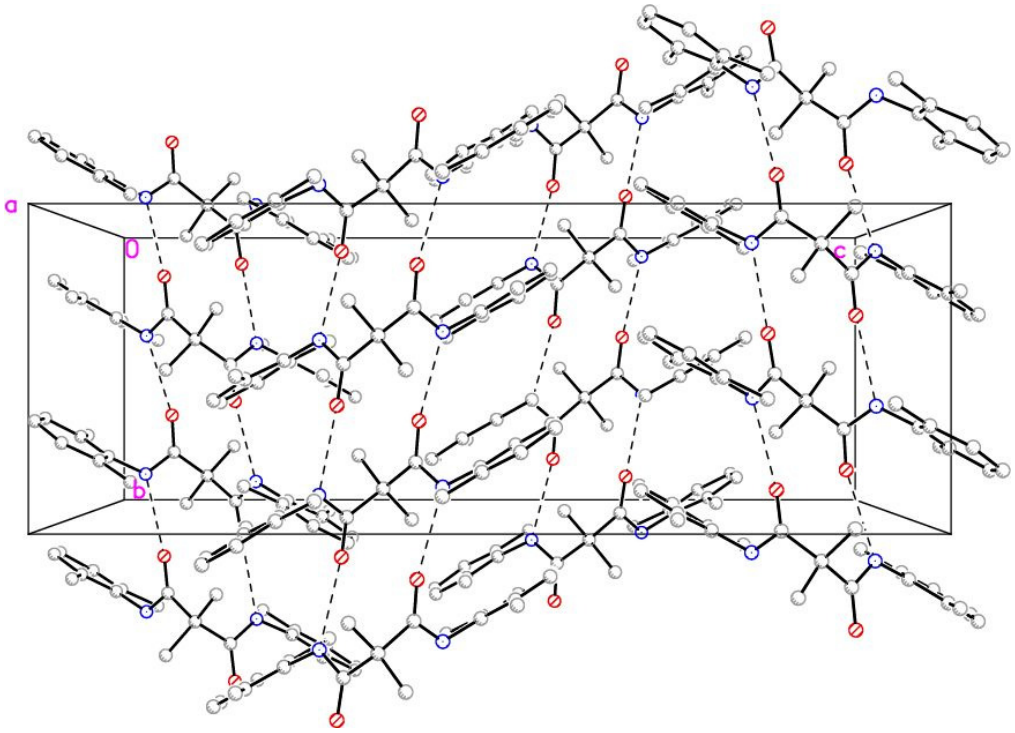

Figure A-2.16 - Packing diagram of **6** viewed normal to the a-axis displaying the hydrogen bonded network (dashed lines). Hydrogen atoms omitted for clarity.

Table A-2.1 - Hydrogen bonds for **6** [Å and °].

D-H...A	d(D-H)	d(H...A)	d(D...A)	<(DHA)
N(9)-H(9)...O(11)#1	0.911(9)	1.937(10)	2.8375(17)	169(2)
N(17)-H(17)...O(16)#2	0.911(9)	1.937(10)	2.8436(17)	173.6(18)

Symmetry transformations used to generate equivalent atoms:

#1 -x+1/2,y-1/2,z #2 -x+1/2,y+1/2,z

Appendix to Chapter 3

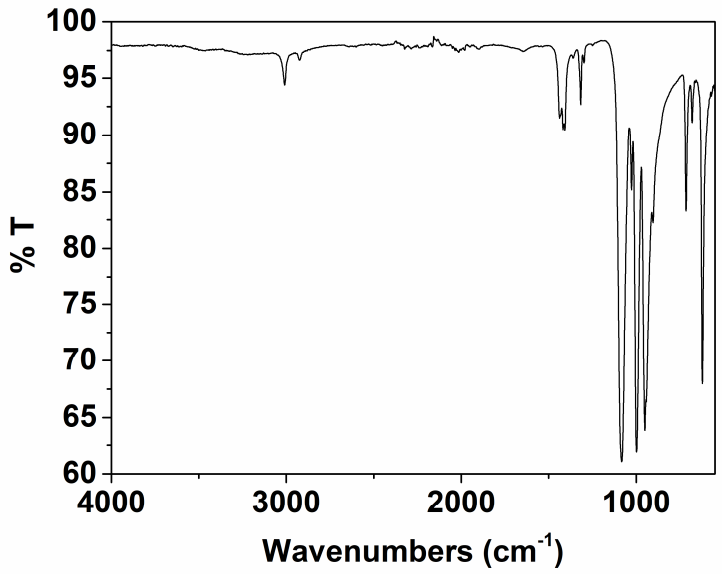

Figure A-3.1 - Attenuated Total Reflectance Fourier transform infrared spectrum of $[Ni(DMSO)_6](ClO_4)_2$.

Table A-3.1 - Selected crystallographic parameters for **8**.

Distances (Å)		**Angles (°)**	
N1–Ni1	1.8820(16)	**N1-Ni1-O15**	163.54(10)
N9-Ni1	1.8820(16)	**N9-Ni1-O15**	165.22(11)
Ni1-O15	1.927(3)	**Geometry indexes τ_4**	
Ni1-O15^{ii}	1.904(3)	**τ_4**	0.22
Ni1···Ni1'	2.8827(7)	**τ_4'**	0.21

Table A-3.2 - Comparison of Ni–O(H) and Ni···Ni distances for Ni bis-μ-hydroxide complexes bearing ligands with different denticity.

Ligand	Denticity	Ni–O (Å)	Ni···Ni (Å)
LH_2 (**6**)	bidentate	1.92	2.88
N,N-bis[2-(2-pyridyl)ethyl]-2-phenylethylamine[1]	tridentate	1.99	3.11
Bis[(6-methyl-2-pyridyl)methyl][(2-pyridyl)methyl]amine[2] (Me_2-tpa)	tetradentate	2.01	3.03
$ArNC(CF_3)CHC(CF_3)NAr$ (Ar = 2,6-$Me_2C_6H_3$)[3]	bidentate	1.86	2.93

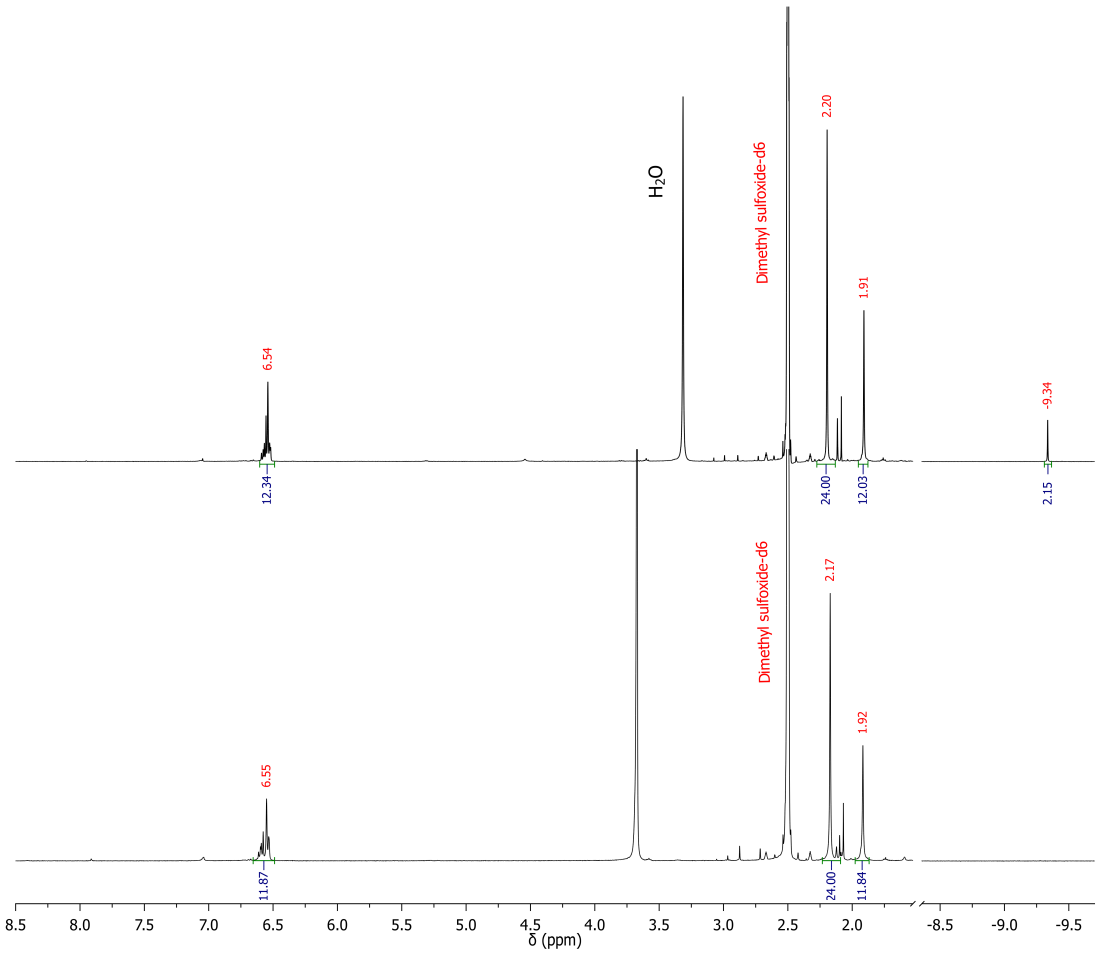

Figure A-3.2 - Top: ^{1}H-NMR spectrum of **8** (400 MHz, [D_6]-DMSO). Bottom: ^{1}H-NMR spectrum of **1** after addition of D_2O (400 MHz, [D_6]-DMSO).

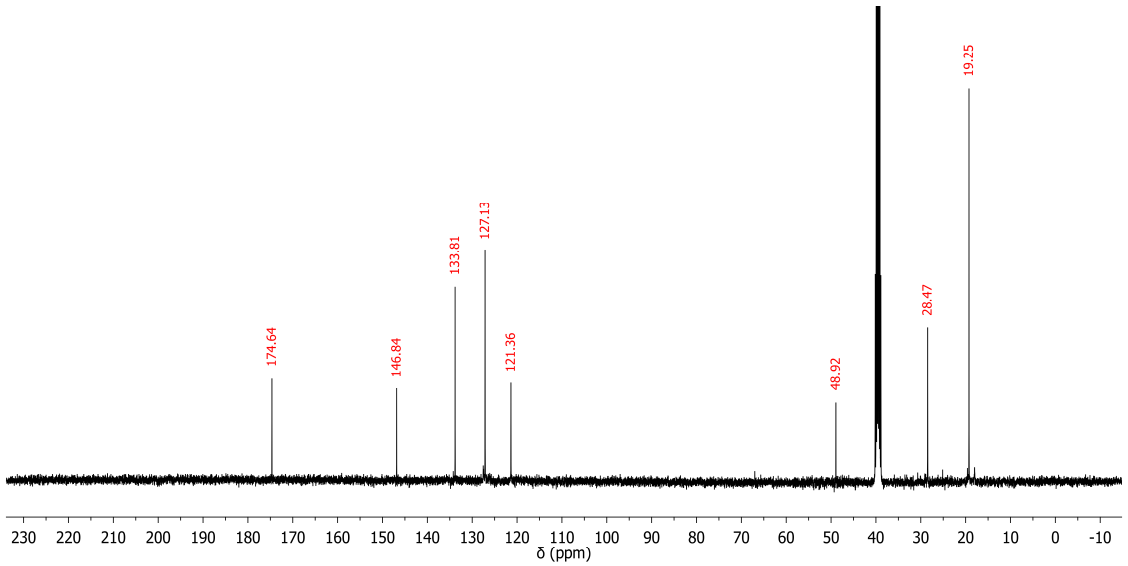

Figure A-3.3 - ^{13}C-NMR spectrum of **8** (100 MHz, [D_6]-DMSO).

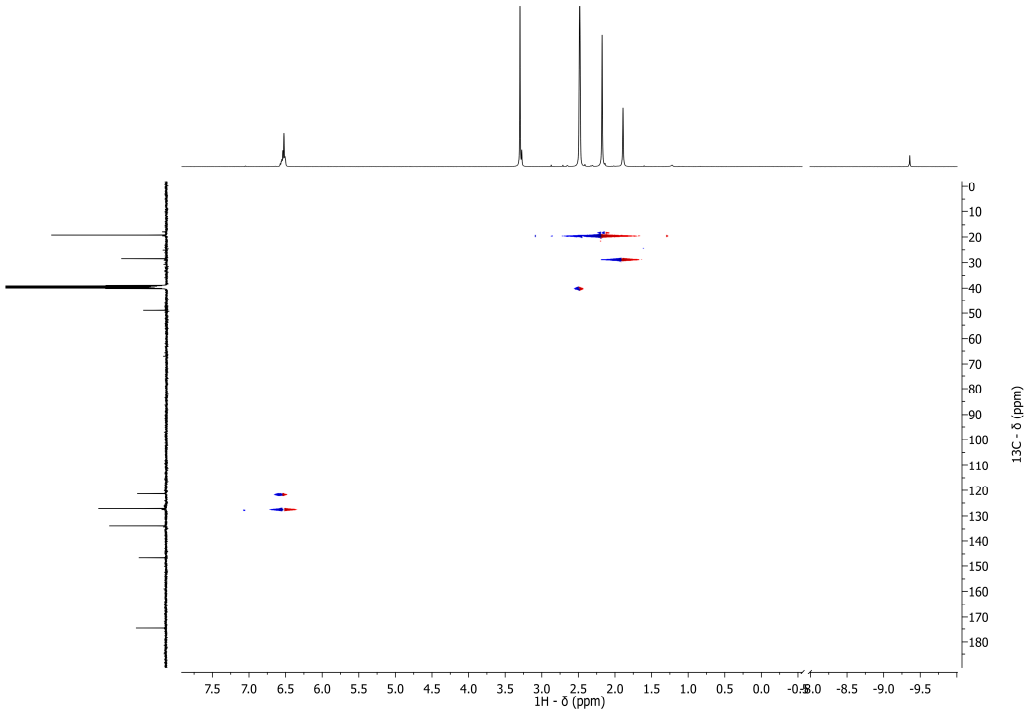

Figure A-3.4 - ^{1}H–^{13}C Heteronuclear single quantum correlation spectrum of **8** ([D_6]-DMSO).

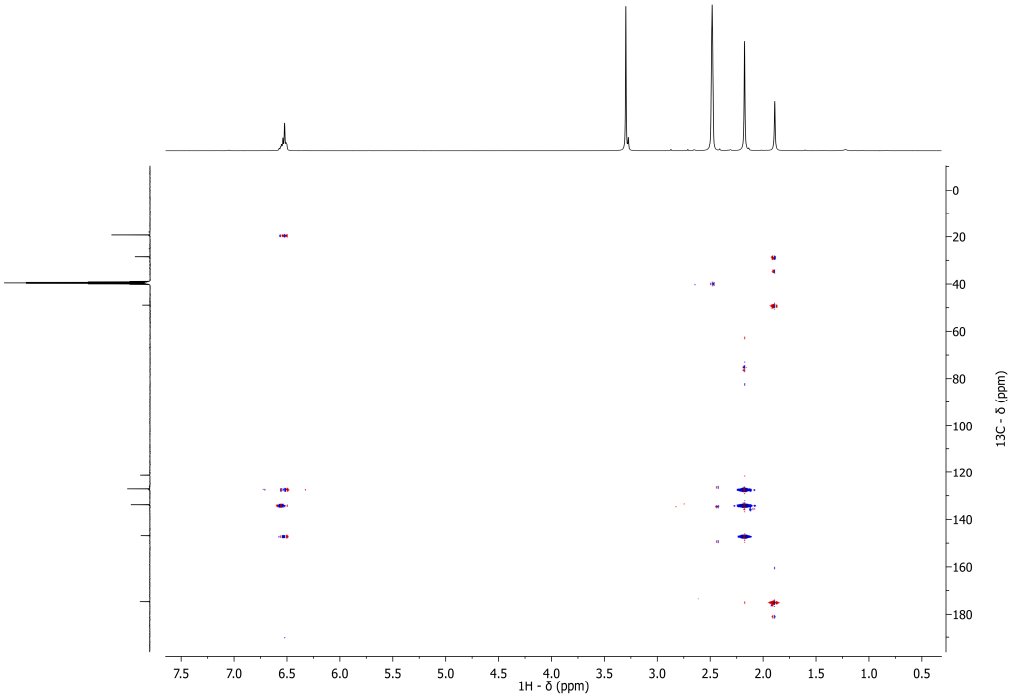

Figure A-3.5 - ^{1}H-^{13}C Heteronuclear multiple bonds correlation spectrum of **8** ([D_6]-DMSO).

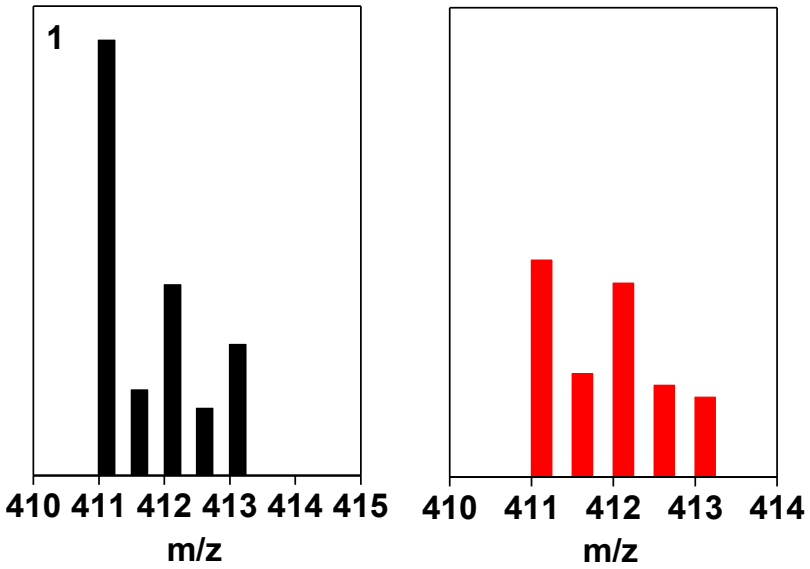

Figure A-3.6 - ESI-MS for **8** (black) and theoretical isotopic pattern (red). Found 411.1225 m/z. ([M^{2-}] $C_{42}H_{50}N_4Ni_2O_6^{2-}$ requires 411.1224 m/z).

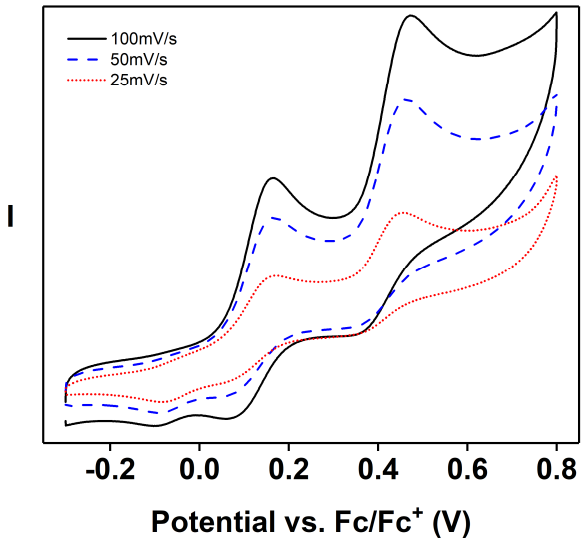

Figure A-3.7 - Cyclic voltammograms of **8**. Conditions: 5.5 mM (DMF), 0.1 M Bu_4NPF_6, scan rate 25 mV/s –100 mV/, room temperature.

Table A-3.3 - Cyclic Voltammetry data for **8,** recorded at different scan rates.

	mV/s	**E_{pa}**	**E_{pc}**	**$E_{1/2}$**	**E_{pa}-E_{pc}**	**I_{pa}**	**I_{pc}**	**$(\Delta E_p)_{complex}/(\Delta E_p)_{Fc}$**
	100	0.177	0.003	0.09	0.174	-7.71E-05	5.55E-05	
Ferrocene	50	0.158	0.008	0.083	0.15	-6.79E-05	4.48E-05	
	25	0.142	0.01	0.076	0.132	-5.63E-05	3.53E-05	
I ox wave	100	-0.007	-0.115	-0.061	0.108	-2.64E-06	1.40E-06	1.611111
	50	0.016	-0.083	-0.033	0.099	-1.47E-06	7.21E-07	1.515152
	25	0.04	-0.077	-0.018	0.117	-8.03E-07	6.50E-07	1.128205
II ox wave	100	0.3	0.182	0.241	0.118	-3.62E-06		1.474576
	50	0.316	0.206	0.261	0.105	-2.17E-06	5.21E-07	1.428571
	25	0.322	0.224	0.273	0.098	-1.24E-06	3.61E-07	1.346939

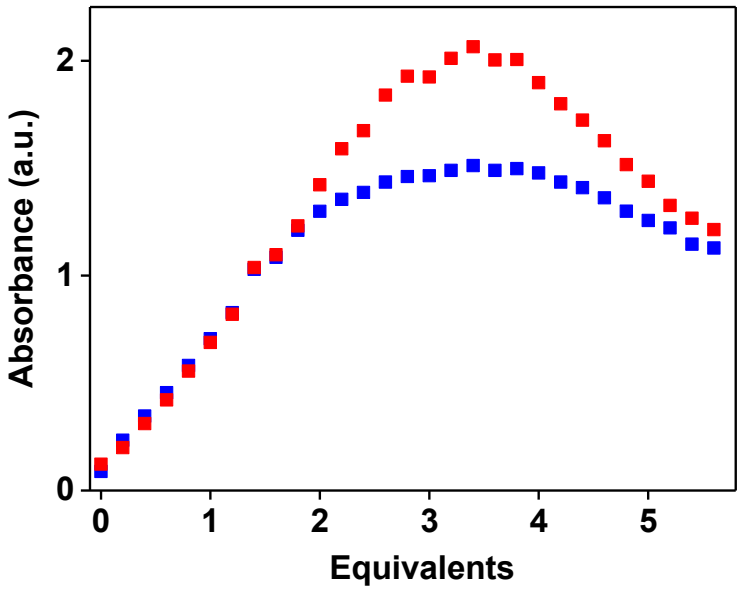

Figure A-3.8 - Plot of equiv. of CAN versus absorption intensity at λ = 410 nm (blue) and 600 nm (red) for the reaction between **8** and CAN.

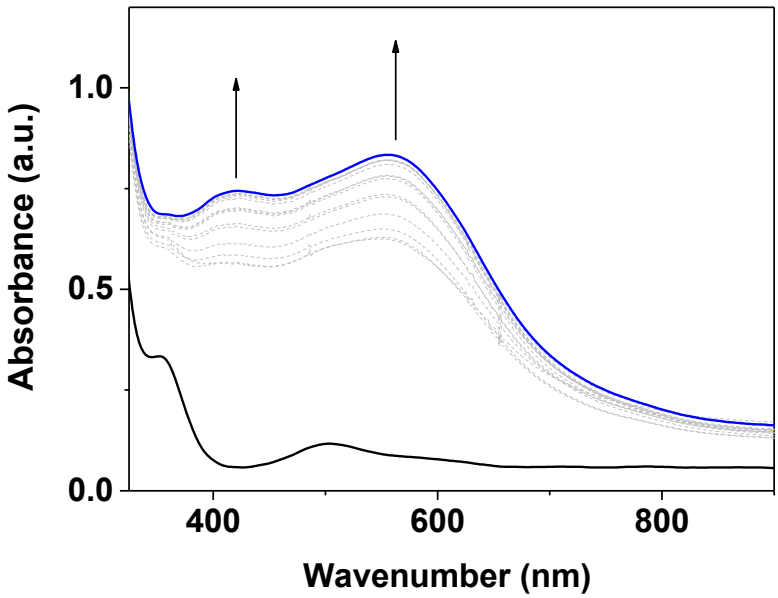

Figure A-3.9 - Electronic absorption spectrum of complex **8** (black trace, 0.2 mM, DMF, -45˚C) and **9** (blue trace), formed from the oxidation of **8** with 1 equiv. of CAN.

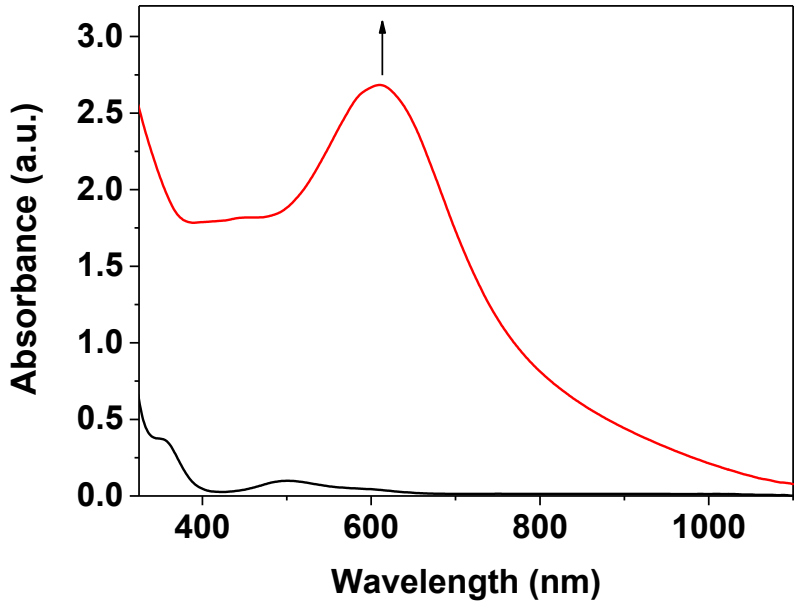

Figure A-3.10 - Electronic absorption spectrum of complex **8** (black trace, 0.2 mM, DMF, -45˚C) and **10** (red trace), formed from the oxidation of **8** with 3.4 equiv. of CAN.

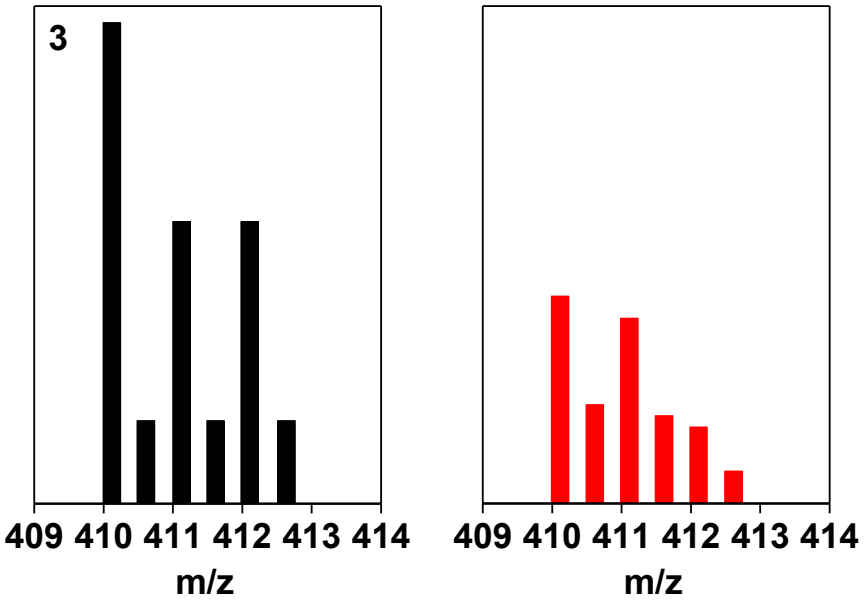

Figure A-3.11 - (-) ESI-Direct Injection for **10** (black) and theoretical isotopic pattern (red)**.** Found 410.1195 m/z. ([M-2H] requires 410.1146 m/z).

XAS Data

Table A-3.4 - XANES pre-edge peak fitting parameters. The values in parentheses correspond to uncertainty in the final digit for each parameter, taken as the standard deviation determined from the three separate fits conducted on each sample.

	$E_{pre\text{-}edge}$ (eV)[a]	Height	FWHM	Area[b]
8	8333.06(1)	0.0249(2)	1.72(1)	5.65(5)
9	8333.08(2)	0.0234(5)	1.80(6)	5.54(29)
10	8334.05(2)	0.0284(4)	2.72(3)	10.17(24)
	8333.06(1)	0.0088(5)	1.18(4)	1.38(12)

[a] The pre-edge energies correspond to the center of the pseudoVoigt functions. [b] Areas are multiplied by 10^2 for convenience.

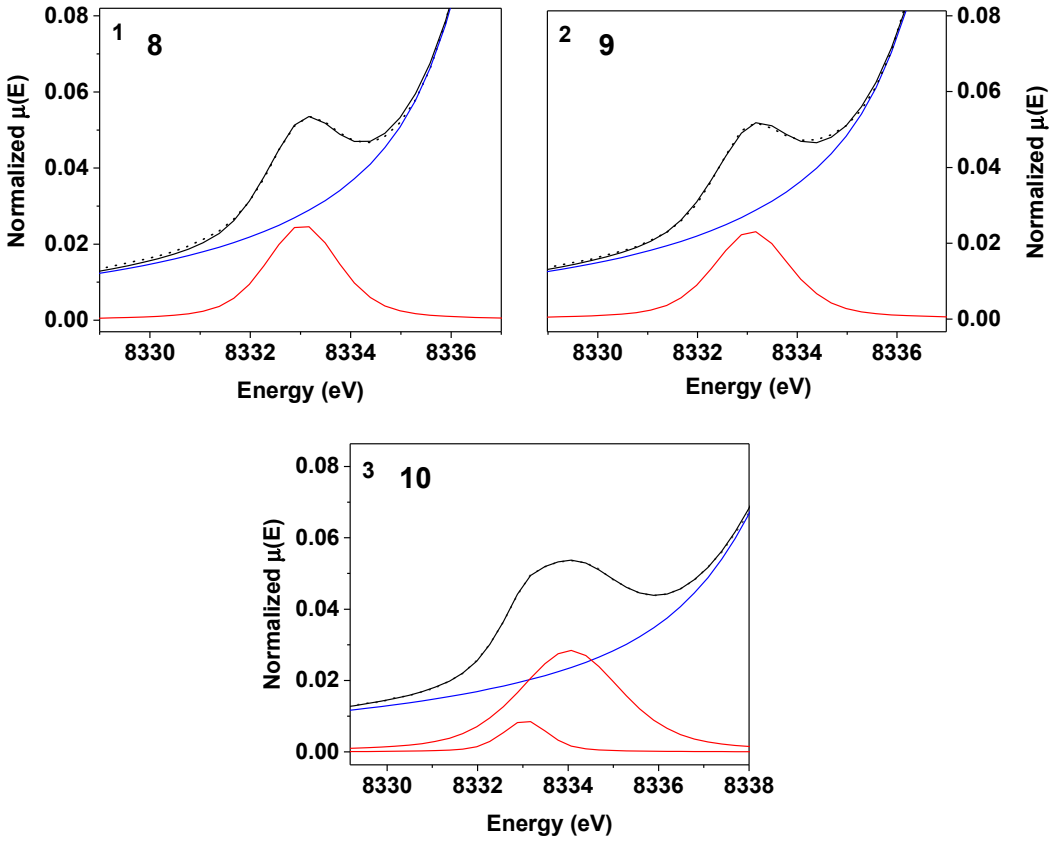

Figure A-3.12 - Representative pre-edge peak fits of **8, 9** and **10**. The experimental data is shown as dots, the background function in a blue line, the component pre-edge functions as red lines, and the sum of the background + component functions as a solid black line.

Table A-3.5 - EXAFS Fitting of the data for **8**. Significant fits are highlighted in bold. Fitting range was k = 2-14.0 Å-1 with back transform ranges of 1-1.95 Å for fits 1-5 and 1-3.20 Å for fits 6-17. r is in units of Å; σ^2 is in units of 10^{-3} Å; ΔE_0 is in units of eV; R represents the fractional mis-fit of the data, while χ^2 is the χ^2 fitting metric normalized by the number of independent data points in a given fit.

	Ni-N/O			Ni-N/O			Ni···Ni			Ni···C					
fit	n	r	σ^2	n	r	σ^2	n	r	σ^2	n	r	σ^2	ΔE_0	χ^2	R
1	4	1.87	6.30										-10.6	121.295	0.1590
2	3	1.90	2.69	1	2.06	0.16							-1.47	27.424	0.0180
3	2	1.88	0.82	2	2.02	5.15							-0.51	24.009	0.0157
4	1	1.67	3.55	3	1.83	3.72							-17.50	146.898	0.0963
5				4	1.86	8.09							-10.59	122.574	0.1607
6	2	1.88	0.60	2	2.03	4.61							0.40	134.162	0.3256
7	2	1.88	1.17	2	2.03	5.18				1	2.85	-4.12	1.14	50.223	0.1008
8	2	1.89	1.10	2	2.03	5.09				2	2.85	-1.86	1.81	42.576	0.0855
9	2	1.89	1.02	2	2.03	5.02				3	2.85	-0.33	2.01	46.032	0.0924
10	2	1.89	0.95	2	2.03	4.97				4	2.85	0.93	2.03	55.436	0.1113
11	2	1.89	0.84	2	2.03	5.06	1	2.82	3.88				0.69	76.442	0.1535
12	2	1.87	1.28	2	2.00	6.31	1	2.80	2.19	1	2.65	-2.96	-2.94	72.760	0.1156
13	2	1.88	1.14	2	2.03	5.22	1	2.63	28.21	2	2.85	-1.90	1.75	53.070	0.0843
14	2	1.88	1.09	2	2.02	5.14	1	2.66	16.14	3	2.85	-0.65	1.79	51.255	0.0814
15	**2**	**1.88**	**0.82**	**2**	**2.03**	**4.55**	**1**	**3.09**	**4.36**	**4**	**2.87**	**1.73**	**2.19**	**10.406**	**0.0165**
16	2	1.88	0.76	2	2.03	4.48	1	3.09	3.77	5	2.87	3.09	2.26	13.246	0.0210
17	2	1.89	0.72	2	2.03	4.42	1	3.09	3.30	6	2.87	4.47	2.29	18.373	0.0292

Table A-3.6 - Comparison of selected bond length between XRD data and EXAFS Fit for **8**.

XRD		EXAFS Fit	
N–Ni	1.88	**N–Ni**	1.88
Ni–O	1.92	**Ni-O**	2.03
Ni···Ni	2.88	**Ni···Ni**	3.09

Table A-3.7 - EXAFS Fitting of the data for **9**. Significant fits are highlighted in bold. Fitting range was k = 2-14.0 Å^{-1} with back transform ranges of 1-1.96 Å for fits 1-9 and 1-2.97 Å for fits 10-25. R is in units of Å; σ² is in units of 10^{-3} Å; ΔE_0 is in units of eV; R represents the fractional mis-fit of the data, while χ^2 is the χ^2 fitting metric normalized by the number of independent data points in a given fit.

	Ni-N/O			Ni-N/O			Ni···Ni			Ni···C					
fit	n	r	σ²	n	r	σ²	n	r	σ²	n	r	σ²	ΔE_0	χ^2	R
1	4	1.89	3.13										-5.50	50.162	0.0118
2	5	1.89	4.38										-6.09	77.855	0.0184
3	6	1.89	5.56										-6.66	174.847	0.0413
4				4	1.87	4.32							-5.12	76.614	0.0181
5				5	1.87	5.83							-5.91	217.162	0.0513
6				6	1.87	7.32							-6.65	403.989	0.0954
7	1	1.87	-0.51	3	1.89	6.56							-3.43	28.300	0.0033
8	2	1.87	1.03	2	1.92	5.25							-2.87	26.842	0.0032
9	3	1.87	0.86	1	1.97	0.73							-2.87	22.784	0.0027
10	4	1.88	3.07										-6.00	536.073	0.2685
11	4	1.90	3.44							3	2.86	-1.11	-2.36	163.402	0.0679
12	4	1.90	3.43							4	2.86	-0.10	-1.74	143.691	0.0597
13	4	1.90	3.42							5	2.86	0.75	-1.33	139.020	0.0577
14	4	1.89	3.30				1	2.83	2.44				-4.29	85.606	0.0356
15	**4**	**1.89**	**3.29**				**1**	**2.85**	**1.20**	**3**	**2.76**	**1.26**	**-3.96**	**63.587**	**0.0210**
16	4	1.89	3.32				1	2.85	2.28	4	2.78	7.78	-3.54	71.766	0.0237
17	4	1.89	3.32				1	2.84	2.4	5	2.79	12.22	-3.38	76.374	0.0252
18	4	1.89	2.46	0.6	2.05	0.98							-2.66	631.647	0.2623

19	4	1.90	2.07	0.6	2.03	-1.49				3	2.87	-1.36	0.09	118.133	0.0389
20	4	1.90	2.11	0.6	2.04	-1.37				4	2.87	-0.31	0.49	86.867	0.0286
21	4	1.90	2.13	0.6	2.04	-1.27				5	2.88	0.57	0.75	76.465	0.0252
22	4	1.89	2.51	0.6	2.03	0.95	1	2.84	2.42				-2.15	73.153	0.0241
	4	**1.89**	**2.35**	**0.6**	**2.03**	**0.22**	**1**	**2.86**	**2.34**	**3**	**2.80**	**2.34**	**-1.59**	**35.440**	**0.0087**
24	4	1.89	2.34	0.6	2.03	0.12	1	2.85	2.66	4	2.82	7.92	-1.21	38.846	0.0095
25	4	1.90	2.34	0.6	2.03	0.1	1	2.85	2.68	5	2.83	11.26	-0.97	43.904	0.0107

Table A-3.8 - EXAFS Fitting of the data for **10**. Significant fits are highlighted in bold. Fitting range was k = 2-14.0 Å-1 with back transform ranges of 1-1.932 Å for fits 1-10 and 1-2.7 Å for fits 11-26. R is in units of Å; σ^2 is in units of 10^{-3} Å; ΔE_0 is in units of eV; R represents the fractional mis-fit of the data, while χ^2 is the χ^2 fitting metric normalized by the number of independent data points in a given fit.

	Ni-N/O			Ni-N/O			Ni-N/O			Ni···Ni			Ni···C					
fit	n	r	σ^2	n	r	σ^2	n	r	σ^2	n	r	σ^2	n	r	σ^2	ΔE_0	χ^2	R
1	4	2.03	7.45													1.98	385.595	0.1372
2	5	2.03	8.93													1.15	240.772	0.0857
3	6	2.02	10.32													0.47	154.120	0.0548
4				4	2.00	8.91										0.88	264.515	0.0941
5				5	2.00	10.6										0.10	151.905	0.0541
6				6	2.00	12.19										-0.59	95.652	0.0340
7	5	1.97	6.58	1	2.08	-0.39										-2.49	16.331	0.0027
8	4	1.94	4.64	2	2.06	1.35										-2.49	5.914	0.0010
9	3	1.92	3.2	3	2.04	2.79										-2.54	3.227	0.0005
10				4	1.94	6.86	1	2.07	-0.03							-2.75	26.112	0.0044
11	3	1.92	3.33	3	2.04	2.98										-2.50	153.286	0.1002
12	3	1.93	3.25	3	2.05	2.74							3	2.93	3.27	-0.39	37.512	0.0183
13	3	1.93	3.31	3	2.05	2.79							4	2.93	4.81	0.03	30.332	0.0148
14	3	1.93	3.35	3	2.06	2.83							5	2.93	6.24	0.32	30.205	0.0147
15	3	1.92	3.09	3	2.04					1	2.91	7.80				-2.66	52.123	0.0254
16	**3**	**1.92**	**3.39**	**3**	**2.05**	**2.89**				**1**	**2.99**	**7.97**	**3**	**2.88**	**3.07**	**-0.79**	**19.677**	**0.0063**
17	3	1.93	3.35	3	2.05	2.87				1	2.99	10.77	4	2.90	5.94	-0.42	27.452	0.0088
18	3	1.93	3.3	3	2.05	2.83				1	2.94	9.78	5	2.92	9.78	-0.52	33.553	0.0107

19		4	1.95	6.93	1	2.07	6.93						-2.67	153.677	0.1005
20		4	1.96	7.19	1	2.08	0.20				3	2.92	3.86	0.03	52.515	0.0256
21		4	1.96	7.22	1	2.09	0.25				4	2.93	5.46	0.45	42.598	0.0207
22		4	1.96	7.24	1	2.09	0.28				5	2.93	6.96	0.72	39.366	0.0192
23		4	1.95	6.9	1	2.07	-0.03	1	2.91	8.35				-2.72	70.847	0.0345
24		**4**	**1.95**	**7.11**	**1**	**2.08**	**0.20**	**1**	**2.97**	**7.24**	**3**	**2.86**	**3.98**	**-0.77**	**28.208**	**0.0090**
25		4	1.96	7.08	1	2.08	0.13	1	2.97	8.82	4	2.87	7.46	-0.60	30.263	0.0097
26		4	1.95	7.07	1	2.08	0.08	1	2.95	9.30	5	2.88	13.18	-0.75	32.284	0.0103

DFT Calculations Data

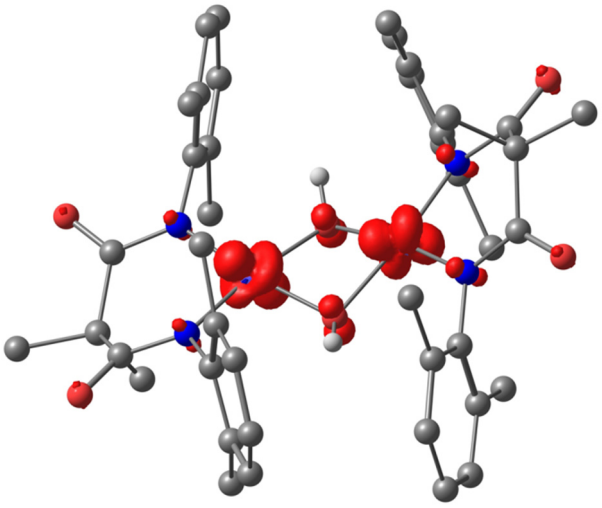

Figure A-3.13 - Electron spin density of the geometry optimised structures of **9-seesaw** (doublet) at an isovalue of 0.01 a.u.. With exception of the Ni(μ-(OH)2)Ni cores, H atoms are omitted for clarity.

Optimized molecular structure and total energies

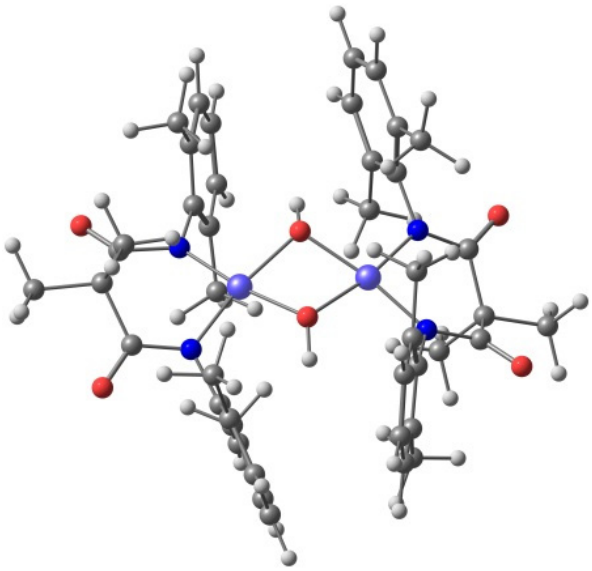

Figure A-3.14 - Optimized molecular structure of **8-seesaw**. Total energy at DFT-uBP86-D3 cc-pVTZ (for C H N O) and SDD (for Ni) level and singlet state: -2644.37886675 a.u.

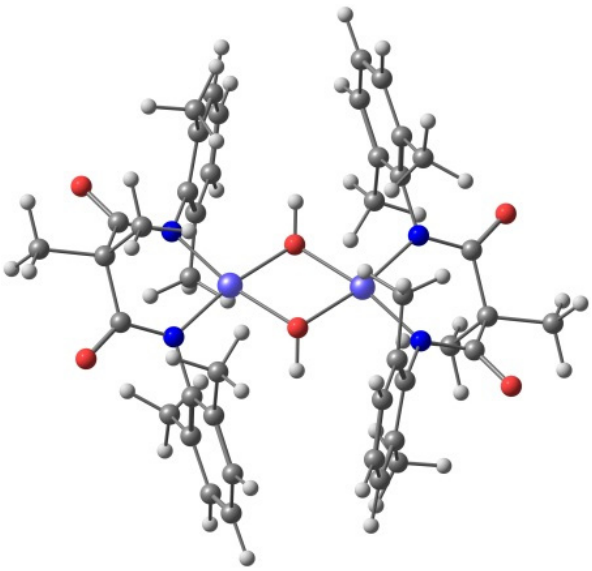

Figure A-3.15 - Optimized molecular structure of **8-plane**. Total energy at DFT-uBP86-D3 cc-pVTZ (for C H N O) and SDD (for Ni) level and singlet state: -2644.37565905 a.u.

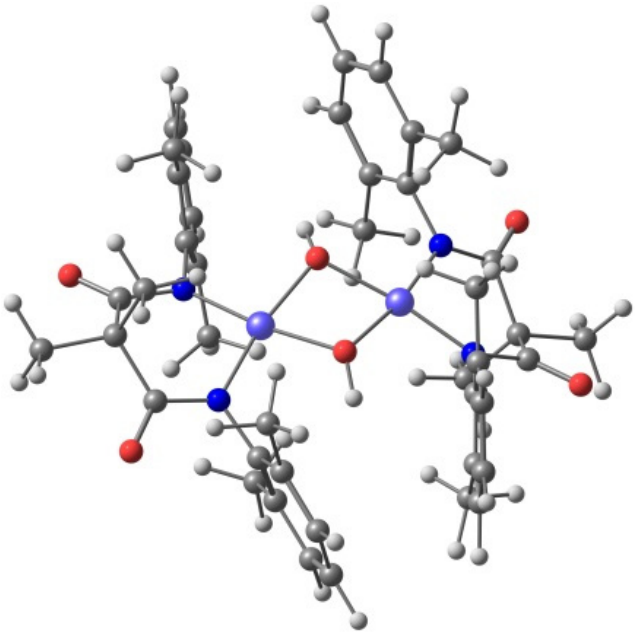

Figure A-3.16 - Optimized molecular structure of **9-seesaw**. Total energy at DFT-uBP86-D3 cc-pVTZ (for C H N O) and SDD (for Ni) level and duplet state: -2644.21315544 a.u.

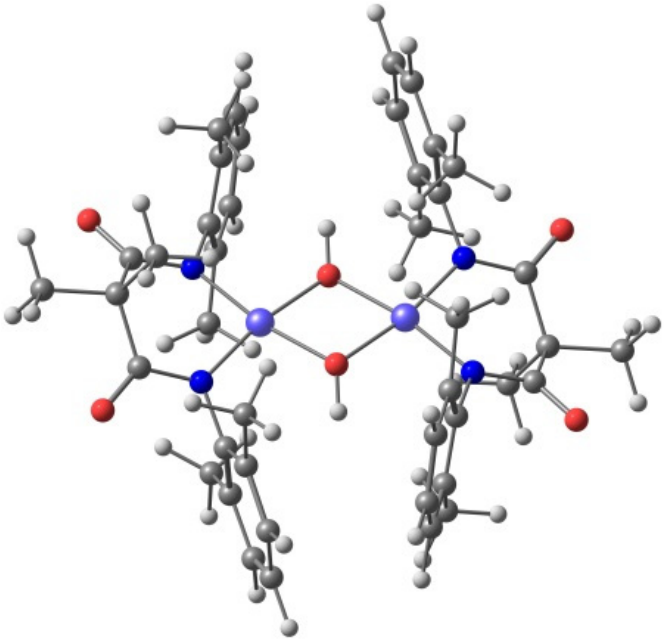

Figure A-3.17 - Optimized molecular structure of **9-plane**. Total energy at DFT-uBP86-D3 cc-pVTZ (for C H N O) and SDD (for Ni) level and duplet state: -2644.21374934 a.u.

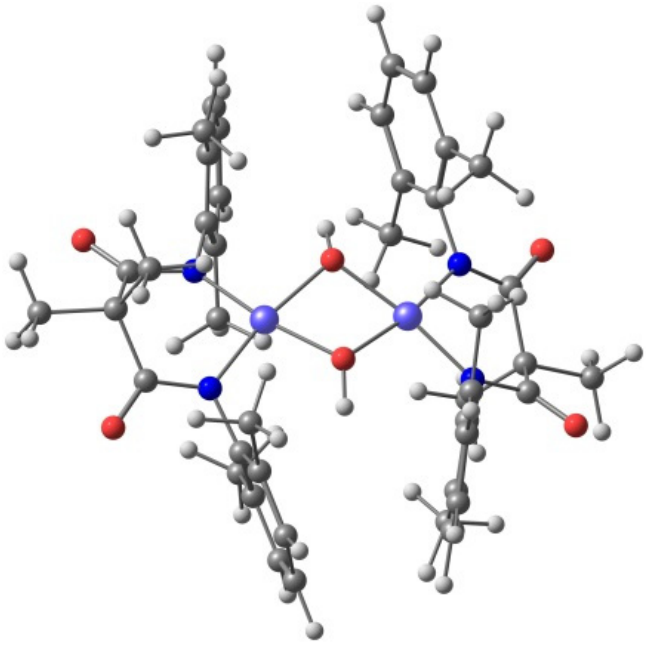

Figure A-3.18 - Optimized molecular structure of **10-seesaw**. Total energy at DFT-uBP86-D3 cc-pVTZ (for C H N O) and SDD (for Ni) level and triplet state: -2644.21374934 a.u.

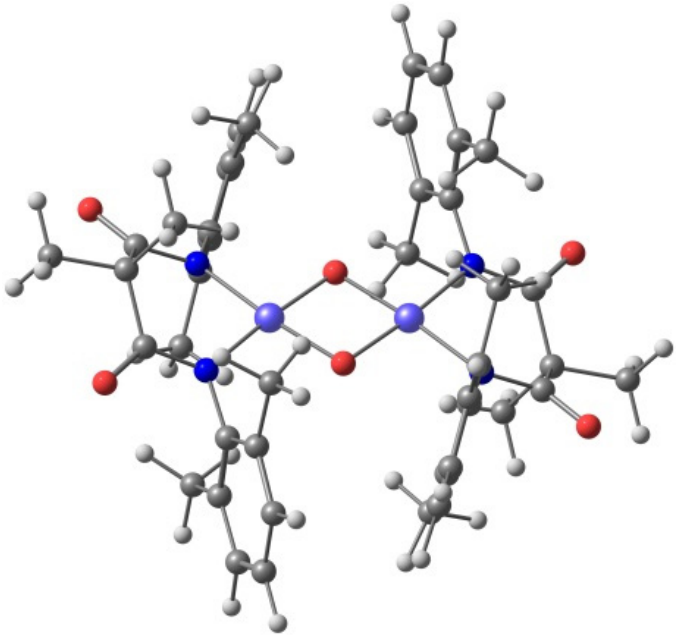

Figure A-3.19 - Optimized molecular structure of **8-oxo**. Total energy at DFT-uBP86-D3 cc-pVTZ (for C H N O) and SDD (for Ni) level and triplet state: -2642.78069431 a.u.

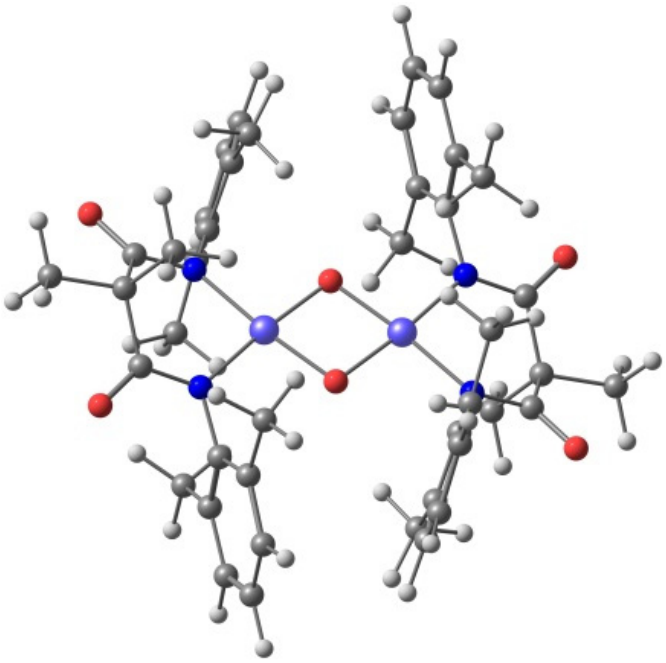

Figure A-3.20 - Optimized molecular structure of **9-oxo**. Total energy at DFT-uBP86-D3 cc-pVTZ (for C H N O) and SDD (for Ni) level and duplet state: -2643.00261240 a.u.

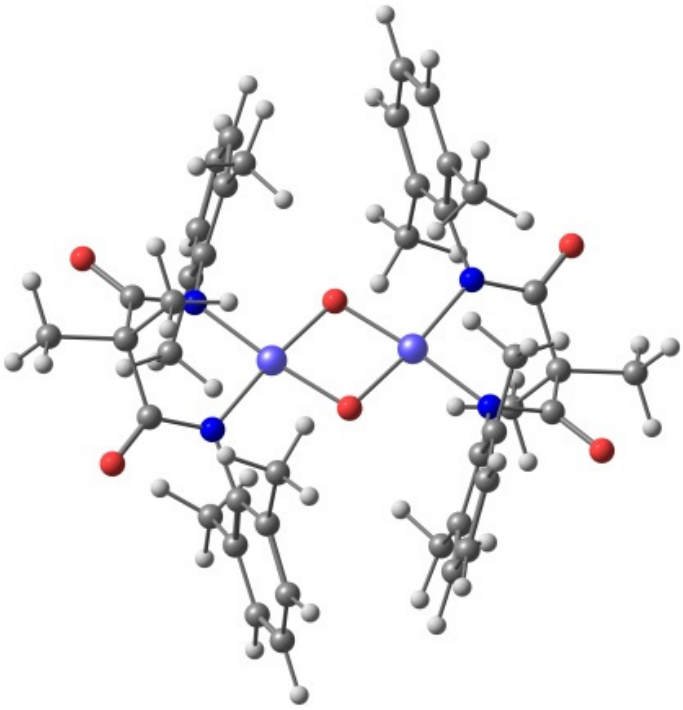

Figure A-3.21 - Optimized molecular structure of **10-oxo**. Total energy at DFT-uBP86-D3 cc-pVTZ (for C H N O) and SDD (for Ni) level and triplet state: -2643.09818167 a.u.

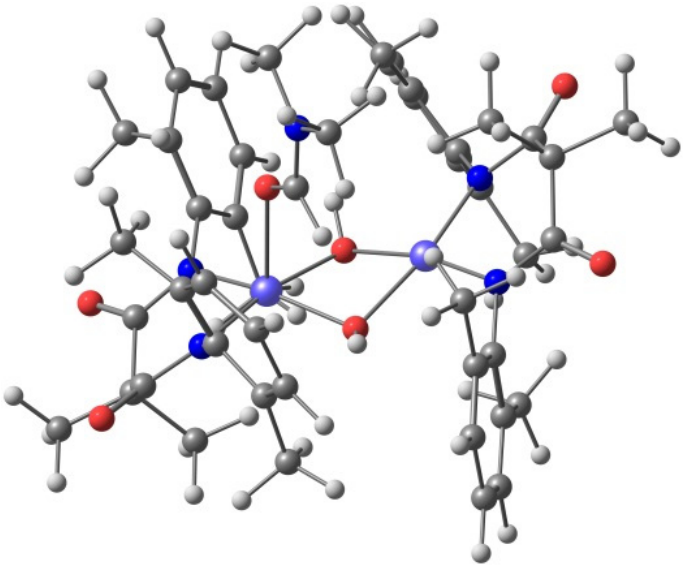

Figure A-3.22 - Optimized molecular structure of **9-DMF**. Total energy at DFT-uBP86-D3 cc-pVTZ (for C H N O) and SDD (for Ni) level and duplet state: -2892.98629936 a.u. Single point total energy of the DMF at DFT-uBP86-D3 cc-pVTZ: -248.61060238 a.u.

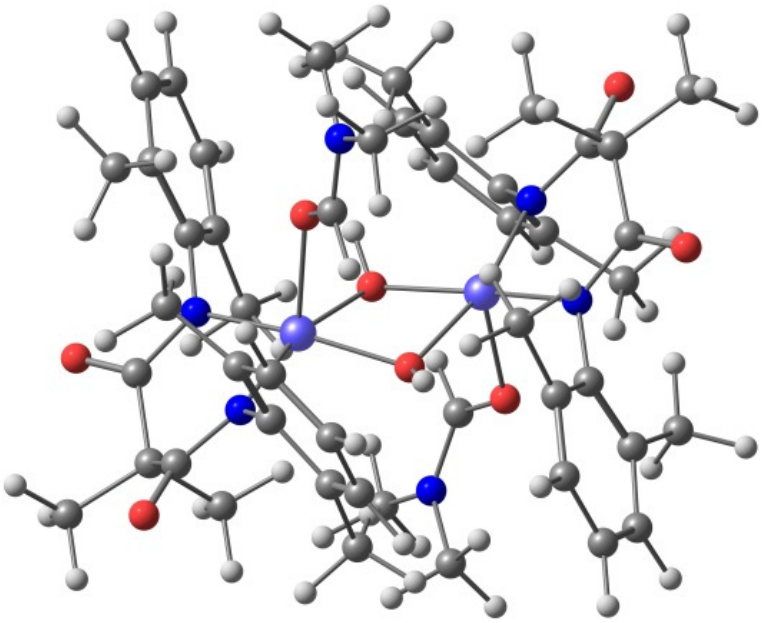

Figure A-3.23 -Optimized molecular structure of **10-2DMF**. Total energy at DFT-uBP86-D3 cc-pVTZ (for C H N O) and SDD (for Ni) level and triplet state: -3141.48766185 a.u. Total energy at DFT-uBP86-D3 cc-pVTZ (for C H N O) and SDD (for Ni) level and antiferromagnetic coupled singlet state: -3141.48747563 a.u. Single point total energy of both DMF at DFT-uBP86-D3 cc-pVTZ: -497.21881604 a.u.

Appendix to Chapter 4

Reactivity of 10 with 4-X-2,6-DTBP

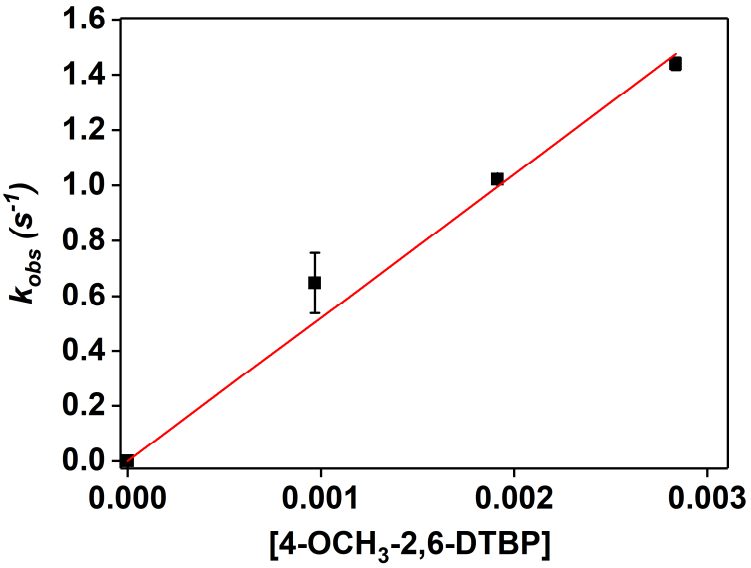

Figure A-4.1 - Plot of k_{obs} vs. [4-OCH_3-2,6-DTBP], for the reaction between **10** and 4-OCH_3-2,6-DTBP at -45 °C in DMF. k_2 = 520(11) $M^{-1}s^{-1}$.

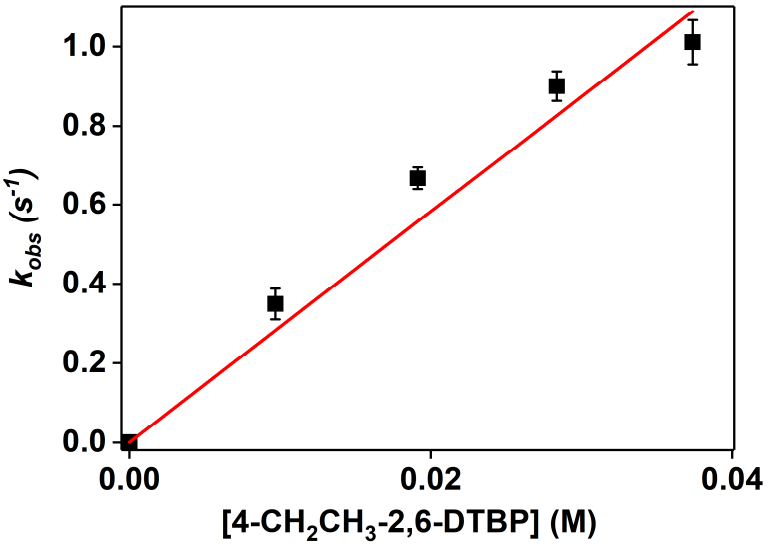

Figure A-4.2 - Plot of k_{obs} vs. [4-CH_2CH_3-2,6-DTBP], for the reaction between **10** and 4-CH_2CH_3-2,6-DTBP at -45 °C in DMF. k_2 = 29(1) $M^{-1}s^{-1}$.

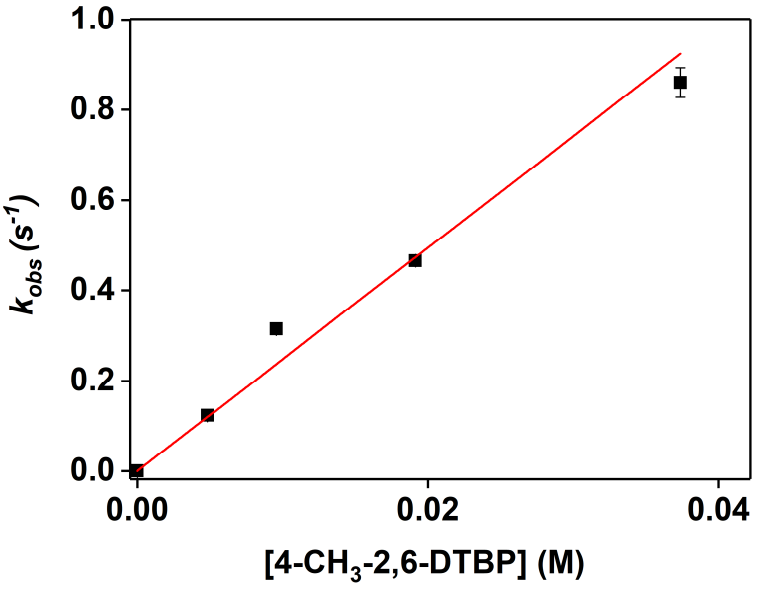

Figure A-4.3 - Plot of k_{obs} vs. [4-CH_3-2,6-DTBP], for the reaction between **10** and 4-CH_3-2,6-DTBP at -45 °C in DMF. k_2 = 24.7(11) $M^{-1}s^{-1}$.

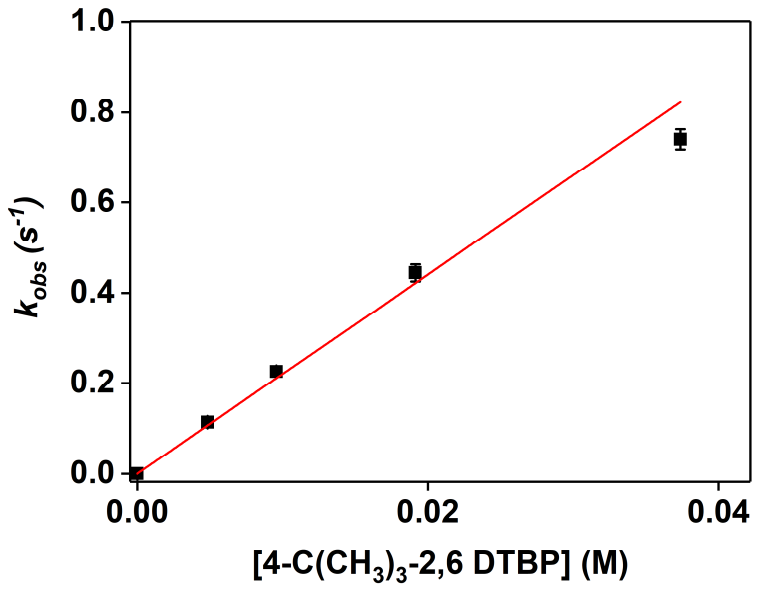

Figure A-4.4 - Plot of k_{obs} vs. [4-$C(CH_3)_3$-2,6-DTBP], for the reaction between **10** and 4-$C(CH_3)_3$-2,6-DTBP at -45 °C in DMF. k_2 = 22(1) $M^{-1}s^{-1}$.

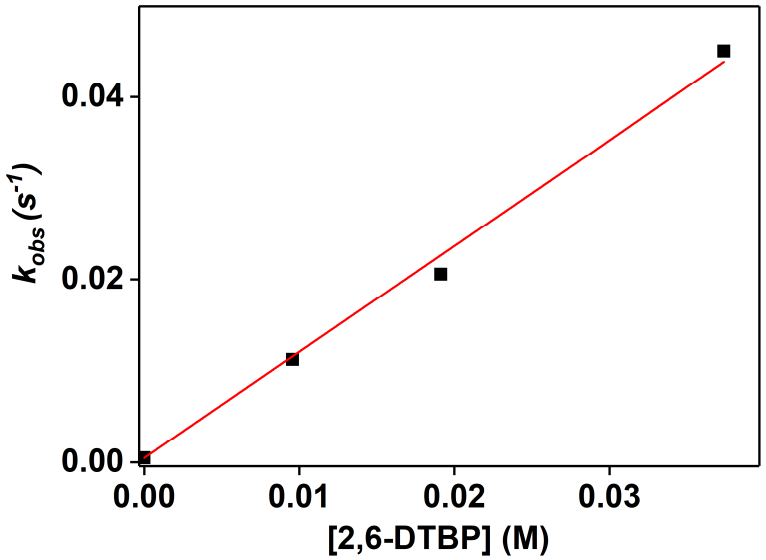

Figure A-4.5 - Plot of k_{obs} vs. [2,6-DTBP], for the reaction between **10** and 2,6-DTBP at -45 °C in DMF. k_2 = 1.16(3) $M^{-1}s^{-1}$.

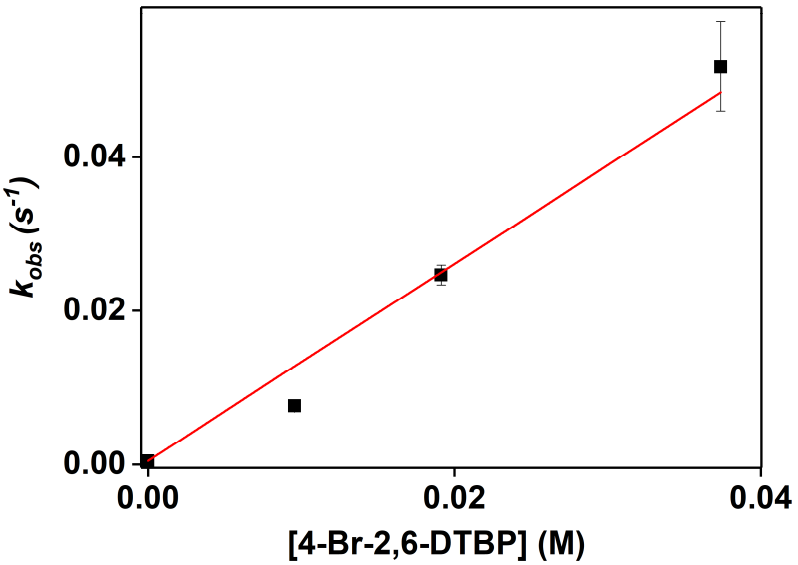

Figure A-4.6 - Plot of k_{obs} vs. [4-Br-2,6-DTBP], for the reaction between **10** and 4-Br-2,6-DTBP at -45 °C in DMF. k_2 = 1.28(4) $M^{-1}s^{-1}$.

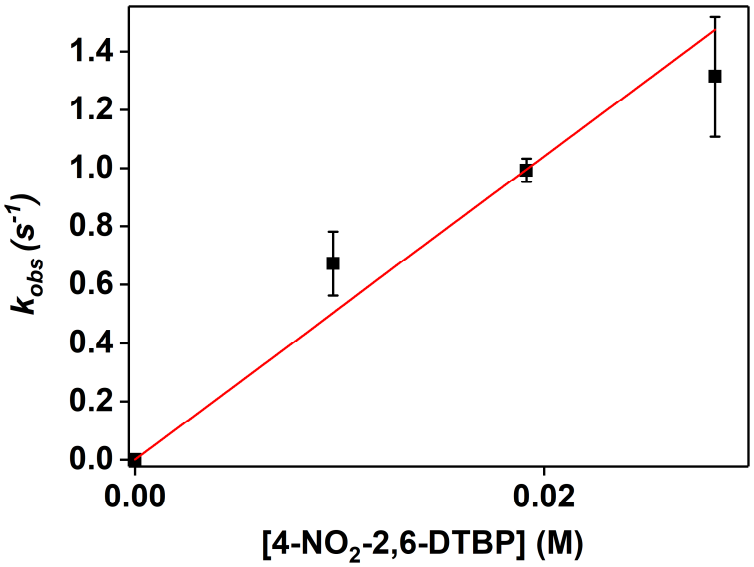

Figure A-4.7 - Plot of k_{obs} vs. [4-NO_2-2,6-DTBP], for the reaction between **10** and 4-NO_2-2,6-DTBP at -45 °C in DMF. k_2 = 52(24) $M^{-1}s^{-1}$.

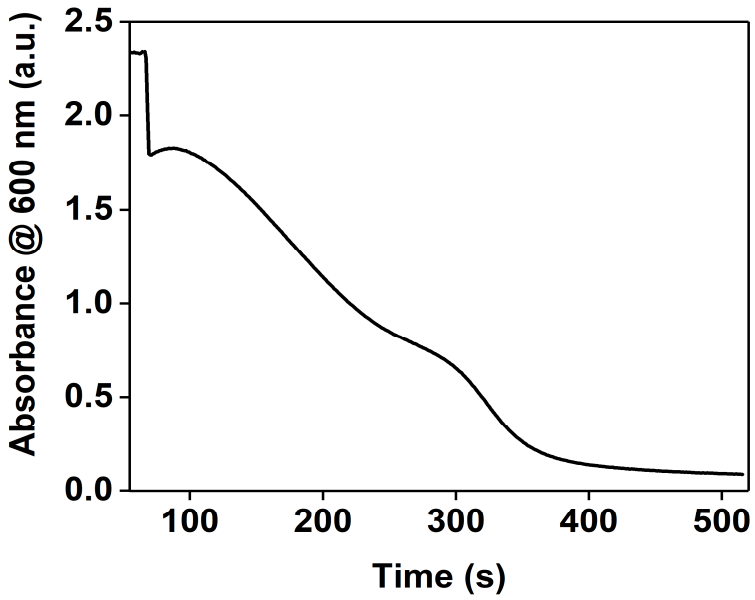

Figure A-4.8 – Variation of the absorbance at 600 nm over the reaction time for the reaction between **10** and 4-CN-2,6-di-*tert*-butyl phenol in DMF at -45 °C.

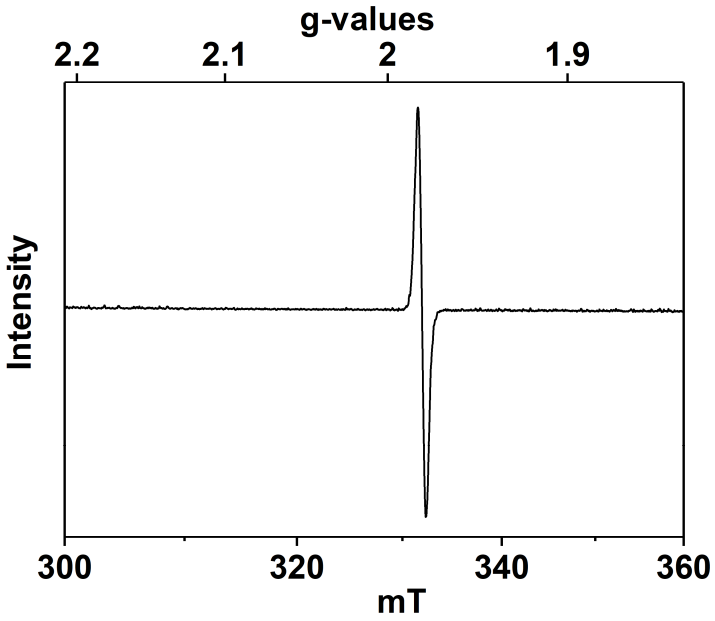

Figure A-4.9 - Electron paramagnetic resonance spectrum of the post reaction mixture for the reaction between **10** and 4-OCH_3-2,6-DTBP at -45 °C in DMF.

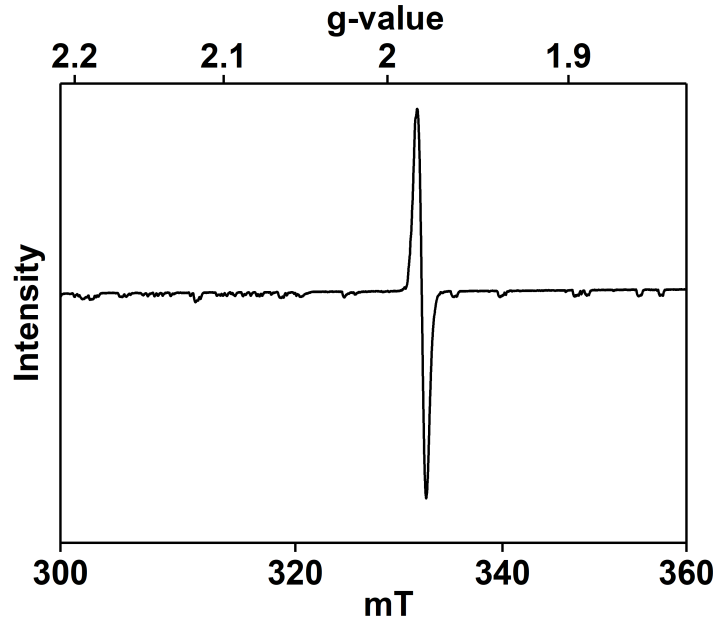

Figure A-4.10 - Electron paramagnetic resonance spectrum of the post reaction mixture for the reaction between **10** and 4-$C(CH_3)_3$-2,6-DTBP at -45 °C in DMF.

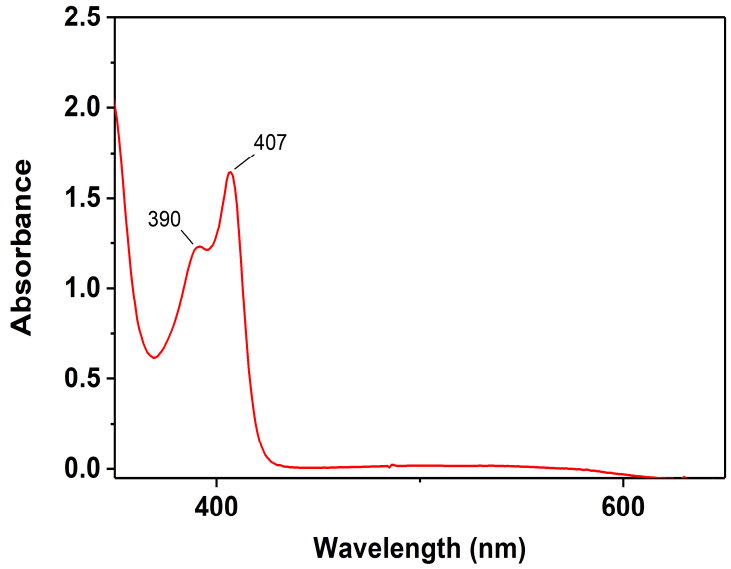

Figure A-4.11 - UV-Vis spectrum of 4-OCH_3-2,6-di-*tert*-butyl phenoxy radical in DMF at 25 °C (ε_{407nm} = 2090 ± 100 $M^{-1}cm^{-1}$).

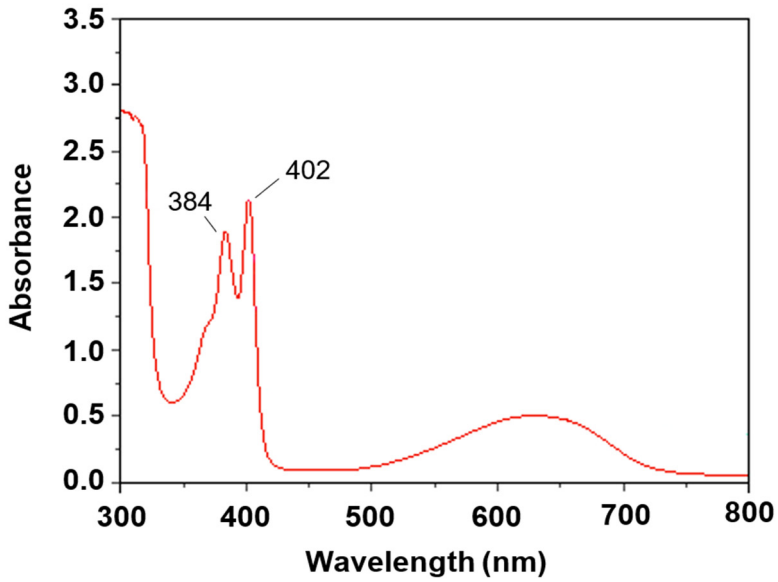

Figure A-4.12 - UV-Vis spectrum of 2,4,6-tris-*tert*-butyl phenoxy radical in DMF at 25 °C (ε_{407nm} 1830 ± 200 $M^{-1}cm^{-1}$).

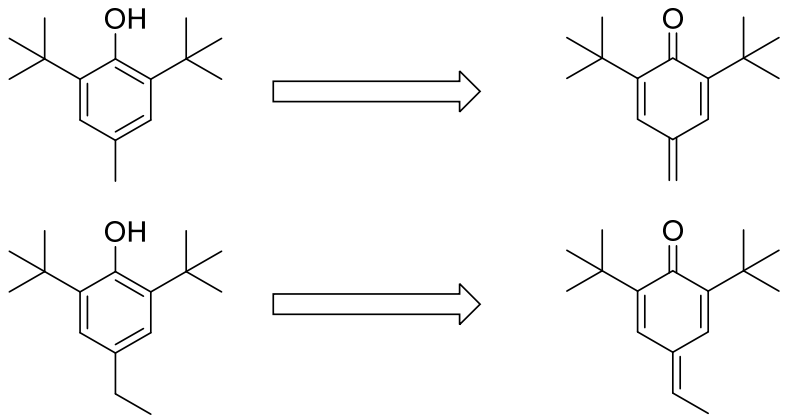

Figure A-4.13 - Identified products from the oxidation of 4-CH_3-2,6-DTBP and 4-CH_2CH_3-2,6-DTBP by **10**. GC-MS and ESI-MS were used for this analysis.

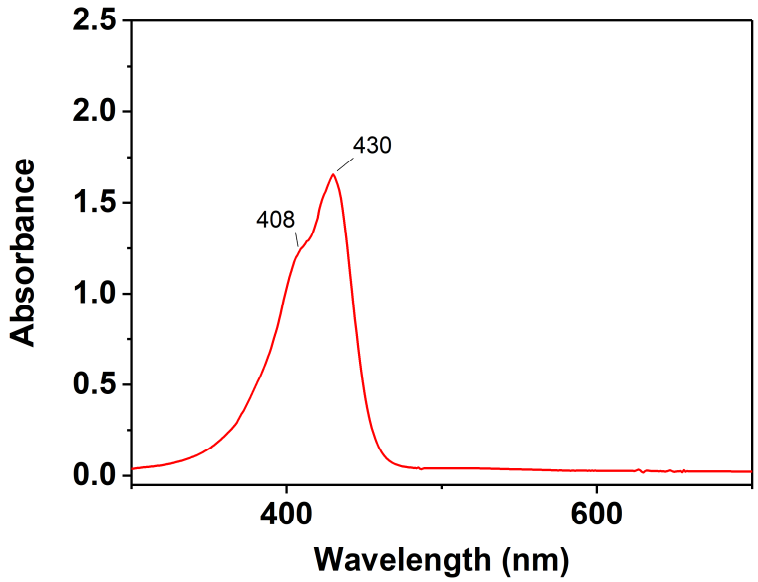

Figure A-4.14 - UV-Vis spectrum of 3,3',5,5'-tetra-tert-butyl-4,4'-diphenoquinone in DMF at -45 °C (ε_{430nm} = 32380 ± 500 $M^{-1}cm^{-1}$).

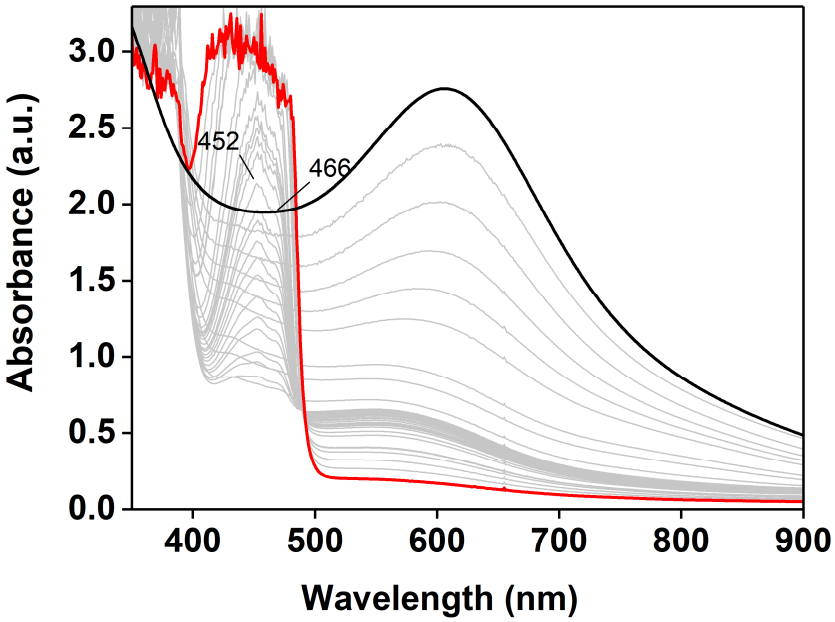

Figure A-4.15 - Electronic absorption spectra showing the formation of the 4-NO_2-2,6-DTB phenolate upon reaction of 4-NO_2-2,6 DTBP with **10** at -45 °C in DMF.

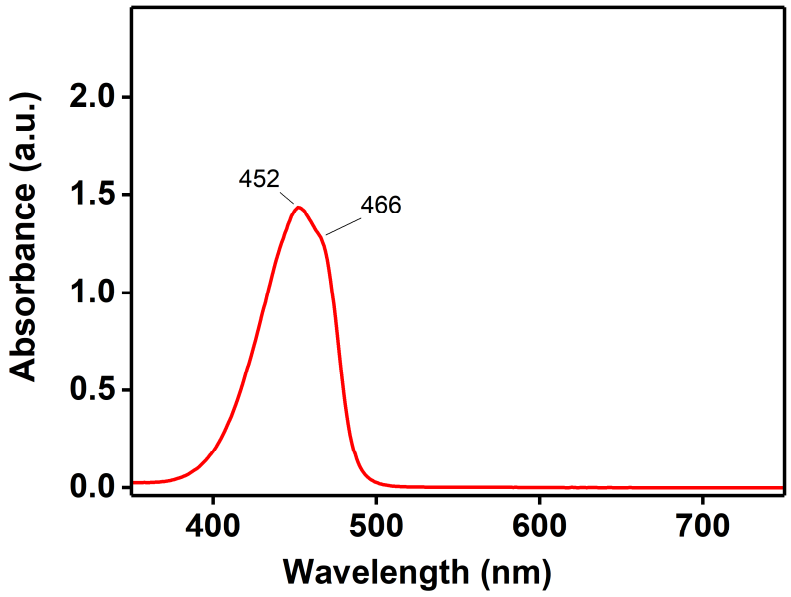

Figure A-4.16 - UV-Vis spectrum of 4-NO_2-2,6-di-*tert*-butyl phenoxide ion in DMF at 25 °C

Reactivity of 9 with 4-X-2,6-DTBP

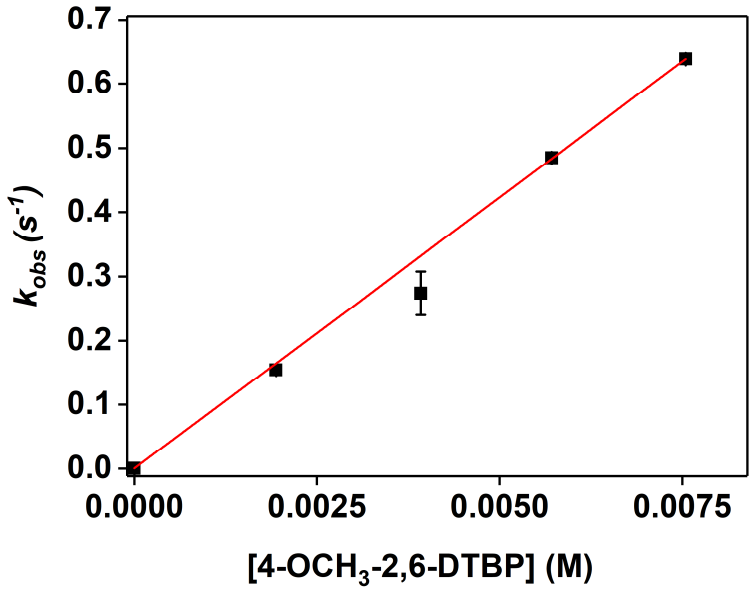

Figure A-4.17 - Plot of k_{obs} vs. [4-OCH_3-2,6-DTBP], for the reaction between **9** and 4-OCH_3-2,6-DTBP at -45 °C in DMF. k_2 = 84.6(3) $M^{-1}s^{-1}$.

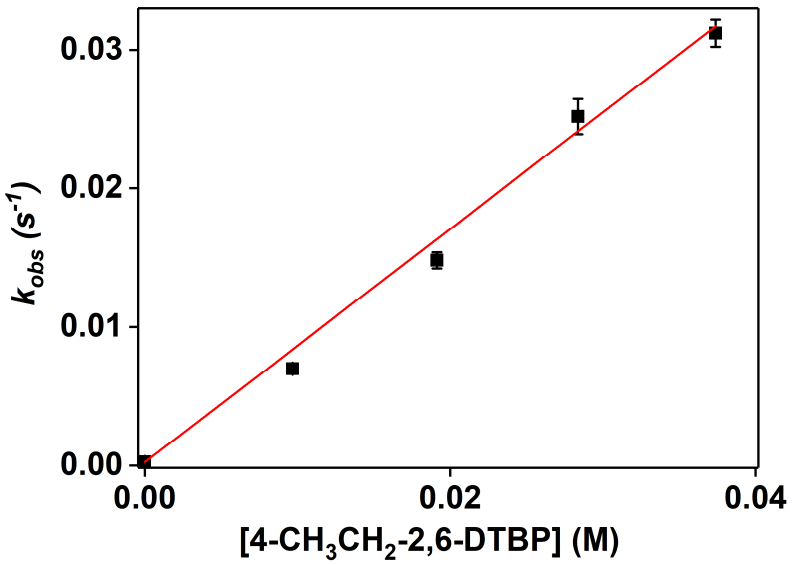

Figure A-4.18 - Plot of k_{obs} vs. [4-CH_2CH_3-2,6-DTBP], for the reaction between **9** and 4-CH_2CH_3-2,6-DTBP at -45 °C in DMF. k_2 = 0.84(2) $M^{-1}s^{-1}$.

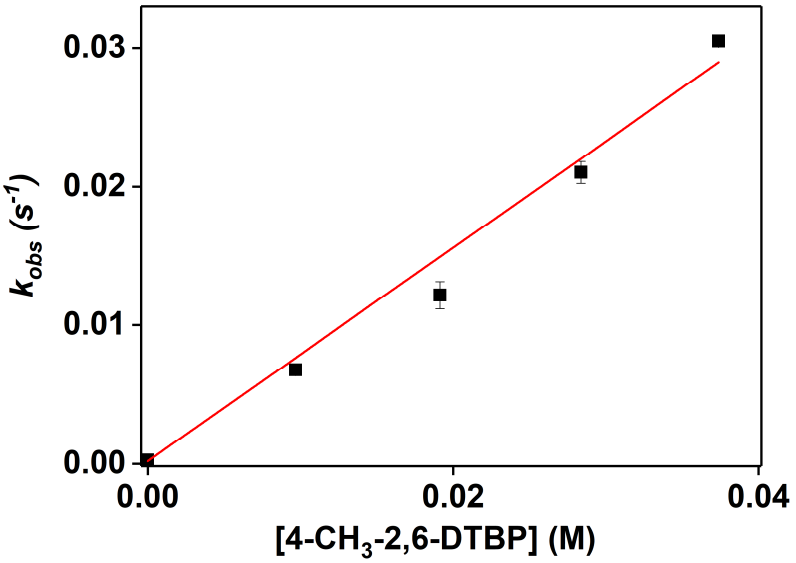

Figure A-4.19 - Plot of k_{obs} vs. [4-CH_3-2,6-DTBP], for the reaction between **9** and 4- CH_3-2,6-DTBP at -45 °C in DMF. k_2 = 0.76(4) $M^{-1}s^{-1}$.

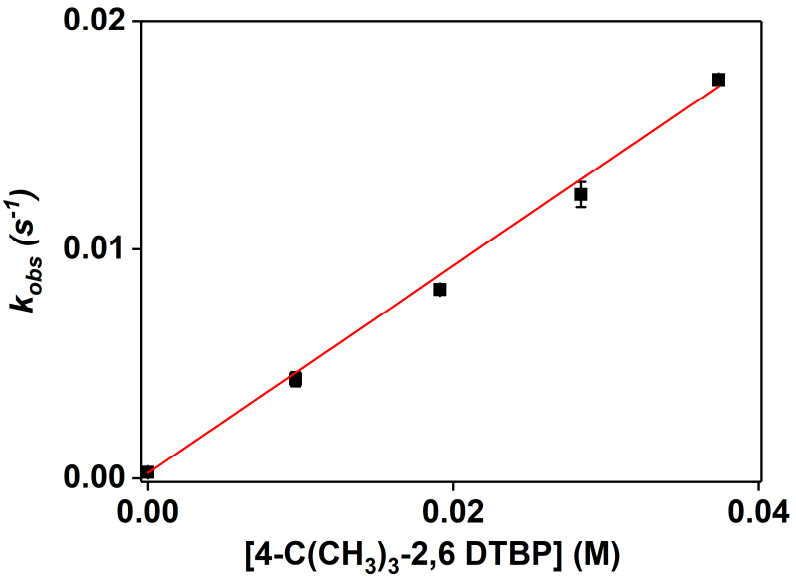

Figure A-4.20 - Plot of kobs vs. [4-$C(CH_3)_3$-2,6 DTBP], for the reaction between **9** and 4-$C(CH_3)_3$-2,6 DTBP at -45 °C in DMF. k_2 = 0.45(1) $M^{-1}s^{-1}$.

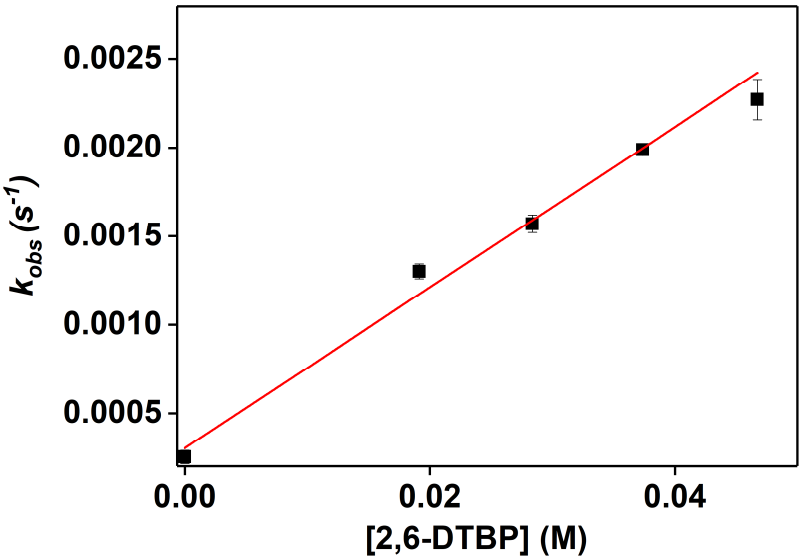

Figure A-4.21 - Plot of k_{obs} vs. [2,6-DTBP], for the reaction between **9** and 2,6-DTBP at -45 °C in DMF. k_2 = 0.045(2) $M^{-1}s^{-1}$.

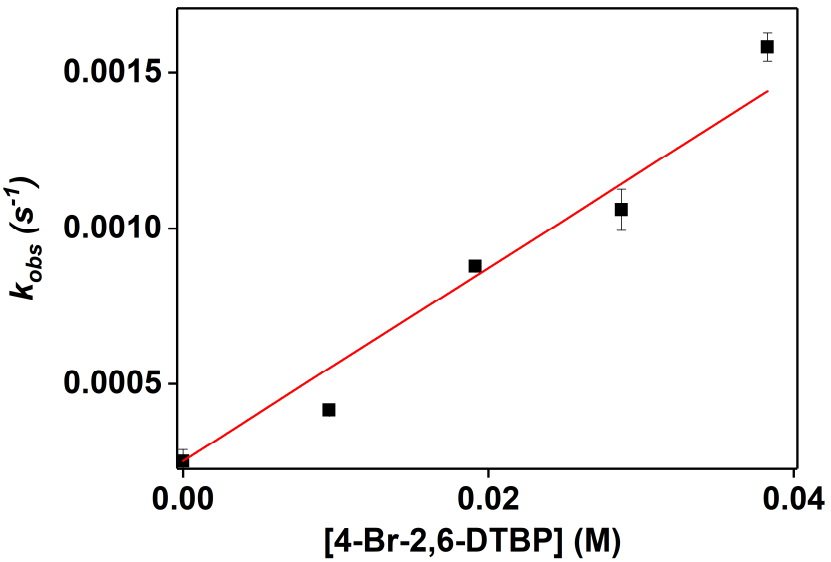

Figure A-4.22 - Plot of k_{obs} vs. [4-Br-2,6-DTBP], for the reaction between **9** and 4-Br-2,6-DTBP at -45 °C in DMF. k_2 = 0.031(3) $M^{-1}s^{-1}$.

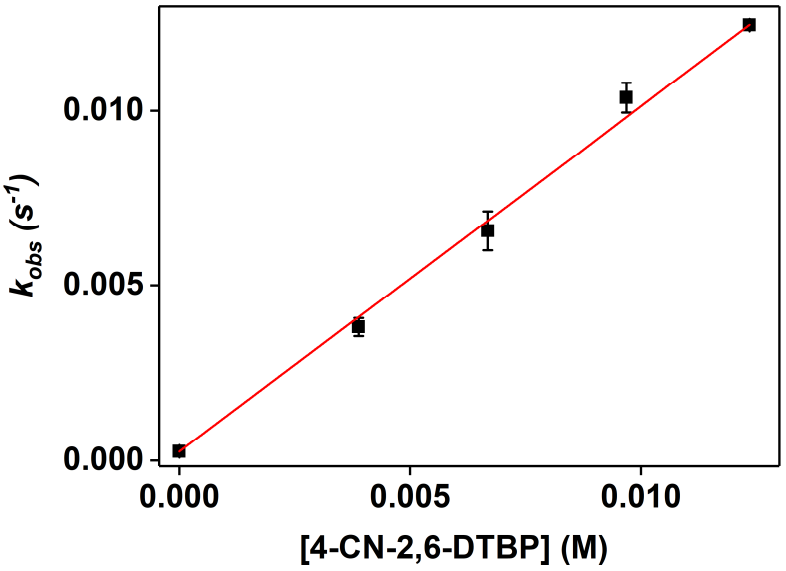

Figure A-4.23 - Plot of k_{obs} vs. [4-CN-2,6-DTBP], for the reaction between **9** and 4-CN-2,6-DTBP at -45 °C in DMF. k_2 = 0.99(1) $M^{-1}s^{-1}$.

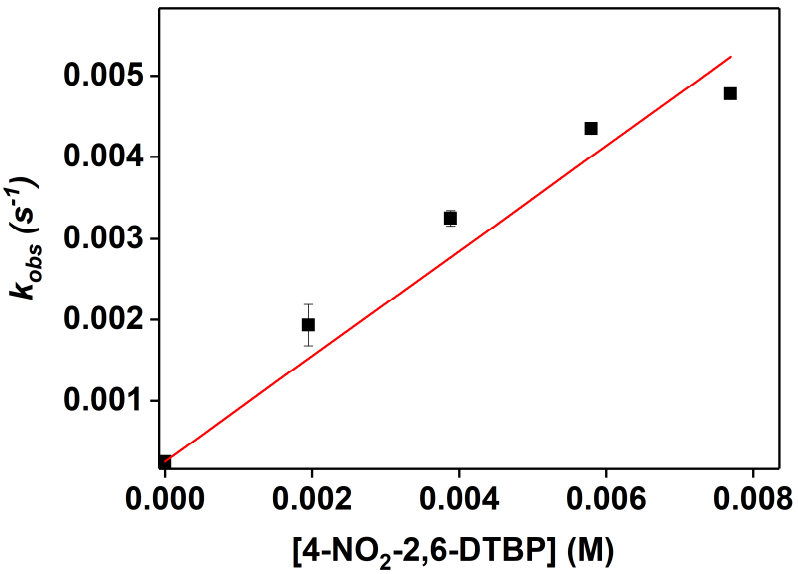

Figure A-4.24 - Plot of k_{obs} vs. [4-NO_2-2,6-DTBP], for the reaction between **9** and 4-NO_2-2,6-DTBP at -45 °C in DMF. k_2 = 0.65(3) $M^{-1}s^{-1}$.

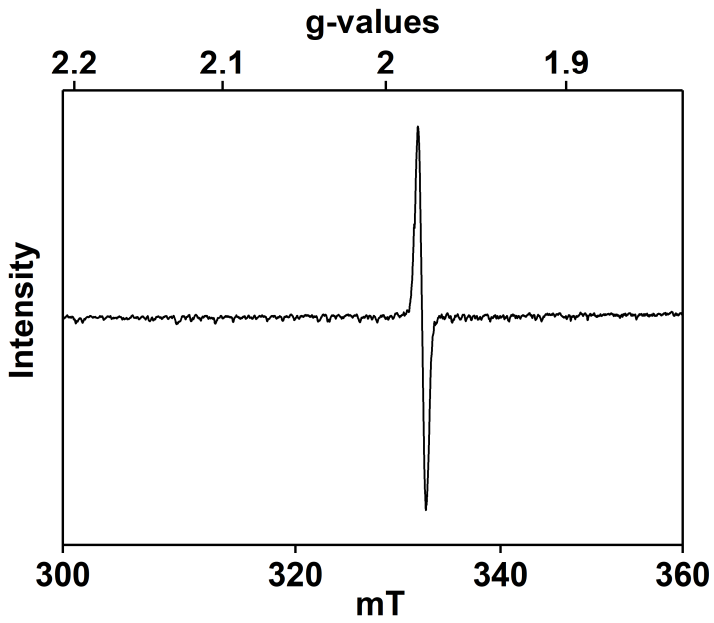

Figure A-4.25 - Electron paramagnetic resonance spectrum of the post reaction mixture for the reaction between **9** and 4-OCH_3-2,6-DTBP at -45 °C in DMF.

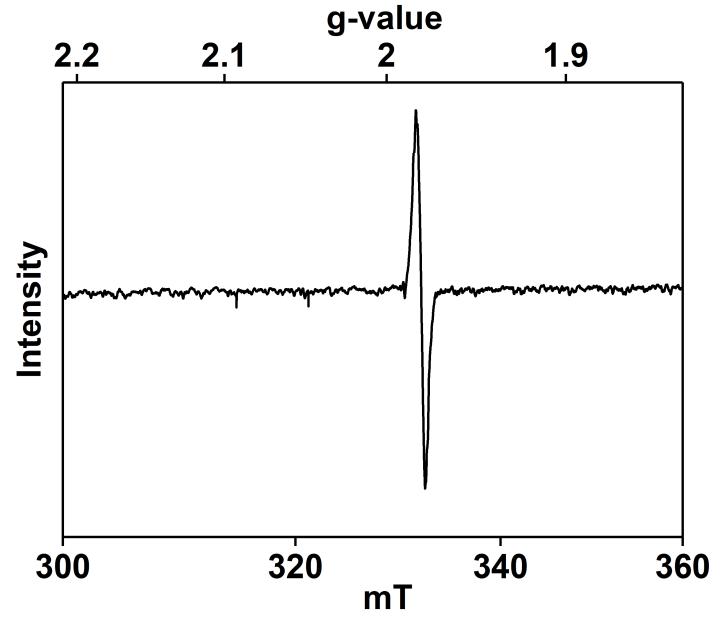

Figure A-4.26 - Electron paramagnetic resonance spectrum of the post reaction mixture for the reaction between **9** and 4-$C(CH_3)_3$-2,6-DTBP at -45 °C in DMF.

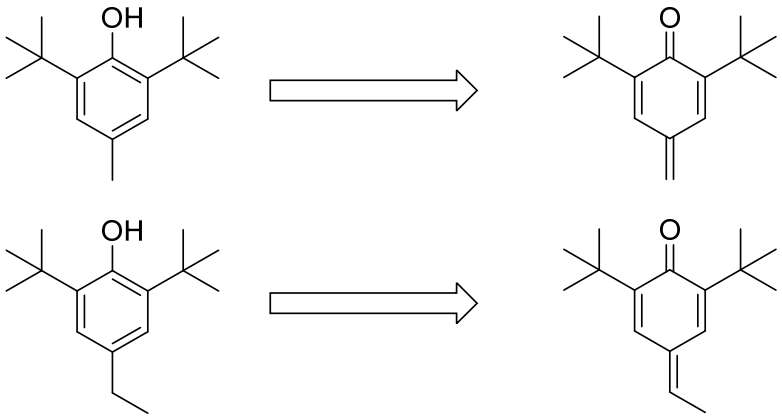

Figure A-4.27 - Identified products from the oxidation of 4-CH_3-2,6-DTBP and 4-CH_2CH_3-2,6-DTBP by **9**. GC-MS and ESI-MS were used for this analysis.

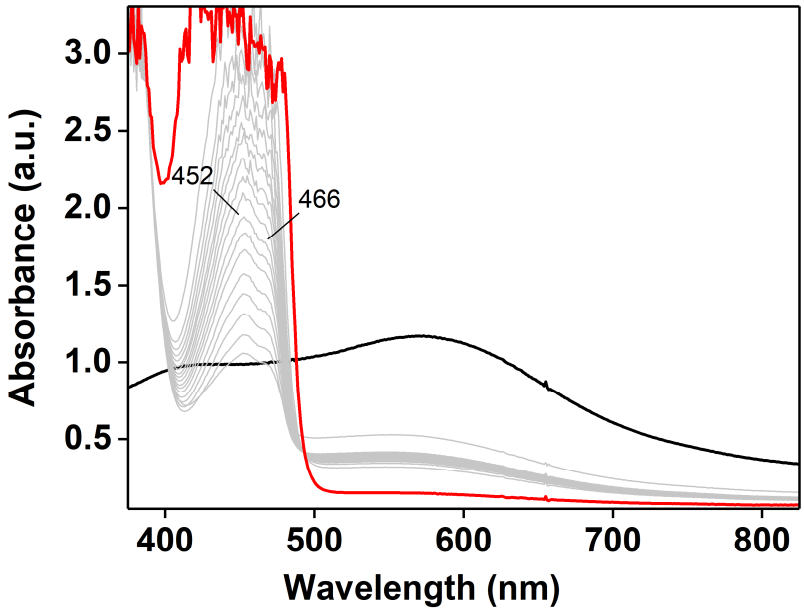

Figure A-4.28 - Electronic absorption spectra showing the formation of the 4-NO_2-2,6 DTB phenolate upon reaction of 4-NO_2-2,6 DTBP with **9** at -45 °C in DMF.

Reactivity of 9' with 4-X-2,6-DTBP

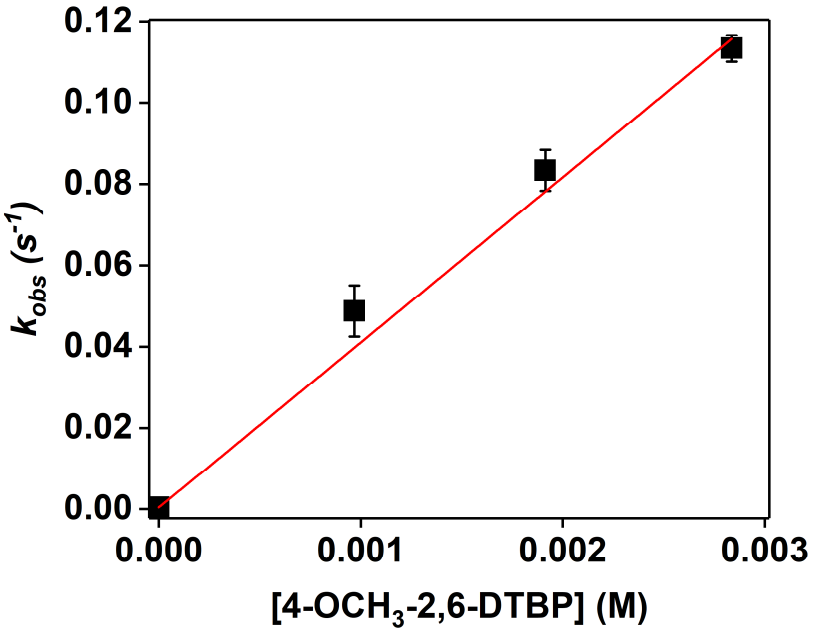

Figure A-4.29 - Plot of k_{obs} vs. [4-OCH_3-2,6-DTBP], for the reaction between **9'** and 4-OCH_3-2,6-DTBP at -45 °C in DMF. k_2 = 41(1) $M^{-1}s^{-1}$.

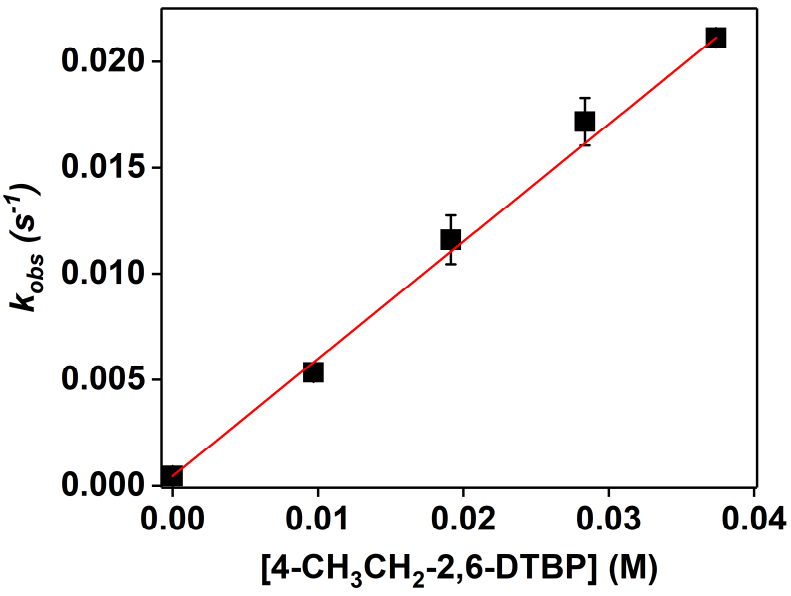

Figure A-4.30 - Plot of k_{obs} vs. [4-CH_3CH_2-2,6-DTBP], for the reaction between **9'** and 4-CH_3CH_2-2,6-DTBP at -45 °C in DMF. k_2 = 0.553(3) $M^{-1}s^{-1}$.

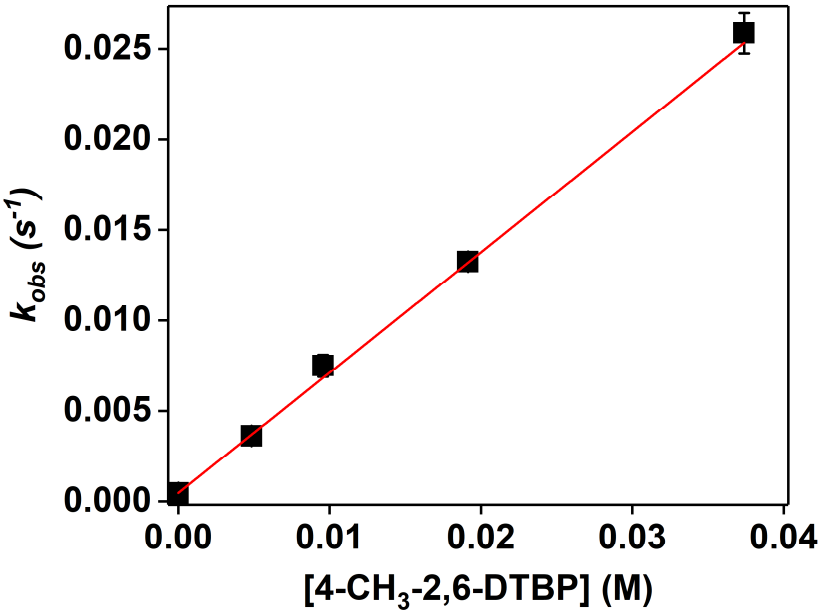

Figure A-4.31 - Plot of k_{obs} vs. [4-CH_3-2,6-DTBP], for the reaction between **9'** and 4-CH_3-2,6-DTBP at -45 °C in DMF. k_2 = 0.67(1) $M^{-1}s^{-1}$.

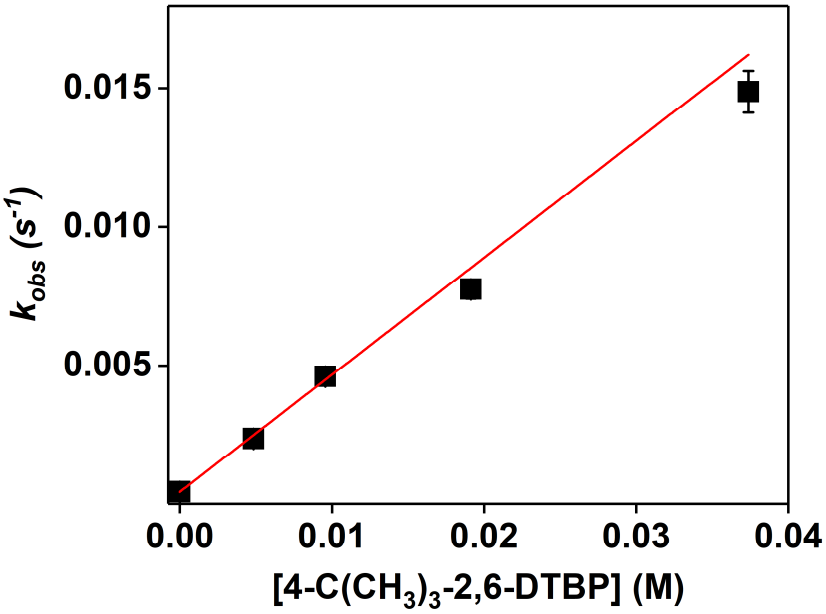

Figure A-4.32 - Plot of k_{obs} vs. [4-$C(CH_3)_3$-2,6-DTBP], for the reaction between **9'** and 4-$C(CH_3)_3$-2,6-DTBP at -45 °C in DMF. k_2 = 0.42(1) $M^{-1}s^{-1}$.

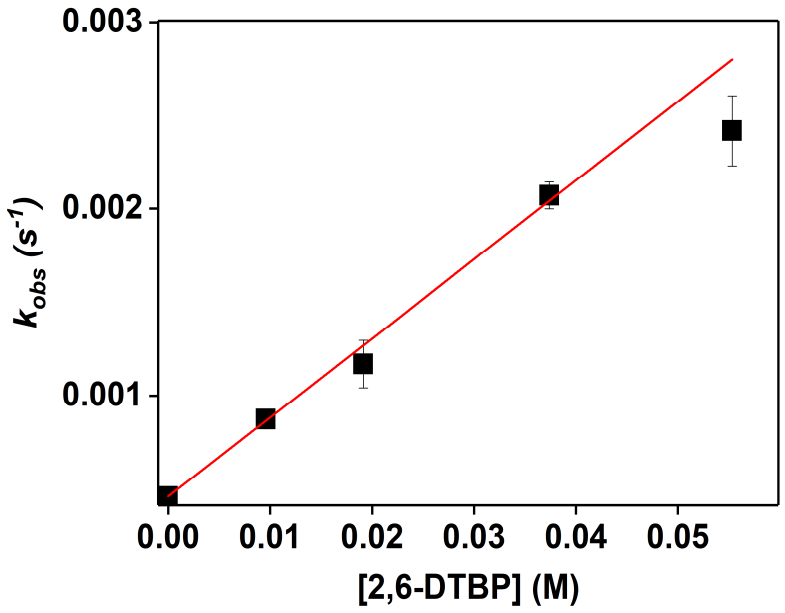

Figure A-4.33 - Plot of k_{obs} vs. [2,6-DTBP], for the reaction between **9'** and 2,6-DTBP at -45 °C in DMF. k_2 = 0.042(2) $M^{-1}s^{-1}$.

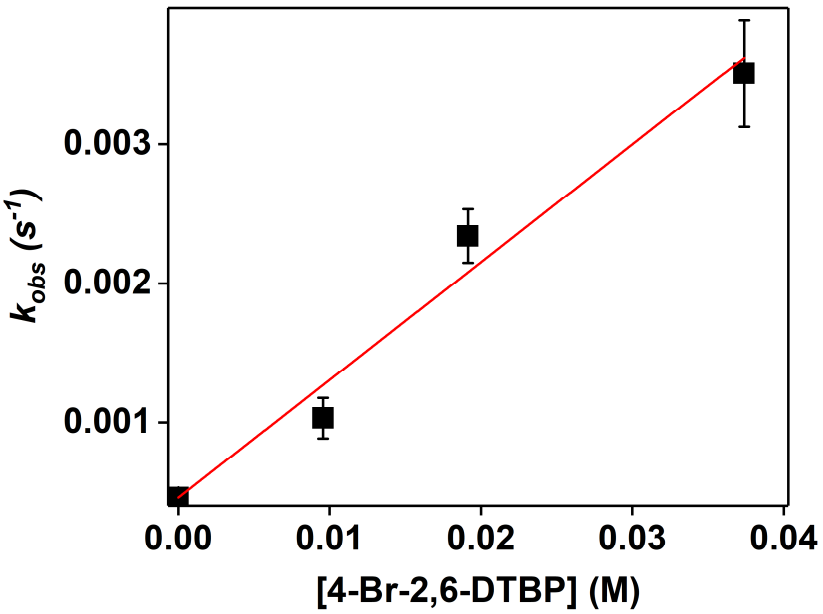

Figure A-4.34 - Plot of k_{obs} vs. [4-Br-2,6-DTBP], for the reaction between **9'** and 4-Br-2,6-DTBP at -45 °C in DMF. k_2 = 0.08(1) $M^{-1}s^{-1}$.

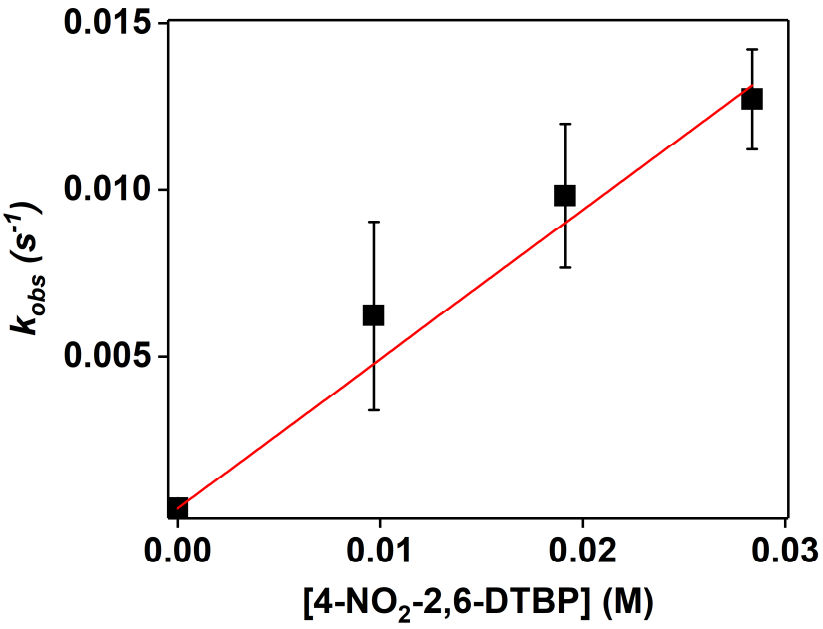

Figure A-4.35 - Plot of k_{obs} vs. [4-NO_2-2,6-DTBP], for the reaction between **9'** and 4-NO_2-2,6-DTBP at -45 °C in DMF. k_2 = 0.45(1) $M^{-1}s^{-1}$.

Kinetic isotopic effect experiments

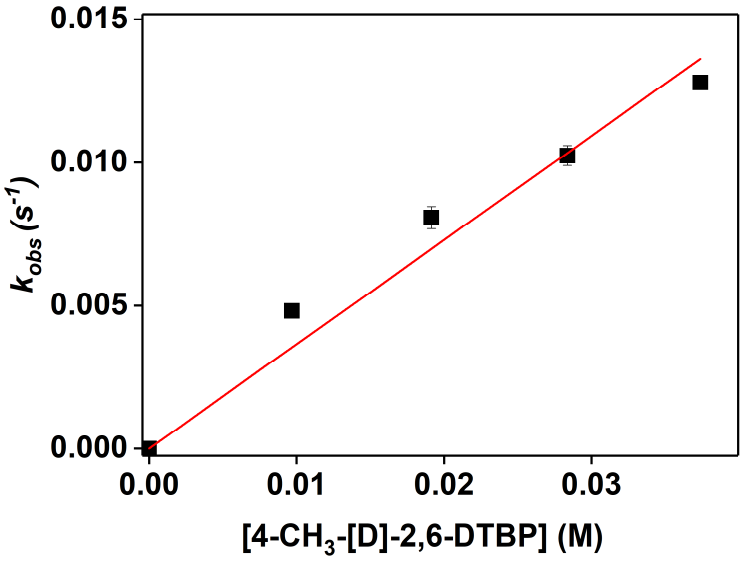

Figure A-4.36 - Plot of k_{obs} vs. [4-CH_3-[D]-2,6-DTBP], for the reaction between **9** and 4-CH_3-[D]-2,6-DTBP at -45 °C in DMF. k_2 = 0.36(2) $M^{-1}s^{-1}$.

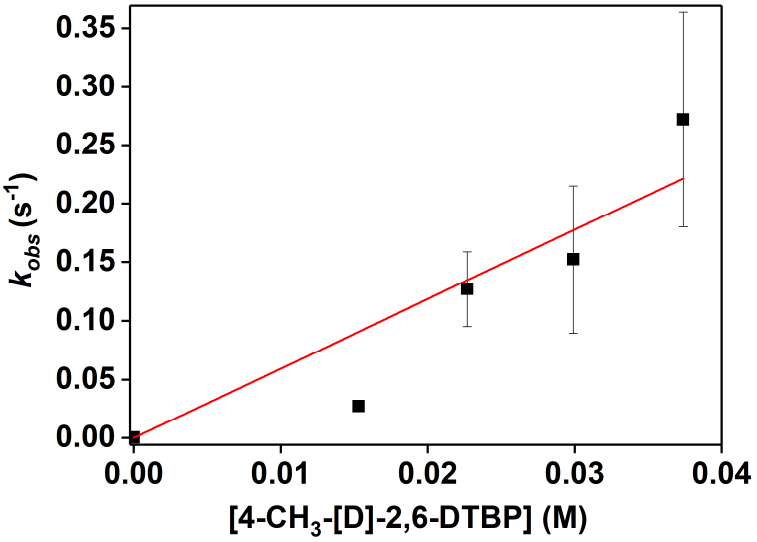

Figure A-4.37 - Plot of k_{obs} vs. [4-CH_3-[D]-2,6-DTBP], for the reaction between **10** and 4-CH_3-[D]-2,6-DTBP at -45 °C in DMF. k_2 = 5.9(8) $M^{-1}s^{-1}$.

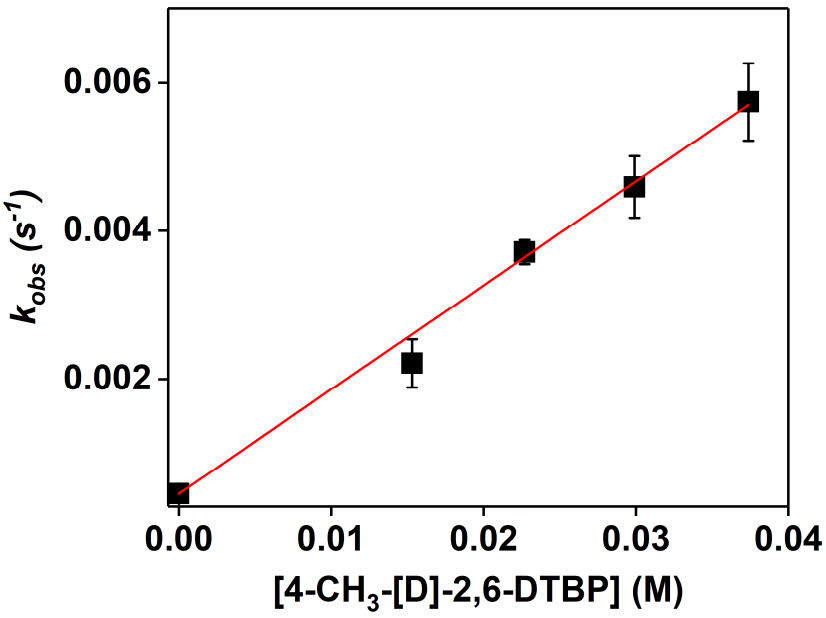

Figure A-4.38 - Plot of k_{obs} vs. [4-CH_3-[D]-2,6-DTBP], for the reaction between **9'** and 4-CH_3-[D]-2,6-DTBP at -45 °C in DMF. k_2 = 0.140(4) $M^{-1}s^{-1}$.

Table A-4.1 - Parameters related to the series of *para*-X-2,6 di-*tert*-butyl phenols used in the kinetic studies

X	BDE_{O-H} (kcal/mol)[a, 4-7]	$BDFE_{O-H}$ (kcal/mol)[b]	E(V) vs Fc/Fc^{+}[8, 9]	σ^{+}_{p}[6]
$-OCH_3$	78.3	73.5	0.53	-0.78
$-CH_2CH_3$	80.1	75.3	0.87	-0.46[10]
$-CH_3$	81	76.2	0.90	-0.31
$-C(CH_3)_3$	81.2	76.4	0.93	-0.26
–H	82.8	78	1.07	0.00
–Br	83.2	78.4	1.10	0.15[11]
–CN	84.2	79.4	1.58	0.66
$-NO_2$	84.9	80.1	1.70[12]	0.78

[a]The values reported are measured in C_6H_6. [b]The $BDFE_{O-H}$ values are extrapolated from a plot BDE_{O-H} vs $BDFE_{O-H}$ based on the values in C_6H_6 reported by Mayer.[13]

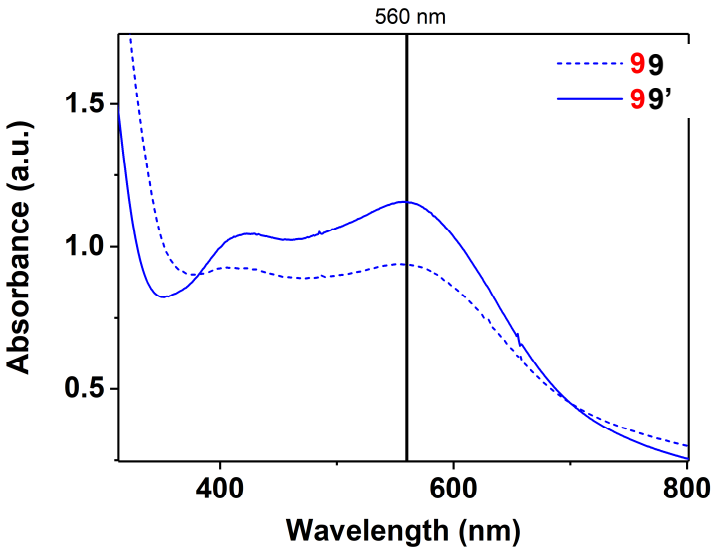

Figure A-4.39 – Comparison between the electronic absorption spectra of **9'** and **9**, in DMF at -45 °C.

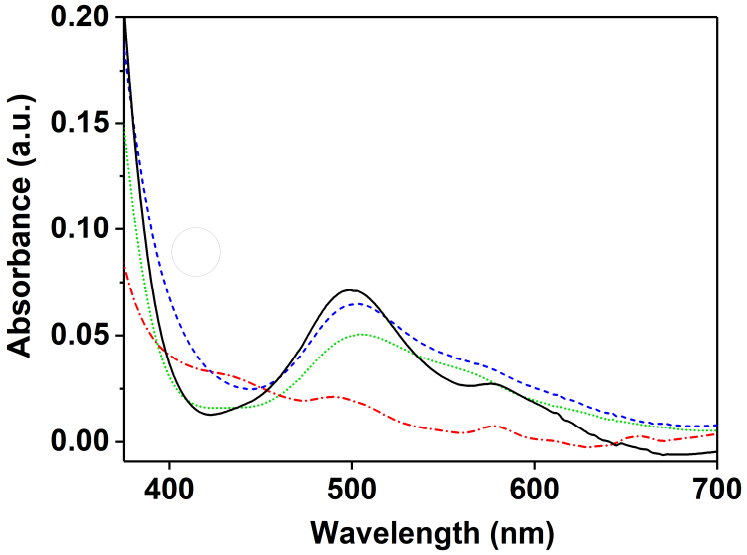

Figure A-4.40– UV-Vis of **8** (502nm feature, black trace) after addiction of 1 equiv. (blue dashed trace), 2 equiv, (green dotted trace) and 4 equiv. (red dot-dashed trace) of pyridinium triflate. Inset: effect of the added acid on the formation of **10** (addition of 3.4 equiv. of CAN) at -45˚C in DMF.

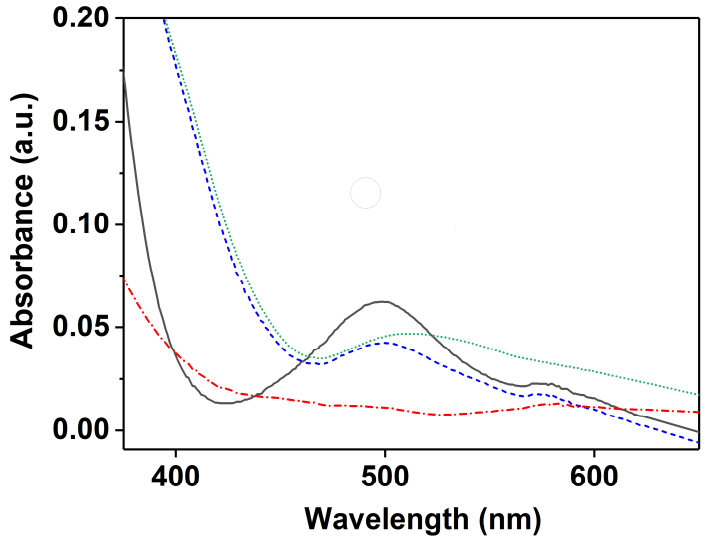

Figure A-4.41– UV-Vis of **8** (502nm feature, black trace) after addiction of 1 equiv. (blue dashed trace), 2 equiv, (green dotted trace) and 4 equiv. (red dot-dashed trace) of picolinic acid. Inset: effect of the added acid on the formation of **10** (addition of 3.4 equiv. of CAN) at -45˚C in DMF.

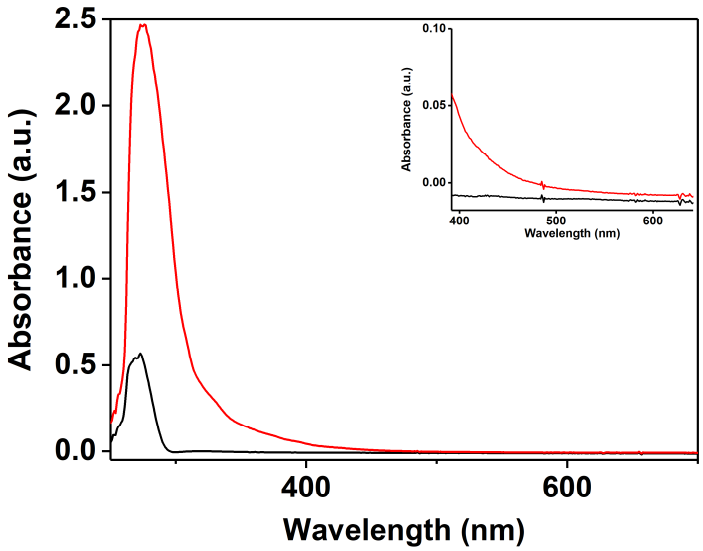

Figure A-4.42 – UV-Vis of 2,6-dimethyl benzoic acid in DMF at -45˚ (black trace) and after addition of DBU (red trace).

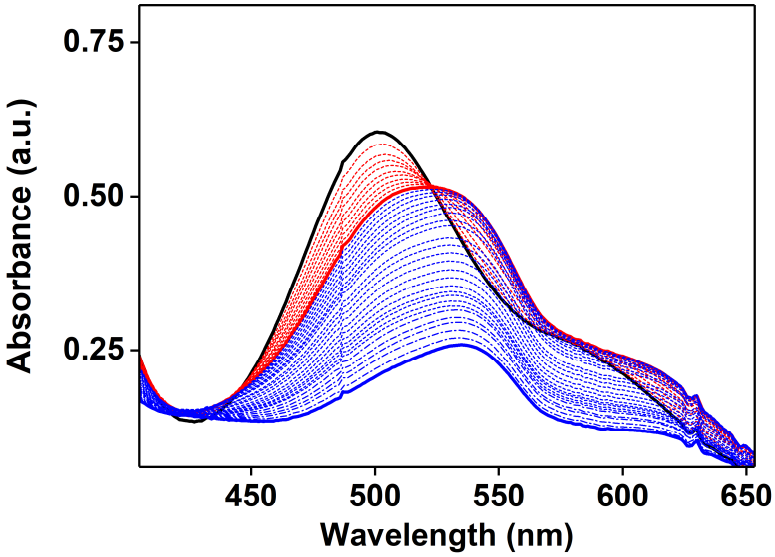

Figure A-4.43 – UV-Vis monitored titration of **8** (black trace) with sub-stoichiometric amount of 2,6 dimethyl benzoic acid at -45˚C in DMF. Each dashed line corresponds to an increment of 0.25 equiv, till a maximum of 2.50 equiv.

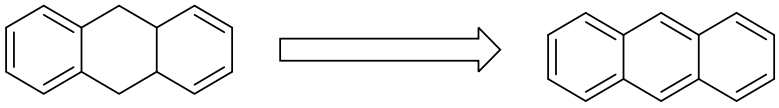

Figure A-4.44 - Identified products from the oxidation 9,10-dhydroanthracene by **10**. GC-MS was used for this analysis.

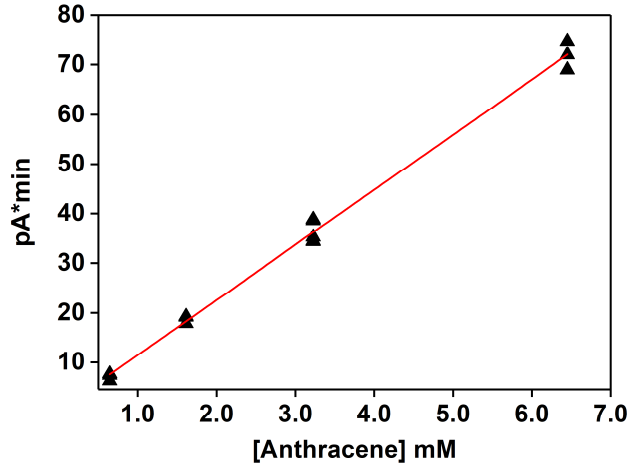

Figure A-4.45 – Calibration curve for the quantification of anthracene by GC-FID. Slope = 11.1(2), Intercept = 0.4(9)

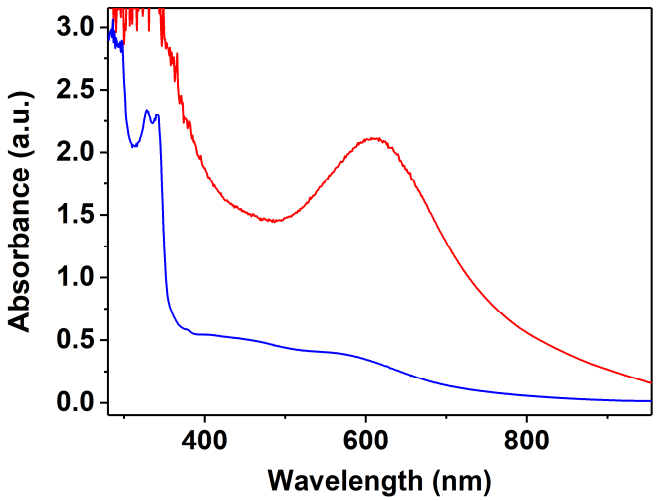

Figure A-4.46– UV-Vis spectra for the reaction of **10** (red trace) with xanthene at -45 °C in DMF.

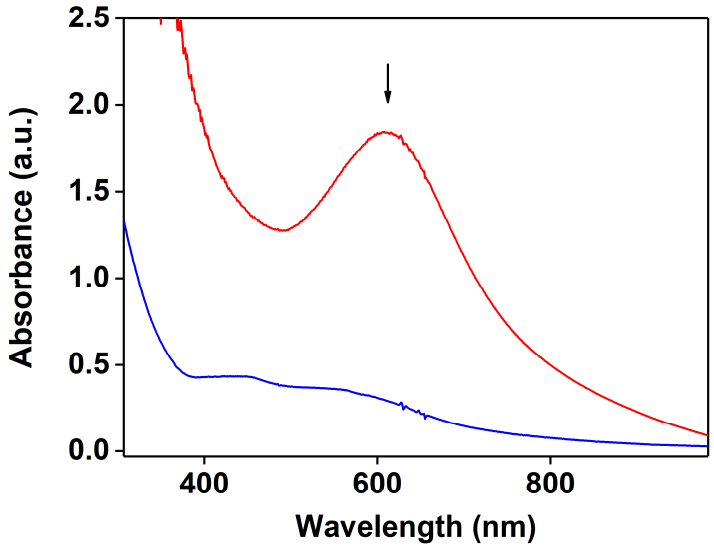

Figure A-4.47 – UV-Vis spectra for the reaction of **10** (red trace) with 1,4 cyclohexadiene at -45 °C in DMF

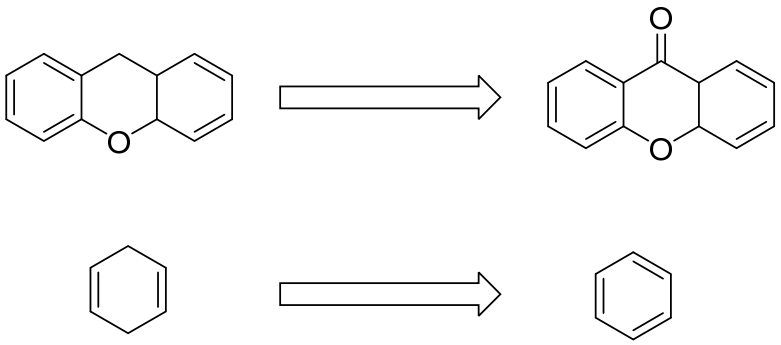

Figure A-4.48 - Identified products from the oxidation 9,10-dhydroanthracene and 1,4 cyclohexadiene by **10**. Both ESI-MS and GC-MS were used for this analysis.

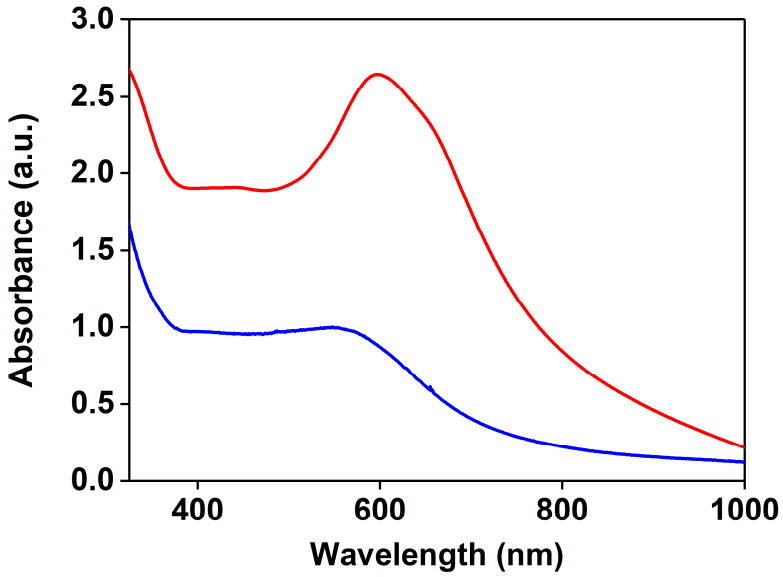

Figure A-4.49 – UV-Vis spectra for the reaction of **10** (red trace) with CH_3OH (blue trace) at -45 °C in DMF

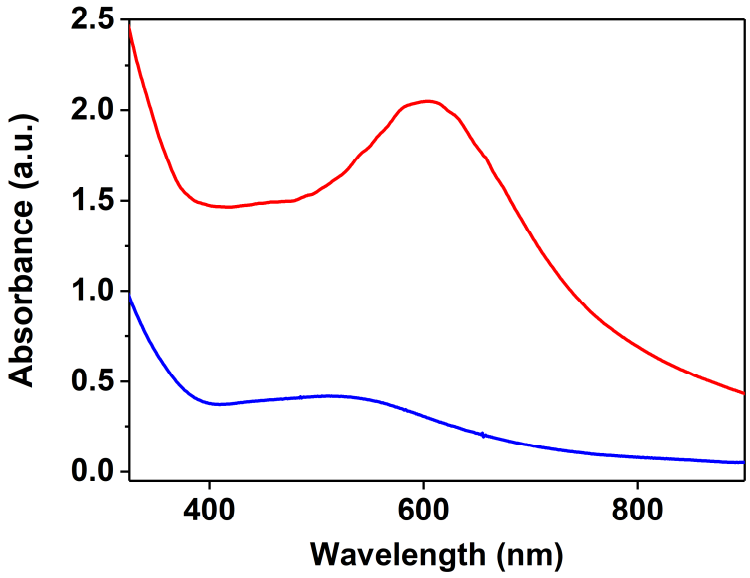

Figure A-4.50 – UV-Vis spectra for the reaction of **10** (red trace) with 2 equiv. of potassium *tert*-butoxide (THF solution, blue trace) at -45 °C in DMF.

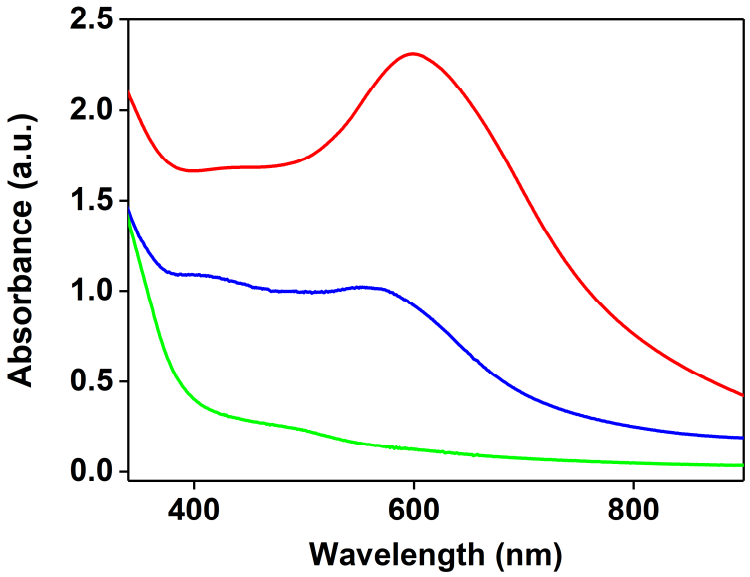

Figure A-4.51 – UV-Vis spectra for the reaction of **10** (red trace) with 2 equiv. (blue trace) and 4 equiv. (green trace) of potassium hydroxide (methanol solution) at -45 °C in DMF.

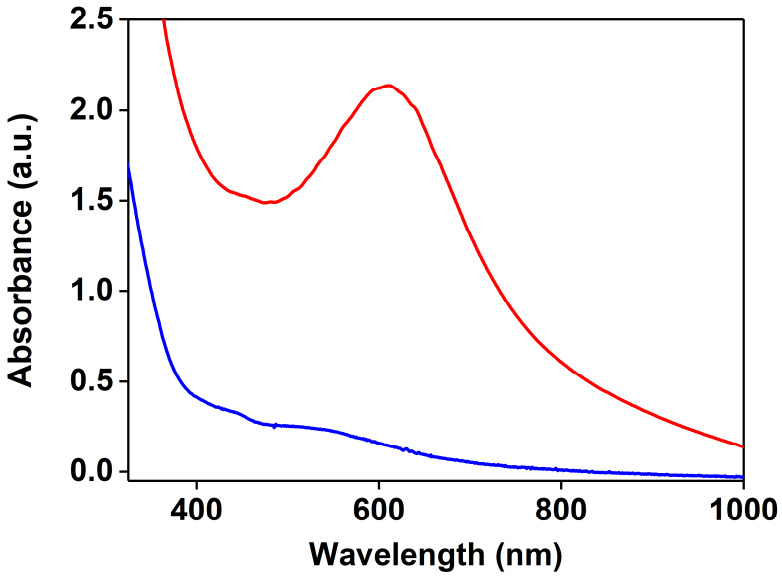

Figure A-4.52 – UV-Vis spectra for the reaction of **10** (red trace) with 100 equiv. of pyridine (blue trace) at -45 °C in DMF.

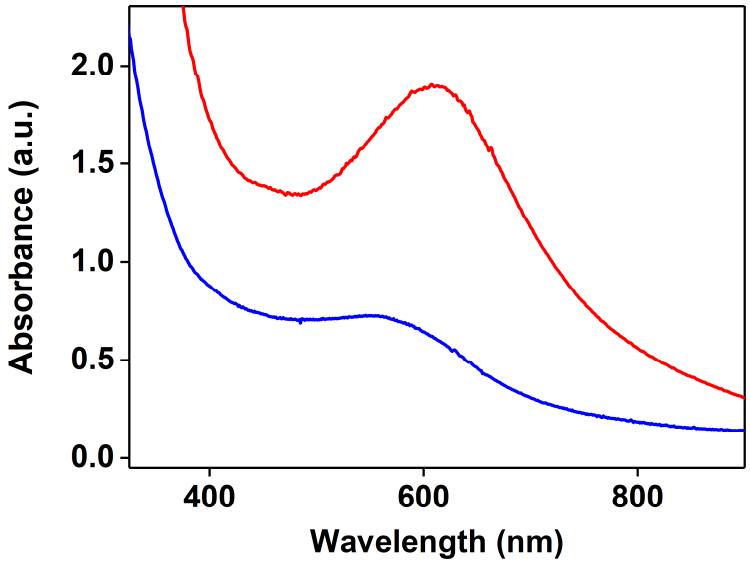

Figure A-4.53 – UV-Vis spectra for the reaction of **10** (red trace) with 100 equiv. of 2,6 lutidine (blue trace) at -45 °C in DMF.

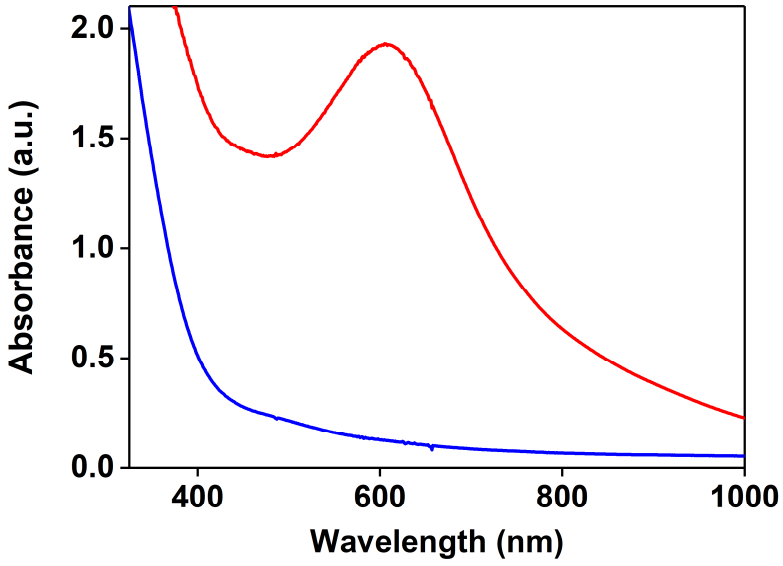

Figure A-4.54 – UV-Vis spectra for the reaction of **10** (red trace) with 2 equiv. of DBU (blue trace) at -45 °C in DMF.

Appendix to Chapter 5

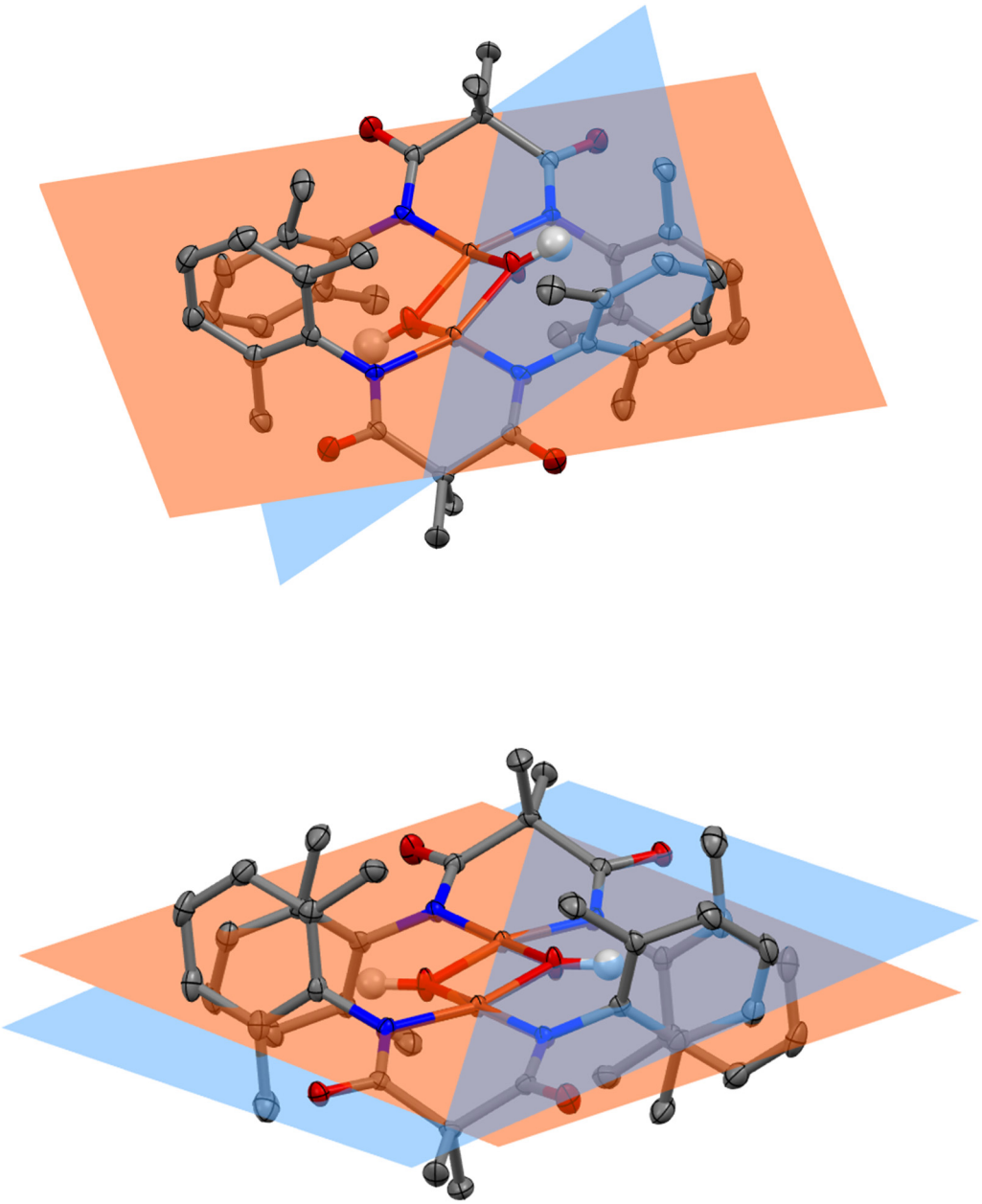

Figure A-5.1 – ORTEP plot of the two differently distorted structure for **11**, highlighting the tilti between the plane contraining the main core of the complex (orange) and the plane formed by the two μ-OH ligands (blue).

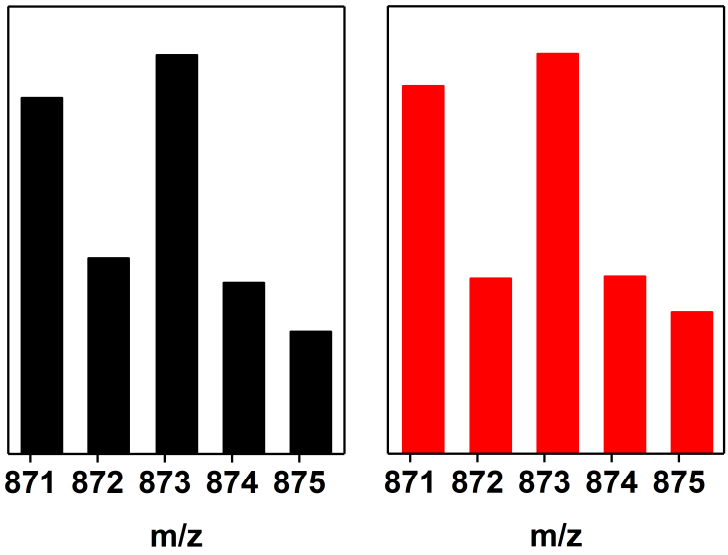

Figure A-5.2 - ESI-MS for **11** (black) and theoretical isotopic pattern (red). Found 871.1825 m/z. ([M+K] $C_{42}H_{50}Cu_2KN_4O_6^-$ requires 871.1965 m/z).

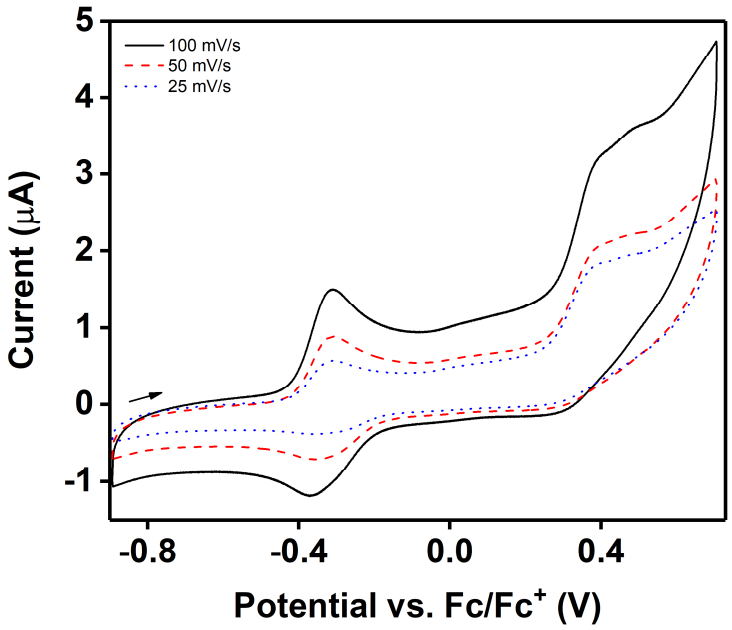

Figure A-5.3 – Cyclic voltammograms of **11** (full range). Conditions: 0.33 mM (DMF), 0.1 M Bu_4NPF_6, scan rate 25 mV/s –100 mV/s, room temperature.

Table A-5.1 - Cyclic Voltammetry data for **11,** recorded at different scan rates.

	mV/s	E_{pa}	E_{pc}	$E_{1/2}$	E_{pa}-E_{pc}	I_{pa}	I_{pc}	I_{pa}/I_{pc}
I oxidation wave	100	-0.312	-0.385	-0.35	0.07	1.58	-1.36	1.16
	50	-0.310	-0.385	-0.348	0.075	0.46	-0.40	1.15
	25	-0.308	-0.382	-0.345	0.074	0.34	-0.30	1.15

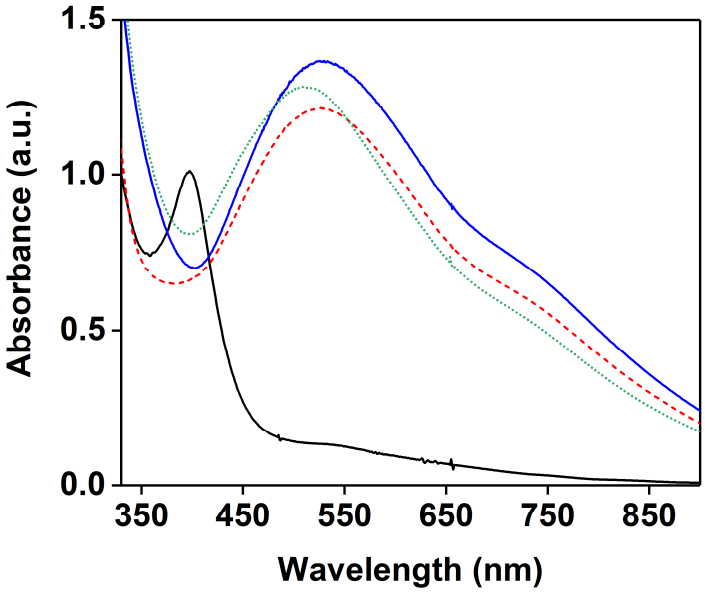

Figure A-5.4 – Elctronic absorption spectra of **11** (black trace) and formation of **12** with 1 equiv. (dashed red trace), 1.5 equiv. (blue solid trace) and 1.6 equiv. (dotted green trace) of CAN, respectively.

XAS Data

Table A-5.2 - XANES pre-edge peak fitting parameters. The values in parentheses correspond to uncertainty in the final digit for each parameter, taken as the standard deviation determined from the three separate fits conducted on each sample.

	$E_{pre\text{-}edge}$ (eV)[a]	Height	FWHM	Area[b]
11	8978.01(1)	0.0155(1)	1.88(1)	3.86(2)
12	8977.62(4)	0.0108(1)	2.27(10)	3.24(16)

[a] The pre-edge energies correspond to the center of the pseudoVoigt functions. [b] Areas are multiplied by 10^2 for convenience.

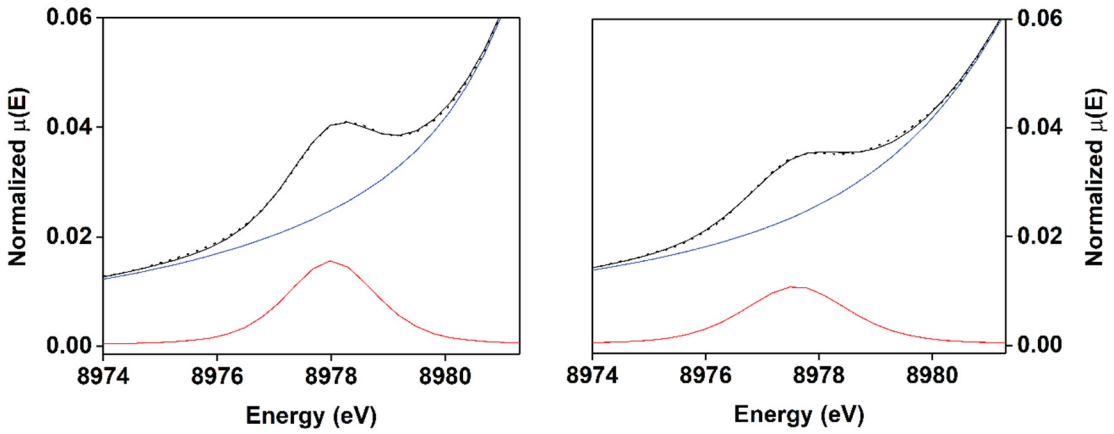

Figure A-5.5 - Representative pre-edge peak fits of **11** and **12**. The experimental data are shown as dots, the background function in a blue line, the component pre-edge functions as red lines, and the sum of the background + component functions as a solid black line.

Table A-5.3 - Comparison of selected bond length between XRD data and EXAFS Fit for **11**.

XRD		EXAFS Fit	
Cu–N/O	1.95	**Cu–N/O**	1.95
Cu···Cu	3.06	**Cu···Cu**	3.03

Table A-5.4 - EXAFS Fitting of the data for **11**. Significant fits are highlighted in bold. Fitting range was k = 2-15.0 Å^{-1} with back transform ranges of 1-2.03 Å for fits 1-5 and 1-3.20 Å for fits 6-. r is in units of Å; σ^2 is in units of 10^{-3} Å; ΔE_0 is in units of eV; R represents the fractional misfit of the data, while χ^2 is the χ^2 fitting metric normalized by the number of independent data points in a given fit.

	Cu-N/O			Cu-N/O			Cu···Cu			Cu···C					
fit	n	r	σ^2	n	r	σ^2	n	r	σ^2	n	r	σ^2	ΔE_0	χ^2	R
1	4	1.95	1.79										2.94	76.171	0.0182
2	3	1.97	0.80	1	1.88	-0.08							3.13	89.939	0.0134
3	2	1.97	1.04	2	1.91	2.23							2.75	96.734	0.0145
4	1	1.96	0.13	3	1.92	3.18							2.74	107.268	0.0160
5				4	1.93	2.75							3.65	89.116	0.0213
6	4	1.95	1.80										2.69	122.392	0.0756
7	4	1.95	1.85							1	3.04	-0.98	3.47	109.847	0.0588
8	4	1.95	1.82							2	3.03	1.76	3.87	104.400	0.0559
9	4	1.95	1.80							3	3.01	4.50	4.02	101.171	0.0541
10	4	1.95	1.80							4	3.00	7.03	4.08	98.601	0.0527
11	4	1.95	1.80							5	2.99	8.88	4.16	97.356	0.0521
12	4	1.95	1.80							6	2.99	10.46	4.24	97.538	0.0522
13	4	1.95	1.81				1	3.01	6.77				3.11	84.284	0.0451
14	4	1.95	1.88				1	3.01	4.35	1	2.88	-1.25	3.10	57.084	0.0258
15	4	1.95	1.82				1	3.02	6.66	2	2.21	39.67	3.71	95.757	0.0433
16	**4**	**1.95**	**1.86**				**1**	**3.03**	**3.61**	**3**	**2.90**	**3.61**	**3.47**	**43.322**	**0.0196**
17	4	1.95	1.85				1	3.03	3.78	4	2.91	3.95	3.63	45.763	0.0207
18	4	1.95	1.84				1	3.04	4.12	5	2.91	5.84	3.78	50.821	0.0230
19	4	1.95	1.83				1	3.04	4.58	6	2.92	8.11	3.90	56.963	0.0258

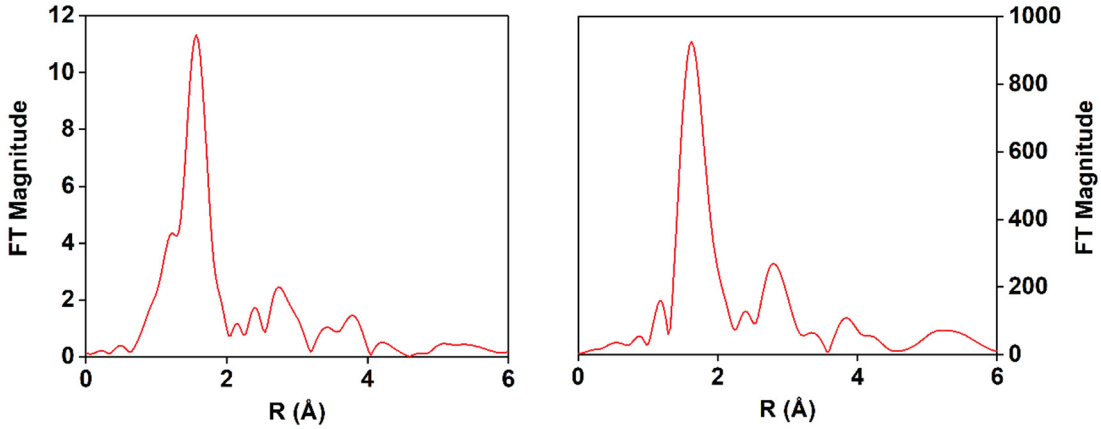

Figure A-5.6 - Comparison between the k^3-weighted (left) and k^5-weighted (right) Fourier trasforms in the EXAFS analysis of **11**.

Table A-5.5- EXAFS Fitting of the data for **12**. Significant fits are highlighted in bold. Fitting range was k = 2-13.0 Å^{-1} with back transform ranges of 1.15-2.12 Å for fits 1-10 and 1.15-3.13 Å for fits 11-37. r is in units of Å; σ² is in units of 10^{-3} Å; ΔE_0 is in units of eV; R represents the fractional mis-fit of the data, while χ^2 is the χ^2 fitting metric normalized by the number of independent data points in a given fit.

	Cu-N/O			Cu-N/O			Cu···Cu			Cu···C					
fit	n	r	σ²	n	r	σ²	n	r	σ²	n	r	σ²	ΔE_0	χ^2	R
1	4	1.97	3.45										2.84	189.711	0.0392
2	5	1.97	4.87										1.74	221.662	0.0458
3	6	1.97	6.21										0.71	328.643	0.0679
4	3	1.92	1.98	1	2.01	-3.17							-0.88	110.937	0.0103
5	2	2.00	-1.87	2	1.88	0.16							-0.80	112.518	0.0104
6	4	1.92	5.07	1	2.00	-2.25							-2.23	115.952	0.0108
7	3	1.89	3.92	2	1.99	-0.65							-2.41	110.601	0.0103
8	5	1.95	2.84	1	1.79	0.77							-3.17	186.276	0.0173
9	4	1.97	1.62	2	1.83	3.53							-3.56	160.096	0.0149
10	3	1.86	5.66	3	1.98	0.90							-3.73	148.343	0.0138
11	4	1.97	3.39										2.76	210.208	0.1124
12	4	1.97	3.29							1	2.87	-1.35	2.86	149.455	0.0663

13	4	1.97	3.30					2	2.88	1.36	3.17	116..879	0.0518
14	4	1.97	3.31					3	2.89	3.25	3.37	101.742	0.0451
15	4	1.97	3.32					4	2.89	4.84	3.52	97.155	0.0431
16	4	1.97	3.33					5	2.90	6.32	3.61	99.584	0.0441
17	4	1.97	3.34					6	2.90	7.80	3.68	106.729	0.0473
18	4	1.97	3.33	1	2.87	7.70					2.49	133.219	0.0591
19	4	1.97	3.42	1	2.88	7.73	1	2.31	4.29	3.72	143.755	0.0491
20	4	1.98	3.50	1	2.85	2.23	2	3.01	-3.47	3.95	75.894	0.0259
21	4	1.98	3.51	1	2.84	2.24	3	3.00	-1.87	4.51	69.850	0.0238
22	4	1.98	3.48	1	2.83	2.70	4	2.99	-0.20	4.82	72.779	0.0248
23	**4**	**1.98**	**3.43**	**1**	**2.82**	**3.87**	**5**	**2.98**	**2.09**	**4.90**	**82.699**	**0.0282**
24	4	1.98	3.33	1	2.85	8.02	6	2.97	10.43	4.46	90.463	0.0308
25	5	1.97	4.81							1.71	222.219	0.1188
26	5	1.97	4.72				1	2.86	-2.28	1.81	173.279	0.0749
27	5	1.97	4.72				2	2.88	1.51	2.13	140.936	0.0609
28	5	1.97	4.73				3	2.88	3.36	2.34	125.723	0.0544
29	5	1.97	4.74				4	2.89	4.92	2.50	120.936	0.0523
30	5	1.97	4.75				5	2.89	6.36	2.62	123.135	0.0533
31	5	1.97	4.76				6	2.90	7.79	2.69	130.078	0.0563
32	5	1.97	4.72	1	2.87	7.81	1	1.68	44.60	1.71	197.058	0.0651
33	5	1.97	4.94	1	2.84	1.98	2	3.00	-3.82	2.86	83.712	0.0277
34	5	1.98	4.95	1	2.83	1.88	3	2.99	-2.33	2.43	77.910	0.0257
35	5	1.98	4.93	1	2.82	2.16	4	2.98	-0.86	3.78	82.202	0.0272
36	5	1.98	4.88	1	2.82	2.88	5	2.98	0.88	3.93	95.095	0.0314
37	5	1.98	4.80	1	2.81	4.58	6	2.97	3.74	3.88	112.061	0.0370

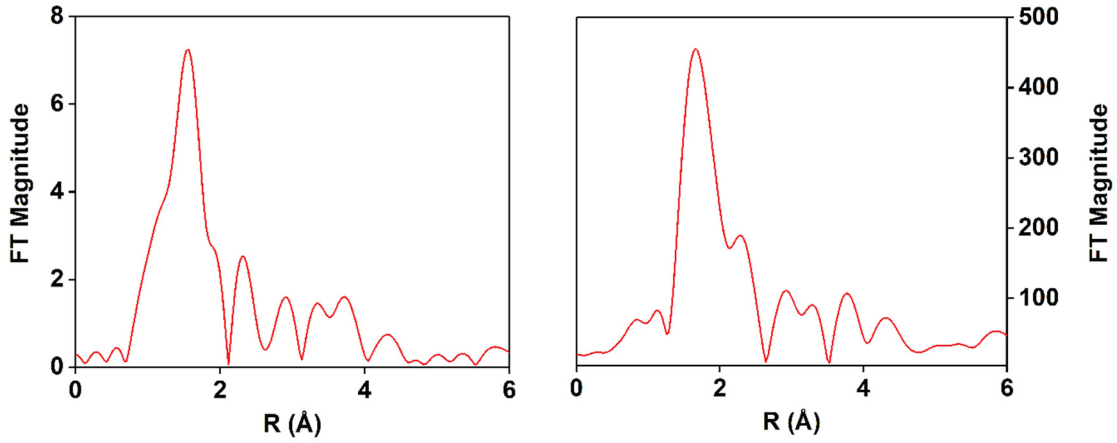

Figure A-5.7 - Comparison between the k^3-weighted (left) and k^5-weighted (right) Fourier trasforms in the EXAFS analysis of **12**.

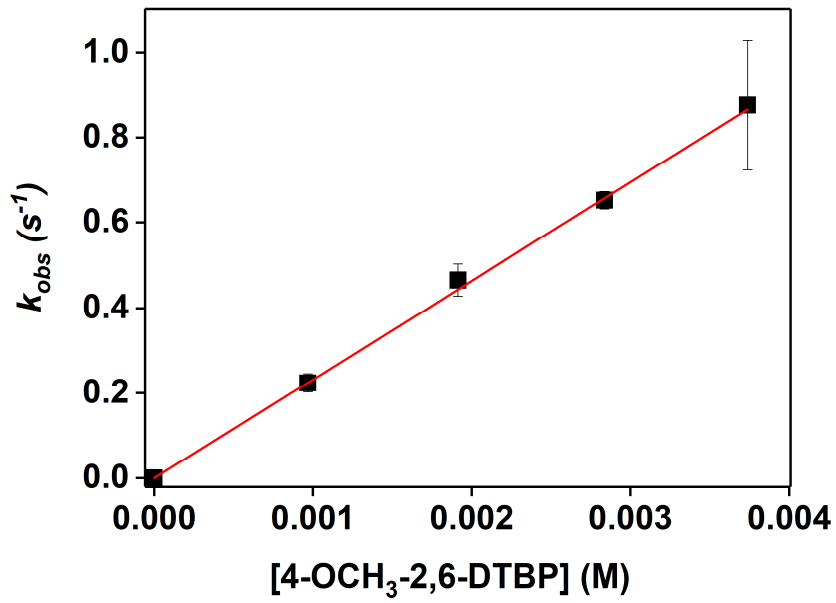

Figure A-5.8 - Plot of k_{obs} vs. [4-OCH_3-2,6-DTBP], for the reaction between **12** and 4-OCH_3-2,6-DTBP at -45 °C in DMF. k_2 = 232(2) $M^{-1}s^{-1}$.

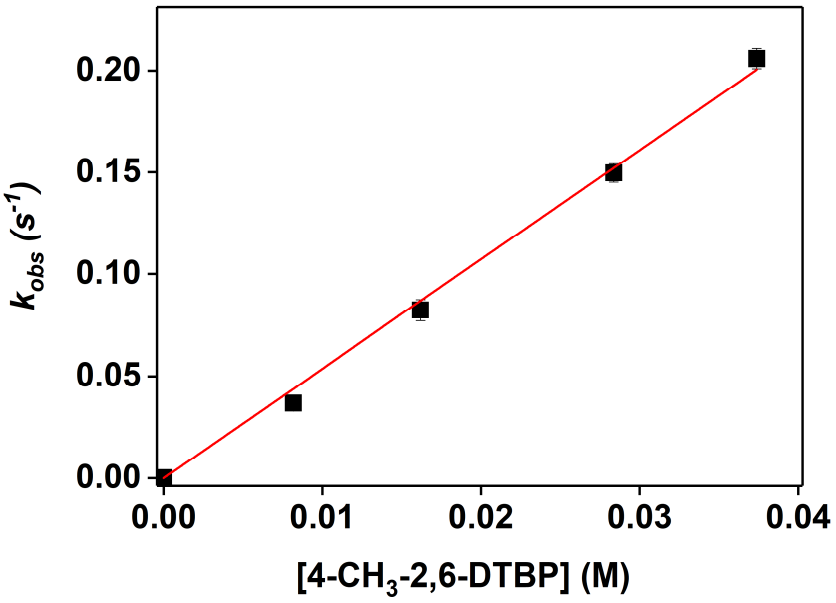

Figure A-5.9 - Plot of k_{obs} vs. [4-CH_3-2,6-DTBP], for the reaction between **12** and 4-CH_3-2,6-DTBP at -45 °C in DMF. k_2 = 5.4(1) $M^{-1}s^{-1}$.

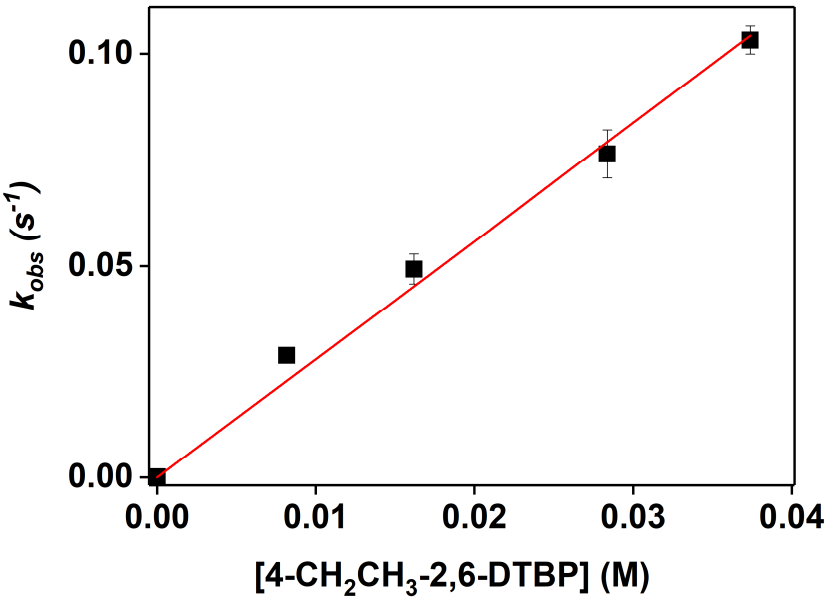

Figure A-5.10 - Plot of k_{obs} vs. [4-CH_2CH_3-2,6-DTBP], for the reaction between **12** and 4-CH_2CH_3-2,6-DTBP at -45 °C in DMF. k_2 = 2.8(1) $M^{-1}s^{-1}$.

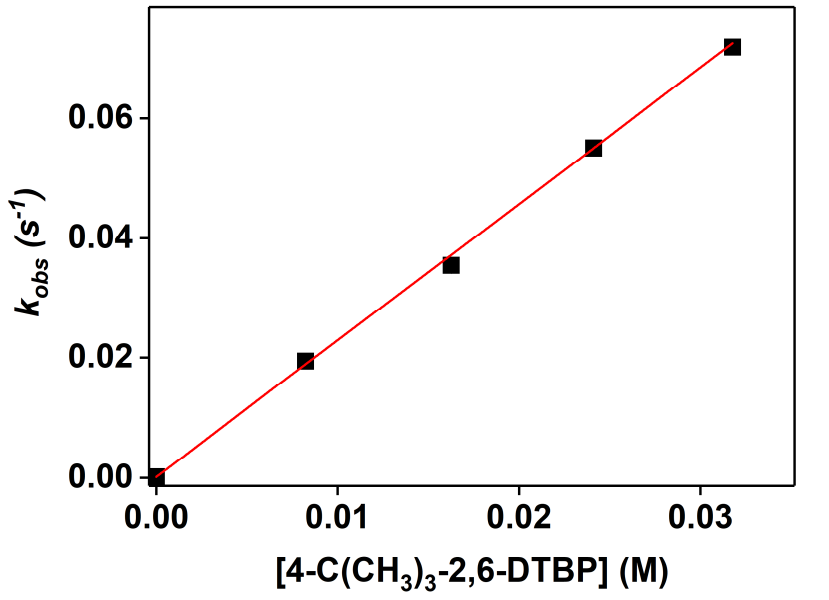

Figure A-5.11 - Plot of k_{obs} vs. [4-$C(CH_3)_3$-2,6-DTBP], for the reaction between **12** and 4-$C(CH_3)_3$-2,6-DTBP at -45 °C in DMF. k_2 = 2.28(1) $M^{-1}s^{-1}$.

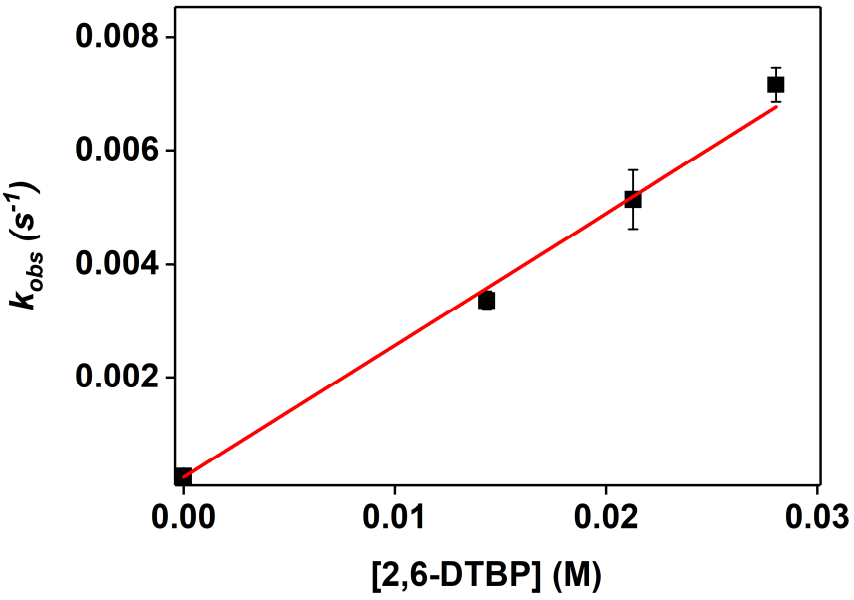

Figure A-5.12 - Plot of k_{obs} vs. [2,6-DTBP], for the reaction between **12** and 2,6-DTBP at -45 °C in DMF. k_2 = 0.23(1) $M^{-1}s^{-1}$.

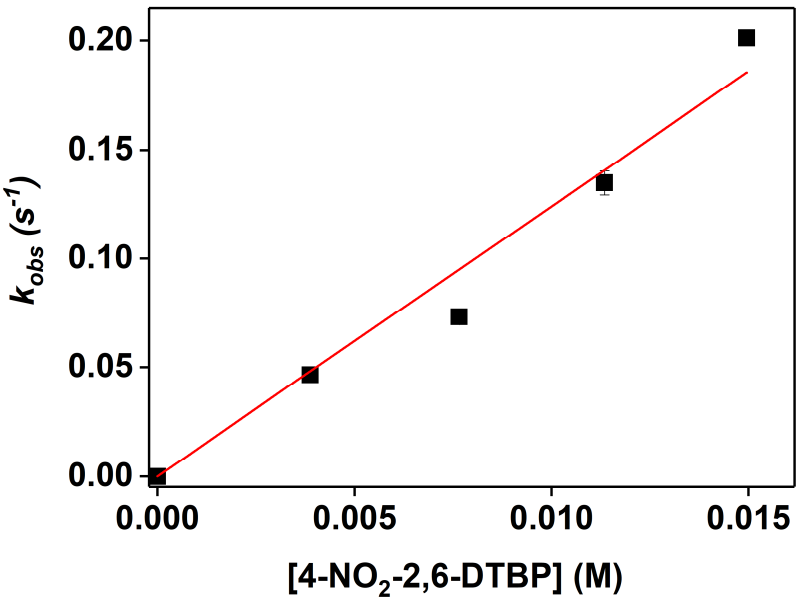

Figure A-5.13 - Plot of k_{obs} vs. [4-NO_2-2,6-DTBP], for the reaction between **12** and 4-NO_2-2,6-DTBP at -45 °C in DMF. k_2 = 12.4(7) $M^{-1}s^{-1}$.

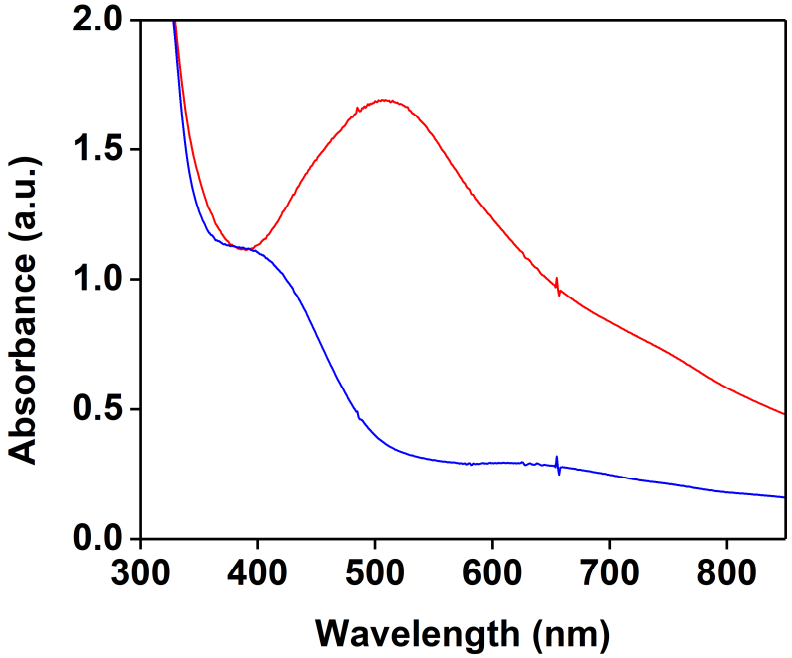

Figure A-5.14 - Electronic absorption spectra showing the self-decay of complex **12** at -45 °C in DMF.

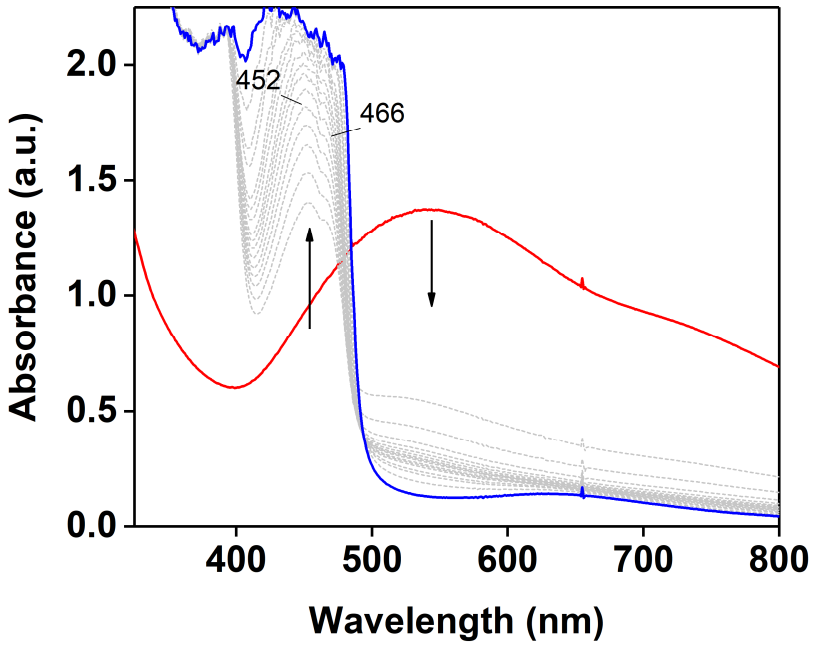

Figure A-5.15 - Electronic absorption spectra showing the formation of the 4-NO_2-2,6-DTB phenolate upon reaction of 4-NO_2-2,6 DTBP with **12** at -45 °C in DMF.

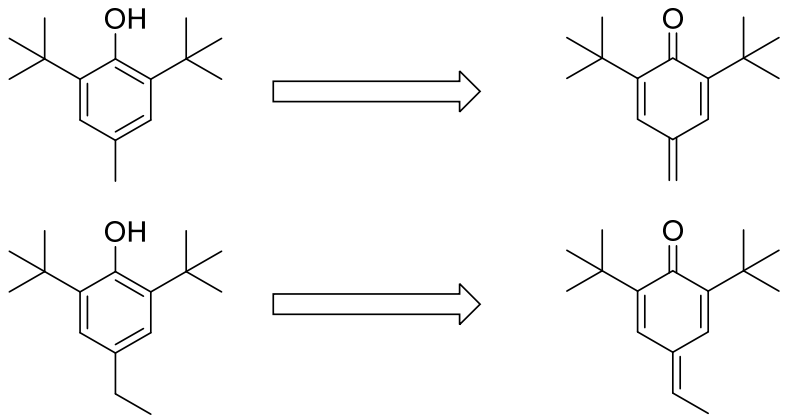

Figure A-5.16 - Identified products from the oxidation of 4-CH_3-2,6-DTBP and 4-CH_2CH_3-2,6-DTBP by **12**. ESI-MS was used for this analysis.

References

(1) S. Itoh, H. Bandoh, M. Nakagawa, S. Nagatomo, T. Kitagawa, K. D. Karlin and S. Fukuzumi, *J. Am. Chem. Soc.*, 2001, **123**, 11168-11178.

(2) C. Jaeheung, F. Hideki, F. Shuhei and S. Masatatsu, *Angew. Chem. Int. Ed.*, 2004, **43**, 3300-3303.

(3) Y. Li, L. Jiang, L. Wang, H. Gao, F. Zhu and Q. Wu, *Appl. Organomet. Chem.*, 2006, **20**, 181-186.

(4) Y.-R. Luo, *Handbook of bond dissociation energies in organic compounds*, CRC press, 2002.

(5) G. Brigati, M. Lucarini, V. Mugnaini and G. F. Pedulli, *J. Org. Chem.*, 2002, **67**, 4828-4832.

(6) S. Kundu, P. Chernev, X. Engelmann, C. S. Chung, H. Dau, E. Bill, J. England, W. Nam and K. Ray, *Dalton Trans.*, 2016, **45**, 14538-14543.

(7) M. Lucarini, P. Pedrielli, G. F. Pedulli, S. Cabiddu and C. Fattuoni, *J. Org. Chem.*, 1996, **61**, 9259-9263.

(8) J. Y. Lee, R. L. Peterson, K. Ohkubo, I. Garcia-Bosch, R. A. Himes, J. Woertink, C. D. Moore, E. I. Solomon, S. Fukuzumi and K. D. Karlin, *J. Am. Chem. Soc.*, 2014, **136**, 9925-9937.

(9) S. Kundu, E. Miceli, E. R. Farquhar and K. Ray, *Dalton Trans.*, 2014, **43**, 4264-4267.

(10) The Hammett parameter for this substrate was extrapolated from the linear relationship between the sigma values and BDEs of the other substrates.

(11) J. Cho, J. Woo, J. Eun Han, M. Kubo, T. Ogura and W. Nam, *Chemical Science*, 2011, **2**.

(12) P. Mondal, P. Pirovano, A. Das, E. R. Farquhar and A. R. McDonald, *J. Am. Chem. Soc.*, 2018, **140**, 1834-1841.

(13) J. J. Warren, T. A. Tronic and J. M. Mayer, *Chem. Rev.*, 2010, **110**, 6961-7001.

Appendix B

Atom coordinates for optimised molecular structures

Table B-1 - Atomic coordinates of optimized structure of **8-seesaw**.

Ni	-0.521700	1.356600	-0.102400
O	-3.681600	3.738400	0.434500
N	-2.179600	2.027300	0.219900
C	-2.556400	3.368300	0.102100
C	-1.547200	4.333000	-0.527000
C	-2.057100	5.770600	-0.367000
C	-1.414500	3.998700	-2.038800
C	-3.253900	1.125500	0.503300
C	-3.362900	0.562100	1.793200
C	-4.499500	-0.197600	2.089600
H	-4.614100	-0.605500	3.095200
C	-5.478100	-0.431100	1.124300
H	-6.359200	-1.023500	1.373400
C	-5.314400	0.064400	-0.169900
H	-6.055000	-0.161100	-0.938500
C	-4.206900	0.847400	-0.504600
C	-2.287800	0.790400	2.816300
H	-1.346400	0.321800	2.486900
H	-2.561500	0.360500	3.787500
H	-2.074100	1.859800	2.946900
C	-4.020700	1.384200	-1.896800
H	-4.213100	2.467400	-1.924600
H	-4.706000	0.897100	-2.601300
H	-2.989400	1.223500	-2.241900
H	-1.068800	2.969400	-2.202500
H	-1.350000	6.467400	-0.831300
H	-0.693800	4.686300	-2.501200
H	-2.154400	6.037800	0.691800
O	0.519600	5.234100	0.327700
N	0.364500	2.956200	0.289700
C	-0.137300	4.212800	0.094200
C	1.748200	2.870100	0.641300
C	2.111300	2.458200	1.942700
C	3.465400	2.465400	2.295200
H	3.751200	2.171000	3.306600
C	4.441700	2.848500	1.376000
H	5.492500	2.858000	1.668400
C	4.076800	3.190800	0.074100
H	4.844000	3.449100	-0.657200
C	2.734900	3.196600	-0.320800
C	1.058000	2.006100	2.912800
H	0.641700	1.036500	2.592700
H	1.465700	1.884100	3.924000
H	0.215000	2.709100	2.946200
C	2.340300	3.554000	-1.726600
H	1.916300	4.569300	-1.758600
H	3.205600	3.515100	-2.400000
H	1.570600	2.864500	-2.101700
H	-3.043300	5.869800	-0.835700
H	-2.385700	4.125000	-2.536200
Ni	0.494600	-1.335200	-0.351500
O	-0.457700	-5.146700	0.608700
N	-0.343300	-2.999200	-0.160300
C	0.156800	-4.079100	0.514600
C	1.508600	-3.901100	1.246100
C	2.041500	-5.271100	1.680300
C	1.241000	-3.029700	2.504700
C	-1.702000	-3.071700	-0.590300
C	-1.994700	-3.107600	-1.972000
C	-3.332900	-3.180600	-2.372700
H	-3.565900	-3.218900	-3.438500
C	-4.361900	-3.218700	-1.431300
H	-5.400500	-3.282200	-1.758400
C	-4.061800	-3.165500	-0.070000
H	-4.865300	-3.181100	0.666300
C	-2.739200	-3.073100	0.375000
C	-0.885600	-3.050100	-2.983000
H	-0.471400	-2.031200	-3.033100
H	-1.241600	-3.321700	-3.984700
H	-0.057600	-3.715900	-2.704400
C	-2.423800	-2.992600	1.843000
H	-1.995200	-3.942500	2.195800
H	-3.326000	-2.774400	2.425800
H	-1.681800	-2.205900	2.045300
H	0.877800	-2.027400	2.240100
H	2.987700	-5.148200	2.221600
H	2.163200	-2.924400	3.091700
H	2.226800	-5.914100	0.812500
O	3.669300	-3.685800	0.182400
N	2.190100	-1.985400	-0.209400
C	2.549800	-3.213400	0.363600
C	3.261300	-1.181700	-0.697200
C	3.343300	-0.890200	-2.081200
C	4.418400	-0.121900	-2.537200
H	4.498600	0.092300	-3.604300
C	5.387000	0.355300	-1.654600
H	6.221300	0.950300	-2.027800
C	5.278200	0.085000	-0.289900
H	6.016600	0.485800	0.404700
C	4.218700	-0.670800	0.216200
C	2.305000	-1.397800	-3.040100
H	1.381700	-0.803600	-2.944600
H	2.651000	-1.320500	-4.078400
H	2.039500	-2.441900	-2.832200
C	4.087300	-0.905100	1.696100
H	4.342300	-1.943500	1.954000

H	4.751500	-0.234900	2.254000	O	1.048700	0.468600	-0.541600
H	3.057700	-0.721400	2.034600	H	1.913300	0.802100	-0.223000
H	1.305800	-5.767600	2.323100	O	-1.111500	-0.395300	-0.526200
H	0.483600	-3.519500	3.131000	H	-1.966100	-0.762100	-0.217000

Table B-2 - Atomic coordinates of optimized structure of **8-plane**.

Ni	0.009300	0.106600	1.502000	H	0.937900	-2.941000	4.116700
O	2.260500	-0.175200	4.895900	Ni	-0.009300	-0.106600	-1.502000
N	1.395100	0.198400	2.796900	O	2.262000	0.250500	-4.875500
C	1.318500	-0.256100	4.077600	N	1.359900	-0.170900	-2.805400
C	0.017700	-0.990900	4.498300	C	1.300800	0.295100	-4.075400
C	0.018900	-1.177800	6.021400	C	-0.017700	0.990900	-4.498300
C	0.033400	-2.387700	3.821000	C	-0.018900	1.177800	-6.021400
C	2.682800	0.625600	2.357700	C	-0.033400	2.387700	-3.821000
C	2.904200	1.976400	2.009100	C	2.635700	-0.625100	-2.356100
C	4.178700	2.379100	1.594900	C	2.884000	-2.007200	-2.222300
H	4.341400	3.427500	1.330100	C	4.128000	-2.434800	-1.739800
C	5.229400	1.464900	1.507500	H	4.315100	-3.506700	-1.629700
H	6.218600	1.790700	1.177700	C	5.118500	-1.512200	-1.399200
C	4.991800	0.121600	1.799300	H	6.080500	-1.855000	-1.011500
H	5.790500	-0.613500	1.674800	C	4.861500	-0.145900	-1.526900
C	3.727900	-0.318100	2.208400	H	5.614700	0.581700	-1.220700
C	1.761200	2.947700	2.042500	C	3.625700	0.316400	-1.990900
H	1.067100	2.708700	1.219200	C	1.799500	-2.987600	-2.569900
H	2.105700	3.985600	1.926300	H	0.971600	-2.900500	-1.850900
H	1.184000	2.851500	2.971900	H	2.171500	-4.022600	-2.558900
C	3.471600	-1.777000	2.468400	H	1.367500	-2.763600	-3.555700
H	3.402700	-1.966400	3.551500	C	3.314600	1.784600	-2.070500
H	4.268300	-2.399700	2.037600	H	3.173200	2.090300	-3.118900
H	2.508500	-2.080400	2.031300	H	4.117300	2.383000	-1.618200
H	0.020200	-2.289800	2.726600	H	2.376400	1.985400	-1.532200
H	-0.884300	-1.722000	6.326000	H	-0.020200	2.289800	-2.726600
H	-0.851800	-2.964000	4.131300	H	-0.922400	1.719900	-6.328900
H	0.017600	-0.206000	6.531900	H	-0.937900	2.941000	-4.116700
O	-2.262000	-0.250500	4.875500	H	-0.017600	0.206000	-6.531900
N	-1.359900	0.170900	2.805400	O	-2.260500	0.175200	-4.895900
C	-1.300800	-0.295100	4.075400	N	-1.395100	-0.198400	-2.796900
C	-2.635700	0.625100	2.356100	C	-1.318500	0.256100	-4.077600
C	-2.884000	2.007200	2.222300	C	-2.682800	-0.625600	-2.357700
C	-4.128000	2.434800	1.739800	C	-2.904200	-1.976400	-2.009100
H	-4.315100	3.506700	1.629700	C	-4.178700	-2.379100	-1.594900
C	-5.118500	1.512200	1.399200	H	-4.341400	-3.427500	-1.330100
H	-6.080500	1.855000	1.011500	C	-5.229400	-1.464900	-1.507500
C	-4.861500	0.145900	1.526900	H	-6.218600	-1.790700	-1.177700
H	-5.614700	-0.581700	1.220700	C	-4.991800	-0.121600	-1.799300
C	-3.625700	-0.316400	1.990900	H	-5.790500	0.613500	-1.674800
C	-1.799500	2.987600	2.569900	C	-3.727900	0.318100	-2.208400
H	-0.971600	2.900500	1.850900	C	-1.761200	-2.947700	-2.042500
H	-2.171500	4.022600	2.558900	H	-1.067100	-2.708700	-1.219200
H	-1.367500	2.763600	3.555700	H	-2.105700	-3.985600	-1.926300
C	-3.314600	-1.784600	2.070500	H	-1.184000	-2.851500	-2.971900
H	-3.173200	-2.090300	3.118900	C	-3.471600	1.777000	-2.468400
H	-4.117300	-2.383000	1.618200	H	-3.402700	1.966400	-3.551500
H	-2.376400	-1.985400	1.532200	H	-4.268300	2.399700	-2.037600
H	0.922400	-1.719900	6.328900	H	-2.508500	2.080400	-2.031300

H	0.884300	1.722000	-6.326000
H	0.851800	2.964000	-4.131300
O	-1.208900	-0.232400	0.017300
H	-2.020400	0.307200	-0.013500
O	1.208900	0.232400	-0.017300
H	2.020400	-0.307200	0.013500

Table B-3 - Atomic coordinates of optimized structure of **9-seesaw**.

Ni	-0.521700	1.356600	-0.102400
O	-3.681600	3.738400	0.434500
O	1.048700	0.468600	-0.541600
N	-2.179600	2.027300	0.219900
C	-2.556400	3.368300	0.102100
C	-1.547200	4.333000	-0.527000
C	-2.057100	5.770600	-0.367000
C	-1.414500	3.998700	-2.038800
C	-3.253900	1.125500	0.503300
C	-3.362900	0.562100	1.793200
C	-4.499500	-0.197600	2.089600
H	-4.614100	-0.605500	3.095200
C	-5.478100	-0.431100	1.124300
H	-6.359200	-1.023500	1.373400
C	-5.314400	0.064400	-0.169900
H	-6.055000	-0.161100	-0.938500
C	-4.206900	0.847400	-0.504600
C	-2.287800	0.790400	2.816300
H	-1.346400	0.321800	2.486900
H	-2.561500	0.360500	3.787500
H	-2.074100	1.859800	2.946900
C	-4.020700	1.384200	-1.896800
H	-4.213100	2.467400	-1.924600
H	-4.706000	0.897100	-2.601300
H	-2.989400	1.223500	-2.241900
H	-1.068800	2.969400	-2.202500
H	-1.350000	6.467400	-0.831300
H	-0.693800	4.686300	-2.501200
H	-2.154400	6.037800	0.691800
O	0.519600	5.234100	0.327700
N	0.364500	2.956200	0.289700
C	-0.137300	4.212800	0.094200
C	1.748200	2.870100	0.641300
C	2.111300	2.458200	1.942700
C	3.465400	2.465400	2.295200
H	3.751200	2.171000	3.306600
C	4.441700	2.848500	1.376000
H	5.492500	2.858000	1.668400
C	4.076800	3.190800	0.074100
H	4.844000	3.449100	-0.657200
C	2.734900	3.196600	-0.320800
C	1.058000	2.006100	2.912800
H	0.641700	1.036500	2.592700
H	1.465700	1.884100	3.924000
H	0.215000	2.709100	2.946200
C	2.340300	3.554000	-1.726600
H	1.916300	4.569300	-1.758600
H	3.205600	3.515100	-2.400000
H	1.570600	2.864500	-2.101700
H	-3.043300	5.869800	-0.835700
H	-2.385700	4.125000	-2.536200
Ni	0.494600	-1.335200	-0.351500
O	-0.457700	-5.146700	0.608700
N	-0.343300	-2.999200	-0.160300
C	0.156800	-4.079100	0.514600
C	1.508600	-3.901100	1.246100
C	2.041500	-5.271100	1.680300
C	1.241000	-3.029700	2.504700
C	-1.702000	-3.071700	-0.590300
C	-1.994700	-3.107600	-1.972000
C	-3.332900	-3.180600	-2.372700
H	-3.565900	-3.218900	-3.438500
C	-4.361900	-3.218700	-1.431300
H	-5.400500	-3.282200	-1.758400
C	-4.061800	-3.165500	-0.070000
H	-4.865300	-3.181100	0.666300
C	-2.739200	-3.073100	0.375000
C	-0.885600	-3.050100	-2.983000
H	-0.471400	-2.031200	-3.033100
H	-1.241600	-3.321700	-3.984700
H	-0.057600	-3.715900	-2.704400
C	-2.423800	-2.992600	1.843000
H	-1.995200	-3.942500	2.195800
H	-3.326000	-2.774400	2.425800
H	-1.681800	-2.205900	2.045300
H	0.877800	-2.027400	2.240100
H	2.987700	-5.148200	2.221600
H	2.163200	-2.924400	3.091700
H	2.226800	-5.914100	0.812500
O	3.669300	-3.685800	0.182400
N	2.190100	-1.985400	-0.209400
C	2.549800	-3.213400	0.363600
C	3.261300	-1.181700	-0.697200
C	3.343300	-0.890200	-2.081200
C	4.418400	-0.121900	-2.537200
H	4.498600	0.092300	-3.604300

C	5.387000	0.355300	-1.654600
H	6.221300	0.950300	-2.027800
C	5.278200	0.085000	-0.289900
H	6.016600	0.485800	0.404700
C	4.218700	-0.670800	0.216200
C	2.305000	-1.397800	-3.040100
H	1.381700	-0.803600	-2.944600
H	2.651000	-1.320500	-4.078400
H	2.039500	-2.441900	-2.832200
C	4.087300	-0.905100	1.696100
H	4.342300	-1.943500	1.954000
H	4.751500	-0.234900	2.254000
H	3.057700	-0.721400	2.034600
H	1.305800	-5.767600	2.323100
H	0.483600	-3.519500	3.131000
O	-1.111500	-0.395300	-0.526200
H	1.913300	0.802100	-0.223000
H	-1.966100	-0.762100	-0.217000

Table B-4 - Atomic coordinates of optimized structure of **9-plane**.

Ni	0.001900	0.097300	1.454700
O	2.247900	-0.172000	4.801900
O	-1.166600	-0.190900	0.010300
N	1.360600	0.208700	2.725300
C	1.293900	-0.254500	4.011700
C	0.002700	-0.986400	4.440000
C	-0.000400	-1.153200	5.964800
C	0.016100	-2.389900	3.775600
C	2.651100	0.624500	2.274500
C	2.896100	1.987200	2.002900
C	4.177100	2.378200	1.597600
H	4.369200	3.434400	1.395800
C	5.200800	1.441600	1.454200
H	6.196800	1.760500	1.141800
C	4.936300	0.090800	1.677500
H	5.719500	-0.652200	1.519000
C	3.664500	-0.341000	2.069100
C	1.781100	2.985400	2.114400
H	1.072200	2.835300	1.284400
H	2.155000	4.017000	2.068100
H	1.209000	2.846100	3.041100
C	3.374200	-1.804000	2.264000
H	3.310500	-2.044000	3.336700
H	4.154500	-2.423100	1.802500
H	2.405400	-2.071300	1.816800
H	0.010800	-2.313100	2.679900
H	-0.898500	-1.700700	6.275500
H	-0.871000	-2.958800	4.089200
H	-0.008300	-0.176500	6.464200
O	-2.258100	-0.199000	4.785900
N	-1.359200	0.166900	2.713800
C	-1.296600	-0.279700	4.004600
C	-2.640700	0.605800	2.257500
C	-2.875800	1.980700	2.046800
C	-4.142700	2.391700	1.614300
H	-4.328500	3.456200	1.454000
C	-5.161300	1.463300	1.399600
H	-6.145600	1.796700	1.066300
C	-4.909300	0.103700	1.584600
H	-5.690400	-0.628900	1.377500
C	-3.650900	-0.348300	1.994700
C	-1.769300	2.971800	2.268800
H	-0.998600	2.859800	1.490600
H	-2.141200	4.004700	2.240700
H	-1.263000	2.793900	3.227300
C	-3.359100	-1.815700	2.143200
H	-3.259000	-2.082800	3.206600
H	-4.156400	-2.421500	1.693400
H	-2.408900	-2.064100	1.648700
H	0.902600	-1.689000	6.281000
H	0.915600	-2.941200	4.084900
Ni	-0.001900	-0.097300	-1.454700
O	2.258100	0.199000	-4.785900
N	1.359200	-0.166900	-2.713800
C	1.296600	0.279700	-4.004600
C	-0.002700	0.986400	-4.440000
C	0.000400	1.153200	-5.964800
C	-0.016100	2.389900	-3.775600
C	2.640700	-0.605800	-2.257500
C	2.875800	-1.980700	-2.046800
C	4.142700	-2.391700	-1.614300
H	4.328500	-3.456200	-1.454000
C	5.161300	-1.463300	-1.399600
H	6.145600	-1.796700	-1.066300
C	4.909300	-0.103700	-1.584600
H	5.690400	0.628900	-1.377500
C	3.650900	0.348300	-1.994700
C	1.769300	-2.971800	-2.268800
H	0.998600	-2.859800	-1.490600
H	2.141200	-4.004700	-2.240700
H	1.263000	-2.793900	-3.227300
C	3.359100	1.815700	-2.143200
H	3.259000	2.082800	-3.206600
H	4.156400	2.421500	-1.693400

H	2.408900	2.064100	-1.648700
H	-0.010800	2.313100	-2.679900
H	-0.902600	1.689000	-6.281000
H	-0.915600	2.941200	-4.084900
H	0.008300	0.176500	-6.464200
O	-2.247900	0.172000	-4.801900
N	-1.360600	-0.208700	-2.725300
C	-1.293900	0.254500	-4.011700
C	-2.651100	-0.624500	-2.274500
C	-2.896100	-1.987200	-2.002900
C	-4.177100	-2.378200	-1.597600
H	-4.369200	-3.434400	-1.395800
C	-5.200800	-1.441600	-1.454200
H	-6.196800	-1.760500	-1.141800
C	-4.936300	-0.090800	-1.677500
H	-5.719500	0.652200	-1.519000
C	-3.664500	0.341000	-2.069100
C	-1.781100	-2.985400	-2.114400
H	-1.072200	-2.835300	-1.284400
H	-2.155000	-4.017000	-2.068100
H	-1.209000	-2.846100	-3.041100
C	-3.374200	1.804000	-2.264000
H	-3.310500	2.044000	-3.336700
H	-4.154500	2.423100	-1.802500
H	-2.405400	2.071300	-1.816800
H	0.898500	1.700700	-6.275500
H	0.871000	2.958800	-4.089200
O	1.166600	0.190900	-0.010300
H	-2.088900	0.129200	-0.005000
H	2.088900	-0.129200	0.005000

Table B-5 - Atomic coordinates of optimized structure of **10-seesaw**

Ni	-0.521700	1.356600	-0.102400
O	-3.681600	3.738400	0.434500
O	1.048700	0.468600	-0.541600
N	-2.179600	2.027300	0.219900
C	-2.556400	3.368300	0.102100
C	-1.547200	4.333000	-0.527000
C	-2.057100	5.770600	-0.367000
C	-1.414500	3.998700	-2.038800
C	-3.253900	1.125500	0.503300
C	-3.362900	0.562100	1.793200
C	-4.499500	-0.197600	2.089600
H	-4.614100	-0.605500	3.095200
C	-5.478100	-0.431100	1.124300
H	-6.359200	-1.023500	1.373400
C	-5.314400	0.064400	-0.169900
H	-6.055000	-0.161100	-0.938500
C	-4.206900	0.847400	-0.504600
C	-2.287800	0.790400	2.816300
H	-1.346400	0.321800	2.486900
H	-2.561500	0.360500	3.787500
H	-2.074100	1.859800	2.946900
C	-4.020700	1.384200	-1.896800
H	-4.213100	2.467400	-1.924600
H	-4.706000	0.897100	-2.601300
H	-2.989400	1.223500	-2.241900
H	-1.068800	2.969400	-2.202500
H	-1.350000	6.467400	-0.831300
H	-0.693800	4.686300	-2.501200
H	-2.154400	6.037800	0.691800
O	0.519600	5.234100	0.327700
N	0.364500	2.956200	0.289700
C	-0.137300	4.212800	0.094200
C	1.748200	2.870100	0.641300
C	2.111300	2.458200	1.942700
C	3.465400	2.465400	2.295200
H	3.751200	2.171000	3.306600
C	4.441700	2.848500	1.376000
H	5.492500	2.858000	1.668400
C	4.076800	3.190800	0.074100
H	4.844000	3.449100	-0.657200
C	2.734900	3.196600	-0.320800
C	1.058000	2.006100	2.912800
H	0.641700	1.036500	2.592700
H	1.465700	1.884100	3.924000
H	0.215000	2.709100	2.946200
C	2.340300	3.554000	-1.726600
H	1.916300	4.569300	-1.758600
H	3.205600	3.515100	-2.400000
H	1.570600	2.864500	-2.101700
H	-3.043300	5.869800	-0.835700
H	-2.385700	4.125000	-2.536200
Ni	0.494600	-1.335200	-0.351500
O	-0.457700	-5.146700	0.608700
N	-0.343300	-2.999200	-0.160300
C	0.156800	-4.079100	0.514600
C	1.508600	-3.901100	1.246100
C	2.041500	-5.271100	1.680300
C	1.241000	-3.029700	2.504700
C	-1.702000	-3.071700	-0.590300
C	-1.994700	-3.107600	-1.972000
C	-3.332900	-3.180600	-2.372700
H	-3.565900	-3.218900	-3.438500
C	-4.361900	-3.218700	-1.431300
H	-5.400500	-3.282200	-1.758400

C	-4.061800	-3.165500	-0.070000
H	-4.865300	-3.181100	0.666300
C	-2.739200	-3.073100	0.375000
C	-0.885600	-3.050100	-2.983000
H	-0.471400	-2.031200	-3.033100
H	-1.241600	-3.321700	-3.984700
H	-0.057600	-3.715900	-2.704400
C	-2.423800	-2.992600	1.843000
H	-1.995200	-3.942500	2.195800
H	-3.326000	-2.774400	2.425800
H	-1.681800	-2.205900	2.045300
H	0.877800	-2.027400	2.240100
H	2.987700	-5.148200	2.221600
H	2.163200	-2.924400	3.091700
H	2.226800	-5.914100	0.812500
O	3.669300	-3.685800	0.182400
N	2.190100	-1.985400	-0.209400
C	2.549800	-3.213400	0.363600
C	3.261300	-1.181700	-0.697200
C	3.343300	-0.890200	-2.081200
C	4.418400	-0.121900	-2.537200
H	4.498600	0.092300	-3.604300
C	5.387000	0.355300	-1.654600
H	6.221300	0.950300	-2.027800
C	5.278200	0.085000	-0.289900
H	6.016600	0.485800	0.404700
C	4.218700	-0.670800	0.216200
C	2.305000	-1.397800	-3.040100
H	1.381700	-0.803600	-2.944600
H	2.651000	-1.320500	-4.078400
H	2.039500	-2.441900	-2.832200
C	4.087300	-0.905100	1.696100
H	4.342300	-1.943500	1.954000
H	4.751500	-0.234900	2.254000
H	3.057700	-0.721400	2.034600
H	1.305800	-5.767600	2.323100
H	0.483600	-3.519500	3.131000
O	-1.111500	-0.395300	-0.526200
H	1.913300	0.802100	-0.223000
H	-1.966100	-0.762100	-0.217000

Table B-6 - Atomic coordinates of optimized structure of **8-oxo**.

Ni	-1.346000	0.038600	0.000000
O	-4.716800	-0.471900	2.242500
O	0.000100	-0.000200	-1.177400
N	-2.652000	0.059000	1.379100
C	-3.893700	-0.491300	1.304800
C	-4.243800	-1.253200	0.000000
C	-5.742100	-1.583500	0.000000
C	-3.439900	-2.581300	0.000000
C	-2.275200	0.561200	2.660200
C	-2.302700	1.947500	2.905100
C	-1.980400	2.421700	4.182900
H	-2.002300	3.498900	4.371300
C	-1.636400	1.537600	5.206600
H	-1.388900	1.916200	6.201300
C	-1.576800	0.168100	4.941500
H	-1.257500	-0.526400	5.720900
C	-1.869800	-0.334700	3.670400
C	-2.649600	2.888900	1.786700
H	-1.859700	2.864000	1.020400
H	-2.755400	3.923000	2.145800
H	-3.575400	2.583800	1.279000
C	-1.723900	-1.795000	3.349100
H	-2.702200	-2.247300	3.122700
H	-1.254400	-2.337500	4.180800
H	-1.087600	-1.901800	2.457600
H	-2.357800	-2.395100	0.000000
H	-5.995400	-2.153900	-0.902900
H	-3.691400	-3.171500	-0.894400
H	-6.342500	-0.664900	0.000000
O	-4.716800	-0.471900	-2.242500
N	-2.652000	0.059000	-1.379100
C	-3.893700	-0.491300	-1.304800
C	-2.275200	0.561200	-2.660200
C	-2.302700	1.947500	-2.905100
C	-1.980400	2.421700	-4.182900
H	-2.002300	3.498900	-4.371300
C	-1.636400	1.537600	-5.206600
H	-1.388900	1.916200	-6.201300
C	-1.576800	0.168100	-4.941500
H	-1.257500	-0.526400	-5.720900
C	-1.869800	-0.334700	-3.670400
C	-2.649600	2.888900	-1.786700
H	-1.859700	2.864000	-1.020400
H	-2.755400	3.923000	-2.145800
H	-3.575400	2.583800	-1.279000
C	-1.723900	-1.795000	-3.349100
H	-2.702200	-2.247300	-3.122700
H	-1.254400	-2.337500	-4.180800
H	-1.087600	-1.901800	-2.457600
H	-5.995400	-2.153900	0.902900
H	-3.691400	-3.171500	0.894400
Ni	1.346200	-0.039100	-0.000000

O	4.716100	0.474200	2.243000
N	2.652200	-0.059600	1.379000
C	3.893200	0.492200	1.304900
C	4.242900	1.254200	-0.000000
C	5.741100	1.585200	-0.000000
C	3.438500	2.581900	-0.000000
C	2.275500	-0.561600	2.660200
C	2.302500	-1.948000	2.905000
C	1.980500	-2.422200	4.182800
H	2.002000	-3.499400	4.371200
C	1.637200	-1.538000	5.206800
H	1.389900	-1.916600	6.201600
C	1.577900	-0.168500	4.941800
H	1.259000	0.526000	5.721300
C	1.870600	0.334300	3.670600
C	2.648500	-2.889500	1.786400
H	1.858300	-2.864100	1.020500
H	2.753900	-3.923700	2.145400
H	3.574200	-2.584800	1.278400
C	1.725000	1.794600	3.349400
H	2.703500	2.247000	3.124200
H	1.254600	2.337000	4.180800
H	1.089500	1.901700	2.457400
H	2.356500	2.395400	-0.000000
H	5.994100	2.155700	-0.902900
H	3.689800	3.172200	-0.894400
H	6.342000	0.666900	-0.000000
O	4.716100	0.474200	-2.243000
N	2.652200	-0.059600	-1.379000
C	3.893200	0.492200	-1.304900
C	2.275500	-0.561600	-2.660200
C	2.302500	-1.948000	-2.905000
C	1.980500	-2.422200	-4.182800
H	2.002000	-3.499400	-4.371200
C	1.637200	-1.538000	-5.206800
H	1.389900	-1.916600	-6.201600
C	1.577900	-0.168500	-4.941800
H	1.259000	0.526000	-5.721300
C	1.870600	0.334300	-3.670600
C	2.648500	-2.889500	-1.786400
H	1.858300	-2.864100	-1.020500
H	2.753900	-3.923700	-2.145400
H	3.574200	-2.584800	-1.278400
C	1.725000	1.794600	-3.349400
H	2.703500	2.247000	-3.124200
H	1.254600	2.337000	-4.180800
H	1.089500	1.901700	-2.457400
H	5.994100	2.155700	0.902900
H	3.689800	3.172200	0.894400
O	0.000100	-0.000200	1.177400

Table B-7 - Atomic coordinates of optimized structure of **9-oxo**.

Ni	-1.346000	0.038600	0.000000
O	-4.716800	-0.471900	2.242500
O	0.000100	-0.000200	-1.177400
N	-2.652000	0.059000	1.379100
C	-3.893700	-0.491300	1.304800
C	-4.243800	-1.253200	0.000000
C	-5.742100	-1.583500	0.000000
C	-3.439900	-2.581300	0.000000
C	-2.275200	0.561200	2.660200
C	-2.302700	1.947500	2.905100
C	-1.980400	2.421700	4.182900
H	-2.002300	3.498900	4.371300
C	-1.636400	1.537600	5.206600
H	-1.388900	1.916200	6.201300
C	-1.576800	0.168100	4.941500
H	-1.257500	-0.526400	5.720900
C	-1.869800	-0.334700	3.670400
C	-2.649600	2.888900	1.786700
H	-1.859700	2.864000	1.020400
H	-2.755400	3.923000	2.145800
H	-3.575400	2.583800	1.279000
C	-1.723900	-1.795000	3.349100
H	-2.702200	-2.247300	3.122700
H	-1.254400	-2.337500	4.180800
H	-1.087600	-1.901800	2.457600
H	-2.357800	-2.395100	0.000000
H	-5.995400	-2.153900	-0.902900
H	-3.691400	-3.171500	-0.894400
H	-6.342500	-0.664900	0.000000
O	-4.716800	-0.471900	-2.242500
N	-2.652000	0.059000	-1.379100
C	-3.893700	-0.491300	-1.304800
C	-2.275200	0.561200	-2.660200
C	-2.302700	1.947500	-2.905100
C	-1.980400	2.421700	-4.182900
H	-2.002300	3.498900	-4.371300
C	-1.636400	1.537600	-5.206600
H	-1.388900	1.916200	-6.201300
C	-1.576800	0.168100	-4.941500
H	-1.257500	-0.526400	-5.720900
C	-1.869800	-0.334700	-3.670400
C	-2.649600	2.888900	-1.786700

H	-1.859700	2.864000	-1.020400
H	-2.755400	3.923000	-2.145800
H	-3.575400	2.583800	-1.279000
C	-1.723900	-1.795000	-3.349100
H	-2.702200	-2.247300	-3.122700
H	-1.254400	-2.337500	-4.180800
H	-1.087600	-1.901800	-2.457600
H	-5.995400	-2.153900	0.902900
H	-3.691400	-3.171500	0.894400
Ni	1.346200	-0.039100	-0.000000
O	4.716100	0.474200	2.243000
N	2.652200	-0.059600	1.379000
C	3.893200	0.492200	1.304900
C	4.242900	1.254200	-0.000000
C	5.741100	1.585200	-0.000000
C	3.438500	2.581900	-0.000000
C	2.275500	-0.561600	2.660200
C	2.302500	-1.948000	2.905000
C	1.980500	-2.422200	4.182800
H	2.002000	-3.499400	4.371200
C	1.637200	-1.538000	5.206800
H	1.389900	-1.916600	6.201600
C	1.577900	-0.168500	4.941800
H	1.259000	0.526000	5.721300
C	1.870600	0.334300	3.670600
C	2.648500	-2.889500	1.786400
H	1.858300	-2.864100	1.020500
H	2.753900	-3.923700	2.145400
H	3.574200	-2.584800	1.278400
C	1.725000	1.794600	3.349400
H	2.703500	2.247000	3.124200
H	1.254600	2.337000	4.180800
H	1.089500	1.901700	2.457400
H	2.356500	2.395400	-0.000000
H	5.994100	2.155700	-0.902900
H	3.689800	3.172200	-0.894400
H	6.342000	0.666900	-0.000000
O	4.716100	0.474200	-2.243000
N	2.652200	-0.059600	-1.379000
C	3.893200	0.492200	-1.304900
C	2.275500	-0.561600	-2.660200
C	2.302500	-1.948000	-2.905000
C	1.980500	-2.422200	-4.182800
H	2.002000	-3.499400	-4.371200
C	1.637200	-1.538000	-5.206800
H	1.389900	-1.916600	-6.201600
C	1.577900	-0.168500	-4.941800
H	1.259000	0.526000	-5.721300
C	1.870600	0.334300	-3.670600
C	2.648500	-2.889500	-1.786400
H	1.858300	-2.864100	-1.020500
H	2.753900	-3.923700	-2.145400
H	3.574200	-2.584800	-1.278400
C	1.725000	1.794600	-3.349400
H	2.703500	2.247000	-3.124200
H	1.254600	2.337000	-4.180800
H	1.089500	1.901700	-2.457400
H	5.994100	2.155700	0.902900
H	3.689800	3.172200	0.894400
O	0.000100	-0.000200	1.177400

Table B-8 - Atomic coordinates of optimized structure of **10-oxo**.

Ni	-0.002700	0.147600	1.339500
O	2.210800	-0.036200	4.761700
O	-1.175700	-0.029300	0.004600
N	1.368200	0.282500	2.646200
C	1.284100	-0.148800	3.933500
C	-0.014400	-0.894700	4.336900
C	-0.021800	-1.099900	5.857300
C	0.001000	-2.284300	3.645400
C	2.651200	0.758900	2.240600
C	2.916400	2.141600	2.234200
C	4.190400	2.590300	1.864200
H	4.394400	3.664900	1.856300
C	5.192800	1.683500	1.515400
H	6.184900	2.042100	1.230000
C	4.912900	0.316000	1.510800
H	5.678300	-0.398300	1.202600
C	3.643500	-0.162400	1.850100
C	1.827100	3.105100	2.613800
H	1.013000	3.065900	1.876000
H	2.202800	4.137400	2.666800
H	1.378900	2.834500	3.580800
C	3.309100	-1.625400	1.777300
H	3.053900	-2.020800	2.772800
H	4.144500	-2.201800	1.357800
H	2.431500	-1.758400	1.126700
H	0.013300	-2.188100	2.551800
H	-0.920900	-1.656400	6.151600
H	-0.893900	-2.856300	3.934400
H	-0.034200	-0.134800	6.379600
O	-2.265100	-0.094900	4.730700
N	-1.390000	0.272800	2.634300
C	-1.322300	-0.174700	3.917000

C	-2.667300	0.746000	2.212200
C	-2.890900	2.129700	2.074300
C	-4.169800	2.584400	1.729600
H	-4.341300	3.659500	1.625400
C	-5.214700	1.683800	1.517600
H	-6.210300	2.047700	1.252300
C	-4.968100	0.312300	1.606100
H	-5.763400	-0.401900	1.382500
C	-3.697400	-0.173900	1.927100
C	-1.747000	3.084800	2.264400
H	-1.010300	2.942200	1.457100
H	-2.084200	4.131400	2.247800
H	-1.211000	2.888500	3.203100
C	-3.397300	-1.645800	1.933300
H	-3.188800	-1.999700	2.955300
H	-4.233300	-2.220500	1.511600
H	-2.501300	-1.830100	1.321700
H	0.884700	-1.638500	6.162500
H	0.894600	-2.847600	3.955100
Ni	0.002700	-0.147600	-1.339500
O	2.265100	0.094900	-4.730700
N	1.390000	-0.272800	-2.634300
C	1.322300	0.174700	-3.917000
C	0.014400	0.894700	-4.336900
C	0.021800	1.099900	-5.857300
C	-0.001000	2.284300	-3.645400
C	2.667300	-0.746000	-2.212200
C	2.890900	-2.129700	-2.074300
C	4.169800	-2.584400	-1.729600
H	4.341300	-3.659500	-1.625400
C	5.214700	-1.683800	-1.517600
H	6.210300	-2.047700	-1.252300
C	4.968100	-0.312300	-1.606100
H	5.763400	0.401900	-1.382500
C	3.697400	0.173900	-1.927100
C	1.747000	-3.084800	-2.264400
H	1.010300	-2.942200	-1.457100
H	2.084200	-4.131400	-2.247800
H	1.211000	-2.888500	-3.203100
C	3.397300	1.645800	-1.933300
H	3.188800	1.999700	-2.955300
H	4.233300	2.220500	-1.511600
H	2.501300	1.830100	-1.321700
H	-0.013300	2.188100	-2.551800
H	-0.884700	1.638500	-6.162500
H	-0.894600	2.847600	-3.955100
H	0.034200	0.134800	-6.379600
O	-2.210800	0.036200	-4.761700
N	-1.368200	-0.282500	-2.646200
C	-1.284100	0.148800	-3.933500
C	-2.651200	-0.758900	-2.240600
C	-2.916400	-2.141600	-2.234200
C	-4.190400	-2.590300	-1.864200
H	-4.394400	-3.664900	-1.856300
C	-5.192800	-1.683500	-1.515400
H	-6.184900	-2.042100	-1.230000
C	-4.912900	-0.316000	-1.510800
H	-5.678300	0.398300	-1.202600
C	-3.643500	0.162400	-1.850100
C	-1.827100	-3.105100	-2.613800
H	-1.013000	-3.065900	-1.876000
H	-2.202800	-4.137400	-2.666800
H	-1.378900	-2.834500	-3.580800
C	-3.309100	1.625400	-1.777300
H	-3.053900	2.020800	-2.772800
H	-4.144500	2.201800	-1.357800
H	-2.431500	1.758400	-1.126700
H	0.920900	1.656400	-6.151600
H	0.893900	2.856300	-3.934400
O	1.175700	0.029300	-0.004600

Table B-9 - Atomic coordinates of optimized structure of **9-DMF**.

Ni	-1.341600	-0.561500	-0.329400
O	-3.371800	-4.101500	-0.414500
N	-1.907000	-2.375500	-0.148400
C	-3.059100	-2.913100	-0.619000
C	-3.936400	-1.997400	-1.492800
C	-5.275200	-2.692300	-1.766900
C	-3.199700	-1.759800	-2.838100
C	-1.031600	-3.226100	0.579800
C	-1.186200	-3.368800	1.977300
C	-0.215800	-4.079400	2.695200
H	-0.319400	-4.173100	3.779100
C	0.870900	-4.666600	2.041900
H	1.633900	-5.198000	2.614100
C	0.958700	-4.603700	0.649800
H	1.777600	-5.100700	0.128200
C	0.000200	-3.910400	-0.103300
C	-2.402900	-2.795500	2.644000
H	-2.320900	-2.830200	3.739200
H	-3.292400	-3.365900	2.334400
H	-2.569000	-1.760700	2.324800
C	0.000700	-3.967600	-1.609800
H	-0.790500	-4.661200	-1.936400
H	0.967100	-4.313000	-1.996600
H	-0.228300	-2.992100	-2.055600

H	-2.233600	-1.256100	-2.694100
H	-5.899100	-2.057900	-2.408300
H	-3.817700	-1.134400	-3.498400
H	-5.819500	-2.870600	-0.831500
O	-5.342300	-0.122500	-0.889700
N	-3.142500	0.051400	-0.307100
C	-4.202200	-0.617600	-0.846000
C	-3.381600	1.410700	0.061900
C	-3.672200	1.744100	1.401100
C	-3.904600	3.086800	1.728500
H	-4.133500	3.347700	2.764700
C	-3.879400	4.078400	0.748700
H	-4.058000	5.121100	1.018000
C	-3.621100	3.734300	-0.578200
H	-3.597400	4.507500	-1.347700
C	-3.371000	2.408000	-0.943400
C	-3.796700	0.666500	2.441500
H	-2.817300	0.217900	2.652300
H	-4.212500	1.066100	3.377100
H	-4.450600	-0.140800	2.081300
C	-3.147900	2.030100	-2.382600
H	-3.995100	1.428300	-2.747000
H	-3.053100	2.924500	-3.012700
H	-2.236700	1.426900	-2.485700
H	-5.097600	-3.663300	-2.246100
H	-3.013000	-2.722400	-3.336200
O	-0.575200	1.149200	-0.776800
H	-0.899600	1.898300	-0.239700
Ni	1.349700	0.689500	-0.577500
O	5.355500	-0.001400	-0.287200
N	3.090100	-0.047000	-0.632800
C	4.226400	0.480100	-0.086200
C	4.065600	1.659800	0.898200
C	5.445400	2.264200	1.189300
C	3.476300	1.079200	2.210900
C	3.240400	-1.276100	-1.348300
C	3.005200	-1.321000	-2.742300
C	3.159000	-2.535900	-3.419400
H	2.982900	-2.565700	-4.497000
C	3.538000	-3.696500	-2.743000
H	3.659100	-4.635400	-3.286200
C	3.744700	-3.650300	-1.364400
H	4.030900	-4.555800	-0.824200
C	3.589200	-2.456600	-0.649100
C	2.581600	-0.081800	-3.480000
H	1.516500	0.125900	-3.283500
H	2.715900	-0.194800	-4.564400
H	3.141600	0.796400	-3.132800
C	3.816800	-2.424400	0.835600
H	4.822200	-2.033600	1.056800
H	3.703800	-3.422100	1.279800
H	3.105700	-1.737700	1.315300
H	2.473600	0.672000	2.031600
H	5.345200	3.082900	1.911900
H	3.403200	1.870300	2.972000
H	5.891800	2.670600	0.273100
O	3.371300	3.965500	0.720900
N	1.934900	2.413400	-0.154800
C	3.103500	2.781900	0.449800
C	0.992700	3.471500	-0.356200
C	0.818400	4.020200	-1.641200
C	-0.089600	5.073200	-1.805000
H	-0.224100	5.509000	-2.797900
C	-0.816700	5.566300	-0.721300
H	-1.525300	6.384100	-0.863300
C	-0.667000	4.985400	0.538700
H	-1.271100	5.335900	1.376800
C	0.224600	3.927200	0.738600
C	1.588100	3.453800	-2.801100
H	1.443600	4.052100	-3.710800
H	2.662200	3.396000	-2.574200
H	1.255700	2.423800	-3.001100
C	0.370500	3.263600	2.081700
H	1.359000	3.482200	2.514700
H	-0.409000	3.604600	2.776200
H	0.293700	2.170700	1.977800
H	6.118000	1.488700	1.575900
H	4.127300	0.279000	2.592800
O	0.450200	-0.982600	-0.917400
H	0.902600	-1.794800	-0.620400
N	0.626700	-0.641800	3.506700
C	1.739000	-1.427600	4.014000
H	2.084500	-2.117200	3.235600
H	2.571000	-0.772500	4.314000
H	1.414500	-2.021400	4.882900
C	-0.023400	0.286000	4.421000
H	0.715500	1.003700	4.808600
H	-0.805100	0.828100	3.879300
H	-0.472200	-0.259000	5.266000
O	-0.776900	-0.167200	1.765000
C	0.207500	-0.771000	2.233500
H	0.816300	-1.455900	1.623200

Table B-10 - Atomic coordinates of optimized structure of **10-2DMF**.

Ni	1.455900	0.033100	0.010000	Ni	-1.536600	0.013400	0.210000
O	4.739000	-2.048500	1.169400	O	-4.464600	-2.497000	-1.083500
N	2.795100	-1.290200	0.263800	N	-2.771000	-1.404300	-0.032000
C	3.937500	-1.119000	0.995500	C	-3.779700	-1.473200	-0.951400
C	4.145400	0.238500	1.686300	C	-3.984000	-0.275300	-1.894400
C	5.579300	0.317000	2.225000	C	-5.360100	-0.386100	-2.562600
C	3.150500	0.329100	2.874000	C	-2.876100	-0.346200	-2.978600
C	2.548700	-2.607000	-0.223300	C	-2.512100	-2.569300	0.748200
C	2.931900	-2.945300	-1.540500	C	-2.973400	-2.652400	2.079800
C	2.647200	-4.230900	-2.018700	C	-2.619000	-3.774000	2.841100
H	2.933300	-4.494800	-3.039300	H	-2.965200	-3.840500	3.875000
C	2.054600	-5.184900	-1.188600	C	-1.879000	-4.818500	2.287700
H	1.854400	-6.189300	-1.564600	H	-1.623700	-5.690200	2.892200
C	1.747800	-4.859800	0.133800	C	-1.500500	-4.762900	0.945400
H	1.331500	-5.617200	0.798400	H	-0.972200	-5.600300	0.489900
C	1.975000	-3.572800	0.636600	C	-1.801500	-3.645600	0.161500
C	3.704900	-1.958400	-2.370500	C	-3.898700	-1.616800	2.659900
H	3.650600	-2.195000	-3.441900	H	-3.438400	-1.101300	3.514100
H	4.764100	-1.975200	-2.069500	H	-4.824800	-2.095600	3.010500
H	3.356200	-0.933900	-2.204600	H	-4.160700	-0.860600	1.913400
C	1.709100	-3.247200	2.082200	C	-1.454300	-3.628600	-1.304100
H	2.662700	-3.238200	2.633600	H	-2.287800	-4.050600	-1.886600
H	1.037700	-3.986800	2.536200	H	-0.543900	-4.210100	-1.506600
H	1.257200	-2.252800	2.185500	H	-1.320400	-2.600200	-1.665000
H	2.102800	0.279400	2.542400	H	-1.880300	-0.219800	-2.534400
H	5.731600	1.272100	2.741500	H	-5.502100	0.445300	-3.263100
H	3.301800	1.280800	3.402900	H	-3.027500	0.453200	-3.717600
H	6.305600	0.254600	1.406000	H	-6.160000	-0.339200	-1.813700
O	4.631400	2.431400	0.798500	O	-4.629800	2.018200	-1.498600
N	2.771200	1.414500	-0.031500	N	-2.789700	1.295700	-0.374400
C	3.882300	1.444600	0.763500	C	-3.854600	1.095900	-1.210800
C	2.442800	2.621400	-0.717100	C	-2.582900	2.626600	0.091100
C	2.759100	2.767500	-2.087500	C	-3.157400	3.048800	1.309500
C	2.437300	3.969900	-2.728600	C	-2.884200	4.346000	1.760400
H	2.683600	4.089500	-3.785800	H	-3.316800	4.681900	2.705200
C	1.862600	5.029500	-2.025400	C	-2.113900	5.224500	0.994100
H	1.637200	5.967500	-2.535200	H	-1.925600	6.238600	1.350000
C	1.607000	4.894700	-0.661200	C	-1.619000	4.816900	-0.245000
H	1.197800	5.733100	-0.096100	H	-1.061100	5.514500	-0.868400
C	1.877600	3.697900	0.010000	C	-1.832500	3.514900	-0.710900
C	3.509800	1.695700	-2.828500	C	-4.108500	2.146900	2.045900
H	2.834000	0.902500	-3.175500	H	-4.444400	2.603000	2.986300
H	4.024700	2.114300	-3.703400	H	-4.992400	1.954900	1.418300
H	4.254700	1.222900	-2.175300	H	-3.655300	1.173300	2.263000
C	1.659200	3.600200	1.496400	C	-1.345200	3.086900	-2.072800
H	2.593500	3.847800	2.024400	H	-2.199900	3.014000	-2.763900
H	0.869900	4.292700	1.820400	H	-0.616800	3.801200	-2.475400
H	1.377400	2.580600	1.782400	H	-0.877700	2.090200	-2.056000
H	5.766800	-0.519200	2.909300	H	-5.443200	-1.344800	-3.088000
H	3.329200	-0.498800	3.574900	H	-2.917700	-1.317800	-3.492000
O	-0.024500	1.247500	0.310400	O	0.005200	-1.137200	0.468000
H	-0.029000	2.014300	-0.292800	H	-0.021800	-2.075100	0.202300

N	0.346400	-1.052500	-3.881000
C	0.037100	-2.340000	-4.492300
H	0.258300	-3.145100	-3.781300
H	-1.026500	-2.385100	-4.770100
H	0.648500	-2.482400	-5.394900
C	0.198100	0.149800	-4.696500
H	-0.834300	0.218400	-5.068200
H	0.424300	1.028200	-4.083200
H	0.886700	0.109200	-5.552500
O	0.955700	0.093100	-2.001500
C	0.690600	-0.981500	-2.591900
H	0.750100	-1.949200	-2.075400
N	-0.232400	0.816300	3.974000
C	-0.099600	-0.526300	4.535300
H	-0.506300	-1.248800	3.818700
H	0.963800	-0.738500	4.714200
H	-0.645500	-0.602700	5.487400
C	0.395600	1.923400	4.682900
H	0.271500	2.846700	4.104900
H	-0.060000	2.054100	5.676200
H	1.469400	1.725600	4.808000
O	-1.567700	0.103000	2.279100
C	-0.933200	1.019400	2.850200
H	-0.916800	2.047200	2.458000